TECHNISCHE UNIVERSITÄT MÜNCHEN

Lehrstuhl für Kommunikation und Navigation

Reliable Carrier Phase Positioning

Patrick Henkel

Vollständiger Abdruck der von der Fakultät für Elektrotechnik und Informationstechnik der Technischen Universität München zur Erlangung des akademischen Grades eines

Doktor–Ingenieurs

genehmigten Dissertation.

Vorsitzender:	Univ.–Prof. Dr.–techn. J. A. Nossek
Prüfer der Dissertation:	
	1. Univ.–Prof. Dr. sc. nat. Chr.-G. Günther
	2. Prof. P. Enge, Ph.D., Stanford University, California/USA
	3. Prof. Dr. ir. S. Verhagen, Delft University of Technology, Niederlande

Die Dissertation wurde am 5.07.2010 bei der Technischen Universität München eingereicht und durch die Fakultät für Elektrotechnik und Informationstechnik am 30.08.2010 angenommen.

Preface

Currently, the Global Navigation Satellite Systems (GNSS) GPS and GLONASS are modernized and new GNSS such as Galileo and Compass are developed. The modernization of GPS includes an additional signal on L5 which lies in an aeronautical band. This will enable a dual frequency positioning on board an aircraft and an elimination of the dispersive ionospheric delay, which is one of the largest error sources for current single frequency receivers. Dataless pilot signals will be introduced on all GPS frequencies which will enable a longer integration time and faster signal acquisition. Moreover, the Multiplexed Binary Offset Carrier (MBOC) modulation will be used on L1. Galileo uses larger signal bandwidths than GPS, which will substantially reduce the code tracking error and improve the positioning accuracy. For example, the Alternate BOC modulated E5 signal has a bandwidth of 92.07 MHz, which enables a five times lower code tracking error than the BPSK(10) modulated GPS L5 signal. The additional frequencies and new signals will improve the estimation and elimination of ionospheric delays, which is one of the major error sources for positioning.

The GPS and Galileo satellites transmit spread spectrum signals that enable a positioning accuracy of 1 m. A significantly higher positioning accuracy can be achieved with the carrier phase which can be tracked with millimeter accuracy. However, the carrier phase is period and requires the resolution of an integer ambiguity for each satellite. The reliability of this integer ambiguity resolution was so far limited by the small carrier wavelength of 19.0 cm, receiver and satellite biases, multipath and a large number of unknown atmospheric delays, which result in an ill-conditioned equation system and a probability of wrong fixing of a few percent. This thesis provides new algorithms and methods to reduce the failure rate by more than seven orders of magnitude. The key to reliable integer ambiguity resolution are multi-frequency linear combinations that eliminate the ionospheric delay, increase the wavelength to more than 3 m and keep the noise at a centimeter level. There exist two further challenges for carrier phase positioning that are addressed in this thesis: one is a continuous tracking of the carrier phases in environments with strong multipath and/ or during ionospheric scintillations, and the second one is a precise estimation of both receiver and satellite phase biases.

The first chapter gives an intuitive introduction to the suggested methods for reliable integer ambiguity resolution. Moreover, the benefits of the Galileo system are described, and a model for the code and carrier phase measurements is given.

In the second chapter, different groups of new multi-frequency mixed code carrier linear combinations are derived. The chapter starts with the derivation of phase-only linear combinations and then shows the benefit of including code measurements. The additional degrees of freedom are used to minimize the noise, to maximize the wavelength, to constrain the worst-case bias amplification and/ or to maximize the ratio between the wavelength and the combined noise. For the latter approach, geometry-preserving, ionosphere-free linear code carrier combinations with a wavelength of more than 3 m and a noise of a few centimeters were found. The large wavelength in relation to the geometry-preserving property substantially improves the robustness of ambiguity resolution over orbital errors, satellite clock offsets and tropospheric modeling errors. Therefore, this group of multi-frequency linear combinations are an interesting candidate for both Wide-Area Real-Time Kinematics and Precise Point Positioning applications. For dual frequency measurements, these combinations show a substantial benefit over phase-only linear combinations, which can not simultaneously increase the wavelength and eliminate the ionospheric delay. The use of further frequencies enables an even larger ambiguity discrimination and a lower probability of wrong fixing. This chapter also includes the derivation of a multi-frequency carrier smoothing where the phase-only combination and the code carrier combination are jointly optimized. Two further groups of new carrier smoothed multi-frequency code carrier linear combinations are analyzed: the first one includes geometry-free, ionosphere-preserving and the second one geometry-free, ionosphere-free linear combinations. The latter ones provide a direct estimate of the integer ambiguities. Additionally, the capability of detecting erroneous fixings is maximized by a set of linear combinations that minimizes the probability of the most likely undetectable uncombined integer error vector. The chapter ends with code carrier linear combinations including next generation C-band signals and with linear combinations for estimating second order ionospheric effects.

The third chapter contains several methods to improve the reliability of carrier phase integer ambiguity resolution, and starts with a description of the currently used integer ambiguity resolution techniques: rounding, sequential conditional rounding (bootstrapping), integer least-squares estimation (including a search) and integer aperture estimation. It is shown that the optimized multi-frequency code carrier linear combinations enable a reduction of the probability of wrong fixing by several orders of magnitude, and that a flat ambiguity spectrum and an extremely efficient search can be achieved with two multi-frequency linear combinations even without an integer decorrelation. A sequential conditional ambiguity fixing is proposed which outperforms the traditional bootstrapping as it reduces the impact of erroneous fixings by slightly lower weights. A partial integer decorrelation transformation is used to obtain an optimum trade-off between variance reduction and worst-case bias amplification, a new cascaded ambiguity resolution scheme with three carrier smoothed ionosphere-free code carrier combinations is provided, and a partial ambiguity fixing is given where the optimal fixing order is obtained from a combined forward-backward search while traditional approaches use only a pure forward search. The optimal fixing order enables a significant increase in the number of reliably fixable ambiguities for worst-case biases. Finally, the integrity risk due to an erroneous fixing is evaluated for aircraft landings. The most stringent landing category CAT IIIc with a vertical alarm limit of 5.3 m and a time to alert of only 2 s has been chosen. The

integrity risk is substantially lower than the probability of wrong fixing as a large number of erroneous fixings does not necessarily result in an integrity threat. It is shown that the risk of an integrity threat is two orders of magnitude lower than the probability of wrong fixing for the optimized dual frequency E1-E5a linear combinations. Moreover, the large wavelength of the optimized dual frequency E1-E5a code carrier linear combination ensures that the set of erroneous fixing vectors remains sufficiently small, and that the probability of wrong fixing is significantly lower than for uncombined measurements.

The fourth chapter focuses on a new method for improving the reliability of carrier phase tracking. A vector phase locked loop for joint tracking of carrier phases and Doppler shifts is presented. Additionally, a method for correcting the signal distortion due to wideband ionospheric effects is suggested. It is required for precise point positioning with Galileo as the bandwidth of the E5 signal is so large that the ionospheric dispersion within the E5 band can no longer be neglected.

In chapter 5, a method for estimating the receiver and satellite phase and code biases as well as for estimating the vertical ionospheric grid based on measurements from a network of reference stations is suggested. The method includes several parameter mappings and a Kalman filter, and is validated with dual frequency GPS measurements from CORS and SAPOS reference stations.

Chapter 6 includes a validation of the analyzed differential carrier phase positioning algorithms with real data. GPS measurements from a stationary baseline on top of the university's building as well as kinematic measurements from a flight campaign of the institute were used. Range residuals of less than 10 % of the wavelength were observed which indicate a quite reliable integer ambiguity resolution. Finally, chapter 7 summarizes this work.

List of publications

Journals:

[1] Patrick Henkel and Christoph Günther, Partial integer decorrelation for optimum trade-off between variance reduction and bias amplification, *Journal of Geodesy*, pp. 51-63, vol. 84, numb. 1, 2009.

[2] Patrick Henkel, Geometry-free linear combinations for Galileo, *Acta Astronautica*, vol. 65, pp. 1487-1499, 2009.

[3] Patrick Henkel, Kaspar Giger and Christoph Günther, Multi-satellite, multi-frequency Vector Phase Locked Loop for Robust Carrier Tracking, *IEEE Journal of Selected Topics in Signal Processing* (J-STSP), Spec. Issue on Advanced Signal Processing for GNSS and Robust Navigation, vol. 3, iss. 4, pp. 674-681, Aug. 2009.

[4] Christoph Günther and Patrick Henkel, Reduced noise, ionosphere-free carrier smoothed code, *IEEE Transactions on Aerospace Engineering*, vol. 46, iss. 1, pp. 323-334, 2008.

[5] Patrick Henkel and Christoph Günther, Joint L/C-Band Code and Carrier Phase Linear Combinations for Galileo, *International Journal of Navigation and Observation*, vol. 2008, Hindawi publ., 8 pages, Jan. 2008.

Conferences:

[1] Patrick Henkel and Christoph Günther, Reliable Integer Ambiguity Resolution with Multi-Frequency Code Carrier Linear Combinations, *Proc. of 23rd ION Int. Techn. Meeting* (ION-GNSS), Portland, USA, Sep. 2010

[2] Patrick Henkel, Zhibo Wen and Christoph Günther, Estimation of satellite and receiver biases on multiple Galileo frequencies with a Kalman filter, *Proc. of ION Int. Techn. Meeting*, San Diego, USA, pp. 1067-1074, Jan. 2010

[3] Kaspar Giger, Patrick Henkel and Christoph Günther, Joint satellite code and carrier tracking, *Proc. of ION Int. Techn. Meeting*, San Diego, USA, pp. 636-645, Jan. 2010.

[4] Markus Rippl, Susanne Schlötzer and Patrick Henkel, High integrity carrier phase based positioning for precision landing using a robust nonlinear filter, *Proc. of ION Int. Techn. Meeting*, San Diego, USA, pp. 577-590, Jan. 2010.

[5] Patrick Henkel, Zhibo Wen and Christoph Günther, Estimation of code and phase biases on multiple frequencies with a Kalman filter, *Proc. of 4-th European Workshop on GNSS Signals and Signal Processing*, Oberpfaffenhofen, Germany, Dec. 2009.

[6] Kaspar Giger, Patrick Henkel and Christoph Günther, Multifrequency, multisatellite carrier tracking, *Proc. of 4-th European Workshop on GNSS Signals and Signal Processing*, Oberpfaffenhofen, Germany, Dec. 2009.

[7] Patrick Henkel, Bootstrapping with Partial Integer Decorrelation and Multi-frequency combinations of Galileo measurements in the presence of Biases, *Proc. of Intern. Assoc. of Geodesy Scient. Assembly* (IAG), Buenoes Aires, Argentina, Sep. 2009.

[8] Patrick Henkel, Grace Gao, Todd Walter and Christoph Günther, Robust Multi-Carrier, Multi-Satellite Vector Phase Locked Loop with Wideband Ionospheric Correction and Integrated Weighted RAIM, *Proc. of European Navigation Conference* (ENC), Naples, Italy, May 2009.

[9] Patrick Henkel, Victor Gomez and Christoph Günther, Modified LAMBDA for precise carrier phase positioning with multiple frequencies in the presence of biases, *Proc. of ION Intern. Techn. Meeting* (ITM), Anaheim, USA, pp. 642-651, Jan. 2009.

[10] Patrick Henkel and Christoph Günther, Precise Point Positioning with multiple Galileo frequencies, *Proc. of ION/ IEEE Position, Location and Navigation Symposium* (PLANS), Monterey, USA, pp. 592-599, May 2008.

[11] Patrick Henkel, Kaspar Giger and Christoph Günther, Multi-Carrier Vector Phase Locked Loop for Robust Carrier Tracking, *Proc. of European Navigation Conference* (ENC), Toulouse, France, Apr. 2008.

[12] Patrick Henkel and Christoph Günther, Schätzung der Trägerphasenmehrdeutigkeit bei Galileo, *Proc. of "10. ITG-Fachgruppensitzung Signalverarbeitung in der Navigation"*, Oberpfaffenhofen, Oct. 2007.

[13] Patrick Henkel, Geometry-free linear combinations for Galileo, *Proc. of 58-th International Astronautical Congress* (IAC), 1st prize of international student contest (Pierre Contensou Gold Medal), Hyderabad, India, Sep. 2007.

[14] Matthias Süss, Patrick Henkel and Yuan Lu, Steering of the reference timescale for German Galileo test environment, *Proc. of European Frequency and Time Forum* (EFTF), Geneva, Switzerland, May 2007.

[15] Patrick Henkel, Doping of Extended Mappings for Signal Shaping, *Proc. of 65-th IEEE Vehicular Technology Conference* (VTC), Dublin, Ireland, May 2007.

[16] Patrick Henkel and Christoph Günther, Sets of robust full-rank linear combinations for wide-area differential ambiguity fixing, *Proc. of 2nd Workshop on GNSS Signals and Signal Processing*, Noordwijk (ESTEC), The Netherlands, 5 pp., Apr. 2007.

[17] Patrick Henkel and Christoph Günther, Three frequency linear combinations for Galileo, *Proc. of 4-th IEEE Workshop on Positioning, Navigation and Communication* (WPNC Æ07), Hannover, Germany, pp. 239-245, Mar. 2007.

[18] Patrick Henkel and Christoph Günther, Integrity Analysis of Cascade Integer Resolution with Decorrelation Transformations, *Proc. of ION National Technical Meeting* (NTM), San Diego, USA, pp. 903-910, Jan. 2007.

[19] Patrick Henkel, Extended Mappings for Bit-Interleaved Coded Modulation, *Proc. of 17-th IEEE Symposium on Personal, Indoor and Mobile Communications* (PIMRC), Helsinki, Finland, Sep. 2006.

[20] Patrick Henkel, Integrity of differential carrier phase positioning, *Proc. of 14-th Joint Conference on Coding and Communications*, Sölden, Austria, Mar. 2006.

[21] Frank Schreckenbach and Patrick Henkel, Signal Shaping using Non-Unique Symbol Mappings, *Proc. of 43rd Annual Allerton Conference on Communication, Control, and Computing*, Monticello, USA, Sep. 2005.

[22] Frank Schreckenbach, Patrick Henkel, Norbert Görtz and Gerhard Bauch, Analysis and Design of Mappings for Iterative Decoding of BICM, *Proc. of 11-th National Symposium on Radio Sciences*, URSI, Poznan, Poland, pp. 82-87, Apr. 2005.

Invited talks:

[1] Patrick Henkel, Single and multi-frequency Differential GNSS, *Carl Cranz Gesellschaft*, Oberpfaffenhofen, Oct. 2009.

[2] Patrick Henkel, Vector Phase Locked Loops for Reliable Carrier Tracking during Ionospheric Scintillations, *Stanford University*, Oct. 2008.

[3] Patrick Henkel, Vector Loops for Interference Robust Navigation, *Stanford-DLR Workshop*, Oberpfaffenhofen, Sep. 2008.

[4] Patrick Henkel, Zuverlässige Schätzung der Trägerphasenmehrdeutigkeiten bei Galileo, *Kolloquium Satellitennavigation*, Technische Universität München (TUM), July 2008.

[5] Patrick Henkel, Integrität bei Trägerphasenmessungen, *ITG Sitzung Galileo und Anwendungen*, Deutsches Zentrum für Luft- und Raumfahrt (DLR), Oberpfaffenhofen, June 2008.

[6] Patrick Henkel, Precise Carrier Phase Positioning with Galileo, *Moscow-Bavarian Joint Advanced Student School* (MB-JASS), Moscow, Russia, Mar. 2008.

[7] Patrick Henkel, Wide-Area RTK and Precise Point Positioning with mixed Code-Carrier Combinations, *Deutsches Zentrum für Luft- und Raumfahrt*, Neustrelitz, Germany, Jan. 2008.

[8] Patrick Henkel, Wide-Area RTK and Precise Point Positioning with mixed Code-Carrier Combinations, *Delft Institute of Earth Observation and Space Systems*, Delft University of Technology, The Netherlands, Dec. 2007.

[9] Patrick Henkel, Linear Carrier Phase Combinations for Galileo, *Delft Institute of Earth Observation and Space Systems*, Delft University of Technology, The Netherlands, May. 2007.

[10] Patrick Henkel, Integrity Analysis of Cascaded Integer Resolution with Decorrelation Transformations, *4-th GNSS Integrity Meeting*, Deutsches Zentrum für Luft- und Raumfahrt (DLR), Oberpfaffenhofen, Feb. 2007.

Patents:

[1] Patrick Henkel, Zhibo Wen and Christoph Günther, Estimation of satellite and receiver biases on multiple frequencies with a Kalman filter, European Patent Application, Dec. 2009.

[2] Patrick Henkel and Victor Gomez, Partial ambiguity fixing for multi-frequency ionospheric delay estimation, European Patent Application, Oct. 2009.

[3] Patrick Henkel, A Method for Tracking a plurality of global positioning satellite signals: Multi-Carrier Vector Phase Locked Loop, European Patent Application (08 007 248.1), Apr. 2008.

[4] Patrick Henkel, Method for Processing a Set of Signals of a Global Navigation Satellite System with at least Two Carriers: Single difference Phase and Code Bias Estimation for Precise Point Positioning, European Patent Application (08 007 781.1), Apr. 2008.

[5] Patrick Henkel, Method for Processing a Set of Signals of a Global Navigation Satellite System with at least Three Carriers: Geometry-free Linear Combinations, European Patent Application (PCT/EP2008/053300), Mar. 2007.

[6] Patrick Henkel, Method for Processing a Set of Signals of a Global Navigation Satellite System with at least Three Carriers: Three-Frequency Linear Combinations, European Patent Application (07 112 008), Mar. 2007.

[7] Patrick Henkel and Christoph Günther, Method for Transmitting Satellite Data: Reduced Almanac Information Schemes, PCT application number: PCT/EP2007/056781, July 2006.

Awards:

Bavarian regional prize (2010) 3rd prize in intern. competition	European Satellite Navigation Competition Incentive funding of the *Bavarian ministry of Economic Affairs* for the development of a Differential carrier phase receiver system with extremely reliable integer ambiguity resolution for stabilization of freights carried by cranes and helicopters
Publication award (2010)	Award of the TUM *Graduate School* (faculty of electrical engineering) for publications in peer-reviewed journals.
ION travel grant (2010)	Travel grant of the *Institute of Navigation* (ION) for a trip to the Intern. Technical Meeting in San Diego, USA.
DAAD travel grant (2009)	Travel grant of the *German Academic Exchange Service* (DAAD) for a trip to the Int. Assoc. of Geodesy Scient. Assembly in Buenos Aires, Argentina.
ESA travel grant (2009)	Travel grant of the *European Space Agency* (ESA) for a trip to the European Navigation Conference in Naples, Italy.
DAAD fellowship (2008)	Fellowship of the *German Academic Exchange Service* (DAAD) for a research visit of the GPS Lab at Stanford University, USA.
Pierre Contensou Gold Medal, Inter. Astronautical Federation (2007)	Distinction for the 1st price of an international student contest: National selection at EADS in Bremen: Award of "Deutsche Gesellschaft für Luft- u. Raumfahrt Lilienthal Oberth" (DGLR). International competition at the International Astronautical Congress (IAC) in Hyderabad, India: 1st price for a paper on "Geometry-free linear combinations for Galileo".

Acknowledgments

First of all, I would like to thank my supervisor, Prof. Christoph Günther, an exceptional researcher and mentor with a tremendous creativity. His passion and inspiration in every meeting brightened my whole week. His guidance and encouragement let me set goals that I could not even imagine before. It is the greatest pleasure to work with Christoph and I am looking forward to continue my work at his institute after my PhD. Christoph always gave me a lot of freedom during my work, he enabled me a research visit at TU Delft and Stanford University, and he allowed me to present my work at numerous conferences.

I would also like to thank my second supervisor, Prof. Per Enge, head of the GPS Lab at Stanford University, for his excellent host during my research visit from October 1, 2008 until December 1, 2008, and in June 2010. I enjoyed the excellent atmosphere and the several discussions with my direct supervisors at Stanford University, Dr. Grace Xingxin Gao and Dr. Todd Walter who also enabled me to be session chair at the ION Int. Technical Meeting at San Diego in January 2010.

I would also like to thank my third supervisor, Prof. Sandra Verhagen from the Institute of Mathematical Geodesy and Positioning at TU Delft. Sandra shared her own office with me during my research visit in 2007, and explained me several issues on integer least-squares estimation for ambiguity resolution. I also enjoyed several discussions with Prof. Christian Tiberius, Dr. Hans van der Marel, Peter Buist and Peter Baaker at TU Delft.

I am also grateful to Prof. Dr. techn. Josef A. Nossek for being the chairman of my examination committee, and for his interest in my work during several joint project workshops.

Special thanks go also to my colleagues at the Technische Universität München, Kaspar Giger and Sebastian Knogl, for a lot of joint activities beside the work. Kaspar also supported me in the project P-LAGAL where he prepared a flight test with two Galileo capable receivers of Javad and Septentrio.

I would also like to thank my master students Victor Gomez and Zhibo Wen. Victor worked on partial ambiguity fixing and Zhibo focused on bias estimation, and their results were included in two publications as well as in this thesis. I am also grateful for my bachelor student Patryk Jurkowski for working with the NavX-NCS Galileo signal simulator of IFEN. I would also like to mention our "Werkstudenten" Todor Makashelov, Chen Tang and Ganesh Lalgudi Gopalakrishnan who worked on different smoothing algorithms, multi-frequency code carrier linear combinations and attitude determination.

I would also like to acknowledge Ruediger Schmidt (CEO) and Markus Schwendener from the Flight Calibration Services GmbH in Braunschweig for their support in the frame of the project P-LAGAL.

I would also like to mention my friends at the navigation department of the German Aerospace Center (DLR), especially Markus Rippl and Boubeker Belabbas, and my colleagues from the institute of communications engineering at the Technische Universität

München, especially Dr. Vladimir Kurychev. Vladimir created an excellent atmosphere during his time at our neighbored institute with a lot of discussions during long research evenings.

I would also like to thank Annemarie Frey for loving me. I am grateful for your understanding and patience, and the wonderful time with you.

Finally and most importantly, I would like to thank my parents, my mother Sylvia Henkel and my father Bernhard Henkel. You always wanted the best for me and continuously supported me during all phases of my life. It is my greatest honour to dedicate this work to you.

München, September 2010 Patrick Henkel

Contents

1

Introduction

Currently, there exist two operational global navigation satellite systems: GPS and GLONASS. Europe is building its own global navigation satellite system Galileo which has many common properties with GPS, e.g. the use of Medium Earth Orbit (MEO) satellites, spreading codes, overlapping frequency bands and range based positioning. The joint use of signals from both systems will roughly double the number of available satellites which will substantially improve the positioning in environments where several satellites are not visible, e.g. in street canyons. Although GPS and Galileo are rather similar, Galileo will offer some additional innovations that GPS does currently not provide to the civilian user. Tab. 1.1 summarizes the most important contributions.

Table 1.1: Innovations of Galileo

Orbits	Altitude of 23200 km: ⇒ Groundtrack repetition period of 10 days (instead of 1 day) ⇒ Reduction in resonances due to periodic movement over areas with irregular gravitational field ⇒ Less satellite maneuvers required.
Signals	- Three frequency bands with larger signal bandwidths: E1: 40.92 MHz, E5: 92.07 MHz and E6: 40.92 MHz. ⇒ Improved estimation and elimination of ionospheric delays of first and second order ⇒ Increased reliability of carrier phase integer ambiguity resolution. - Binary Offset Carrier (BOC) modulation: Power shift to the edges of the spectrum ⇒ Lower Cramer Rao bound ⇒ Improved code delay tracking and stronger multipath suppression.

Signals	- Composite BOC on E1 Linear combination of BOC(1,1) and BOC(6,1) modulations: ⇒ Receivable signal for narrowband receivers ⇒ Low noise level and multipath for wideband receivers.
Satellites	H2 maser as satellite clock: Improved stability over relevant time intervals ⇒ Improved estimation of satellite clock errors.

Zandbergen et al. have described the final Galileo orbit selection in [2]. Fig. 1.1 shows the nominal Galileo Walker constellation with 27 MEO satellites that are arranged in three orbital planes with an inclination of 56° and an altitude of 23200 km. The right ascension of the ascending node is $\Omega = l \cdot 120°$ and the initial mean anomaly is given by $M_0 = k \cdot 40° + l \cdot 40°/3$ with the satellite index $k \in \{0, \ldots, 8\}$ in the orbital plane $l \in \{0, 1, 2\}$. Each satellite is transmitting the positions of all other satellites in the almanac to simplify the acquisition of rising satellites. Fig. 1.1 also shows the intersatellite links for one selected satellite. They are currently not foreseen for Galileo although they would dramatically simplify the orbit determination due to a significantly improved geometry and the absence of atmospheric errors.

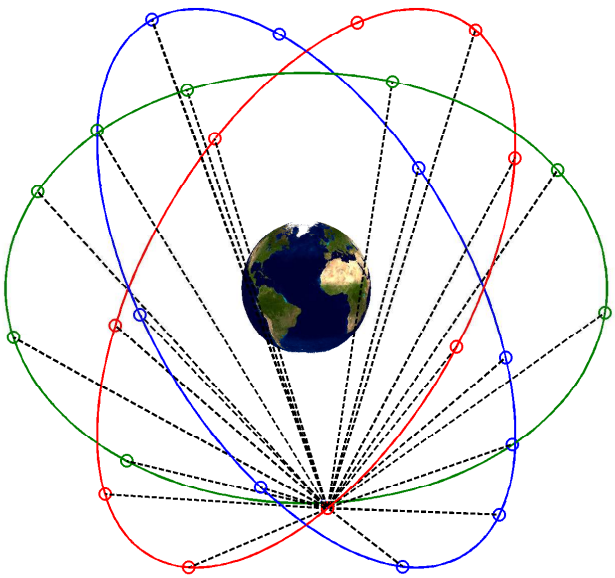

Figure 1.1: Galileo Walker constellation: 27 satellites are arranged in three orbital planes with an inclination of 56° and an altitude of 23200 km (MEO). Each satellite is transmitting the positions of all other satellites in the almanac. Intersatellite links are currently not foreseen although they would dramatically simplify the orbit determination due to a significantly improved geometry and the absence of atmospheric errors.

Fig. 1.2 shows the groundtrack for one Galileo satellite which repeats after 10 days. This repetition period is ten times longer than for GPS to avoid resonances due to a periodic movement over areas with irregularities in the gravitational field of the earth. A more stable orbit requires less maneuvers which turns into a higher availability of the satellites.

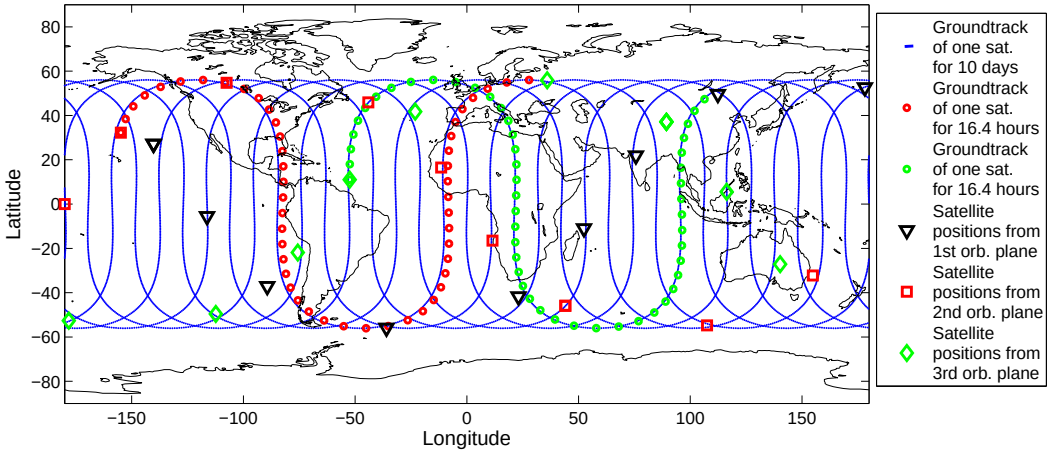

Figure 1.2: Groundtracks for Galileo: The Walker constellation consists of three orbital planes which are indicated by different colors. The groundtrack of each satellite repeats after 10 days. This large period reduces the resonances due to a periodic movement over areas with irregularities in the gravitational field of the earth. After 16.4 hours, a user can see the same satellite constellation although different satellites are in the positions. This is indicated by the two dotted lines. This short constellation period is helpful for multipath detection at reference stations.

1.1 Carrier phase positioning

The Galileo satellites transmit spreading codes that are modulated onto three carriers. Both the code and the carrier phase can be used for ranging. The first one is unambiguous but can be measured only with a centimeter to decimeter accuracy. The carrier phase can be measured with a millimeter accuracy but it is ambiguous as the carrier phase is periodic. This means that the integer number of cycles between the satellite and the receiver is unknown, i.e. only a fractional part can be measured.

Fig. 1.3 to 1.6 visualize the problem of integer ambiguity resolution and the approaches of this thesis to improve its reliability. The wavefronts are shown, which can be considered parallel with distances equal to the wavelength. The intersections of the wavefronts from three satellites result in several possible receiver positions. The infinite search space can be reduced by the unambiguous code solution which is indicated by the grey shaded area. However, Fig. 1.3 shows that there exist still numerous ambiguity candidates. A reliable decision requires a.) measurements from multiple epochs to reduce the search space given by the float solution and b.) a continuous phase tracking to avoid cycle slips.

Fig. 1.4 shows our first approach to improve the reliability of integer ambiguity resolution: As the ambiguity resolution suffers from the small carrier wavelength, the received carrier phases on multiple frequencies are linear combined to achieve a large artificial wavelength. This results in a larger distance between the wavefronts and an unambiguous position solution as any other candidate is shifted outside the search space.

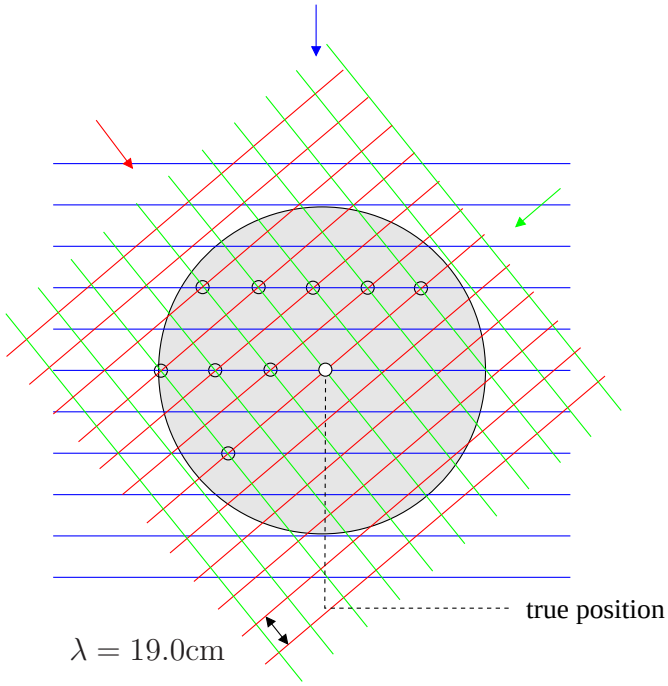

Figure 1.3: Integer ambiguity grid: The wavefronts from three satellites intersect at multiple points which results in an ambiguity. The float solution constrains the search space to a certain area (shown in grey) but leaves some ambiguity (i.e. black circles).

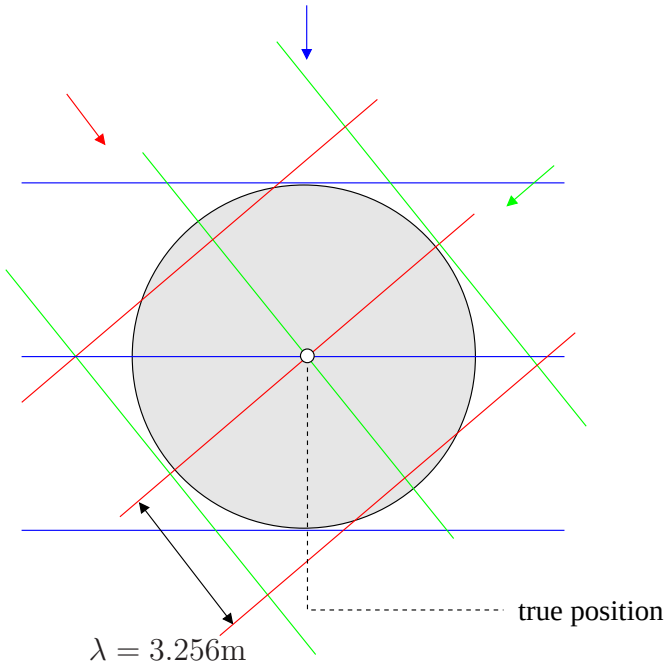

Figure 1.4: Integer ambiguity grid: The carrier phases on two or more frequencies can be combined to increase the wavelength by more than one order of magnitude. The ambiguous solutions are moved out of the search space spanned by the pure code solution. An unambiguous widelane solution remains, which is characterized by a noise level of a few centimeters.

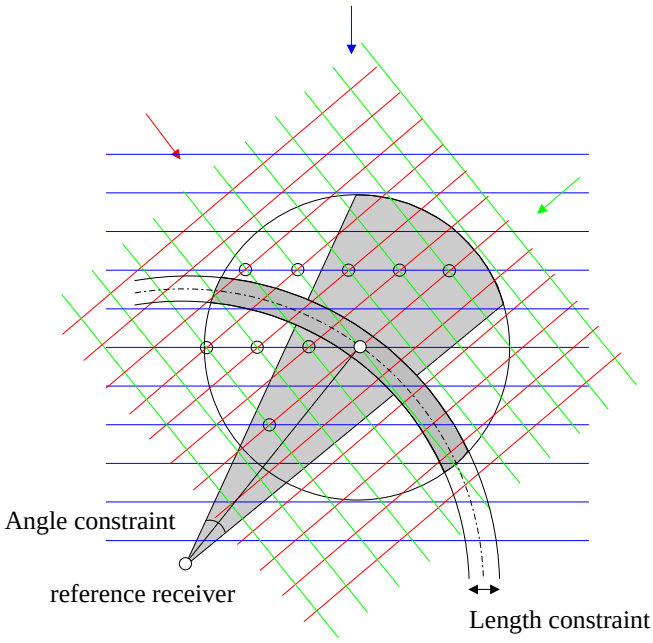

Figure 1.5: Integer ambiguity grid: The search space volume of the float solution is substantially reduced by constraints on the baseline length and direction. As the length and direction are not perfectly known in many applications, a certain variation is allowed.

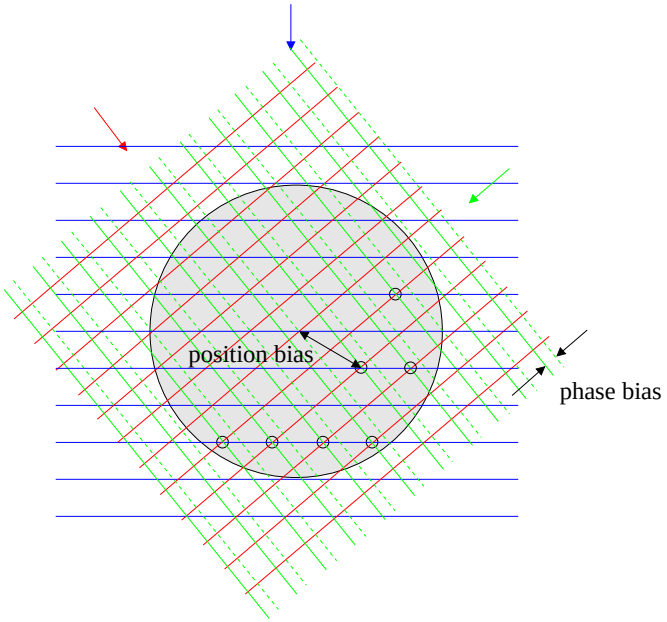

Figure 1.6: Integer ambiguity grid: The wavefront of one satellite signal is shifted by a phase bias. The intersection point for the true solution disappears and also the other intersection points change. The one closest to the true position is characterized by a position bias which is substantially larger than the phase bias. This is a strong motivation for bias estimation.

Fig. 1.5 shows a second option to improve the reliability of ambiguity resolution: spatial constraints on the search space due to an a priori knowledge about the receiver position. This knowledge can be a distance or direction information w.r.t. a reference receiver. It can be an exact or a soft constraint allowing some variations. These spatial constraints can be ideally combined with the increase in wavelength by a multi-frequency linear combination. Fig. 1.6 addresses another challenge of carrier phase positioning: the existence of unknown phase biases due to delays in the receiver and satellite hardware. The phase bias on a single satellite shifts the wavefronts, which results in new intersection points. The true receiver position does no longer correspond to a candidate and the closest candidate suffers from a position bias which in general significantly exceeds the phase biases. This indicates the need for precise bias estimation which is analyzed in Chapter 5.

1.2 Code and carrier phase measurements

The transmit signal of each satellite includes an inphase and a quadrature component on M frequencies, i.e.

$$\begin{aligned} s^k(t) &= \sum_{m=1}^{M} \left(s^k_{\mathrm{I},m}(t) \cos\left(\omega_{\mathrm{c},m}(t-\tau^k_{0,m}(t)) + \phi^k_{0,m}(t)\right) \right. \\ &\quad \left. + j \cdot s^k_{\mathrm{Q},m}(t) \sin\left(\omega_{\mathrm{c},m}(t-\tau^k_{0,m}(t)) + \phi^k_{0,m}(t)\right)\right), \end{aligned} \tag{1.1}$$

with the carrier frequencies $\omega_{\mathrm{c},m}$, the phase $\phi_{0,m}$ and the time offset $\tau^k_{0,m}$ between the transmitter clock and an arbitrary reference. The in-phase and quadrature components are modeled as

$$s^k_{\{\mathrm{I,Q}\},m}(t) = \sqrt{\mathcal{P}^k_{\{\mathrm{I,Q}\},m}} b^k_{\{\mathrm{I,Q}\},m}(t-\tau^k_{0,m}) c^k_{\{\mathrm{I,Q}\},m}(t-\tau^k_{0,m}), \tag{1.2}$$

where $\mathcal{P}^k_{\{\mathrm{I,Q}\},m}$ denotes the transmit power, $b^k_{\{\mathrm{I,Q}\},m}$ is the navigation bit, and $c^k_{\{\mathrm{I,Q}\},m}$ is the chip of a spreading code which is used to overcome the free space loss.

The received signal is attenuated by α^k_m, delayed by the propagation time $\tau^k_m - \tau^k_{0,m}$, shifted in frequency by the Doppler shift $\omega^k_{\mathrm{D},m}$ due to the relative movement, and superimposed by white Gaussian noise $n^k_m(t)$, i.e.

$$\begin{aligned} r(t) &= \sum_{k=1}^{K} \sum_{m=1}^{M} \left(\alpha^k_m s^k_{\mathrm{I},m}(t) \cos\left((\omega_{\mathrm{c},m} - \omega^k_{\mathrm{D},m}(t))(t-\tau^k_m(t)) + \phi^k_m(t)\right) \right. \\ &\quad \left. + j \cdot \alpha^k_m s^k_{\mathrm{Q},m}(t) \sin\left((\omega_{\mathrm{c},m} - \omega^k_{\mathrm{D},m}(t))(t-\tau^k_m(t)) + \phi^k_m(t)\right) + n^k_m(t)\right). \end{aligned} \tag{1.3}$$

The propagation delay $\tau^k_m - \tau^k_{0,m}$ times the speed of light c gives the pseudoranges $\rho^k_{r,m}(t_n)$ for the r-th user, which can be further decomposed into

$$\begin{aligned} \rho^k_{r,m}(t_n) &= r^k_r(t_n) - (\boldsymbol{e}^k_r(t_n))^T \delta \boldsymbol{x}^k(t'_n) + c\left(\delta\tau_r(t_n) - \delta\tau^k(t'_n)\right) + T^k_r(t_n) \\ &\quad + q^2_{1m} I'^k_{1,r}(t_n) + q^3_{1m} I''^k_{1,r}(t_n) + o_{r,m}(t_n) + o^k_m(t'_n) + b_{m,r} + b^k_m + \eta^k_{r,m}(t_n), \end{aligned} \tag{1.4}$$

with

$r_r^k(t_n)$	true range between satellite and receiver
$\boldsymbol{e}_r^k(t_n)$	unit vector pointing from the satellite to the receiver
$\delta\boldsymbol{x}^k(t'_n)$	satellite position error at time of transmission t'_n
$\delta\tau_r(t_n)$	receiver clock offset
c	speed of light
$\delta\tau^k(t'_n)$	satellite clock offset at time of transmission t'_n
$T_r^k(t_n)$	tropospheric slant delay [1], [8]
$I_{1,r}^{\prime k}(t_n)$	ionospheric slant delay of first order on frequency L1 [1], [8]
$I_{1,r}^{\prime\prime k}(t_n)$	ionospheric slant delay of second order on frequency L1 [1], [8]
$q_{1m} = f_1/f_m$	ratio of carrier frequencies
$o_{r,m}(t_n)$	receiver antenna code center variations
$o_m^k(t'_n)$	satellite antenna code center variations
$b_{m,r}$, b_m^k	receiver and satellite code biases
$\eta_{r,m}^k(t_n)$	receiver code noise including multipath.

The dispersive behaviour of the ionosphere with a $1/f^2$ dependency enables the elimination of this delay by multi-frequency linear combinations. The carrier phase can be modeled similarly as the code phase, i.e.

$$\begin{aligned}\lambda_m\phi_{r,m}^k(t_n) &= r_r^k(t_n) - (\boldsymbol{e}_r^k(t_n))^T\delta\boldsymbol{x}^k(t'_n) + c\left(\delta\tau_r(t_n) - \delta\tau^k(t'_n)\right) + T_r^k(t_n)\\ &\quad -q_{1m}^2 I_{1,r}^{\prime k}(t_n) - \frac{1}{2}q_{1m}^3 I_{1,r}^{\prime\prime k}(t_n)\\ &\quad +\lambda_m N_{r,m}^k + p_{r,m}(t_n) + p_m^k(t'_n) + \beta_{m,r} + \beta_m^k + \varepsilon_{r,m}^k(t_n), \qquad (1.5)\end{aligned}$$

with the following additional parameters:

λ_m	wavelength of m-th carrier
$N_{r,m}^k$	carrier phase integer ambiguity
$p_{r,m}(t_n)$	receiver antenna phase center variations [1], [8]
$p_m^k(t'_n)$	satellite antenna phase center variations [1], [8]
$\beta_{m,r}$, β_m^k	receiver and satellite phase biases
$\varepsilon_{r,m}^k(t_n)$	receiver phase noise including multipath.

The slant atmospheric delays can be factorized into a zenith delay and a mapping function:

$$\begin{aligned}T_r^k(t_n) &= m_{\mathrm{T}}(E_r^k(t_n)) \cdot T_{r,\mathrm{z}}(t_n) \qquad (1.6)\\ I_r^{\prime k}(t_n) &= m_{\mathrm{I}}(E_r^k(t_n)) \cdot I'_{r,\mathrm{z}}(t_n) \qquad (1.7)\\ I_r^{\prime\prime k}(t_n) &= m_{\mathrm{I}}(E_r^k(t_n)) \cdot I''_{r,\mathrm{z}}(t_n), \qquad (1.8)\end{aligned}$$

where the mapping functions $m_{\mathrm{T}}(\cdot)$ and $m_{\mathrm{I}}(\cdot)$ depend on the elevation angle E_r^k. A variety of mapping functions were proposed over the last decades which are described in details by Günther in [1] and by Misra and Enge in [8].

1.3 Accuracy of carrier phase measurements

The carrier phase is continuously tracked by a phase locked loop (PLL). The standard deviation of the tracking error can be easily derived from the pre-detection result which can be written in the general form

$$C(\Delta\phi) = \alpha \cdot e^{j\Delta\phi} + n_m, \tag{1.9}$$

with amplitude α, phase tracking error $\Delta\phi$ and noise n_m. The Costa's discriminator extracts the phase by

$$D_{\mathrm{PLL_c}} = 1/\alpha^2 \cdot \Re(C(\Delta\phi)) \cdot \Im(C(\Delta\phi)), \tag{1.10}$$

which is independent of the sign of α, i.e. it does not require any knowledge of the navigation bit. The discrimination result can be expanded into

$$D_{\mathrm{PLL_C}} = \frac{1}{2}\sin(2\Delta\phi) + \frac{1}{\alpha}(\cos(\Delta\phi)n_y + \sin(\Delta\phi)n_x) + \frac{1}{\alpha^2}n_x n_y, \tag{1.11}$$

with the expectation value $\mathrm{E}\{D_{\mathrm{PLL_C}}\} = \frac{1}{2}\sin(2\Delta\phi) \approx \Delta\phi$. Assuming $E\{n_x^2\} = E\{n_y^2\} = T_i\mathcal{N}_0$ with integration time T_i, the variance of the discrimination result follows as

$$\begin{aligned}\sigma^2_{D_{\mathrm{PLL_C}}} &= \frac{1}{\alpha^2}(\cos^2(\Delta\phi)\mathrm{E}\{n_y^2\} + \sin^2(\Delta\phi)\mathrm{E}\{n_x^2\}) + \frac{1}{\alpha^4}\mathrm{E}\{n_x n_y n_x n_y\} \\ &= \frac{T_i\mathcal{N}_0}{\alpha^2} + \frac{T_i^2\mathcal{N}_0^2}{\alpha^4} = \frac{1}{2\mathcal{E}_i/\mathcal{N}_0}\left(1 + \frac{1}{2\mathcal{E}_i/\mathcal{N}_0}\right),\end{aligned} \tag{1.12}$$

where the latter term denotes the squaring loss. The variance of the tracked carrier phase is obtained from the variance of the discriminator result and the transfer function of the tracking loop:

$$\sigma^2_\phi = \sigma^2_{D_{\mathrm{PLL_C}}} \cdot \frac{1}{2\pi}\int_0^{2\pi} |H(e^{j\phi})|^2 d\phi, \tag{1.13}$$

where $H(\cdot)$ denotes the transfer function of the tracking loop. For white Gaussian noise, the transfer function is fully characterized by the one sided bandwidth of the loop filter B_{L}. Thus, the variance of the tracked carrier phases is given by

$$\sigma^2_\phi = \frac{2B_{\mathrm{L}}}{1/T_i} \cdot \frac{1}{2\mathcal{E}_i/\mathcal{N}_0}\left(1 + \frac{1}{2\mathcal{E}_i/\mathcal{N}_0}\right), \tag{1.14}$$

in units of rad^2. The standard deviation σ_ϕ is often written in units of meters and the received energy $\mathcal{E}_i$ is commonly replaced by the product between received power C and integration time T_i, i.e.

$$\sigma_\phi = \frac{\lambda}{2\pi}\sqrt{\frac{B_{\mathrm{L}}}{C/\mathcal{N}_0}\left(1 + \frac{1}{2C/\mathcal{N}_0 T_i}\right)}. \tag{1.15}$$

Typical filter parameters are $B_{\mathrm{L}} = 20$Hz and $T_i = 20$ms, which results in a σ_ϕ of less than 1 millimeter for $C/\mathcal{N}_0 = 45$dB-Hz and $\lambda = 19.0$cm (L1).

1.4 Accuracy of code phase measurements

The code phase is continuously tracked by a delay locked loop. The standard deviation of its tracking error can be lower bounded by the Cramer Rao bound which was derived by Betz in [3] as

$$\sigma_{\rho_m} \geq \sqrt{\frac{c^2}{\frac{C}{\mathcal{N}_0} T_i \cdot \frac{\int (2\pi f)^2 |S_m(f)|^2 df}{\int |S_m(f)|^2 df}}}, \tag{1.16}$$

with the power spectral density $S_m(f)$. The Binary Offset Carrier modulation shifts the power to higher frequencies which increases $\int |S(f)|^2 (2\pi f)^2 df$ and, thus, results in a lower CRB than for BPSK modulation. Tab. 1.2 and 1.3 show the CRBs for the Galileo and GPS signals for a signal to noise power ratio of $C/N_0 = 45$dB-Hz. Low cost GPS receivers use only a bandwidth of 2 MHz which results in a CRB of 78.29 cm for the BPSK(1) modulated L1 signal. A BOC(1,1) modulated signal with sine phasing and a bandwidth of 20 MHz benefits from a CRB of 14.81 cm, and the MBOC modulation further reduces the CRB to 11.13 cm. The lowest noise level of only 1.62 cm is achieved by the AltBOC(15,10) modulated Galileo signal on E5 with a bandwidth of $90 \cdot 1.023$ MHz. This low code noise substantially improves the reliability of carrier phase integer ambiguity resolution.

Table 1.2: Cramer Rao bounds for Galileo signals and $C/N_0 = 45$dB-Hz

	Signal	Service	BW [MHz]	Γ [cm]
E1-A	BOC(15,2.5), cosine phasing	PRS	$40 \cdot 1.023$	1.74
E1-B, E1-C (pilot)	BOC(1,1), sine phasing	OS/SoL	$4 \cdot 1.023$	31.12
E1-B, E1-C (pilot)	BOC(1,1), sine phasing	OS/SoL	$20 \cdot 1.023$	14.81
E1-B, E1-C (pilot)	CBOC, sine phasing	OS/SoL	$20 \cdot 1.023$	11.13
E5	AltBOC(15,10)	OS/SoL	$90 \cdot 1.023$	1.62
E5	AltBOC(15,10)	OS/SoL	$50 \cdot 1.023$	1.95
E5a-I, E5a-Q (pilot)	BPSK(10)	OS	$20 \cdot 1.023$	7.83
E5b-I, E5b-Q (pilot)	BPSK(10)	SoL	$20 \cdot 1.023$	7.83
E6-A	BOC(10,5), cosine phasing	PRS	$40 \cdot 1.023$	2.41
E6-B, E6-C (pilot)	BPSK(5)	CS	$10 \cdot 1.023$	15.66
E6-B, E6-C (pilot)	BPSK(5)	CS	$20 \cdot 1.023$	11.36

Table 1.3: Cramer Rao bounds for GPS signals and $C/N_0 = 45$dB-Hz

	Signal	Service	BW [MHz]	Γ [cm]
L1-I	BPSK(1)	OS (C/A)	$2 \cdot 1.023$	78.29
L1-I	BPSK(1)	OS (C/A)	$20 \cdot 1.023$	25.92
new L1-C	MBOC, sine phasing	OS	$20 \cdot 1.023$	11.13
new L2-C	BPSK(1)	OS	$20 \cdot 1.023$	25.92
L5-I, L5-Q (pilot)	BPSK(10)	OS	$20 \cdot 1.023$	7.83

2

Multi-frequency mixed code carrier combinations

Linear combinations of GPS measurements are widely used to improve the reliability of integer ambiguity resolution. One of the most simplest linear combinations is the single difference between the measurements of two receivers which eliminates the clock offset, phase and code biases of a satellite. Similarly, single differences can be computed between the measurements of two satellites to remove the clock offset, phase and code biases of the receiver. Double difference measurements additionally suppress the spatially correlated atmospheric errors and are used for baseline estimation and orbit determination (e.g. in the Bernese software [87]) in geodesy. Linear combinations between the measurements of at least two frequencies are applied to remove the first order ionospheric delay. However, the L1-L2 ionosphere-free linear combination suffers from a wavelength of only 6 mm which prevents any reliable ambiguity resolution. The dual frequency Melbourne-Wübbena combination includes both code and carrier phase measurements, and eliminates the range, the clock offsets, the tropospheric and ionospheric delays. It only leaves the superposition of phase and code biases and widelane ambiguities which are commonly estimated by this linear combination. In this section, new linear combinations are derived for Galileo and GPS. The use of carrier phase measurements on three frequencies (E1,E5a,E5b or L1,L2,L5) enables linear combinations that increase the wavelength and simultaneously suppress the ionospheric delay. Four frequency linear combinations benefit from an even stronger suppression of the ionospheric error. The set of integer preserving phase-only widelane combinations is discrete and finite. The properties of these linear combinations can be significantly improved if code measurements are included with a small weight. There exists an infinite set of ionosphere-free mixed code-carrier combinations of arbitrary wavelength.

2.1 Design of multi-frequency phase combinations

A multi-frequency linear combination weights the phase measurements of (1.4) by α_m, i.e.

$$\begin{aligned}\lambda\phi_u^k(t_i) &= \sum_{m=1}^{M}\alpha_m\lambda_m\phi_{u,m}^k(t_i)\\ &= \sum_{m=1}^{M}\alpha_m\left(r_u^k(t_i)+\delta r_u^k(t_i)+c\left(\delta\tau_u(t_i)-\delta\tau^k(t_i)\right)+T_u^k(t_i)\right)-\sum_{m=1}^{M}(\alpha_m q_{1m}^2)I_u^k(t_i)\\ &\quad+\sum_{m=1}^{M}\left(\alpha_m\lambda_m N_{u,m}^k\right)+\sum_{m=1}^{M}\left(\alpha_m b_{\phi_{u,m}}^k\right)+\sum_{m=1}^{M}\left(\alpha_m\varepsilon_{\phi_{u,m}}^k(t_i)\right),\end{aligned}\tag{2.1}$$

with the wavelength λ, the frequency ratio $q_{1m}=f_1/f_m$, and the combined phase $\phi_u^k(t_i)$ in units of cycles. The linear combination shall be geometry-preserving (GP), i.e.

$$\sum_{m=1}^{M}\alpha_m=1,\tag{2.2}$$

which also leaves the orbital errors, the clock offsets and tropospheric delay invariant. Moreover, the linear combination shall preserve the integer nature of ambiguities, i.e.

$$\sum_{m=1}^{M}\alpha_m\lambda_m N_{u,m}^k\stackrel{!}{=}\lambda N_u^k.\tag{2.3}$$

with the integer ambiguity N_u^k. Solving (2.3) for λ yields

$$N_u^k=\sum_{m=1}^{M}\frac{\alpha_m\lambda_m}{\lambda}N_{u,m}^k,\tag{2.4}$$

which is integer valued for any arbitrary $N_{u,m}^k$ if

$$j_m=\frac{\alpha_m\lambda_m}{\lambda}\in\mathcal{Z}\quad\forall m,\tag{2.5}$$

with $\mathcal{Z}$ being the amount of integer numbers. Solving for α_m yields

$$\alpha_m=\frac{j_m\lambda}{\lambda_m}.\tag{2.6}$$

Combining (2.2) and (2.6) yields the wavelength of the linear combination:

$$\lambda=\frac{1}{\sum\limits_{m=1}^{M}\frac{j_m}{\lambda_m}}.\tag{2.7}$$

The Galileo and GPS carrier frequencies $f_m = c/\lambda_m$ can be expressed as an integer multiple of $f_0 = 10.23$ MHz which corresponds to a wavelength $\lambda_0 = 29.31$m, i.e. (2.7) is rewritten as

$$\lambda = \frac{\lambda_0}{l} \quad \text{with} \quad l = \sum_{m=1}^{M} j_m n_m \tag{2.8}$$

and $n_1 = 154$ (E1), $n_2 = 125$ (E6), $n_3 = 118$ (E5b) and $n_4 = 115$ (E5a). Cocard et al. [39] have used the lane number l to split the integer preserving linear combinations into three groups: For $0 < l \leq 115$, the group of widelane combinations is obtained which are characterized by wavelengths larger than the largest wavelength of all carriers. The intermediate-lane region is described by $115 < l \leq 154$, i.e. the resulting wavelengths are between the smallest (E1) and the largest (E5a) wavelength. For $l > 154$, the group of narrowlane combinations is obtained which are characterized by wavelengths smaller than the smallest wavelength of all carriers.

Cocard and Geiger have performed a systematic search of all possible L1-L2 widelanes in [40], and Collins has evaluated ionospheric, noise and multipath properties of these linear combinations in [41]. This approach is generalized to three frequencies by Henkel and Günther in [42] and to M frequencies here: A widelane combination satisfies the inequality

$$\frac{1}{\sum\limits_{m=1}^{M} \frac{j_m}{\lambda_m}} > \lambda_M > 0, \tag{2.9}$$

which is equivalent to

$$1 > \left(\lambda_M \cdot \sum_{m=1}^{M-1} \frac{j_m}{\lambda_m} \right) + j_M > 0, \tag{2.10}$$

and has the unique solution

$$j_M = \left\lceil -\lambda_M \cdot \sum_{m=1}^{M-1} \frac{j_m}{\lambda_m} \right\rceil. \tag{2.11}$$

Replacing j_M in (2.7) by (2.11) yields the wavelength of the linear combination

$$\lambda(j_1, \ldots, j_{M-1}) = \frac{1}{\left(\sum\limits_{m=1}^{M-1} \frac{j_m}{\lambda_m} \right) + \frac{1}{\lambda_M} \cdot \left\lceil -\lambda_M \cdot \sum\limits_{m=1}^{M-1} \frac{j_m}{\lambda_m} \right\rceil}. \tag{2.12}$$

This wavelength is periodic w.r.t. j_m, i.e.

$$\begin{aligned} &\lambda(j_1, \ldots, j_{s-1}, j_s + P_s, j_{s+1}, \ldots, j_{M-1}) \\ &\quad = \frac{1}{\left(\sum\limits_{m=1, m\neq s}^{M-1} \frac{j_m}{\lambda_m} \right) + \frac{j_s + P_s}{\lambda_s} + \frac{1}{\lambda_M} \cdot \left\lceil -\lambda_M \left(\frac{j_s + P_s}{\lambda_s} + \sum\limits_{m=1, m\neq s}^{M-1} \frac{j_m}{\lambda_m} \right) \right\rceil} \end{aligned} \tag{2.13}$$

$$= \frac{1}{\left(\sum\limits_{m=1,m\neq s}^{M-1} \frac{j_m}{\lambda_m}\right) + \frac{j_s}{\lambda_s} + \frac{1}{\lambda_M} \cdot \left\lceil -\lambda_M \left(\frac{j_s}{\lambda_s} + \sum\limits_{m=1,m\neq s}^{M-1} \frac{j_m}{\lambda_m}\right)\right\rceil} \quad \forall s \in \{1,\ldots,M-1\}, \tag{2.14}$$

where the minimum period P_s is obtained from

$$\frac{\lambda_M P_s}{\lambda_s} = \frac{n_s P_s}{n_M} \overset{!}{\in} \mathcal{Z} \tag{2.15}$$

as $P_s = n_M/\gcd(n_s, n_M)$ with $\gcd(n_s, n_M)$ being the greatest common divisor between n_s and n_M. The periodicity of the wavelength enables an exhaustive search of all integer-preserving widelane combinations. The linear combination scales the ionospheric delay on L1 to

$$I_u^k = \underbrace{\sum_{m=1}^{M} \alpha_m q_{1m}^2}_{S_{\mathrm{I[m]}}} \cdot I_{u,1}^k, \tag{2.16}$$

where the index [m] denotes that the ionospheric delays are measured in units of meters. The noise standard deviation of the linear combination is given for statistically independent white Gaussian noise by

$$\sigma_u^k = \sqrt{\sum_{m=1}^{M} \alpha_m^2 \sigma_{\phi_{u,m}^k}^2} \approx \underbrace{\sqrt{\sum_{m=1}^{M} \alpha_m^2}}_{S_{\mathrm{n[m]}}} \sigma_{\phi_u^k}. \tag{2.17}$$

Collins has suggested an evaluation of the ionospheric and noise figures in units of cycles in [41] to remove the wavelength scaling. The linear combination in units of cycles is obtained from (2.1) as

$$\phi_u^k = \sum_{m=1}^{M} j_m \phi_{u,m}^k, \tag{2.18}$$

with $\phi_{u,m}^k$ being the phase measurement in units of cycles. The scaling of the ionospheric delay I_1/λ_1 on L1 follows as

$$\frac{I_u^k}{\lambda} = \underbrace{\sum_{m=1}^{M} j_m q_{1m}}_{S_{\mathrm{I[cyc]}}} \cdot \frac{I_{u,1}^k}{\lambda_1}, \tag{2.19}$$

and the noise standard deviation is written as

$$\sigma_{u\,[\mathrm{cyc}]}^k = \underbrace{\sqrt{\sum_{m=1}^{M} j_m^2}}_{S_{\mathrm{n[cyc]}}} \cdot \sigma_{\phi_u^k [\mathrm{cyc}]}. \tag{2.20}$$

Tab. 2.1 shows that several E1-E6-E5b-E5a widelane combinations of minimum noise amplification significantly reduce the ionospheric delay in units of cycles. A phase noise of $\sigma_\phi = 1$ mm has been assumed for the computation of σ_n. In [43], Richert and El-Sheimy point out that geometry-preserving combinations also scale the geometry-dependant errors in units of cycles by λ_1/λ, i.e. the tropospheric delay and clock offsets are effectively reduced by widelane combinations and increased by narrowlane combinations.

λ [m]	j_1	j_2	j_3	j_4	$S_{\mathrm{I[cyc]}}$ dB	$S_{\mathrm{I[m]}}$ dB	$S_{\mathrm{n[cyc]}}$ dB	$S_{\mathrm{n[m]}}$ dB	σ_n [cm]
29.310	0	1	-3	2	-23.0	-1.1	5.7	26.4	44.0
14.652	1	-4	1	2	-12.6	6.3	6.7	24.7	29.2
9.768	0	0	1	-1	-14.7	2.4	1.5	17.4	5.5
7.326	0	1	-2	1	-14.1	1.8	3.9	18.6	7.3
5.861	1	-4	2	1	-16.7	-1.8	6.7	20.7	11.7
4.884	1	-3	-1	3	-17.9	-3.8	6.5	19.6	9.1
4.187	0	1	-1	0	-11.4	2.1	1.5	13.9	2.5
3.663	1	-4	3	0	-18.9	-6.1	7.1	19.0	7.4
3.256	1	-3	0	2	-17.5	-5.2	5.7	17.1	5.2
2.931	0	1	0	-1	-9.7	2.2	1.5	12.3	1.7
2.664	0	2	-3	1	-9.5	2.0	5.7	16.1	4.1
2.442	1	-3	1	1	-12.9	-1.8	5.4	15.6	3.6
2.254	0	1	1	-2	-8.5	2.2	3.9	13.4	2.2
2.093	-3	1	2	1	3.4	13.8	5.9	15.9	3.9

Table 2.1: E1-E6-E5b-E5a widelane combinations of minimum noise amplification

Eq. (2.19) shows that the ionospheric delay is lowered in cycle domain if

$$\left| \sum_{m=1}^{M} j_m q_{1m} \right| < 1, \tag{2.21}$$

which can be solved for j_M:

$$\frac{1}{q_{1M}} \left(-1 - \sum_{m=1}^{M-1} j_m q_{1m} \right) < j_M < \frac{1}{q_{1M}} \left(1 - \sum_{m=1}^{M-1} j_m q_{1m} \right). \tag{2.22}$$

The number ν of integer solutions can be bounded from below and above, i.e.

$$\left\lfloor \frac{2}{q_{1M}} \right\rfloor < \nu < \left\lceil \frac{2}{q_{1M}} \right\rceil, \tag{2.23}$$

which results in at least one solution and at most two solutions for the GPS and Galileo frequencies. These integer solutions are given by

$$j_M = \left\{ \left\lceil \frac{1}{q_{1M}} \cdot (-1 - \sum_{m=1}^{M-1} j_m q_{1m}) \right\rceil, \quad \left\lfloor \frac{1}{q_{1M}} \cdot (+1 - \sum_{m=1}^{M-1} j_m q_{1m}) \right\rfloor \right\}. \tag{2.24}$$

These two solutions converge to a single solution if

$$\left| \frac{1}{q_{1M}} \cdot \sum_{m=1}^{M-1} j_m q_{1m} + \left[-\frac{1}{q_{1M}} \cdot \sum_{m=1}^{M-1} j_m q_{1m} \right] \right| < 1 - \frac{1}{q_{1M}}. \tag{2.25}$$

The two integer candidates of (2.24) correspond to the wavelengths

$$\lambda = \left\{ \begin{array}{l} \left(\sum_{m=1}^{M-1} \frac{j_m}{\lambda_m} + \frac{1}{\lambda_M} \cdot \left\lceil \frac{1}{q_{1M}} \cdot \left(-1 - \sum_{m=1}^{M-1} j_m q_{1m} \right) \right\rceil \right)^{-1} \\ \left(\sum_{m=1}^{M-1} \frac{j_m}{\lambda_m} + \frac{1}{\lambda_M} \cdot \left\lfloor \frac{1}{q_{1M}} \cdot \left(+1 - \sum_{m=1}^{M-1} j_m q_{1m} \right) \right\rfloor \right)^{-1} \end{array} \right\}, \tag{2.26}$$

which is periodic w.r.t. j_m with periods $P_m = n_m / \gcd(n_m, n_M)$. Fig. 2.1 shows the ionospheric suppression $S_{\mathrm{I[m]}}$ as a function of the wavelength for widelane combinations with $|j_m| \leq 20$. A four frequency combination enables a suppression of up to 31.7 dB, a three frequency combination of up to 16.4 dB and a dual frequency combination does not allow any ionospheric suppression. The capability of ionospheric reduction also depends on the maximum $|j_m|$, i.e. the ionospheric reduction of 31.7 dB lowers to 12.1 dB if the maximum value of $|j_m|$ is lowered from 20 to 5.

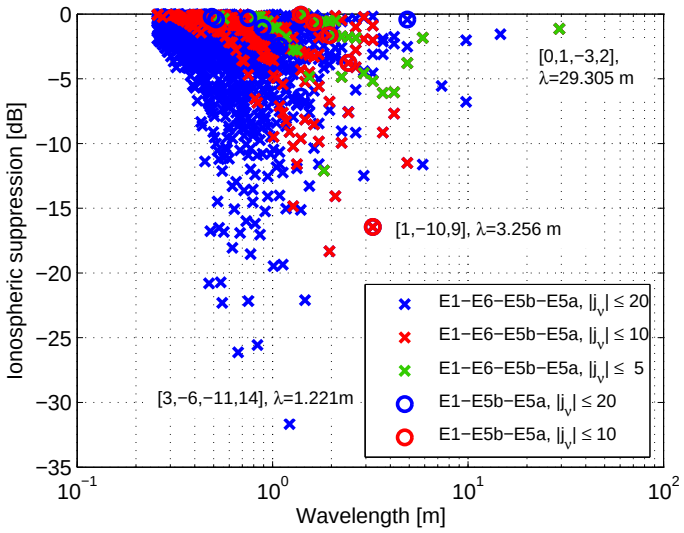

Figure 2.1: Reduced ionosphere widelane combinations with $|j_\nu| \leq 20$ for Galileo

Table 2.2 shows the weighting coefficients and properties of widelane combinations of maximum ionospheric suppression for $|j_m| \leq 10$. The linear combination with $\lambda = 1.954$ m benefits from an ionospheric suppression of 28.4 dB and a low noise level of a few centimeters. For $\lambda = 3.256$ m, the three frequency E1-E5b-E5a linear combination achieves a similar ionospheric suppression but suffers from a larger noise level.

The properties of the linear combinations can be further improved by including the phase measurements on a fifth carrier, e.g. the wideband E5 signal. Wübbena found a widelane

λ [m]	j_1	j_2	j_3	j_4	$S_{\mathrm{I[cyc]}}$ dB	$S_{\mathrm{I[m]}}$ dB	$S_{\mathrm{n[cyc]}}$ dB	$S_{\mathrm{n[m]}}$ dB	σ_{n} [cm]
29.310	0	1	-3	2	-23.0	-1.1	5.7	26.4	44.0
14.653	0	-1	4	-3	-15.4	3.5	7.1	24.7	29.9
9.768	1	-6	8	-3	-15.0	2.1	10.2	26.2	42.1
7.326	1	-5	5	-1	-15.8	0.1	8.6	23.4	22.0
5.861	1	-4	2	1	-16.7	-1.8	6.7	20.7	11.7
4.884	1	-6	9	-4	-25.6	-11.5	10.6	23.6	23.1
4.187	1	-5	6	-2	-21.1	-7.7	9.1	21.5	14.1
3.663	1	-1	-7	7	-22.0	-9.1	10.0	21.7	14.6
3.256	1	0	-10	9	-28.8	-16.4	11.3	22.4	17.5
2.931	1	-2	-3	4	-16.4	-4.6	7.4	18.1	6.5
2.664	1	-1	-6	6	-15.6	-4.1	9.3	19.6	9.2
2.442	2	-9	8	-1	-18.7	-7.6	10.9	21.0	12.5
2.254	2	-8	5	1	-20.7	-9.9	9.9	19.7	9.3
2.093	2	-7	2	3	-24.5	-14.1	9.1	18.6	7.3
1.954	2	-6	-1	5	-28.4	-18.3	9.1	18.2	6.7

Table 2.2: E1-E6-E5b-E5a widelane combinations of maximum ionospheric suppression

combination with a wavelength of $\lambda = 3.907$m and an ionospheric suppression of almost 30 dB in [44].

Richert and El-Sheimy [43] and Cocard et al. [39] introduced a graphical representation of the search of optimal three frequency linear combinations: The lane number, the ionospheric elimination and the removal of the tropospheric delay are three constraints that can be described by three planes in the three-dimensional search space of j_1, j_2 and j_3: The planes of different lane numbers are parallel and their normal vector is obtained from (2.8) as $\boldsymbol{n}_l = [n_1, n_2, n_3]^T$. The plane of the ionospheric elimination crosses the origin and its normal vector is obtained from (2.16) as $\boldsymbol{n}_{\mathrm{I}} = [q_{11}, q_{12}, q_{13}]^T$. The tropospheric delay in units of cycles is eliminated for $\sum_{m=1}^{M} \frac{j_m}{\lambda_m} = \frac{j_m n_m}{\lambda_0} = 0$ which corresponds to a plane with normal vector $\boldsymbol{n}_{\mathrm{T}} = [n_1, n_2, n_3]^T$. The angle between the ionosphere-free plane and the troposphere-free plane is 14.6° for E1,E5b,E5a and 15.0° in the case of L1,L2,L5. An optimum linear combination is on a plane of a lane number, close to the intersection of the ionosphere-free and troposphere-free planes, and close to the origin to minimize noise amplification. As the lane planes and the troposphere-free plane do not overlap and as the group of integer preserving combinations is discrete and finite, the choice of the optimum linear combination is a trade-off between several criteria and also depends on the baseline length. In [43], Richert and El-Sheimy have found only narrowlane combinations as optimal combinations for baseline lengths of up to 60 km.

Table 2.3 contains a list of 4F narrowlane combinations of maximum ionospheric suppression with $|j_m| \leq 10$ and $\lambda > 5$ cm. The linear combination with $\lambda = 11.19$ cm suppresses the ionospheric delay by 36.9 dB and benefits from a low noise level of $\sigma_{\mathrm{n}} = 3.2$ cm, which makes this combination preferable to an ionosphere-free combination. If E6 measurements are not available, the linear combination with $\lambda = 5.44$ cm benefits from a noise level that

is 10.4 dB lower than of the ionosphere-free combination of comparable wavelength.

λ [cm]	j_1	j_2	j_3	j_4	$S_{\mathrm{I[cyc]}}$ dB	$S_{\mathrm{I[m]}}$ dB	$S_{\mathrm{n[cyc]}}$ dB	$S_{\mathrm{n[m]}}$ dB	σ_{n} [mm]
11.19	3	3	0	-5	-34.6	-36.9	8.2	5.0	3.2
10.93	4	0	-1	-2	-17.8	-20.2	6.6	4.0	2.5
10.81	4	3	-10	4	-27.8	-30.2	10.7	7.3	5.4
10.58	5	-3	-1	0	-29.6	-32.2	7.7	4.9	3.1
5.50	7	6	-10	-1	-26.9	-32.3	11.3	5.2	3.3
5.44	8	0	-1	-5	-31.3	-36.8	9.8	4.0	2.5
5.38	9	-6	8	-9	-24.6	-30.1	12.1	5.9	3.9
5.30	10	-7	1	-2	-25.5	-31.0	10.9	5.1	3.2
6.11	0	25	0	-23	$-\infty$	$-\infty$	15.3	9.3	8.5
4.19	0	0	118	-115	$-\infty$	$-\infty$	22.2	14.4	27.5

Table 2.3: 4F narrowlane combinations of maximum ionospheric suppression

Fig. 2.2 shows the ionospheric suppression $S_{\mathrm{I[m]}}$ and wavelength λ of dual and triple frequency narrowlane combinations. In the region around $\lambda = 11$ cm, the dual frequency E1-E5a combination with $j_1 = 4, j_2 = -3$ achieves an ionospheric suppression of 20 dB which is hardly improved by the third frequency or higher values of j_m. For smaller λ, the ionospheric delay can be reduced to a much larger extent, e.g. the linear combination with $j_1 = 17$, $j_2 = -12$ and $j_3 = -1$ suppresses the ionospheric delay by 46.8 dB.

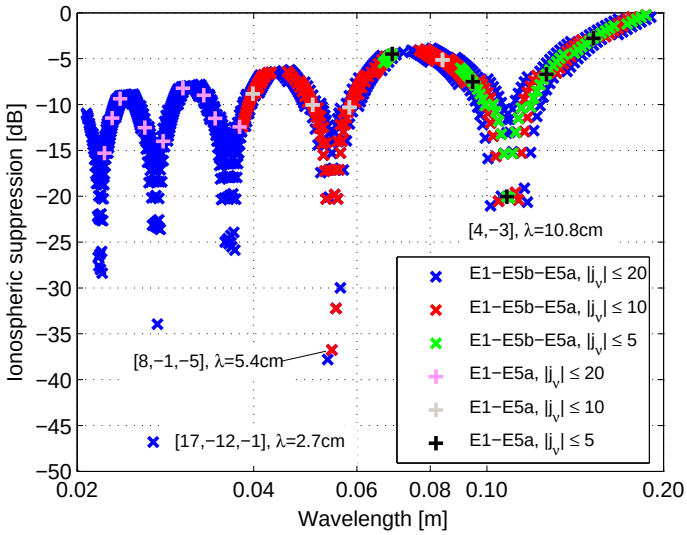

Figure 2.2: Reduced ionosphere narrowlane combinations with $|j_\nu| \leq 20$ for Galileo

Fig. 2.3 shows that the noise amplification $S_{\mathrm{n}[m]}$ exceeds the wavelength scaling by at least 8 dB for the depicted widelane combinations. Among all linear combinations with an ionospheric suppression of at least 15 dB, the linear combination with $j_1 = 2$, $j_2 = -6$, $j_3 = -1$ and $j_4 = 5$ achieves the lowest noise level in units of cycles.

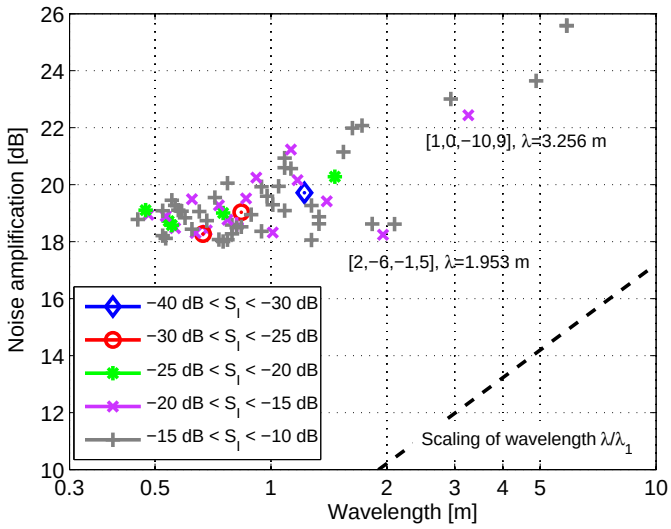

Figure 2.3: Noise amplification of reduced ionosphere widelane combinations of E1, E5b, E5a and E6 phase measurements with $|j_\nu| \leq 20$

Fig. 2.4 shows a comparison of triple frequency Galileo and triple frequency GPS reduced ionosphere widelane combinations. For both systems, a linear combination with a wavelength of 3.256m exists that suppresses the ionospheric delay by at least 10 dB. The Galileo combination benefits from a 5 dB stronger ionospheric suppression than the GPS combination at the price of a slightly larger ambiguity discrimination which is defined as

$$D = \frac{\lambda}{2\sigma} \tag{2.27}$$

It will be used in the next section to find an ionosphere-free mixed code-carrier combination which minimizes the probability of wrong fixing.

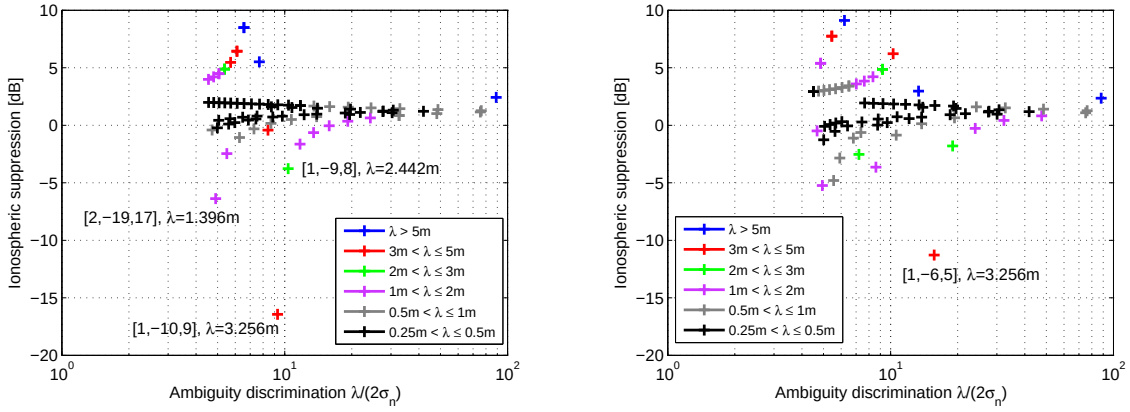

(a) E1-E5b-E5a widelane combinations

(b) L1-L2-L5 widelane combinations

Figure 2.4: Reduced ionosphere widelane combinations with $|j_\nu| \leq 20$

2.2 Design of multi-frequency mixed code carrier combinations

Multi-frequency phase-only combinations are sensitive to carrier phase multipath from reflections of the ground and nearby obstacles. As different multipath errors can occur on each carrier, the worst case multipath of a linear combination is obtained from (**??**) in units of cycles by

$$\mu_{\max} = \sum_{m=1}^{M} |j_m| \cdot \left| \frac{1}{2\pi} \arctan \left(\frac{\sum\limits_{i=1}^{n_r} \alpha_{i,m} \sin(\theta_{i,m})}{1 + \sum\limits_{i=1}^{n_r} \alpha_{i,m} \cos(\theta_{i,m})} \right) \right|, \tag{2.28}$$

where $\alpha_{i,m}$ and $\theta_{i,m}$ denote the fading coefficient and the phase offset of the i-th reflected signal on the m-th frequency. If there is only a single reflected signal with equal power as the direct signal, the worst-case multipath induced phase error is 1/4 cycle on each carrier. This explains the preference of linear combinations with small $|j_m|$.

Linear combinations that comprise both code and carrier phase measurements enable the use of smaller j_m but are also advantageous with respect to ionospheric elimination at large wavelengths. A mixed code-carrier combination weights the phase measurements by α_m and the code measurements by β_m, i.e.

$$\begin{aligned}
\lambda\phi_u^k(t_i) &= \sum_{m=1}^{M} \alpha_m \lambda_m \phi_{u,m}^k(t_i) + \beta_m \rho_{u,m}^k(t_i) \\
&= \sum_{m=1}^{M} (\alpha_m + \beta_m) \cdot \left(r_u^k(t_i) + \delta r_u^k(t_i) + c\left(\delta\tau_u(t_i) - \delta\tau^k(t_i)\right) + T_u^k(t_i) \right) \\
&\quad - \sum_{m=1}^{M} (\alpha_m - \beta_m) q_{1m}^2 \cdot I_u^k(t_i) \\
&\quad + \sum_{m=1}^{M} \left(\alpha_m \lambda_m N_{u,m}^k \right) + \sum_{m=1}^{M} \left(\alpha_m b_{\phi_{u,m}}^k \right) + \sum_{m=1}^{M} \left(\beta_m b_{\rho_{u,m}}^k \right) \\
&\quad + \sum_{m=1}^{M} \left(\alpha_m \varepsilon_{\phi_{u,m}}^k(t_i) + \beta_m \varepsilon_{\rho_{u,m}}^k(t_i) \right).
\end{aligned} \tag{2.29}$$

The linear combination should be geometry-preserving (GP), i.e.

$$\sum_{m=1}^{M} (\alpha_m + \beta_m) = 1. \tag{2.30}$$

and scale the ionospheric delay by $S_{\mathrm{I[m]}}$, i.e.

$$\left| \sum_{m=1}^{M} (\alpha_m - \beta_m) q_{1m}^2 \right| = S_{\mathrm{I[m]}}, \tag{2.31}$$

with $S_{\mathrm{I[m]}} = 0$ for ionosphere-free combinations. Moreover, the integer nature of ambiguities should be preserved (NP) which leads to the same constraints as for a phase-only combination. The wavelength of the mixed code-carrier combination is obtained from (2.3)-(2.6) and (2.30) as

$$\lambda = \tilde{\lambda}_0 \cdot w_\phi \quad \text{with} \quad \tilde{\lambda}_0 = \frac{1}{\sum\limits_{m=1}^{M} \frac{j_m}{\lambda_m}} \quad \text{and} \quad w_\phi = 1 - \sum_{m=1}^{M} \beta_m = \sum_{m=1}^{M} \alpha_m, \tag{2.32}$$

where w_ϕ is the weighting of phase measurements and $1 - w_\phi$ is the weighting of code measurements in the linear combination. The selection of linear combinations consists of two steps: a numerical search of $j_1, \ldots, j_M$ and an analytic computation of $\beta_1, \ldots, \beta_M$ and w_ϕ for each integer set $j_1, \ldots, j_M$. The computation of the $M+1$ unknowns with the GP and IF constraints leaves some additional degrees of freedom for further optimization.

First, a group of GP-NP mixed code-carrier combinations is analysed which fulfills

$$\sum_{m=1}^{M} \beta_m = 0, \tag{2.33}$$

i.e. different code weights β_m do not change the phase weighting w_ϕ and the wavelength λ of (2.32). Moreover, the noise amplification should be minimized, i.e.

$$\min_{\beta_m} \sigma_{\mathrm{n}}^2 = \min_{\beta_m} \sum_{m=1}^{M} \alpha_m^2 \sigma_{\phi_m}^2 + \beta_m^2 \sigma_{\rho_m}^2. \tag{2.34}$$

Fig. 2.5 shows σ_{n} as a function of $S_{\mathrm{I[m]}}$ for a triple frequency Galileo combination with $\lambda = 3.256$m. If only phase measurements are used, the ionospheric delay is suppressed by 16.4 dB which is not enough to neglect the residual ionospheric delay for precise positioning. However, the consideration of code measurements with a small weight allows the complete elimination of the ionospheric delay while σ_{n} is increased by only 0.5 mm.

Eq. (2.33) is a stringent constraint on λ which prevents the computation of linear combinations of maximum ambiguity discrimination $D = \frac{\lambda}{2\sigma_{\mathrm{n}}}$. It is therefore no longer considered. Fig. 2.6 shows that D varies significantly with the phase weighting w_ϕ and that the maximum of D does in general not occur at $w_\phi = 1$. Note that the legend only shows the base wavelength $\tilde{\lambda}$ which has to be scaled by w_ϕ to obtain λ. The largest discrimination of $D = 13.32$ is achieved by the linear combination with $j_1 = 1$, $j_2 = -5$ and $j_3 = 4$ at $\lambda = 2.89$m.

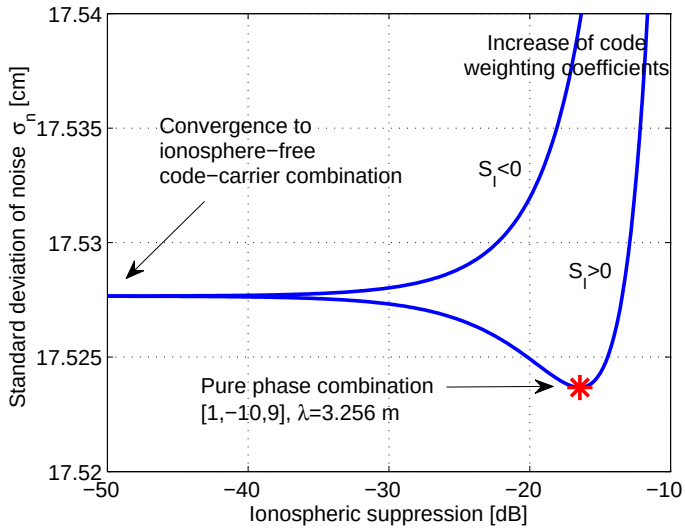

Figure 2.5: E1-E5b-E5a mixed code-carrier combinations with $\lambda = 3.256$ m, $j_1 = 1$, $j_2 = -10$, $j_3 = 9$: Elimination of ionospheric delay by a small code contribution

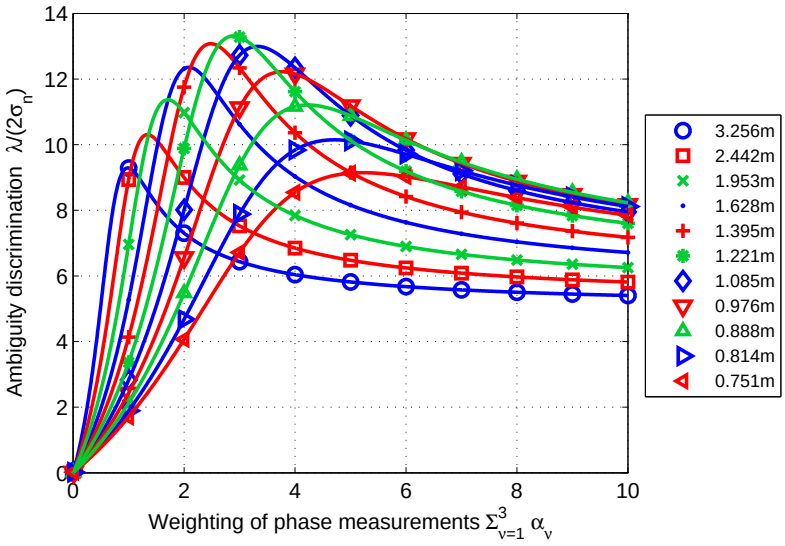

Figure 2.6: Optimal weighting of phase measurements in ionosphere-free E1-E5b-E5a mixed code-carrier combinations with $j_1 = 1$, $j_2 = \{-10, \ldots, 0\}$ and $j_3 = -j2 - 1$

It is shown in the next chapter that this GP-IF-NP mixed code-carrier combination minimizes the probability of wrong widelane fixing amongst all triple frequency GP-IF-NP linear combinations if no multipath is present. Unlike GP-NP phase-only combinations, there exist GP-NP mixed code carrier combinations for any arbitrary wavelength. Fig. 2.7 shows the impact of λ on the minimum noise standard deviation σ_n for $j_1 = 1$, $j_2 = -5$ and $j_3 = 4$. A wavelength of 1 m is preferred when the ionospheric delay is accurately known or sufficiently canceled by double differencing. A larger λ becomes optimal when an ionospheric suppression is required, e.g. the lowest noise level of an ionosphere-free

combination is achieved for $\lambda = 3$ m.

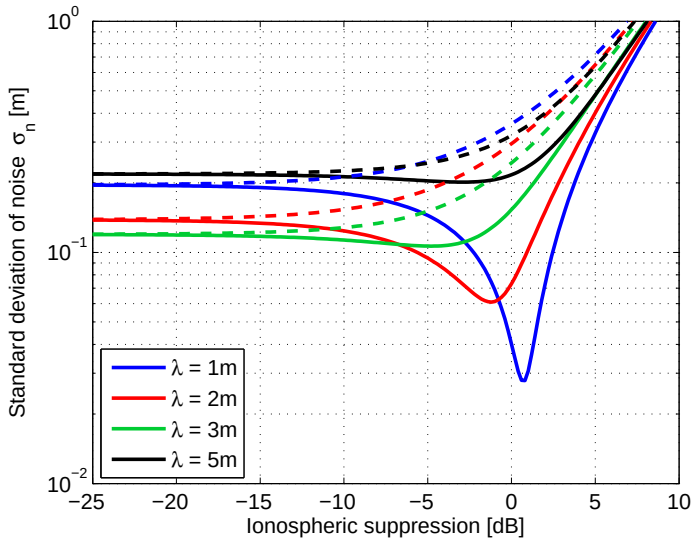

Figure 2.7: Minimum noise standard deviation of E1-E5b-E5a mixed code-carrier combinations with $j_1 = 1$, $j_2 = -5$, $j_3 = 4$, constant λ and variable ionospheric suppression

Henkel and Günther have computed triple frequency GP-IF-NP mixed code-carrier combinations of maximum ambiguity discrimination in [46]. The derivation of the weighting coefficients is generalized to 4 frequencies in [45] and to M frequencies in [47]. It starts with the optimization criterion, i.e.

$$\max_{\substack{\alpha_1,\ldots,\alpha_M \\ \beta_1,\ldots,\beta_M}} D(\alpha_1,\ldots,\alpha_M,\beta_1,\ldots,\beta_M) = \max_{\substack{\alpha_1,\ldots,\alpha_M \\ \beta_1,\ldots,\beta_M}} \frac{\lambda(\alpha_1,\ldots,\alpha_M,\beta_1,\ldots,\beta_M)}{2\sigma_{\mathrm{n_1}}(\alpha_1,\ldots,\alpha_M,\beta_1,\ldots,\beta_M)}. \tag{2.35}$$

The constraint on the geometry term of the linear combination is generalized to

$$\sum_{m=1}^{M}(\alpha_m + \beta_m) = h_1, \tag{2.36}$$

where $h_1 = 0$ corresponds to a geometry-free and $h_1 = 1$ to a geometry-preserving linear combination. Similarly, the combined ionospheric delay is constrained by

$$\sum_{m=1}^{M}(\alpha_m - \beta_m)q_{1m}^2 = h_2, \tag{2.37}$$

where $h_2 = 0$ corresponds to an ionosphere-free and $h_2 = 1$ to an ionosphere-preserving linear combination. Both constraints can be rewritten with the definition of the total

phase weight of (2.32) as

$$\boldsymbol{\Upsilon}_1 \begin{bmatrix} \beta_1 \\ \beta_2 \end{bmatrix} + \boldsymbol{\Upsilon}_2 \begin{bmatrix} w_\phi \\ \beta_3 \\ \vdots \\ \beta_M \end{bmatrix} = \boldsymbol{h}, \tag{2.38}$$

with

$$\boldsymbol{\Upsilon}_1 = \begin{bmatrix} 1 & 1 \\ -1 & -q_{12}^2 \end{bmatrix}, \quad \boldsymbol{\Upsilon}_2 = \begin{bmatrix} 1 & 1 & \cdots & 1 \\ \tilde{\lambda}_0 \sum_{m=1}^{M} \frac{j_m}{\lambda_m} q_{1m}^2 & -q_{13}^2 & \cdots & -q_{1M}^2 \end{bmatrix}, \quad \text{and} \quad \boldsymbol{h} = \begin{bmatrix} h_1 \\ h_2 \end{bmatrix}. \tag{2.39}$$

Solving (2.38) for $[\beta_1, \beta_2]^T$ yields

$$\begin{bmatrix} \beta_1 \\ \beta_2 \end{bmatrix} = \boldsymbol{\Upsilon}_1^{-1} \left(\boldsymbol{h} - \boldsymbol{\Upsilon}_2 \begin{bmatrix} w_\phi \\ \beta_3 \\ \vdots \\ \beta_M \end{bmatrix} \right) = \begin{bmatrix} s_1 + s_2 w_\phi + \sum_{m=3}^{M} s_m \beta_m \\ t_1 + t_2 w_\phi + \sum_{m=3}^{M} t_m \beta_m \end{bmatrix}, \tag{2.40}$$

where s_m and t_m are implicitly defined by $\boldsymbol{\Upsilon}_1$, $\boldsymbol{\Upsilon}_2$ and $\boldsymbol{h}$. Eq. (2.40) allows us to express D as a function of w_ϕ and β_m, $m \geq 3$:

$$\begin{aligned} D \;=\; & \frac{\tilde{\lambda}}{2} \cdot w_\phi \cdot \left(\tilde{\eta}^2 w_\phi^2 + \left(s_1 + s_2 w_\phi + \sum_{m=3}^{M} s_m \beta_m \right)^2 \sigma_{\rho_1}^2 \right. \\ & \left. + \left(t_1 + t_2 w_\phi + \sum_{m=3}^{M} t_m \beta_m \right)^2 \sigma_{\rho_2}^2 + \sum_{m=3}^{M} \beta_m^2 \sigma_{\rho_m}^2 \right)^{-1/2} \end{aligned} \tag{2.41}$$

with

$$\tilde{\eta}^2 = \tilde{\lambda}^2 \cdot \sum_{m=1}^{M} \frac{j_m^2}{\lambda_m^2} \sigma_{\phi_m}^2. \tag{2.42}$$

The discrimination can be written in matrix-vector notation as

$$\begin{aligned} D \;=\; & \frac{\tilde{\lambda}}{2} \cdot w_\phi \cdot \left(\tilde{\eta}^2 w_\phi^2 + \left(s_1 + s_2 w_\phi + \boldsymbol{s}^T \boldsymbol{\beta} \right)^2 \sigma_{\rho_1}^2 \right. \\ & \left. + \left(t_1 + t_2 w_\phi + \boldsymbol{t}^T \boldsymbol{\beta} \right)^2 \sigma_{\rho_2}^2 + \boldsymbol{\beta}^T \boldsymbol{\Sigma} \boldsymbol{\beta} \right)^{-1/2}, \end{aligned} \tag{2.43}$$

with $\boldsymbol{s} = [s_3, \ldots, s_M]^T$, $\boldsymbol{t} = [t_3, \ldots, t_M]^T$, $\boldsymbol{\beta} = [\beta_3, \ldots, \beta_M]^T$ and the diagonal matrix $\boldsymbol{\Sigma}$ that is given by

$$\boldsymbol{\Sigma} = \begin{bmatrix} \sigma_{\rho_3}^2 & \cdots & \sigma_{\rho_3 \rho_M} \\ \vdots & \ddots & \vdots \\ \sigma_{\rho_3 \rho_M} & \cdots & \sigma_{\rho_M}^2 \end{bmatrix}. \tag{2.44}$$

The maximum discrimination is given by

$$\frac{\partial D}{\partial w_\phi} = 0 \tag{2.45}$$

and

$$\frac{\partial D}{\partial \boldsymbol{\beta}} = \mathbf{0}. \tag{2.46}$$

Eq. (2.46) is equivalent to

$$\begin{aligned}
&(s_1 + s_2 w_\phi + \boldsymbol{s}^T\boldsymbol{\beta})\boldsymbol{s} \cdot \sigma_{\rho_1}^2 + (t_1 + t_2 w_\phi + \boldsymbol{t}^T\boldsymbol{\beta})\boldsymbol{t} \cdot \sigma_{\rho_2}^2 + \boldsymbol{\Sigma}\boldsymbol{\beta} \\
&\quad = \sigma_{\rho_1}^2 \boldsymbol{s}(s_1 + s_2 w_\phi + \boldsymbol{s}^T\boldsymbol{\beta}) + \sigma_{\rho_2}^2 \boldsymbol{t}(t_1 + t_2 w_\phi + \boldsymbol{t}^T\boldsymbol{\beta}) + \boldsymbol{\Sigma}\boldsymbol{\beta} \\
&\quad = \underbrace{\left[\sigma_{\rho_1}^2 \boldsymbol{s}\boldsymbol{s}^T + \sigma_{\rho_2}^2 \boldsymbol{t}\boldsymbol{t}^T + \boldsymbol{\Sigma}\right]}_{\boldsymbol{A}} \boldsymbol{\beta} + \underbrace{\left[s_2\sigma_{\rho_1}^2 \boldsymbol{s} + t_2\sigma_{\rho_2}^2 \boldsymbol{t}\right]}_{\boldsymbol{b}} w_\phi + \underbrace{\left[s_1\sigma_{\rho_1}^2 \boldsymbol{s} + t_1\sigma_{\rho_2}^2 \boldsymbol{t}\right]}_{\boldsymbol{c}} = \mathbf{0}.
\end{aligned} \tag{2.47}$$

Solving (2.47) for $\boldsymbol{\beta}$ yields

$$\boldsymbol{\beta} = -\boldsymbol{A}^{-1}(\boldsymbol{c} + \boldsymbol{b} \cdot w_\phi). \tag{2.48}$$

Constraint (2.45) is written in full terms as

$$\begin{aligned}
&\left(s_1 + s_2 w_\phi + \boldsymbol{s}^T\boldsymbol{\beta}\right)\left(s_1 + \boldsymbol{s}^T\boldsymbol{\beta}\right)\sigma_{\rho_1}^2 + \left(t_1 + t_2 w_\phi + \boldsymbol{t}^T\boldsymbol{\beta}\right) \\
&\cdot \left(t_1 + \boldsymbol{t}^T\boldsymbol{\beta}\right)\sigma_{\rho_2}^2 + \boldsymbol{\beta}^T\boldsymbol{\Sigma}\boldsymbol{\beta} = 0.
\end{aligned} \tag{2.49}$$

Replacing $\boldsymbol{\beta}$ by (2.48) yields

$$\begin{aligned}
&\left(s_1 + s_2 w_\phi - \boldsymbol{s}^T\boldsymbol{A}^{-1}(\boldsymbol{c} + \boldsymbol{b}w_\phi)\right) \cdot \left(s_1 - \boldsymbol{s}^T\boldsymbol{A}^{-1}(\boldsymbol{c} + \boldsymbol{b}w_\phi)\right) \cdot \sigma_{\rho_1}^2 \\
&+ \left(t_1 + t_2 w_\phi - \boldsymbol{t}^T\boldsymbol{A}^{-1}(\boldsymbol{c} + \boldsymbol{b}w_\phi)\right) \cdot \left(t_1 - \boldsymbol{t}^T\boldsymbol{A}^{-1}(\boldsymbol{c} + \boldsymbol{b}w_\phi)\right) \cdot \sigma_{\rho_2}^2 \\
&+ (\boldsymbol{c} + \boldsymbol{b}w_\phi)^T(\boldsymbol{A}^{-1})^T\boldsymbol{\Sigma}\boldsymbol{A}^{-1}(\boldsymbol{c} + \boldsymbol{b}w_\phi) = 0,
\end{aligned} \tag{2.50}$$

Eq. (2.50) can be rewritten as a quadratic equation, i.e.

$$r_0 + r_1 \cdot w_\phi + r_2 \cdot w_\phi^2 = 0, \tag{2.51}$$

with

$$\begin{aligned}
r_0 &= \left(s_1 - \boldsymbol{s}^T\boldsymbol{A}^{-1}\boldsymbol{c}\right)^2 \sigma_{\rho_1}^2 + \left(t_1 - \boldsymbol{t}^T\boldsymbol{A}^{-1}\boldsymbol{c}\right)^2 \sigma_{\rho_2}^2 + \boldsymbol{c}^T(\boldsymbol{A}^{-1})^T\boldsymbol{\Sigma}\boldsymbol{A}^{-1}\boldsymbol{c} \\
r_1 &= \left((s_1 - \boldsymbol{s}^T\boldsymbol{A}^{-1}\boldsymbol{c})(-\boldsymbol{s}^T\boldsymbol{A}^{-1}\boldsymbol{b}) + (s_2 - \boldsymbol{s}^T\boldsymbol{A}^{-1}\boldsymbol{b})(s_1 - \boldsymbol{s}^T\boldsymbol{A}^{-1}\boldsymbol{c})\right) \cdot \sigma_{\rho_1}^2 \\
&\quad + \left((t_1 - \boldsymbol{t}^T\boldsymbol{A}^{-1}\boldsymbol{c})(-\boldsymbol{t}^T\boldsymbol{A}^{-1}\boldsymbol{b}) + (t_2 - \boldsymbol{t}^T\boldsymbol{A}^{-1}\boldsymbol{b})(t_1 - \boldsymbol{t}^T\boldsymbol{A}^{-1}\boldsymbol{c})\right) \cdot \sigma_{\rho_2}^2 \\
&\quad + \left(\boldsymbol{c}^T(\boldsymbol{A}^{-1})^T\boldsymbol{\Sigma}\boldsymbol{A}^{-1}\boldsymbol{b} + \boldsymbol{b}^T(\boldsymbol{A}^{-1})^T\boldsymbol{\Sigma}\boldsymbol{A}^{-1}\boldsymbol{c}\right) \\
r_2 &= (s_2 - \boldsymbol{s}^T\boldsymbol{A}^{-1}\boldsymbol{b})(-\boldsymbol{s}^T\boldsymbol{A}^{-1}\boldsymbol{b}) \cdot \sigma_{\rho_1}^2 \\
&\quad + (t_2 - \boldsymbol{t}^T\boldsymbol{A}^{-1}\boldsymbol{b})(-\boldsymbol{t}^T\boldsymbol{A}^{-1}\boldsymbol{b}) \cdot \sigma_{\rho_2}^2 + \boldsymbol{b}^T(\boldsymbol{A}^{-1})^T\boldsymbol{\Sigma}\boldsymbol{A}^{-1}\boldsymbol{b}.
\end{aligned}$$

The latter one can be further simplified by replacing $\boldsymbol{A}$, $\boldsymbol{b}$, $\boldsymbol{s}$ and $\boldsymbol{t}$ by their definitions of

(2.47). In the case of 4 frequencies, one obtains (using Mathematica for simplification)

$$
\begin{aligned}
&(s_2 - \boldsymbol{s}^T\boldsymbol{A}^{-1}\boldsymbol{b})(-\boldsymbol{s}^T\boldsymbol{A}^{-1}\boldsymbol{b}) \cdot \sigma_{\rho_1}^2 \\
&\quad = \frac{-\sigma_{\rho_1}^2 \left(s_2\sigma_{\rho_1}^2 \left((s_4t_3 - s_3t_4)^2\sigma_{\rho_2}^2 + s_4^2\sigma_{\rho_3}^2 + s_3^2\sigma_{\rho_4}^2\right) + t_2\sigma_{\rho_2}^2(s_4t_4\sigma_{\rho_3}^2 + s_3t_3\sigma_{\rho_4}^2)\right)}{\left(\sigma_{rho_3}^2\sigma_{\rho_4}^2 + \sigma_{\rho_1}^2 \left((s_4t_3 - s_3t_4)^2\sigma_{\rho_2}^2 + s_4^2\sigma_{\rho_3}^2 + s_3^2\sigma_{\rho_4}^2\right) + \sigma_{\rho_2}^2 \left(t_4^2\sigma_{\rho_3}^2 + t_3^2\sigma_{\rho_4}^2\right)\right)^2} \\
&\qquad \cdot \left(s_2\sigma_{\rho_3}^2\sigma_{\rho_4}^2 + \sigma_{\rho_2}^2 \left(t_4(-s_4t_2 + s_2t_4)\sigma_{\rho_3}^2 + t_3(-s_3t_2 + s_2t_3)\sigma_{\rho_4}^2\right)\right), \qquad (2.52)
\end{aligned}
$$

and

$$
\begin{aligned}
&(t_2 - \boldsymbol{t}^T\boldsymbol{A}^{-1}\boldsymbol{b})(-\boldsymbol{t}^T\boldsymbol{A}^{-1}\boldsymbol{b}) \cdot \sigma_{\rho_2}^2 \\
&\quad = \frac{-\sigma_{\rho_2}^2 \left(t_2\sigma_{\rho_3}^2\sigma_{\rho_4}^2 + \sigma_{\rho_1}^2 \left(s_4(s_4t_2 - s_2t_4)\sigma_{\rho_3}^2 + s_3(s_3t_2 - s_2t_3)\sigma_{\rho_4}^2\right)\right)}{\left(\sigma_{\rho_3}^2\sigma_{\rho_4}^2 + \sigma_{\rho_1}^2 \left((s_4t_3 - s_3t_4)^2\sigma_{\rho_2}^2 + s_4^2\sigma_{\rho_3}^2 + s_3^2\sigma_{\rho_4}^2\right) + \sigma_{\rho_2}^2 \left(t_4^2\sigma_{\rho_3}^2 + t_3^2\sigma_{\rho_4}^2\right)\right)^2} \\
&\qquad \cdot \left(t_2\sigma_{\rho_2}^2(t_4^2\sigma_{\rho_3}^2 + t_3^2\sigma_{\rho_4}^2) + \sigma_{\rho_1}^2 \left(t_2(s_4t_3 - s_3t_4)^2\sigma_{\rho_2}^2 + s_2(s_4t_4\sigma_{\rho_3}^2 + s_3t_3\sigma_{\rho_4}^2)\right)\right), \qquad (2.53)
\end{aligned}
$$

and

$$
\begin{aligned}
&\boldsymbol{b}^T(\boldsymbol{A}^{-1})^T\boldsymbol{\Sigma}\boldsymbol{A}^{-1}\boldsymbol{b} \\
&= \frac{t_2^2\sigma_{\rho_2}^4\sigma_{\rho_3}^2\sigma_{\rho_4}^2(t_4^2\sigma_{\rho_3}^2 + t_3^2\sigma_{\rho_4}^2) + \sigma_{\rho_1}^4 \left(2s_2^2(s_4t_3 - s_3t_4)^2\sigma_{\rho_2}^2\sigma_{\rho_3}^2\sigma_{\rho_4}^2\right)}{\left(\sigma_{\rho_3}^2\sigma_{\rho_4}^2 + \sigma_{\rho_1}^2 \left((s_4t_3 - s_3t_4)^2\sigma_{\rho_2}^2 + s_4^2\sigma_{\rho_3}^2 + s_3^2\sigma_{\rho_4}^2\right) + \sigma_{\rho_2}^2 \left(t_4^2\sigma_{\rho_3}^2 + t_3^2\sigma_{\rho_4}^2\right)\right)^2} \\
&\quad + \frac{2t_2\sigma_{\rho_1}^2\sigma_{\rho_2}^2\sigma_{\rho_3}^2\sigma_{\rho_4}^2 \left(t_2(s_4t_3 - s_3t_4)^2\sigma_{\rho_2}^2 + s_2(s_4t_4\sigma_{\rho_3}^2 + s_3t_3\sigma_{\rho_4}^2)\right)}{\left(\sigma_{\rho_3}^2\sigma_{\rho_4}^2 + \sigma_{\rho_1}^2 \left((s_4t_3 - s_3t_4)^2\sigma_{\rho_2}^2 + s_4^2\sigma_{\rho_3}^2 + s_3^2\sigma_{\rho_4}^2\right) + \sigma_{\rho_2}^2 \left(t_4^2\sigma_{\rho_3}^2 + t_3^2\sigma_{\rho_4}^2\right)\right)^2} \\
&\quad + \frac{\sigma_{\rho_1}^4 \left(s_2^2\sigma_{\rho_3}^2\sigma_{\rho_4}^2(s_4^2\sigma_{\rho_3}^2 + s_3^2\sigma_{\rho_4}^2) + (s_4t_3 - s_3t_4)^2\sigma_{\rho_2}^4 \left((s_4t_2 - s_2t_4)^2\sigma_{\rho_3}^2 + (s_3t_2 - s_2t_3)^2\sigma_{\rho_4}^2\right)\right)}{\left(\sigma_{\rho_3}^2\sigma_{\rho_4}^2 + \sigma_{\rho_1}^2 \left((s_4t_3 - s_3t_4)^2\sigma_{\rho_2}^2 + s_4^2\sigma_{\rho_3}^2 + s_3^2\sigma_{\rho_4}^2\right) + \sigma_{\rho_2}^2 \left(t_4^2\sigma_{\rho_3}^2 + t_3^2\sigma_{\rho_4}^2\right)\right)^2} \\
&\qquad\qquad\qquad\qquad\qquad\qquad\qquad\qquad\qquad\qquad\qquad\qquad\qquad\qquad (2.54)
\end{aligned}
$$

Adding up these three terms yields $r_2 = 0$ and solving (2.51) for w_ϕ gives the optimal phase weight:

$$w_{\phi_{\text{opt}}} = -r_0/r_1, \qquad (2.55)$$

which is used in (2.48) and (2.40) to obtain the code weights. Eq. (2.32) provides the optimum wavelength for the computation of the phase weights with (2.6).

Tab. 2.4 shows the weighting coefficients and properties of GP-IF-NP linear combinations of maximum ambiguity discrimination based on code and carrier phase measurements on up to five frequencies. The dual frequency E1-E5a combination is characterized by a noise level of 31.4cm and a wavelength of 4.309m which allows reliable ambiguity resolution within a few epochs. As only the E1 and E5 frequencies lie in aeronautical bands, this linear combination might be useful for aviation.

Linear combinations that comprise the wideband E5 and E6 code measurements benefit from a substantially lower noise level which turns into a larger ambiguity discrimination. It increases to 25.1 for the E1-E5 combination, to 39.2 for the E1-E5-E6 combination, and to 41.2 for the E1-E5a-E5b-E5-E6 combination. The large wavelength of these combinations

makes them robust to the non-dispersive orbital errors and satellite clock offsets. The linear combination of measurements on 5 frequencies has the additional advantageous property of $|\beta_m| < 1.26$ and $|j_m| \leq 2$ for all m. A correlation of 50 % has been assumed between the E5 signal and the E5a and E5b signals.

An even higher ambiguity discrimination can be achieved if the 10 MHz wide main lobe between the E5a and E5b bands is used as an additional E5c signal. However, the benefit is negligible as the power spectral density is 17 dB lower than for the E1 signal and, thus, the Cramer Rao bound equals 54.8 cm.

Table 2.4: GP-IF-NP mixed code-carrier widelane combinations of max. discrimination for $\sigma_\phi = 1$mm, $\sigma_{\rho_m} = \Gamma_m$

	E1	E5a	E5b	E5	E6	λ	σ_{n}	D
j_m	1.0000			−1.0000				
α_m	17.2629			−13.0593		3.285m	6.5cm	25.1
β_m	−0.0552			−3.1484				
j_m	1.0000	−1.0000						
α_m	22.6467	−16.9115				4.309m	31.4cm	6.9
β_m	−1.0227	−3.7125						
j_m	1.0000	4.0000	−5.0000					
α_m	18.5565	55.4284	−71.0930			3.531m	13.3cm	13.3
β_m	−0.2342	−0.8502	−0.8075					
j_m	1.0000			1.0000	−2.0000			
α_m	21.1223			15.9789	−34.2894	4.019m	5.1cm	39.2
β_m	−0.0200			−1.1422	−0.6495			
j_m	1.0000	1.0000	0.0000		−2.0000			
α_m	23.4845	17.5371	0.0000		−38.1242	4.469m	6.3cm	35.3
β_m	−0.0468	−0.1700	−0.1615		−1.5191			
j_m	1.0000	1.0000	0.0000	0.0000	−2.0000			
α_m	20.5896	15.3754	0.0000	0.0000	−33.4247	3.918m	4.7cm	41.3
β_m	−0.0147	0.1034	0.1060	−1.2584	−0.4766			

Tab. 2.5 shows the weighting coefficients and properties of the optimum widelane and narrowlane linear combinations for an increased noise level. The larger noise assumptions result in lower code weights and a slightly larger E6 phase weight for the 4F E1-E5a-E5b-E6 widelane combination. For all other frequency settings, the weighting coefficients are the same as in Tab. 2.4. For narrowlane combinations, the use of additional frequencies has only a negligible impact on λ and σ_{n}. The ambiguity discrimination varies between 10.1 and 11.2 which is larger than in the case of the first 3 combinations of Tab. 2.5 but smaller than in the case of the remaining widelane combinations.

The maximization of the ambiguity discrimination in (2.35) does not consider residual biases due to multipath or other un-modeled effects. Therefore, the maximization of D

Table 2.5: GP-IF-NP mixed code-carrier widelane and narrowlane combinations of maximum ambiguity discrimination for $\sigma_\phi = 2\text{mm}$, $\sigma_{\rho_m} = 3 \cdot \Gamma_m$

	E1	E5a	E5b	E5	E6	λ	σ_n	D
j_m	1.0000			−1.0000				
α_m	17.2629			−13.0593		3.285m	19.0cm	8.6
β_m	−0.0552			−3.1484				
j_m	1.0000	−1.0000						
α_m	22.6467	−16.9115				4.309m	93.8cm	2.3
β_m	−1.0227	−3.7125						
j_m	1.0000	4.0000	−5.0000					
α_m	18.5565	55.4284	−71.0930			3.531m	34.0cm	5.2
β_m	−0.2342	−0.8502	−0.8075					
j_m	1.0000			1.0000	−2.0000			
α_m	21.1223			15.9789	−34.2894	4.019m	11.9cm	16.9
β_m	−0.0200			−1.1422	−0.6495			
j_m	1.0000	1.0000	1.0000		−3.0000			
α_m	22.5147	16.8130	17.2516		−54.8249	4.284m	13.7cm	15.6
β_m	−0.0186	−0.0676	−0.0642		−0.6040			
j_m	1.0000	1.0000	0.0000	0.0000	−2.0000			
α_m	20.6978	15.4562	0.0000	0.0000	−33.6004	3.9387m	10.9cm	18.1
β_m	−0.0159	−0.0578	−0.0549	−0.9084	−0.5166			
	E1	E5a	E5b	E5	E6	λ	σ_n	D
j_m	4.0000			−3.0000				
α_m	2.2853			−1.2966		10.87cm	5.3mm	10.3
β_m	0.0002			0.0111				
j_m	4.0000	−3.0000						
α_m	2.2870	−1.2809				10.88cm	5.4mm	10.1
β_m	−0.0013	−0.0048						
j_m	4.0000	−2.0000	−1.0000					
α_m	2.2853	−0.8533	−0.4378			10.87cm	5.0mm	10.8
β_m	0.0007	0.0026	0.0025					
j_m	4.0000			−3.0000	0.0000			
α_m	2.2841			−1.2959	0.0000	10.87cm	5.3mm	10.3
β_m	0.0001			0.0075	0.0042			
j_m	4.0000	−2.0000	−1.0000		0.0000			
α_m	2.2844	−0.8529	−0.4376		0.0000	10.87cm	5.0mm	10.9
β_m	0.0002	0.0006	0.0005		0.0049			
j_m	4.0000	−1.0000	−1.0000	−1.0000	0.0000			
α_m	2.2845	−0.4265	−0.4376	−0.4321	0.0000	10.87cm	4.8mm	11.2
β_m	0.0002	0.0004	0.0004	0.0068	0.0039			

shall be constrained by bounding the combination bias b_{n} to a predefined value, i.e.

$$b_{\mathrm{n}} = \sum_{m=1}^{M} \alpha_m \lambda_m b_{\phi_m} + \beta_m b_{\rho_m} \leq \sum_{m=1}^{M} |\alpha_m| \cdot b_{\phi_{\max}} + |\beta_m| \cdot b_{\rho_{\max}} = b_{\max}, \tag{2.56}$$

where b_{ϕ_m} and b_{ρ_m} denote the phase and code measurement biases, and $b_{\max}$ represents the bound on the combination bias. The equality in (2.56) is fulfilled when all measurement biases accumulate positively. Tab. 2.6 shows the weighting coefficients and properties of widelane mixed code-carrier combinations of maximum ambiguity discrimination with different constraints on the worst-case combination bias. Obviously, the bias constraint prefers linear combinations with smaller absolute values of the weighting coefficients, and tends to smaller wavelengths if the bias constraint becomes more strict. On the other hand, less and less constrained biases lead to larger wavelengths and ambiguity discriminations.

Table 2.6: GP-IF-NP mixed code-carrier widelane combinations of maximum ambiguity discrimination $D = \frac{\lambda}{2\sigma_{\mathrm{n}}}$ for $\sigma_\phi = 1\mathrm{mm}$, $\sigma_{\rho_m} = \Gamma_m$ with constrained worst-case combination biases for $b_{\phi_{\max}} = 1\mathrm{cm}$ and $b_{\rho_{\max}} = 5\mathrm{cm}$ on all frequencies

	E1	E5a	E5b	λ	σ_{n}	b_{n}	D
j_m	0.0000	1.0000	−1.0000				
α_m	0.0000	3.8699	−3.9708	0.986m	26.9cm	25.0cm	1.84
β_m	2.2890	−0.7957	0.0000				
j_m	0.0000	1.0000	−1.0000				
α_m	0.0000	−5.7874	5.9384	1.475m	27.4cm	30.0cm	2.69
β_m	2.2519	−1.4029	0.0000				
j_m	0.0000	1.0000	−1.0000				
α_m	0.0000	9.1037	−9.3412	2.320m	26.6cm	35.0cm	4.35
β_m	2.2743	−1.0368	0.0000				
j_m	1.0000	−1.0000	0.0000				
α_m	14.3260	−10.6980	0.0000	2.726m	22.2cm	40.0cm	6.15
β_m	0.1836	−2.8116	0.0000				

An alternative to the fixed bias constraint is the generalization of the ambiguity discrimination to the ratio between the combination wavelength and the weighted sum of the combination noise and combination bias, i.e.

$$D = \frac{\lambda}{\kappa_1 \sigma_{\mathrm{n}} + \kappa_2 b_{\mathrm{n}}}, \tag{2.57}$$

with the weights κ_1 and κ_2. The maximization of (2.57) tends to large wavelengths as both σ_{n} and b_{n} increase slower than λ. Tab. 2.7 shows the weighting coefficients and properties of the optimized combinations for $\kappa_1 = 1$ and $\kappa_2 = 1$. The bias bounds have been set to 1 cm for the phase and to 5 cm for the code measurements which results in worst-case combination biases that exceed the combination noise. A wavelength of 5 m is required to achieve a generalized ambiguity discrimination of more than 6.

Table 2.7: GP-IF-NP mixed code-carrier widelane combinations of maximum discrimination $D = \frac{\lambda}{\sigma_{\mathrm{n}}+b_{\mathrm{n}}}$ for $\sigma_\phi = 1\mathrm{mm}$, $\sigma_{\rho_m} = \Gamma_m$ for $b_{\phi_{\max}} = 1\mathrm{cm}$ and $b_{\rho_{\max}} = 5\mathrm{cm}$ on all frequencies

	E1	E5a	E5b	λ	σ_{n}	b_{n}	D
j_m	1.0000	0.0000	−1.0000				
α_m	4.2040	0.0000	−3.2213	0.80m	21.7cm	24.3cm	1.74
β_m	1.6978	−1.3107	−0.3699				
j_m	1.0000	0.0000	−1.0000				
α_m	5.2550	0.0000	−4.0266	1.00m	20.6cm	26.0cm	2.15
β_m	1.5554	−1.3366	−0.4472				
j_m	1.0000	0.0000	−1.0000				
α_m	10.5101	0.0000	−8.0532	2.00m	16.3cm	34.3cm	3.96
β_m	0.8414	−1.4805	−0.8178				
j_m	1.0000	0.0000	−1.0000				
α_m	15.7651	0.0000	−12.0798	3.00m	16.0cm	42.5cm	5.13
β_m	0.1229	−1.6604	−1.1478				
j_m	0.0000	1.0000	−1.0000				
α_m	0.0000	15.6969	−16.1063	4.00m	26.6cm	48.1cm	5.36
β_m	2.3306	−0.5115	−0.4097				
j_m	0.0000	1.0000	−1.0000				
α_m	0.0000	19.6211	−20.1329	5.00m	26.5cm	55.5cm	6.10
β_m	2.3310	−0.4579	−0.3613				

2.3 Carrier smoothed multi-frequency linear combinations

In the previous mixed code-carrier widelane combinations, the major noise contribution arises from the code measurements. The code noise and code multipath can be efficiently reduced by carrier smoothing which has been introduced by Hatch in [48]. Fig. 2.8 shows the smoothing of a multi-frequency mixed code-carrier combination with a low noise phase-only combination. The difference between both combinations is geometry free, i.e. it eliminates the true range, the clock offsets and the tropospheric delay. The remaining noise and multipath are suppressed by the low pass filter. The integer ambiguities are not affected by the filtering so that the integer ambiguities of the smoothed combination equal the integer ambiguities of the unsmoothed code-carrier combination. After filtering, the phase-only combination is added to recover the range information. Note that the phase only combination is considered twice with different signs such that its ambiguities do not appear in the smoothed output.

Hatch has used no linear combinations to eliminate the ionospheric delay, i.e. he chose the L1 C/A code measurement for the upper input and the L1 phase measurement for the lower input. As the ionosphere affects the code and phase with opposite signs, the doubled ionospheric delay enters the low pass filter. Thus, the smoothed output is affected

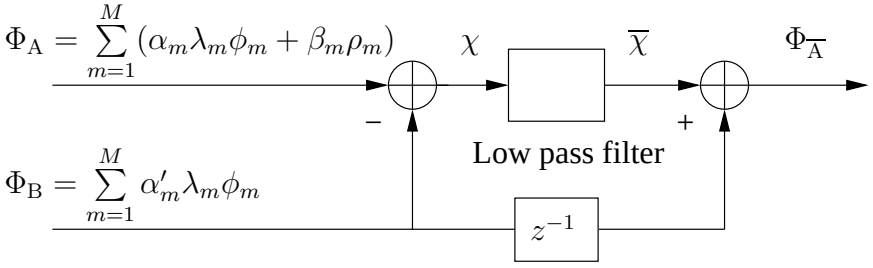

Figure 2.8: Carrier smoothing of a multi-frequency code-carrier linear combination

by the ionospheric delay of the current and previous time instants. Hwang et al. [49] and Mc Graw et al. [50] have suggested a dual-frequency divergence-free and a dual frequency ionosphere-free carrier smoothing. The divergence-free smoothing removes the ionospheric delay from the previous epochs and only leaves the ionospheric delay of the current epoch. The dual-frequency ionosphere-free smoothing eliminates the ionospheric delay completely but requires a certain smoothing period to overcome the noise amplification from the dual-frequency combination. Therefore, Günther and Henkel have suggested a triple frequency ionosphere-free carrier smoothing in [51] to achieve reduced noise, ionosphere-free carrier smoothed code measurements. A first order low pass filter is typically used for smoothing and implemented as

$$\overline{\chi}(t_k) = \left(1 - \frac{1}{\tau}\right) \cdot \overline{\chi}(t_{k-1}) + \frac{1}{\tau} \cdot \chi(t_k) \tag{2.58}$$

with the smoothing constant τ. The recursive form of (2.58) can be solved for $\overline{\chi}(t_k)$ by series expansion:

$$\overline{\chi}(t_k) = \frac{1}{\tau} \cdot \sum_{n=0}^{k-2} \left(1 - \frac{1}{\tau}\right)^n \cdot \chi(t_{k-n}) + \left(1 - \frac{1}{\tau}\right)^{k-1} \cdot \chi(t_1). \tag{2.59}$$

Assuming independent measurements $\chi(t_k)$, the variance of $\overline{\chi}(t_k)$ is given by

$$\begin{aligned} \sigma^2_{\overline{\chi}} &= \frac{1}{\tau^2} \cdot \frac{1 - (1 - \frac{1}{\tau})^{2(k-1)}}{1 - (1 - \frac{1}{\tau})^2} \cdot \sigma^2_\chi + \left(1 - \frac{1}{\tau}\right)^{2(k-1)} \cdot \sigma^2_\chi \\ &= \frac{1}{2\tau - 1} \cdot \sigma^2_\chi + \frac{2\tau - 2}{2\tau - 1} \left(1 - \frac{1}{\tau}\right)^{2(k-1)} \cdot \sigma^2_\chi, \end{aligned} \tag{2.60}$$

which converges for large k to

$$\lim_{k \to \infty} \sigma^2_{\overline{\chi}} = \frac{1}{2\tau - 1} \cdot \sigma^2_\chi. \tag{2.61}$$

In the case of zero-mean white Gaussian noise, the ideal averaging would be

$$\overline{\chi}(t_k) = \frac{1}{k} \cdot \sum_{n=0}^{k-1} \chi(t_{k-n}), \tag{2.62}$$

with the variance $\sigma^2_{\overline{\chi}} = \frac{1}{k} \cdot \sigma^2_{\chi}$, which converges to 0 for large k. However, the low pass filter of (2.58) has been preferred so far as it can better adapt to changing conditions, e.g. code-multipath which is not perfectly stationary.

The multi-frequency GP-IF mixed code-carrier combination Φ_{A} and the GP-IF phase-only combination Φ_{B} can be jointly optimized to maximize the ambiguity discrimination of the smoothed combination $\Phi_{\overline{\mathrm{A}}}$, i.e.

$$\max_{\substack{\alpha_1,\ldots,\alpha_M \\ \beta_1,\ldots,\beta_M \\ \alpha'_1,\ldots,\alpha'_M}} \quad D = \frac{\lambda}{2\sigma_{\Phi_{\overline{\mathrm{A}}}}}, \tag{2.63}$$

with the smoothed variance

$$\begin{aligned} \sigma^2_{\Phi_{\overline{\mathrm{A}}}} &= \mathrm{E}\{(\Phi_{\overline{\mathrm{A}}}(t_k))^2\} - (\mathrm{E}\{\Phi_{\overline{\mathrm{A}}}(t_k)\})^2 \\ &= \mathrm{E}\{\overline{\chi}^2(t_k) + 2\overline{\chi}(t_k)\Phi_{\mathrm{B}}(t_k) + \Phi^2_{\mathrm{B}}(t_k)\} - (\mathrm{E}\{\Phi_{\overline{\mathrm{A}}}(t_k)\})^2 . \end{aligned} \tag{2.64}$$

The covariance of $\overline{\chi}(t_k)\Phi_{\mathrm{B}}(t_k)$ is obtained from (2.59) as

$$\begin{aligned} &\mathrm{E}\left\{\overline{\chi}(t_k)\Phi_{\mathrm{B}}(t_k)\right\} - \mathrm{E}\left\{\overline{\chi}(t_k)\right\}\mathrm{E}\left\{\Phi_{\mathrm{B}}(t_k)\right\} \\ &\quad = \mathrm{E}\left\{\frac{1}{\tau}\cdot\sum_{n=0}^{k-2}\left(1-\frac{1}{\tau}\right)^n (\Phi_{\mathrm{A}}(t_{k-n}) - \Phi_{\mathrm{B}}(t_{k-n}))\cdot\Phi_{\mathrm{B}}(t_k)\right. \\ &\qquad \left. + \left(1-\frac{1}{\tau}\right)^{k-1}(\Phi_{\mathrm{A}}(t_1) - \Phi_{\mathrm{B}}(t_1))\cdot\Phi_{\mathrm{B}}(t_k)\right\} - \mathrm{E}\left\{\overline{\chi}(t_k)\right\}\mathrm{E}\left\{\Phi_{\mathrm{B}}(t_k)\right\} \\ &\quad = \frac{1}{\tau}\cdot\left(\sigma_{\mathrm{AB}} - \sigma^2_{\mathrm{B}}\right), \end{aligned} \tag{2.65}$$

with the covariance σ_{AB} between Φ_{A} and Φ_{B}. Thus, (2.64) is rewritten as

$$\sigma^2_{\Phi_{\overline{\mathrm{A}}}} = \frac{1}{2\tau-1}\cdot(\sigma^2_{\mathrm{A}} + \sigma^2_{\mathrm{B}} - 2\sigma_{\mathrm{AB}}) + \frac{2}{\tau}\cdot\left(\sigma_{\mathrm{AB}} - \sigma^2_{\mathrm{B}}\right) + \sigma^2_{\mathrm{B}} = \kappa_1\cdot\sigma^2_{\mathrm{A}} + \kappa_2\cdot\sigma^2_{\mathrm{B}} + \kappa_3\cdot\sigma_{\mathrm{AB}}, \tag{2.66}$$

with

$$\kappa_1 = \frac{1}{2\tau-1}, \quad \kappa_2 = 1 + \frac{1}{2\tau-1} - \frac{2}{\tau}, \quad \kappa_3 = \frac{2}{\tau} - \frac{2}{2\tau-1}. \tag{2.67}$$

The phase-only combination Φ_{B} is constrained w.r.t. the geometry similar to (2.36), i.e.

$$\sum_{m=1}^{M}\alpha'_m = h_1, \tag{2.68}$$

and the combined ionospheric delay is constrained to

$$\sum_{m=1}^{M}\alpha'_m q^2_{1m} = h_2. \tag{2.69}$$

Both constraints can be written in matrix-vector notation as

$$\underbrace{\begin{bmatrix} 1 & 1 \\ 1 & q_{12}^2 \end{bmatrix}}_{\boldsymbol{\Psi}'_1} \begin{bmatrix} \alpha'_1 \\ \alpha'_2 \end{bmatrix} + \underbrace{\begin{bmatrix} 1 & \dots & 1 \\ q_{13}^2 & \dots & q_{1M}^2 \end{bmatrix}}_{\boldsymbol{\Psi}'_2} \underbrace{\begin{bmatrix} \alpha'_3 \\ \vdots \\ \alpha'_M \end{bmatrix}}_{\boldsymbol{\alpha}'} = \underbrace{\begin{bmatrix} h_1 \\ h_2 \end{bmatrix}}_{\boldsymbol{h}}, \tag{2.70}$$

which can be solved for α'_1 and α'_2:

$$\begin{bmatrix} \alpha'_1 \\ \alpha'_2 \end{bmatrix} = (\boldsymbol{\Psi}'_1)^{-1} (\boldsymbol{h} - \boldsymbol{\Psi}'_2 \boldsymbol{\alpha}') = \begin{bmatrix} c_0 \\ d_0 \end{bmatrix} + \begin{bmatrix} \boldsymbol{c}_1^T \\ \boldsymbol{d}_1^T \end{bmatrix} \boldsymbol{\alpha}', \tag{2.71}$$

where c_0, d_0, $\boldsymbol{c}_1$ and $\boldsymbol{d}_1$ are implicitly defined by $\boldsymbol{\Psi}'_1$, $\boldsymbol{\Psi}'_2$ and $\boldsymbol{h}$. Thus, the variance of Φ_{B} can be expressed as a function of $\boldsymbol{\alpha}'$:

$$\sigma_{\mathrm{B}}^2 = \left(c_0 + \boldsymbol{c}_1^T \boldsymbol{\alpha}'\right)^2 \cdot \sigma_\phi^2 + \left(d_0 + \boldsymbol{d}_1^T \boldsymbol{\alpha}'\right)^2 \cdot \sigma_\phi^2 + \boldsymbol{\alpha}'^T \boldsymbol{\alpha}' \cdot \sigma_\phi^2. \tag{2.72}$$

The covariance σ_{AB} is obtained from (2.6), (2.32) and (2.71), i.e.

$$\begin{aligned} \sigma_{\mathrm{AB}} &= \sum_{m=1}^{M} \alpha_m \alpha'_m \cdot \sigma_\phi^2 = \sum_{m=1}^{M} \frac{j_m \tilde{\lambda}}{\lambda_m} \cdot w_\phi \cdot \alpha'_m \cdot \sigma_\phi^2 \\ &= \frac{j_1 \tilde{\lambda}}{\lambda_1} \sigma_\phi^2 \cdot (c_0 + \boldsymbol{c}_1^T \boldsymbol{\alpha}') \cdot w_\phi + \frac{j_2 \tilde{\lambda}}{\lambda_2} \sigma_\phi^2 \cdot (d_0 + \boldsymbol{d}_1^T \boldsymbol{\alpha}') \cdot w_\phi + \sum_{m=3}^{M} \frac{j_m \tilde{\lambda}}{\lambda_m} \sigma_\phi^2 \cdot \alpha'_m \cdot w_\phi \\ &= \left(v_0 + \boldsymbol{v}_1^T \boldsymbol{\alpha}'\right) \cdot w_\phi \cdot \sigma_\phi^2. \end{aligned} \tag{2.73}$$

The integer ambiguity discrimination can be thus be written as

$$D = \frac{\tilde{\lambda} w_\phi}{2\sqrt{\kappa_1(\tau)\sigma_{\mathrm{A}}^2(w_\phi, \boldsymbol{\beta}) + \kappa_2(\tau)\sigma_{\mathrm{B}}^2(\boldsymbol{\alpha}') + \kappa_3(\tau)\sigma_{\mathrm{AB}}(\boldsymbol{\alpha}', w_\phi)}} \tag{2.74}$$

which is maximized if

$$\frac{\partial D}{\partial w_\phi} \stackrel{!}{=} 0, \quad \frac{\partial D}{\partial \boldsymbol{\beta}} \stackrel{!}{=} \mathbf{0}, \quad \text{and} \quad \frac{\partial D}{\partial \boldsymbol{\alpha}'} \stackrel{!}{=} \mathbf{0}. \tag{2.75}$$

The first constraint is rewritten using (2.64), (2.41), (2.72) and (2.73) as

$$\begin{aligned} \frac{\partial D}{\partial w_\phi} &= \kappa_1(\tau) \cdot \left[\left(s_1 + s_2 w_\phi + \boldsymbol{s}^T \boldsymbol{\beta}\right)\left(s_1 + \boldsymbol{s}^T \boldsymbol{\beta}\right)\sigma_{\rho_1}^2 \right. \\ &\quad \left. + \left(t_1 + t_2 w_\phi + \boldsymbol{t}^T \boldsymbol{\beta}\right)\left(t_1 + \boldsymbol{t}^T \boldsymbol{\beta}\right)\sigma_{\rho_2}^2 + \boldsymbol{\beta}^T \boldsymbol{\Sigma} \boldsymbol{\beta}\right] \\ &\quad + \kappa_2(\tau) \cdot \sigma_\phi^2 \cdot \left[\left(c_0 + \boldsymbol{c}_1^T \boldsymbol{\alpha}'\right)^2 + \left(d_0 + \boldsymbol{d}_1^T \boldsymbol{\alpha}'\right)^2 + \boldsymbol{\alpha}'^T \boldsymbol{\alpha}'\right] \\ &\quad + \kappa_3(\tau) \cdot \left(v_0 + \boldsymbol{v}_1^T \boldsymbol{\alpha}'\right) \cdot w_\phi \cdot \sigma_\phi^2 / 2 = 0. \end{aligned} \tag{2.76}$$

The second constraint corresponds to the constraints of (2.48) as both σ_{B} and σ_{AB} do not

depend on $\boldsymbol{\beta}$, i.e.

$$\boldsymbol{\beta} = -\boldsymbol{A}^{-1}(\boldsymbol{c} + \boldsymbol{b} \cdot w_\phi). \tag{2.77}$$

The third constraint is equivalent to

$$\kappa_2(\tau) \cdot \left(2(c_0 + \boldsymbol{c}_1^T\boldsymbol{\alpha}')\boldsymbol{c}_1\sigma_\phi^2 + 2(d_0 + \boldsymbol{d}_1^T\boldsymbol{\alpha}')\boldsymbol{d}_1\sigma_\phi^2 + 2\boldsymbol{\alpha}'\sigma_\phi^2\right) + \kappa_3(\tau) \cdot \boldsymbol{v}_1 w_\phi \sigma_\phi^2 = \boldsymbol{0}, \tag{2.78}$$

and can also be written as

$$\boldsymbol{X}\boldsymbol{\alpha}' + \boldsymbol{\delta}w_\phi + \boldsymbol{\varepsilon} = \boldsymbol{0}, \tag{2.79}$$

with

$$\boldsymbol{X} = \left[2\kappa_2(\tau)\sigma_\phi^2\left(\boldsymbol{c}_1\boldsymbol{c}_1^T + \boldsymbol{d}_1\boldsymbol{d}_1^T\right) + 2\sigma_\phi^2\boldsymbol{1}\right], \quad \boldsymbol{\delta} = \kappa_3(\tau)\boldsymbol{v}_1\sigma_\phi^2, \quad \boldsymbol{\varepsilon} = \left[2\kappa_2(\tau)\sigma_\phi^2(c_0\boldsymbol{c}_1 + d_0\boldsymbol{d}_1)\right]. \tag{2.80}$$

Solving for $\boldsymbol{\alpha}'$ yields

$$\boldsymbol{\alpha}' = -\boldsymbol{X}^{-1}\left(\boldsymbol{\delta} \cdot w_\phi + \boldsymbol{\epsilon}\right). \tag{2.81}$$

Replacing the code and phase weights in (2.76) by (2.77) and (2.81) gives a constraint that depends only on w_ϕ, i.e.

$$\begin{aligned}
\kappa_1 \cdot \Big[&\left(s_1 + s_2 w_\phi - \boldsymbol{s}^T\boldsymbol{A}^{-1}(\boldsymbol{c} + \boldsymbol{b}w_\phi)\right)\left(s_1 - \boldsymbol{s}^T\boldsymbol{A}^{-1}(\boldsymbol{c} + \boldsymbol{b}w_\phi)\right) \cdot \sigma_{\rho_1}^2 \\
&+ \left(t_1 + t_2 w_\phi - \boldsymbol{t}^T\boldsymbol{A}^{-1}(\boldsymbol{c} + \boldsymbol{b}w_\phi)\right)\left(t_1 - \boldsymbol{t}^T\boldsymbol{A}^{-1}(\boldsymbol{c} + \boldsymbol{b}w_\phi)\right) \cdot \sigma_{\rho_2}^2 \\
&+ (\boldsymbol{c} + \boldsymbol{b}w_\phi)^T\left(\boldsymbol{A}^{-1}\right)^T\boldsymbol{\Sigma}\boldsymbol{A}^{-1}(\boldsymbol{c} + \boldsymbol{b}w_\phi)\Big] + \kappa_2 \cdot \sigma_\phi^2 \cdot \Big[\left(c_0 - \boldsymbol{c}_1^T\boldsymbol{X}^{-1}(\boldsymbol{\delta}w_\phi + \boldsymbol{\epsilon})\right)^2 \\
&+ \left(d_0 - \boldsymbol{d}_1^T\boldsymbol{X}^{-1}(\boldsymbol{\delta}w_\phi + \boldsymbol{\epsilon})\right)^2 + (\boldsymbol{\delta}w_\phi + \boldsymbol{\epsilon})^T\left(\boldsymbol{X}^{-1}\right)^T\boldsymbol{X}^{-1}(\boldsymbol{\delta}w_\phi + \boldsymbol{\epsilon})\Big] \\
\kappa_3 \cdot \Big[&\left(v_0 - \boldsymbol{v}_1^T\boldsymbol{X}^{-1}(\boldsymbol{\delta}w_\phi + \boldsymbol{\epsilon})\right)w_\phi\sigma_\phi^2\Big]/2 = 0,
\end{aligned} \tag{2.82}$$

which is a quadratic function of w_ϕ. It can be shown that the square terms cancel which leaves a linear equation, i.e.

$$r_0 + r_1 \cdot w_\phi = 0 \tag{2.83}$$

with

$$\begin{aligned}
r_0 =&\kappa_1 \cdot \left[\left(s_1 - \boldsymbol{s}^T\boldsymbol{A}^{-1}\boldsymbol{c}\right)^2 \cdot \sigma_{\rho_1}^2 + \left(t_1 - \boldsymbol{t}^T\boldsymbol{A}^{-1}\boldsymbol{c}\right)^2 \cdot \sigma_{\rho_2}^2 + \boldsymbol{c}^T(\boldsymbol{A}^{-1})^T\boldsymbol{\Sigma}\boldsymbol{A}^{-1}\boldsymbol{c}\right] \\
&+ \kappa_2\sigma_\phi^2 \cdot \left[\left(c_0 - \boldsymbol{c}_1^T\boldsymbol{X}^{-1}\boldsymbol{\epsilon}\right)^2 + \left(d_0 - \boldsymbol{d}_1^T\boldsymbol{X}^{-1}\boldsymbol{\epsilon}\right)^2 + \boldsymbol{\epsilon}^T(\boldsymbol{X}^{-1})^T\boldsymbol{X}^{-1}\boldsymbol{\epsilon}\right]
\end{aligned} \tag{2.84}$$

and

$$\begin{aligned}
r_1 =&\kappa_1 \cdot \Big[\left((s_1 - \boldsymbol{s}^T\boldsymbol{A}^{-1}\boldsymbol{c})(-\boldsymbol{s}^T\boldsymbol{A}^{-1}\boldsymbol{b}) + (s_2 - \boldsymbol{s}^T\boldsymbol{A}^{-1}\boldsymbol{b})(s_1 - \boldsymbol{s}^T\boldsymbol{A}^{-1}\boldsymbol{c})\right) \cdot \sigma_{\rho_1}^2 \\
&+ \left((t_1 - \boldsymbol{t}^T\boldsymbol{A}^{-1}\boldsymbol{c})(-\boldsymbol{t}^T\boldsymbol{A}^{-1}\boldsymbol{b}) + (t_2 - \boldsymbol{t}^T\boldsymbol{A}^{-1}\boldsymbol{b})(t_1 - \boldsymbol{t}^T\boldsymbol{A}^{-1}\boldsymbol{c})\right) \cdot \sigma_{\rho_2}^2 \\
&+ \left(\boldsymbol{c}^T(\boldsymbol{A}^{-1})^T\boldsymbol{\Sigma}\boldsymbol{A}^{-1}\boldsymbol{b} + \boldsymbol{b}^T(\boldsymbol{A}^{-1})^T\boldsymbol{\Sigma}\boldsymbol{A}^{-1}\boldsymbol{c}\right)\Big] \\
&+ \kappa_2\sigma_\phi^2 \cdot \Big[-2c_0\boldsymbol{c}_1^T\boldsymbol{X}^{-1}\boldsymbol{\delta} + 2\boldsymbol{c}_1^T\boldsymbol{X}^{-1}\boldsymbol{\epsilon} \cdot \boldsymbol{c}_1^T\boldsymbol{X}^{-1}\boldsymbol{\delta} - 2d_0\boldsymbol{d}_1^T\boldsymbol{X}^{-1}\boldsymbol{\delta} + 2\boldsymbol{d}_1^T\boldsymbol{X}^{-1}\boldsymbol{\epsilon} \cdot \boldsymbol{d}_1^T\boldsymbol{X}^{-1}\boldsymbol{\delta} \\
&+ 2\boldsymbol{\epsilon}^T(\boldsymbol{X}^{-1})^T\boldsymbol{X}^{-1}\boldsymbol{\delta}\Big] + \kappa_3 \cdot \left[\left(v_0 - \boldsymbol{v}_1^T\boldsymbol{X}^{-1}\boldsymbol{\epsilon}\right)\sigma_\phi^2\right]/2.
\end{aligned} \tag{2.85}$$

Solving (2.83) for w_ϕ yields the optimum phase weighting:

$$w_{\phi_{\text{opt}}} = -\frac{r_0}{r_1}, \tag{2.86}$$

which is then used in (2.77) and (2.81) to compute $\boldsymbol{\beta}$ and $\boldsymbol{\alpha}'$. Replacing $\boldsymbol{\alpha}'$ in (2.71) yields the remaining coefficients of the phase-only combination. The code weights β_1 and β_2 are determined from (2.40) and the wavelength from (2.32) which enables the computation of α_m from (2.6).

Tab. 2.8 and 2.9 show optimized multi-frequency GP-IF ($h_1 = 1$, $h_2 = 0$) carrier smoothed code-carrier combinations of maximum ambiguity discrimination for different smoothing periods τ. The weighting coefficients of the code-carrier combination only vary slightly with τ while the coefficients of the phase-only combination strongly depend on τ. A standard deviation of less than 5cm is achieved for $\tau = 20$ s which makes the resolution of the widelane ambiguities ($\lambda = 3.401$m) extremely reliable.

Table 2.8: Triple frequency (E1-E5b-E5a) GP-IF-NP carrier smoothed code-carrier widelane combinations of maximum ambiguity discrimination for $j_1 = 1$, $j_2 = -7$, $j_3 = 6$, $\sigma_\phi = 2$mm and $\sigma_{\rho_m} = 3 \cdot \Gamma_m$

τ	α_1, α_1'	α_2, α_2'	α_3, α_3'	β_1	β_2	β_3	λ [m]	$\sigma_{\overline{\text{A}}}$ [cm]	D
10	17.861	−95.798	80.025	−0.136	−0.464	−0.488	3.399	6.8	24.96
	1.723	4.734	−5.457						
20	17.875	−95.873	80.087	−0.138	−0.464	−0.487	3.401	4.8	35.35
	2.035	1.992	−3.027						
30	17.888	−95.947	80.149	−0.140	−0.464	−0.487	3.404	3.9	43.23
	2.131	1.142	−2.273						
60	17.930	−96.170	80.336	−0.146	−0.464	−0.486	3.412	2.8	60.72
	2.224	0.320	−1.544						
100	17.986	−96.468	80.584	−0.153	−0.465	−0.484	3.423	2.2	77.61
	2.261	−0.002	−1.259						
300	18.263	−97.955	81.827	−0.191	−0.467	−0.477	3.475	1.4	128.12
	2.297	−0.318	−0.979						

Table 2.9: 4-frequency (E1-E6-E5b-E5a) GP-IF-NP carrier smoothed code-carrier widelane combinations of maximum ambiguity discrimination for $j_1 = 1$, $j_2 = -3$, $j_3 = 1$, $j_4 = 1$, $\sigma_\phi = 2$mm and $\sigma_{\rho_m} = 3 \cdot \Gamma_m$

τ	$\alpha_1, \alpha_1', \beta_1$	$\alpha_2, \alpha_2', \beta_2$	$\alpha_3, \alpha_3', \beta_3$	$\alpha_4, \alpha_4', \beta_4$	λ [m]	$\sigma_{\overline{\text{A}}}$ [cm]	D
20	22.554	−54.921	17.282	16.843	4.292	2.2	96.0
	1.807	1.646	−1.041	−1.412			
	−0.022	−0.608	−0.063	−0.065			
60	22.637	−55.122	17.345	16.904	4.308	1.4	158.8
	2.110	0.663	−0.706	−1.068			
	−0.028	−0.617	−0.059	−0.059			

The extension from three to four frequency combinations enables the reduction of the smoothing period by a factor of more than 5 to achieve the same ambiguity discrimination as of the triple frequency combination.

2.4 Fault detection with multi-frequency linear combinations

The previous linear combinations are characterized by worst-case combination biases of several decimeters even if the measurement biases can be constrained to 1 cm for the phase and to 5 cm for the code measurements. However, a fault detection (e.g. Receiver Autnomous Integrity Monitoring, RAIM) can be used to detect severe biases which reduces the largest undetectable biases.

As the true position is unknown, a test statistic is computed for error detection. It can be derived from the ionosphere-free code carrier combination which is modeled as

$$\lambda\phi_u^k = \sum_{m=1}^{M} \alpha_m \lambda_m \phi_{u,m}^k + \beta_m \rho_{u,m}^k = ||\boldsymbol{x}_\mathrm{u} - \boldsymbol{x}^k|| + c(\delta\tau_u - \delta\tau^k) + T_u^k + \lambda N_u^k + b^k + \varepsilon_u^k, \quad (2.87)$$

with the receiver position $\boldsymbol{x}_\mathrm{u}$, the satellite position $\boldsymbol{x}^k$, the receiver and satellite clock offsets $c\delta\tau_u$ and $c\delta\tau^k$, the tropospheric delay T_u^k, the integer ambiguity N_u^k, the combined satellite bias b^k and the noise $\varepsilon_u^k \sim \mathcal{N}(0, \sigma^2)$. The measurements are corrected for the satellite positions and clock offsets, i.e. $\lambda\tilde{\phi}_u^k = \lambda\phi_u^k + \boldsymbol{e}^k\boldsymbol{x}^k + c\delta\tau^k$, as well as for the estimated integer ambiguities which allows to write the combined measurements from K satellites as

$$\lambda(\tilde{\boldsymbol{\phi}} - \check{\boldsymbol{N}}) = \boldsymbol{G}\boldsymbol{\xi} + \boldsymbol{b} + \boldsymbol{\varepsilon} \quad \text{with} \quad \boldsymbol{\varepsilon} \sim \mathcal{N}(\boldsymbol{0}, \boldsymbol{\Sigma}), \quad (2.88)$$

with the extended geometry matrix $\boldsymbol{G}$ and the vector of unknowns $\boldsymbol{\xi} = [\boldsymbol{x}_\mathrm{u}^T, c\delta\tau_u, T_{\mathrm{z}_u}]^T$. The least-squares estimate of $\boldsymbol{\xi}$ is given by

$$\hat{\boldsymbol{\xi}} = \left(\boldsymbol{G}^T\boldsymbol{\Sigma}^{-1}\boldsymbol{G}\right)^{-1}\boldsymbol{G}^T\boldsymbol{\Sigma}^{-1}\lambda(\tilde{\boldsymbol{\phi}} - \check{\boldsymbol{N}}), \quad (2.89)$$

which is used for the computation of weighted range residuals that are given by

$$\begin{aligned} \boldsymbol{w} &= \lambda(\tilde{\boldsymbol{\phi}} - \check{\boldsymbol{N}}) - \boldsymbol{G}\hat{\boldsymbol{\xi}} = \left(\boldsymbol{1} - \boldsymbol{G}(\boldsymbol{G}^T\boldsymbol{\Sigma}^{-1}\boldsymbol{G})^{-1}\boldsymbol{G}^T\boldsymbol{\Sigma}^{-1}\right)\lambda(\tilde{\boldsymbol{\phi}} - \check{\boldsymbol{N}}) \\ &= \left(\boldsymbol{1} - \boldsymbol{G}(\boldsymbol{G}^T\boldsymbol{\Sigma}^{-1}\boldsymbol{G})^{-1}\boldsymbol{G}^T\boldsymbol{\Sigma}^{-1}\right)\lambda(\tilde{\boldsymbol{\phi}} - \boldsymbol{N}) \\ &\quad + \left(\boldsymbol{1} - \boldsymbol{G}(\boldsymbol{G}^T\boldsymbol{\Sigma}^{-1}\boldsymbol{G})^{-1}\boldsymbol{G}^T\boldsymbol{\Sigma}^{-1}\right)\lambda(\boldsymbol{N} - \check{\boldsymbol{N}}), \end{aligned} \quad (2.90)$$

where the first component describes the residuals due to measurement noise and biases for correct ambiguity fixing and the second component denotes the contribution of an erroneous integer fixing. These weighted range residuals are combined to a weighted sum of squared error (WSSE) test statistic that is defined as

$$\mathrm{WSSE} = \boldsymbol{w}^T\boldsymbol{\Sigma}^{-1}\boldsymbol{w}, \quad (2.91)$$

which can also be expressed as a function of the combined measurements $\tilde{\boldsymbol{\phi}}$, i.e.

$$\text{WSSE} = (\lambda(\tilde{\boldsymbol{\phi}} - \check{\boldsymbol{N}}))^T \boldsymbol{S} \lambda(\tilde{\boldsymbol{\phi}} - \check{\boldsymbol{N}}), \tag{2.92}$$

with

$$\boldsymbol{S} = \boldsymbol{\Sigma}^{-1} \left(\mathbf{1} - \boldsymbol{G}(\boldsymbol{G}^T \boldsymbol{\Sigma}^{-1} \boldsymbol{G})^{-1} \boldsymbol{G}^T \boldsymbol{\Sigma}^{-1} \right). \tag{2.93}$$

The weighted sum of squared errors follows a central χ^2 distribution if the ambiguities are fixed correctly and a non-central χ^2 distribution in the case of erroneous fixings. Thus, the probability that the WSSE exceeds a certain threshold γ is given by

$$\begin{aligned} P(\text{WSSE} > \gamma) &= \int_\gamma^\infty \sum_{n=1}^{\infty} p(\text{WSSE} > \gamma | \check{\boldsymbol{N}}_n) \cdot p(\check{\boldsymbol{N}}_n) \, d\text{WSSE} \\ &= P(\check{\boldsymbol{N}}_{n_0}) \cdot \int_\gamma^\infty \frac{1}{2^{d/2}\Gamma(d/2)} \cdot s^{(d/2)-1} \cdot e^{-\frac{s}{2}} ds \\ &\quad + \sum_{n \neq n_0}^{\infty} P(\check{\boldsymbol{N}}_n) \cdot \int_\gamma^\infty \frac{s^{d-1} \sqrt{\mu_n} e^{-\frac{s^2+\mu_n}{2}}}{2(\mu_n s^2)^{d/4}} I_{\frac{d}{2}-1}(\sqrt{\mu_n} s) ds, \end{aligned} \tag{2.94}$$

with the vector of correct ambiguities $\check{\boldsymbol{N}}_{n_0} = \boldsymbol{N}$, the Gamma function Γ, the number of degrees of freedom $d = K - 5$, the modified Bessel function of first kind $I_\nu(z)$, and

$$\mu_n = \lambda^2 \cdot (\boldsymbol{N} - \check{\boldsymbol{N}})^T \boldsymbol{S} (\boldsymbol{N} - \check{\boldsymbol{N}}). \tag{2.95}$$

Setting the probability of (2.94) to the probability of a false alert requirement P_{FA} implicitly defines the threshold γ, i.e.

$$P(\text{WSSE} > \gamma) \stackrel{!}{=} P_{\text{FA}}, \tag{2.96}$$

The test statistic shall detect horizontal and vertical position biases that are related to the measurement biases by

$$b_{\text{H}} = \sqrt{\boldsymbol{b}^T \boldsymbol{D}_{\text{H}} \boldsymbol{b}} \quad \text{and} \quad b_{\text{V}} = \sqrt{\boldsymbol{b}^T \boldsymbol{D}_{\text{V}} \boldsymbol{b}}, \tag{2.97}$$

with

$$\begin{aligned} \boldsymbol{D}_{\text{H}} &= \boldsymbol{\Sigma}^{-1} \boldsymbol{G} \left(\boldsymbol{G}^T \boldsymbol{\Sigma}^{-1} \boldsymbol{G} \right)^{-1} \boldsymbol{H}_{\text{H}}^T \boldsymbol{H}_{\text{H}} \left(\boldsymbol{G}^T \boldsymbol{\Sigma}^{-1} \boldsymbol{G} \right)^{-1} \boldsymbol{G}^T \boldsymbol{\Sigma}^{-1} \\ \boldsymbol{D}_{\text{V}} &= \boldsymbol{\Sigma}^{-1} \boldsymbol{G} \left(\boldsymbol{G}^T \boldsymbol{\Sigma}^{-1} \boldsymbol{G} \right)^{-1} \boldsymbol{H}_{\text{V}}^T \boldsymbol{H}_{\text{V}} \left(\boldsymbol{G}^T \boldsymbol{\Sigma}^{-1} \boldsymbol{G} \right)^{-1} \boldsymbol{G}^T \boldsymbol{\Sigma}^{-1}, \end{aligned} \tag{2.98}$$

and

$$\boldsymbol{H}_{\text{H}} = \begin{bmatrix} 1 & 0 & 0 & 0 & 0 \\ 0 & 1 & 0 & 0 & 0 \end{bmatrix} \quad \text{and} \quad \boldsymbol{H}_{\text{V}} = [0, 0, 1, 0, 0]. \tag{2.99}$$

In [52], Angus has derived the most critical measurement biases that can not be detected from the test statistics. The derivation is reviewed here for the vertical position bias

which is determined from

$$\max_{\boldsymbol{b}} \quad \boldsymbol{b}^T \boldsymbol{D}_{\mathrm{V}} \boldsymbol{b} \quad \text{s.t.} \quad \boldsymbol{b}^T \boldsymbol{S} \boldsymbol{b} \leq \gamma. \tag{2.100}$$

It is in general assumed that only a subset of satellites is biased. If N_{F} satellites are containing biases, the bias vector $\boldsymbol{b}$ can be written as

$$\boldsymbol{b} = \boldsymbol{Q} \boldsymbol{b}^*, \tag{2.101}$$

where $\boldsymbol{b}^*$ is an $N_{\mathrm{F}} \times 1$ non-zero bias vector which is mapped by $\boldsymbol{Q}$ into the $K \times 1$ vector $\boldsymbol{b}$. For $K = 5$ and $N_{\mathrm{F}} = 2$, a valid $\boldsymbol{Q}$ is

$$\boldsymbol{Q} = \begin{bmatrix} 0 & 0 \\ 1 & 0 \\ 0 & 0 \\ 0 & 1 \\ 0 & 0 \end{bmatrix}. \tag{2.102}$$

There exist $\binom{K}{N_{\mathrm{F}}}$ different $\boldsymbol{Q}$ matrices that form the class $Q_{N_{\mathrm{F}}}$. The optimization of (2.100) is rewritten with (2.101) as

$$\max_{\boldsymbol{Q} \in Q_{N_{\mathrm{F}}}} \max_{\boldsymbol{b}^*} \quad \boldsymbol{b}^{*T} \boldsymbol{Q}^T \boldsymbol{D}_{\mathrm{V}} \boldsymbol{Q} \boldsymbol{b}^* \quad \text{s.t.} \quad \boldsymbol{b}^{*T} \boldsymbol{Q}^T \boldsymbol{S} \boldsymbol{Q} \boldsymbol{b}^* \leq \gamma. \tag{2.103}$$

The notation is simplified by introducing $\boldsymbol{A} = \boldsymbol{Q}^T \boldsymbol{D}_{\mathrm{V}} \boldsymbol{Q}$ and $\boldsymbol{B} = \boldsymbol{Q}^T \boldsymbol{S} \boldsymbol{Q}$:

$$\max_{\boldsymbol{Q} \in Q_{N_{\mathrm{F}}}} \max_{\boldsymbol{b}^*} \quad \boldsymbol{b}^{*T} \boldsymbol{A} \boldsymbol{b}^* \quad \text{s.t.} \quad \boldsymbol{b}^{*T} \boldsymbol{B} \boldsymbol{b}^* \leq \gamma, \tag{2.104}$$

which can also be written as

$$\max_{\boldsymbol{Q} \in Q_{N_{\mathrm{F}}}} \max_{\boldsymbol{b}^*} \quad \gamma \cdot \frac{\boldsymbol{b}^{*T} \boldsymbol{A} \boldsymbol{b}^*}{\boldsymbol{b}^{*T} \boldsymbol{B} \boldsymbol{b}^*} \quad \text{s.t.} \quad \boldsymbol{b}^{*T} \boldsymbol{B} \boldsymbol{b}^* \leq \gamma, \tag{2.105}$$

and further expanded to

$$\max_{\boldsymbol{Q} \in Q_{N_{\mathrm{F}}}} \max_{\boldsymbol{b}^*} \quad \gamma \cdot \frac{\boldsymbol{b}^{*T} \boldsymbol{B}^{1/2} \boldsymbol{B}^{-1/2} \boldsymbol{A} \boldsymbol{B}^{-1/2} \boldsymbol{B}^{1/2} \boldsymbol{b}^*}{\boldsymbol{b}^{*T} \boldsymbol{B}^{1/2} \boldsymbol{B}^{1/2} \boldsymbol{b}^*} \quad \text{s.t.} \quad \boldsymbol{b}^{*T} \boldsymbol{B} \boldsymbol{b}^* \leq \gamma. \tag{2.106}$$

Introducing $\boldsymbol{u} = \boldsymbol{B}^{1/2} \boldsymbol{b}^*$ simplifies the maximization to

$$\max_{\boldsymbol{Q} \in Q_{N_{\mathrm{F}}}} \max_{\boldsymbol{u}} \quad \gamma \cdot \frac{\boldsymbol{u}^T \boldsymbol{B}^{-1/2} \boldsymbol{A} \boldsymbol{B}^{-1/2} \boldsymbol{u}}{\boldsymbol{u}^T \boldsymbol{u}} \quad \text{s.t.} \quad \boldsymbol{u}^T \boldsymbol{u} \leq \gamma. \tag{2.107}$$

The solution of the inner maximization is the largest eigenvalue of $\boldsymbol{B}^{-1/2} \boldsymbol{A} \boldsymbol{B}^{-1/2}$, i.e.

$$\max_{\boldsymbol{u}} \frac{\boldsymbol{u}^T \boldsymbol{B}^{-1/2} \boldsymbol{A} \boldsymbol{B}^{-1/2} \boldsymbol{u}}{\boldsymbol{u}^T \boldsymbol{u}} = \lambda_{\max}, \tag{2.108}$$

and the respective eigenvector $\boldsymbol{u}_{\max}$ is scaled by $\sqrt{\gamma}$ to fulfill the constraint of the test statistic. After back-transformation into the $\boldsymbol{b}^*$ space, one obtains

$$\boldsymbol{b}^*_{\max} = \sqrt{\gamma}\boldsymbol{B}^{-1/2}\boldsymbol{u}_{\max}, \tag{2.109}$$

and the maximum undetectable vertical position bias is given by

$$b_{\mathrm{v,max}} = \max_{\boldsymbol{Q}\in Q_{N_\mathrm{F}}} \sqrt{\gamma \cdot \lambda_{\max}}. \tag{2.110}$$

The standard deviation of the vertical position estimate is obtained from (2.89) as

$$\sigma_\mathrm{v} = \boldsymbol{H}_\mathrm{v}\left(\boldsymbol{G}^T\boldsymbol{\Sigma}^{-1}\boldsymbol{G}\right)^{-1}\boldsymbol{H}_\mathrm{v}^T, \tag{2.111}$$

and shown in Fig. 2.9a. The GP-IF E1-E5 mixed code-carrier WL combination of maximum discrimination (Tab. 2.5) benefits from a lower noise level than the GP-IF code-only combination which results in a 3 to 4 times lower σ_v. If the ambiguities of the GP-IF E1-E5 mixed code-carrier NL combination of maximum discrimination can be resolved correctly, a σ_v of less than 1.5cm is achievable. Fig. 2.9b shows a similar gain for the maximum undetectable vertical position bias for $N_\mathrm{F} = 2$ satellite failures. The reduction of $b_{\mathrm{v,max}}$ from 2.3 m to 0.7 m by the additional WL combination increases the availability of RAIM as a lower number of geometries have to be excluded.

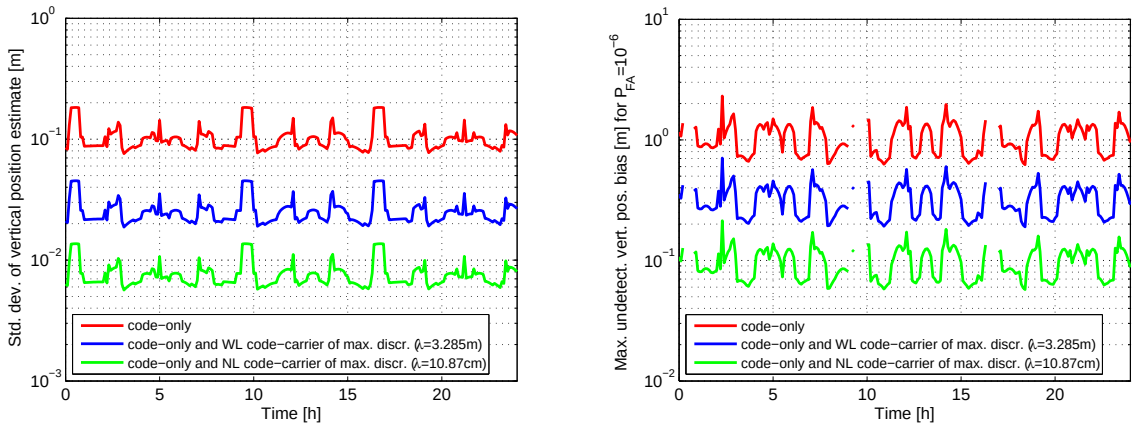

(a) Standard deviation of vertical position

(b) Maximum undetectable vertical position bias

Figure 2.9: Detection of two satellite failures: The mixed code-carrier combination of maximum discrimination is used in addition to the code-only combination to reduce both the standard deviation of the vertical position error and the largest undetectable vertical bias by a factor $3-4$. All combinations include the wideband E1 and E5 signals, and are smoothed over $\tau = 60$s.

Fig. 2.10 shows the impact of the carrier smoothing time on the maximum undetectable vertical position bias for up to 3 satellite failures and different triple frequency linear combinations. For large smoothing periods, $b_{\mathrm{v,max}}$ based on the WL and code-only combinations converges to the $b_{\mathrm{v,max}}$ using the NL and code-only combinations. Thus, the

smoothing period can be tuned to bound the maximum undetectable bias to a predefined value. Obviously, increasing N_{F} also increases $b_{\mathrm{v,max}}$.

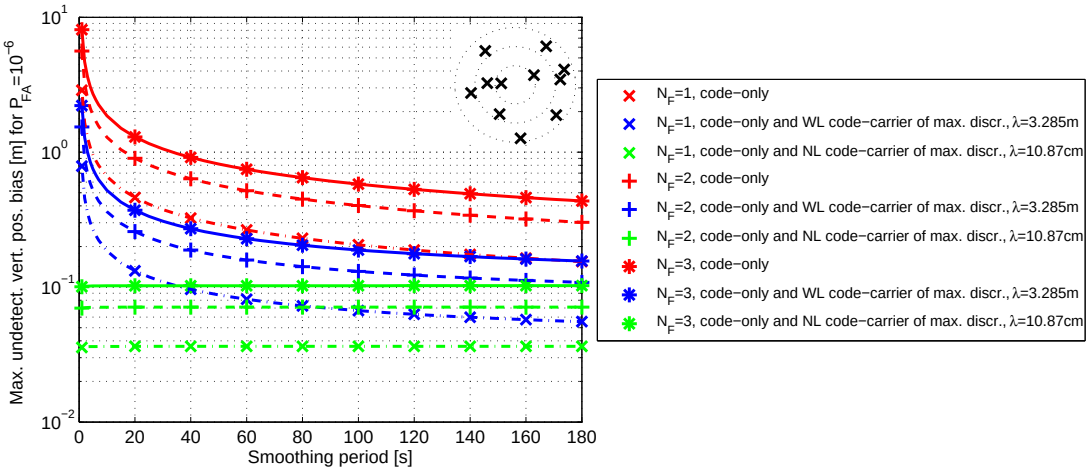

Figure 2.10: Benefit of triple frequency (E1-E5-E6) mixed code-carrier combinations for the detection of multiple satellite failures: The smoothing period can be tuned to bound the maximum undetectable vertical position bias to a predefined value.

2.5 Ionospheric delay estimation with multi-frequency combinations

The ionosphere is one of the major error sources for single frequency differential positioning over long baselines. The differential ionospheric delay is given by

$$\begin{aligned} I_u - I_r &= \frac{40.3}{f^2}\frac{\mathrm{TECV_u}}{\cos(\zeta'_u)} - \frac{40.3}{f^2}\frac{\mathrm{TECV_r}}{\cos(\zeta'_r)} \\ &= \frac{40.3}{f^2}\left(\mathrm{TECV}_r\left(\frac{1}{\cos(\zeta'_u)} - \frac{1}{\cos(\zeta'_r)}\right) + (\mathrm{TECV}_u - \mathrm{TECV}_r)\frac{1}{\cos(\zeta'_u)}\right), \end{aligned}$$

with the carrier frequency f, the vertical total electron contents TECV_u and TECV_r at the ionospheric pierce points of the user and reference receiver, and the zenith angles ζ'_u and ζ'_r at the ionospheric pierce points. The first term in (2.112) represents the error from the differential geometry which is shown in Fig. 2.11. A tight upper bound on this term has been derived by Günther in [1]. The second term describes the impact of the gradient in TECV which varies between a few mm/km during nominal ionospheric conditions and up to 425 mm/km during ionospheric storms [24].

The geometric part of the differential ionospheric error shall now be expressed as a function of r_{E}, h, r_{S}, E_r, $\mathrm{TECV_r}$ and the length of the arc p between both receivers. Let us start with the zenith angle ζ'_u that is obtained from the law of cosine in the triangle C,u,$\mathrm{IPP_u}$, i.e.

$$\zeta'_u = \mathrm{acos}\left(\frac{(r_{\mathrm{E}}+h)^2 + s^2 - r_{\mathrm{E}}^2}{2(r_{\mathrm{E}}+h)\cdot s}\right), \tag{2.112}$$

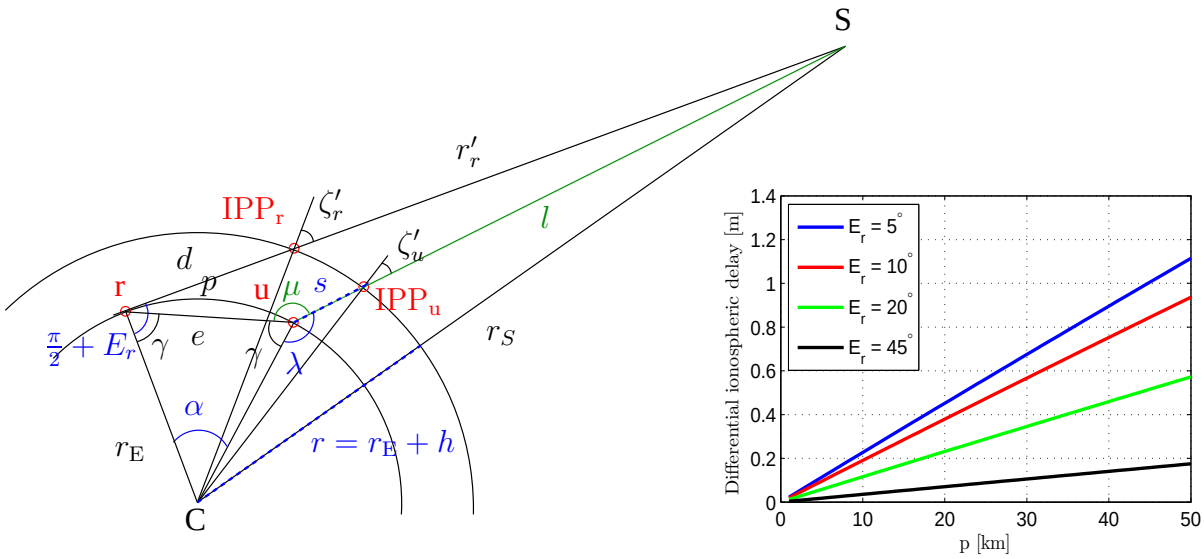

Figure 2.11: Differential ionospheric delay: The delay is given by the difference in slant delays at both ionospheric pierce points. It depends on the vertical TECs at both IPPs, the elevation E_r and the length of the arc between both receivers. A TECV of 100 TECU has been assumed in the right subfigure.

where the length $s = \overline{\mathrm{u,IPP_u}}$ is given by

$$s = r_\mathrm{E}\cos(\lambda) + \sqrt{r_\mathrm{E}^2\cos^2(\lambda) - (r_\mathrm{E}^2 - (r_\mathrm{E}+h)^2)}, \tag{2.113}$$

with $\lambda = 2\pi - \gamma - \mu$ and $\gamma = \pi/2 - p/(2r_\mathrm{E})$. The angle μ is obtained from the law of cosine, i.e.

$$\mu = \mathrm{acos}\left(\frac{e^2 + l^2 - (d + r'_r)^2}{2el}\right), \tag{2.114}$$

where $e = 2r_\mathrm{E}\sin\left(\frac{p}{2r_\mathrm{E}}\right)$ and p denote the lengths of the cord and arc between both receivers. The length l is given by

$$l = \sqrt{(d + r'_r)^2 + e^2 - (d + r'_r)e\cos(\nu)}, \tag{2.115}$$

with $\nu = \frac{\pi}{2} + E_r - \gamma$ and

$$r'_r = -(r_\mathrm{E} + h)\cos(\zeta'_r) + \sqrt{(r_\mathrm{E} + h)^2\sin^2(\zeta'_r) + r_\mathrm{S}^2}. \tag{2.116}$$

The zenith angle ζ'_r is obtained from the law of cosine in the triangle C,R,IPP$_\mathrm{r}$, i.e.

$$\zeta'_r = \mathrm{acos}\left(\frac{d^2 + (r_\mathrm{E} + h)^2 - r_\mathrm{E}^2}{2d(R_\mathrm{e} + h)}\right), \tag{2.117}$$

which depends on $d = \overline{r, \mathrm{IPP_r}}$ that is given by

$$d = r_\mathrm{E} \cos(E_r + \frac{\pi}{2}) + \sqrt{(r_\mathrm{E} + h)^2 - r_\mathrm{E}^2 \sin^2(E_r + \frac{\pi}{2})}. \tag{2.118}$$

Fig. 2.11 shows the geometric part of the differential ionospheric delay for a $\mathrm{TECV_r}$ of 100 TECU and $r_\mathrm{S} = 29600$ km. The differential ionospheric delay exceeds 0.5m for baselines larger than 22 km, 26 km and 44 km and satellite elevations of 5°, 10° and 20°.

The large differential ionospheric delays are a strong motivation for multi-frequency linear combinations that enable an estimation and/ or an elimination of the ionospheric delay. Therefore, an optimized code carrier combination shall be derived for ionospheric delay estimation. It should be geometry-free (GF), i.e.

$$\sum_{m=1}^{M} (\alpha_m + \beta_m) = 0, \tag{2.119}$$

and preserve the ionospheric delay on L1, i.e.

$$\sum_{m=1}^{M} -(\alpha_m - \beta_m) q_{1m}^2 = 1. \tag{2.120}$$

Moreover, the integer nature of ambiguities shall be preserved (NP), i.e.

$$\sum_{m=1}^{M} \alpha_m \lambda_m N_{u,m}^k = \lambda N_u^k. \tag{2.121}$$

An ionospheric delay estimate is obtained from these three constraints and (2.29), i.e.

$$\begin{aligned} \hat{I}_u^k(t_i) &= \sum_{m=1}^{M} \alpha_m \lambda_m \phi_{u,m}^k(t_i) + \beta_m \rho_{u,m}^k(t_i) \\ &= I_u^k(t_i) + \lambda N_u^k + \sum_{m=1}^{M} \left(\alpha_m b_{\phi_{u,m}}^k + \beta_m b_{\rho_{u,m}}^k \right) + \sum_{m=1}^{M} \left(\alpha_m \varepsilon_{\phi_{u,m}}^k(t_i) + \beta_m \varepsilon_{\phi_{\rho u,m}}^k(t_i) \right), \end{aligned} \tag{2.122}$$

which requires the resolution of integer ambiguities. A high reliability can be achieved by a linear combination that maximizes the ambiguity discrimination, i.e.

$$\max_{\alpha_1, \ldots, \alpha_M, \beta_1, \ldots, \beta_M} D = \max_{\alpha_1, \ldots, \alpha_M, \beta_1, \ldots, \beta_M} \frac{\lambda(\alpha_1, \ldots, \alpha_M, \beta_1, \ldots, \beta_M)}{2\sigma(\alpha_1, \ldots, \alpha_M, \beta_1, \ldots, \beta_M)}. \tag{2.123}$$

This constrained optimization problem is of the same type as the one for precise ranging in Section 2.2. Therefore, the derivation of the optimized weighting coefficients follows the approach described in (2.36)-(2.55). The only necessary change is to replace the geometry-

preserving (GP) by a geometry-free (GF) constraint ($h_1 = 0$), and the ionosphere-free (IF) by an ionosphere-preserving (IP) constraint, i.e. $h_2 = -1$.

Tab. 2.10 shows the weighting coefficients and properties of the optimized multi-frequency mixed code carrier combinations for ionospheric delay estimation. The ambiguity discrimination is slightly smaller than for the GP-IF combinations of Tab. 2.5. However, the GF-IP combinations eliminate the clock offsets and tropospheric delay which should compensate for the slightly lower ambiguity discrimination. Another difference between GP-IF and GF-IP combinations is that the latter ones tend to smaller wavelengths and code coefficients if three or more frequencies are considered. The noise level of the 5 frequency combination is one order of magnitude lower than of the E1-E5a combination.

Table 2.10: GF-IP-NP mixed code carrier widelane combinations of maximum ambiguity discrimination for $\sigma_\phi = 2$mm, $\sigma_{\rho_m} = 3 \cdot \Gamma_m$

	E1	E5a	E5b	E5	E6	λ	σ_n	D
j_m	1.0000	−1.0000						
α_m	20.5845	−15.3715				3.917m	100.3cm	2.0
β_m	−1.7238	−3.4892						
j_m	1.0000			−1.0000				
α_m	10.1831			−7.7035		1.938m	14.5cm	6.7
β_m	−0.0737			−2.4059				
j_m	1.0000			2.0000	−3.0000			
α_m	13.1701			19.9263	−32.0702	2.506m	9.2cm	13.6
β_m	−0.0187			−0.6089	−0.3987			
j_m	1.0000	8.0000	−9.0000					
α_m	10.8744	64.9639	−74.9909			2.069m	23.6cm	4.4
β_m	−0.1678	−0.3398	−0.3398					
j_m	1.0000	2.0000	0.0000		−3.0000			
α_m	13.9115	20.7769	0.0000		−33.8753	2.647m	9.9cm	13.3
β_m	−0.0308	−0.0623	−0.0623		−0.6576			
j_m	1.0000	1.0000	0.0000	1.0000	−3.0000			
α_m	12.8805	9.6186	0.0000	9.7440	−31.3649	2.451m	8.2cm	14.9
β_m	−0.0149	−0.0301	−0.0301	−0.4854	−0.3178			

The main noise contribution arises from the code measurements for dual frequency combinations and from the phase measurements for linear combinations with at least three frequencies. The large noise variance can be further reduced by carrier smoothing as shown by the optimized triple frequency combinations in Tab. 2.11.

Table 2.11: Triple frequency E1-E5b-E5a GF-IP-NP carrier smoothed code carrier widelane combinations for integer ambiguity estimation with $\sigma_\phi = 2$mm, $\sigma_{\rho_m} = 3 \cdot \Gamma_m$

τ	j_1, α_1, α'_1	j_2, α_2, α'_2	j_3, α_3, α'_3	β_1	β_2	β_3	λ [m]	$\sigma_{\overline{\Phi}}$ [cm]
20	1	−9	8					
	11.102	−76.561	66.324	−0.198	−0.337	−0.328	2.112	3.84
	−1.548	2.540	−0.991					

The multi-frequency narrowlane combinations of maximum ambiguity discrimination are depicted in Tab. 2.12. The E1-E5a combination achieves a noise level of a few millimeters which is already so low that it can be hardly improved by additional frequencies.

Table 2.12: GF-IP-NP mixed code-carrier narrowlane combinations of maximum ambiguity discrimination for $\sigma_\phi = 2\text{mm}$, $\sigma_{\rho_m} = 3 \cdot \Gamma_m$

	E1	E5a	E5b	E5	E6	λ	σ_n	D
j_m	−3.0000	4.0000						
α_m	−1.2839	1.2783				8.14cm	3.8mm	10.8
β_m	0.0018	0.0037						
j_m	−3.0000			4.0000				
α_m	−1.2862			1.2974		8.16cm	3.7mm	11.0
β_m	−0.0003			−0.0108				
j_m	−3.000			3.0000	1.0000			
α_m	−1.2869			0.9735	0.3482	8.16cm	3.7mm	11.2
β_m	−0.0006			−0.0207	−0.0135			
j_m	−3.0000	3.0000	1.0000					
α_m	−1.2860	0.9603	0.3285			8.16cm	3.3mm	12.3
β_m	−0.0006	−0.0011	−0.0011					
j_m	−3.0000	2.0000	2.0000		0.0000			
α_m	−1.2885	0.6415	0.6582		0.0000	8.17cm	3.2mm	12.6
β_m	−0.0004	−0.0009	−0.0009		−0.0090			
j_m	−3.0000	2.0000	1.0000	1.0000	0.0000			
α_m	−1.2864	0.6404	0.3286	0.3244	0.0000	8.16cm	3.0mm	13.4
β_m	−0.0001	−0.0002	−0.0002	−0.0038	−0.0025			

2.6 Geometry-free ionosphere-free carrier-smoothed ambiguity resolution

In the previous sections, two classes of mixed code-carrier linear combinations were analyzed: GP-IF-NP and GF-IP-NP linear combinations. A third class of linear combinations exists that removes both geometry and ionosphere. These linear combinations can be used in a cascaded approach, i.e. the ambiguities are first resolved with a GF combination and then used for positioning with a GP combination. The noise and multipath of the GF combinations can be reduced again by carrier smoothing. The derivation of the optimum weighting coefficients only slightly differs from the approach of Section 2.3 as both the upper and lower input of Fig. 2.8 have to be GF-IF linear combinations, i.e.

$$\begin{aligned} \sum_{m=1}^{M} \alpha_m + \beta_m = 0 \qquad & \sum_{m=1}^{M} (\alpha_m - \beta_m) q_{1m}^2 = 0 \\ \sum_{m=1}^{M} \alpha'_m = 0 \qquad & \sum_{m=1}^{M} \alpha'_m q_{1m}^2 = 0, \end{aligned} \tag{2.124}$$

which can be solved only for $M \geq 3$.

An integer ambiguity estimate is obtained from (2.29) using the GP, IF and NP constraints and the low pass filter solution of (2.59), i.e.

$$\begin{aligned}
\check{N}(t_k) &= \left[\frac{1}{\lambda}\Phi_{\overline{\mathrm{A}}}(t_k)\right] = \left[\frac{1}{\lambda}\left(\overline{\chi}(t_k) + \Phi_{\mathrm{B}}(t_k)\right)\right] \\
&= \left[\frac{1}{\lambda}\left(\frac{1}{\tau}\sum_{n=0}^{k-2}\left(1-\frac{1}{\tau}\right)^{n}\chi(t_{k-n}) + \left(1-\frac{1}{\tau}\right)^{k-1}\chi(t_1) + \Phi_{\mathrm{B}}(t_k)\right)\right] \\
&= \left[\frac{1}{\lambda}\left(\frac{1}{\tau}\sum_{n=0}^{k-2}\left(1-\frac{1}{\tau}\right)\left(\Phi_{\mathrm{A}}(t_{k-n}) - \Phi_{\mathrm{B}}(t_{k-n})\right)\right.\right. \\
&\quad \left.\left. + \left(1-\frac{1}{\tau}\right)^{k-1}\left(\Phi_{\mathrm{A}}(t_1) - \Phi_{\mathrm{B}}(t_1)\right) + \Phi_{\mathrm{B}}(t_k)\right)\right] \\
&= \left[\frac{1}{\lambda}\left(\frac{1}{\tau}\sum_{n=0}^{k-2}\left(1-\frac{1}{\tau}\right)\sum_{m=1}^{M}\left((\alpha_m - \alpha'_m)\varepsilon_{\phi_m}(t_{k-n}) + \beta_m\varepsilon_{\rho_m}(t_{k-n})\right)\right.\right. \\
&\quad + \left(1-\frac{1}{\tau}\right)^{k-1}\sum_{m=1}^{M}\left((\alpha_m - \alpha'_m)\varepsilon_{\phi_m}(t_1) + \beta_m\varepsilon_{\rho_m}(t_1)\right) + \sum_{m=1}^{M}\alpha'_m\varepsilon_{\phi_m}(t_k)\Bigg) \\
&\quad \left.\left. + \frac{1}{\lambda}\left(\sum_{m=1}^{M}\alpha_m\lambda_m b_{\phi_m} + \beta_m b_{\rho_m}\right)\right], \qquad (2.125)
\end{aligned}$$

where $[\cdot]$ denotes the rounding to the nearest integer. Note that the estimate $\check{N}(t_k)$ is not affected by the biases of the phase-only combination Φ_{B}. It converges to N if the combined biases of Φ_{A} and the filtered noise are sufficiently small. Hatch already suggested an ambiguity resolution with carrier smoothed geometry-free, ionosphere-free three frequency linear combinations in [53]. However, there are three major differences to our approach: First, he did not perform a search over j_m and instead build his three frequency combination as a combination of dual frequency $[1, -1]$ widelane combinations. Second, the variances of the code measurements have not been considered to minimize the combination noise. Finally, he did not perform a joint optimization of the phase-only and code-carrier combination. Hence, the smoothing period has not been taken into account for the optimization which results in an increased noise level of the smoothed linear combination and a lower reliability in ambiguity resolution.

The weighting coefficients of each GF-IF combination can be scaled by an arbitrary factor without violating the constraints of (2.124). The wavelength of the mixed code-carrier combination can be considered as this factor which also scales the noise standard deviation and, thus, does not affect the ambiguity discrimination. Therefore, the wavelength is fixed to a certain value, and then the coefficients are chosen such that the variance of the smoothed combination of (2.64) is minimized. As the phase weighting coefficients of the code-carrier combination are fully determined by j_m and λ and as only the upper combination includes code measurements, the optimization of the weighting coefficients can

be split into two steps. First, the code coefficients are determined such that the variance σ_{A} of the code-carrier combination is minimized. In the second step, the coefficients of the phase-only combination are computed such that the variance of the smoothed code-carrier combination is minimized. This latter step takes the smoothing period τ and the correlation between both combinations into account.

Tab. 2.13 shows the optimized weighting coefficients and properties of GF-IF-NP carrier smoothed widelane combinations. The large ambiguity discrimination of 12.6 for $\tau = 20$s and the removal of the range, the clock offsets, the ionospheric and tropospheric errors enables reliable ambiguity resolution.

Table 2.13: Triple frequency (E1-E5b-E5a) GF-IF-NP carrier smoothed code-carrier widelane combinations for integer ambiguity estimation: The wavelength has been set to $\lambda = 1$m; the noise assumptions are $\sigma_\phi = 2$mm and $\sigma_{\rho_m} = 3 \cdot \Gamma_m$.

τ	j_1, α_1, α_1'	j_2, α_2, α_2'	j_3, α_3, α_3'	β_1	β_2	β_3	$\sigma_{\overline{\mathrm{A}}}$ [cm]	D
20	1	−4	3					
	5.255	−16.106	11.773	−0.718	−0.183	−0.045	4.0	12.64
	−0.045	0.397	−0.352					
20	1	−5	4					
	5.255	−20.133	15.697	−0.717	−0.135	0.033	4.0	12.63
	−0.058	0.507	−0.449					
20	1	−6	5					
	5.255	−24.160	19.621	−0.717	−0.087	0.087	4.0	12.53
	−0.070	0.617	−0.547					
20	1	−7	6					
	5.255	−28.186	23.545	−0.716	−0.039	0.141	4.1	12.53
	−0.082	0.726	−0.644					
60	1	−4	3					
	5.255	−16.106	11.773	−0.718	−0.183	−0.045	2.3	22.07
	−0.015	0.128	−0.113					

Integer ambiguity resolution can also be performed with a geometry-free, ionosphere-free combination without the lower input in Fig. 2.8. In this case, the variance of the smoothed ambiguity estimates is only slightly larger than in Tab. 2.13 and given by

$$\sigma_{\overline{A}}^2 = \frac{1}{2\tau - 1} \cdot \sigma_A^2. \tag{2.126}$$

2.7 C-band aided integer ambiguity resolution

Irsigler et al. have analyzed the benefit of a C-band signal between 5010 and 5030 MHz for next generation Galileo signals in [20]. Assuming an equal transmit power P_{T} on the L- and C-band, the received C-band signal is 10 dB weaker due to the three times larger

carrier frequency, i.e.

$$P_{\mathrm{R}} = P_{\mathrm{T}} \cdot G_{\mathrm{S}} G_{\mathrm{R}} \frac{(4\pi)^2}{\lambda^2}, \tag{2.127}$$

with the satellite gain G_{S}, the receiver gain G_{R} and the carrier wavelength λ. This power loss of 10 dB can be overcome by a phased array antenna at the user receiver.

Tab. 2.14 shows the Cramer Rao bound for some C-band signal candidates at a carrier to noise power ratio of 35 dB-Hz which is 10 dB lower than for the L-band signals in Tab. 1.2. A BOC(7.5,2.5) modulated signal in cosine phasing enables a Cramer Rao bound of 10.89 cm which can be further reduced to 0.7 cm by a phased array antenna with a beam spread angle of 10°. This is an even lower noise level than the CBOC modulated E1 signal with comparable bandwidth and a 10 dB larger E_{s}/N_0.

Table 2.14: Cramer Rao bounds for C-band signal candidates with 20 MHz bandwidth

E_{s}/N_0	Modulation	CRB [cm]	Phased array antenna
35	BOC(1,1), cosine phasing	35.90	no
35	BOC(7.5,2.5), cosine phasing	10.89	no
35	BOC(7.5,2.5), cosine phasing	0.67	10° beam spread angle.

The three times larger carrier frequency ($491 \cdot 10.23$ MHz) of the C-band also results in a 10 times lower ionospheric delay and a 3 times lower phase noise. This low phase noise makes the C-band signal interesting for carrier smoothing, and precise positioning including orbit determination and, thereby, satellite bias estimation.

The joint use of L- and C-band measurements in a linear combination [46] improves the reliability of integer ambiguity resolution despite the small wavelength of 5.97 cm for the C-band signal. Tab. 2.15 shows the benefit of an optimized carrier smoothed geometry-free, ionosphere-free E1-E5a-C-band code carrier combination over a pure L-band combination with wavelengths of 1 m. The low noise C-band signal as well as the lower L-band code coefficients enable a 3.0 times lower noise level and, thereby, a 3.0 times higher ambiguity discrimination. The C-band signal performance was taken from the last line of Tab. 2.14.

Table 2.15: Triple frequency (E1-E5a-C) GF-IF-NP carrier smoothed code-carrier wide-lane combinations for ambiguity resolution: The wavelength has been set to $\lambda = 1$m; the noise assumptions are $\sigma_{\phi_m} = 2$mm (L-band), $\sigma_{\phi_m} = 0.6$mm (C-band), and $\sigma_{\rho_m} = 3 \cdot \Gamma_m$.

τ	j_1, α_1, α_1'	j_2, α_2, α_2'	j_3, α_3, α_3'	β_1	β_2	β_3	$\sigma_{\overline{\mathrm{A}}}$ [cm]	D
	E1	E5a	**C**-band	E1	E5a	**C**-band		
20	7	−5	−1					
	36.785	−19.621	−16.755	−0.002	−0.004	−0.404	1.34	37.45
	−0.968	0.515	0.453					
	E1	E5a	E5b	E1	E5a	E5b		
20	1	3	−4					
	5.255	11.773	−16.106	−0.718	−0.045	−0.183	3.96	12.64
	−0.045	−0.352	0.397					

2.8 Estimation of second order ionospheric delays

Multi-frequency mixed code carrier combinations are also beneficial to estimate the second order ionospheric delay. In this case, the linear combination shall be geometry-free, i.e.

$$\sum_{m=1}^{M}(\alpha_m + \beta_m) = 0. \tag{2.128}$$

The ionospheric delay of first order shall also be eliminated while the second order delay is preserved, i.e.

$$\sum_{m=1}^{M}(\alpha_m - \beta_m)q_{1m}^2 = 0 \quad \text{and} \quad \sum_{m=1}^{M}(\alpha_m/2 - \beta_m)q_{1m}^3 = 1. \tag{2.129}$$

Moreover, the linear combination shall preserve the integer nature of ambiguities, which leads to the combination wavelength given by (2.32):

$$\lambda = \tilde{\lambda}_0 \cdot w_\phi \quad \text{with} \quad \tilde{\lambda}_0 = \frac{1}{\sum\limits_{m=1}^{M}\frac{j_m}{\lambda_m}} \quad \text{and} \quad w_\phi = 1 - \sum_{m=1}^{M}\beta_m = \sum_{m=1}^{M}\alpha_m. \tag{2.130}$$

The first three constraints can be rewritten in matrix-vector notation as

$$\boldsymbol{\Psi}_1 \begin{bmatrix} \beta_1 \\ \beta_2 \\ \beta_3 \end{bmatrix} + \boldsymbol{\Psi}_2 \begin{bmatrix} w_\phi \\ \beta_4 \\ \vdots \\ \beta_M \end{bmatrix} = \boldsymbol{h}, \tag{2.131}$$

with

$$\boldsymbol{\Psi}_1 = \begin{bmatrix} 1 & 1 & 1 \\ -1 & -q_{12}^2 & -q_{13}^2 \\ -1 & -q_{12}^3 & -q_{13}^3 \end{bmatrix}, \quad \boldsymbol{\Psi}_2 = \begin{bmatrix} 1 & 1 & \dots & 1 \\ \tilde{\lambda}\sum\limits_{m=1}^{M}\frac{j_m}{\lambda_m}q_{1m}^2 & -q_{14}^2 & \dots & -q_{1M}^2 \\ \frac{1}{2}\tilde{\lambda}\sum\limits_{m=1}^{M}\frac{j_m}{\lambda_m}q_{1m}^3 & -q_{14}^3 & \dots & -q_{1M}^3 \end{bmatrix}, \quad \boldsymbol{h} = \begin{bmatrix} 0 \\ 0 \\ 1 \end{bmatrix}. \tag{2.132}$$

Eq. (2.131) can be solved for $\beta_1, \dots, \beta_3$:

$$\begin{bmatrix} \beta_1 \\ \beta_2 \\ \beta_3 \end{bmatrix} = \boldsymbol{\Psi}^{-1}\left(\boldsymbol{h} - \boldsymbol{\Psi}_2 \begin{bmatrix} w_\phi \\ \beta_4 \\ \vdots \\ \beta_M \end{bmatrix}\right) = \begin{bmatrix} s_1 + s_2 w_\phi + \sum\limits_{m=4}^{M} s_m\beta_m \\ t_1 + t_2 w_\phi + \sum\limits_{m=4}^{M} t_m\beta_m \\ u_1 + u_2 w_\phi + \sum\limits_{m=4}^{M} u_m\beta_m \end{bmatrix}. \tag{2.133}$$

The total phase weight w_ϕ and the remaining code coefficients β_m, $m \geq 4$ are chosen such that the ambiguity discrimination is maximized. It is given by

$$\begin{aligned} D(w_\phi, \boldsymbol{\beta}) &= \frac{\lambda}{2\sigma} = \frac{\tilde{\lambda} w_\phi}{2} \left(\sum_{m=1}^{M} \alpha_m^2 \sigma_{\phi_m}^2 + \beta_m^2 \sigma_{\rho_m}^2 \right)^{-1/2} \\ &= \tilde{\lambda} w_\phi / 2 \cdot \big(\tilde{\eta}^2 w_\phi^2 + (s_0 + s_1 w_\phi + \boldsymbol{s}^T \boldsymbol{\beta})^2 \sigma_{\rho_1}^2 + (t_0 + t_1 w_\phi + \boldsymbol{t}^T \boldsymbol{\beta})^2 \sigma_{\rho_2}^2 \\ &\quad + (u_0 + u_1 w_\phi + \boldsymbol{u}^T \boldsymbol{\beta})^2 \sigma_{\rho_3}^2 + \boldsymbol{\beta}^T \boldsymbol{\Sigma} \boldsymbol{\beta} \big)^{-1/2} . \end{aligned} \tag{2.134}$$

Setting the derivatives with respect to w_ϕ and $\boldsymbol{\beta} = [\beta_4, \ldots, \beta_M]^T$ to zero, and solving for w_ϕ yields similar to Section 2.2:

$$w_{\phi_{\text{opt}}} = -r_0 / r_1, \tag{2.135}$$

with

$$\begin{aligned} r_0 &= (s_0 - \boldsymbol{s}^T \boldsymbol{A}^{-1} \boldsymbol{c})^2 \sigma_{\rho_1}^2 + (t_0 - \boldsymbol{t}^T \boldsymbol{A}^{-1} \boldsymbol{c})^2 \sigma_{\rho_2}^2 + (u_0 - \boldsymbol{u}^T \boldsymbol{A}^{-1} \boldsymbol{c})^2 \sigma_{\rho_3}^2 \\ &\quad + \boldsymbol{c}^T (\boldsymbol{A}^{-1})^T \boldsymbol{\Sigma} \boldsymbol{A}^{-1} \boldsymbol{c} \\ r_1 &= (s_0 - \boldsymbol{s}^T \boldsymbol{A}^{-1} \boldsymbol{c})(-\boldsymbol{s}^T \boldsymbol{A}^{-1} \boldsymbol{b}) \sigma_{\rho_1}^2 + (s_1 - \boldsymbol{s}^T \boldsymbol{A}^{-1} \boldsymbol{b})(s_0 - \boldsymbol{s}^T \boldsymbol{A}^{-1} \boldsymbol{c}) \sigma_{\rho_1}^2 \\ &\quad + (t_0 - \boldsymbol{t}^T \boldsymbol{A}^{-1} \boldsymbol{c})(-\boldsymbol{t}^T \boldsymbol{A}^{-1} \boldsymbol{b}) \sigma_{\rho_2}^2 + (t_1 - \boldsymbol{t}^T \boldsymbol{A}^{-1} \boldsymbol{b})(t_0 - \boldsymbol{t}^T \boldsymbol{A}^{-1} \boldsymbol{c}) \sigma_{\rho_2}^2 \\ &\quad + (u_0 - \boldsymbol{u}^T \boldsymbol{A}^{-1} \boldsymbol{c})(-\boldsymbol{u}^T \boldsymbol{A}^{-1} \boldsymbol{b}) \sigma_{\rho_3}^2 + (u_1 - \boldsymbol{u}^T \boldsymbol{A}^{-1} \boldsymbol{b})(u_0 - \boldsymbol{u}^T \boldsymbol{A}^{-1} \boldsymbol{c}) \sigma_{\rho_3}^2 \\ &\quad + \boldsymbol{c}^T (\boldsymbol{A}^{-1})^T \boldsymbol{\Sigma} \boldsymbol{A}^{-1} \boldsymbol{b} + \boldsymbol{b}^T (\boldsymbol{A}^{-1})^T \boldsymbol{\Sigma} \boldsymbol{A}^{-1} \boldsymbol{c}, \end{aligned} \tag{2.136}$$

with the abbreviations

$$\begin{aligned} \boldsymbol{A} &= \boldsymbol{s}\boldsymbol{s}^T \sigma_{\rho_1}^2 + \boldsymbol{t}\boldsymbol{t}^T \sigma_{\rho_2}^2 + \boldsymbol{u}\boldsymbol{u}^T \sigma_{\rho_3}^2 + \boldsymbol{\Sigma} \\ \boldsymbol{b} &= s_1 \boldsymbol{s} \sigma_{\rho_1}^2 + t_1 \boldsymbol{t} \sigma_{\rho_2}^2 + u_1 \boldsymbol{u} \sigma_{\rho_3}^2 \\ \boldsymbol{c} &= s_0 \boldsymbol{s} \sigma_{\rho_1}^2 + t_0 \boldsymbol{t} \sigma_{\rho_2}^2 + u_0 \boldsymbol{u} \sigma_{\rho_3}^2 \end{aligned} \qquad \text{and} \qquad \boldsymbol{\Sigma} = \begin{bmatrix} \sigma_{\rho_4}^2 & \cdots & \sigma_{\rho_{4M}} \\ \vdots & \ddots & \vdots \\ \sigma_{\rho_{4M}} & \cdots & \sigma_{\rho_M}^2 \end{bmatrix}. \tag{2.137}$$

Tab. 2.16 shows the weighting coefficients and properties of the optimized linear combinations with 3 and 4 Galileo frequencies. The ambiguity discrimination is rather poor for L-band only combinations but can be dramatically improved with C-band measurements.

Table 2.16: Multi-frequency mixed code carrier linear combinations for the estimation of the second order ionospheric delay (assuming $\sigma_\phi = 1\text{mm}$, $\sigma_{\rho_m} = \Gamma_m$)

	E1	E5a	E5b	C	λ	σ_n	D
j_m	10	-1	-10				
α_m	4.7753	-0.3566	-3.6590		9.0cm	15.0cm	0.3
β_m	1.0055	-1.0581	-0.7071				
j_m	-6	4		1			
α_m	-5.5977	2.8231		2.9746	17.8cm	0.8cm	10.9
β_m	-0.0025	-0.2123		0.0149			
j_m	-7	4	1	1			
α_m	-6.8059	2.9042	0.7450	3.0999	18.5cm	0.9cm	10.6
β_m	0.0026	-0.0106	-0.0088	0.0735			

3

Multi-frequency integer ambiguity resolution

This chapter starts with a description of the currently known integer ambiguity estimation techniques: rounding, sequential conditional rounding (bootstrapping), integer least-squares estimation and integer aperture estimation. These estimators are applied to the linear combinations of the previous chapter for double difference, single difference and undifferenced measurements. The large wavelength enables a substantial reduction of the probability of wrong fixing for both Wide Area Real Time Kinematic and Precise Point Positioning applications. This section also describes several suggestions to further improve the success rate of ambiguity resolution, e.g. a modified bootstrapping where the sequential corrections take the probability of an erroneous fixing into account, a partial integer decorrelation for the optimum trade-off between variance reduction and worst-case bias amplification, a new cascaded ambiguity resolution scheme with three carrier smoothed multi-frequency code carrier combinations, and many others.

3.1 Estimation of carrier phase integer ambiguities

In this section, the measurement model of (1.4) is extended to

$$\begin{aligned}\lambda_m \phi^k_{u,m}(t_i) \;=\; & \boldsymbol{e}^{k,T}_u(t_i) \cdot \left(\boldsymbol{x}_u(t_i) - \left(\hat{\boldsymbol{x}}^k(t_i) + \varepsilon_{\hat{\boldsymbol{x}}^k}(t_i)\right)\right) + c \cdot \left(\delta\tau_u(t_i) - \left(\delta\hat{\tau}^k(t_i) + \varepsilon_{\delta\hat{\tau}^k}(t_i)\right)\right) \\ & + m_{\mathrm{w}}(E^k_u(t_i)) \cdot \left(T_{\mathrm{z,w},u}(t_0) + (t_i - t_0) \cdot \dot{T}_{\mathrm{z,w},u}\right) + T_{\mathrm{d},u}(t_i) + p^k_{u,m}(t_i) \\ & - q^2_{1m}\left(I^k_{u,1}(t_0) + (t_i - t_0)\dot{I}^k_{u,1}\right) + \lambda_m N^k_{u,m} + \lambda_m b_{\phi_{u,m}} + \lambda_m b^k_{\phi_m} + \varepsilon^k_{\phi_{u,m}}(t_i),\end{aligned} \tag{3.1}$$

i.e. a linear increase of the ionospheric delays and of the tropospheric zenith delay is assumed over time.

The estimated satellite position $\hat{\boldsymbol{x}}^k(t_i)$ and satellite clock offset $c\delta\hat{\tau}^k(t_i)$ are provided by the navigation message. The dry component of the tropospheric delay can be accurately modeled and the phase center variations $p^k_{u,m}(t_i)$ are provided by the IGS. These parameters can be brought to the left side, i.e.

$$\begin{aligned}
\lambda_m\tilde{\phi}^k_{u,m}(t_i) &= \lambda_m\phi^k_{u,m}(t_i) + \boldsymbol{e}^{k,T}_u(t_i)\hat{\boldsymbol{x}}^k(t_i) + c\delta\hat{\tau}^k(t_i) - T_{\mathrm{d},u}(t_i) - p^k_{u,m}(t_i) \\
&= \boldsymbol{e}^{k,T}(t_i)\cdot(\boldsymbol{x}_u(t_i) - \varepsilon_{\hat{\boldsymbol{x}}^k}(t_i)) + c\cdot(\delta\tau_u(t_i) - \varepsilon_{\delta\hat{\tau}^k}(t_i)) \\
&\quad + m_{\mathrm{w}}(E^k_u(t_i))\cdot\left(T_{\mathrm{z,w},u}(t_0) + (t_i - t_0)\cdot\dot{T}_{\mathrm{z,w},u}\right) \\
&\quad - q^2_{1m}\left(I^k_{u,1}(t_0) + (t_i - t_0)\cdot\dot{I}^k_{u,1}\right) \\
&\quad + \lambda_m N^k_{u,m} + \lambda_m b_{\phi_{u,m}} + \lambda_m b^k_{\phi_m} + \varepsilon^k_{\phi_{u,m}}(t_i).
\end{aligned} \tag{3.2}$$

A similar model is used for the code measurements, i.e.

$$\begin{aligned}
\tilde{\rho}^k_{u,m}(t_i) &= \rho^k_{u,m}(t_i) + \boldsymbol{e}^{k,T}_u(t_i)\delta\boldsymbol{x}^k(t_i) + c\delta\hat{\tau}^k(t_i) - T_{\mathrm{d},u}(t_i) \\
&= \boldsymbol{e}^{k,T}_u(t_i)\cdot(\boldsymbol{x}_u(t_i) - \varepsilon_{\hat{\boldsymbol{x}}^k}(t_i)) + c\cdot(\delta\tau_u(t_i) - \varepsilon_{\delta\hat{\tau}^k}(t_i)) \\
&\quad + m_{\mathrm{w}}(E^k_u(t_i))\cdot\left(T_{\mathrm{z,w},u}(t_0) + (t_i - t_0)\cdot\dot{T}_{\mathrm{z,w},u}\right) \\
&\quad + q^2_{1m}\left(I^k_{u,1}(t_0) + (t_i - t_0)\cdot\dot{I}^k_{u,1}\right) + b_{\rho_{u,m}} + b^k_{\rho_m} + \varepsilon^k_{\rho_{u,m}}(t_i).
\end{aligned} \tag{3.3}$$

Linear combinations can be computed between satellites (e.g. single or double differences), between epochs (e.g. carrier smoothing), between code and carrier phase, and between frequencies as discussed in the previous chapter. In this chapter, three different applications are considered for linear combinations over phase and code measurements on multiple frequencies: Wide-Area Real-Time Kinematics (WA-RTK) and Precise Point Positioning (PPP).

WA-RTK typically uses double difference measurements to eliminate the receiver and satellite biases in Eq. (3.2) and (3.3). They are denoted by

$$\begin{aligned}
\Delta\tilde{\boldsymbol{\phi}}_{ur,m}(t_i) &= \begin{bmatrix} \left(\tilde{\phi}^1_{u,m}(t_i) - \tilde{\phi}^K_{u,m}(t_i)\right) - \left(\tilde{\phi}^1_{r,m}(t_i) - \tilde{\phi}^K_{r,m}(t_i)\right) \\ \vdots \\ \left(\tilde{\phi}^{K-1}_{u,m}(t_i) - \tilde{\phi}^K_{u,m}(t_i)\right) - \left(\tilde{\phi}^{K-1}_{r,m}(t_i) - \tilde{\phi}^K_{r,m}(t_i)\right) \end{bmatrix} \\
\Delta\tilde{\boldsymbol{\rho}}_{ur,m}(t_i) &= \begin{bmatrix} \left(\tilde{\rho}^1_{u,m}(t_i) - \tilde{\rho}^K_{u,m}(t_i)\right) - \left(\tilde{\rho}^1_{r,m}(t_i) - \tilde{\rho}^K_{r,m}(t_i)\right) \\ \vdots \\ \left(\tilde{\rho}^{K-1}_{u,m}(t_i) - \tilde{\rho}^K_{u,m}(t_i)\right) - \left(\tilde{\rho}^{K-1}_{r,m}(t_i) - \tilde{\rho}^K_{r,m}(t_i)\right) \end{bmatrix}
\end{aligned} \tag{3.4}$$

As the orbital error $\varepsilon_{\hat{\boldsymbol{x}}^k}(t_i)$ is significantly suppressed for baselines up to more than 100 km, the reliability of integer ambiguity resolution was so far mainly limited by the double

difference ionospheric delay. The ionosphere-free linear combinations of the previous chapter eliminate this error source and, therefore, significantly increase the maximum baseline length for reliable integer ambiguity resolution. The code and carrier phase measurements on at least two frequencies can be combined to two ionosphere-free linear combinations for positioning: The first combination is typically a code carrier combination to benefit from the low noise level of the phase measurements while the second combination is a code-only combination to prevent the introduction of further integer ambiguities. Both linear combinations are applied to all double differences, i.e.

$$\begin{bmatrix} \sum_{m=1}^{M} \left(\alpha_m \lambda_m \Delta\tilde{\boldsymbol{\phi}}_{ur,m}(t_i) + \beta_m \Delta\tilde{\boldsymbol{\rho}}_{ur,m}(t_i) \right) \\ \sum_{m=1}^{M} \left(\gamma_m \Delta\tilde{\boldsymbol{\rho}}_{ur,m}(t_i) \right) \end{bmatrix}$$

$$= \left[\begin{array}{c|c} (\Delta \boldsymbol{e}_{ur}^{1K}(t_i))^T & \Delta m_{\mathrm{w},u}^{1K}(t_i) \\ \vdots & \vdots \\ (\Delta \boldsymbol{e}_{ur}^{K-1,K}(t_i))^T & \Delta m_{\mathrm{w},u}^{(K-1,K)}(t_i) \\ \hline (\Delta \boldsymbol{e}_{ur}^{1K}(t_i))^T & \Delta m_{\mathrm{w},u}^{1K}(t_i) \\ \vdots & \vdots \\ (\Delta \boldsymbol{e}_{ur}^{K-1,K}(t_i))^T & \Delta m_{\mathrm{w},u}^{(K-1,K)}(t_i) \end{array}\right] \begin{bmatrix} \boldsymbol{x}_u(t_i) - \boldsymbol{x}_r(t_i) \\ T_{\mathrm{z,w},u}(t_i) \end{bmatrix}$$

$$+ \left[\begin{array}{ccc} \lambda & & \\ & \ddots & \\ & & \lambda \\ \hline 0 & \dots & 0 \\ \vdots & \ddots & \vdots \\ 0 & \dots & 0 \end{array}\right] \left[\sum_{m=1}^{M} j_m \Delta \boldsymbol{N}_{ur,m} \right] + \begin{bmatrix} \sum_{m=1}^{M} \left(\alpha_m \lambda_m \Delta\boldsymbol{\varepsilon}_{\tilde{\phi}_{ur,m}}(t_i) + \beta_m \Delta\boldsymbol{\varepsilon}_{\tilde{\rho}_{ur,m}}(t_i) \right) \\ \sum_{m=1}^{M} \left(\gamma_m \Delta\boldsymbol{\varepsilon}_{\tilde{\rho}_{ur,m}}(t_i) \right) \end{bmatrix} \tag{3.5}$$

with the unknown baseline $\boldsymbol{x}_u(t_i) - \boldsymbol{x}_r(t_i)$, tropospheric zenith delay $T_{\mathrm{z,w},u}(t_i)$ and combined integer ambiguities $\sum_{m=1}^{M} j_m N_{ur,m}^{kK}$. Eq. (3.5) can also be written as

$$\boldsymbol{\Psi} = \boldsymbol{H}\boldsymbol{\xi} + \boldsymbol{A}\boldsymbol{N} + \boldsymbol{n}, \qquad \boldsymbol{\xi} \in \mathbb{R}^4, \quad \boldsymbol{N} \in \mathbb{Z}^{K-1}, \quad \text{and} \quad \boldsymbol{n} = \mathcal{N}(\boldsymbol{0}, \boldsymbol{\Sigma}). \tag{3.6}$$

The second application of linear combinations in this chapter is Precise Point Positioning. Satellite-satellite single difference measurements are typically used to eliminate receiver dependant biases and clock offsets. The satellite-satellite single difference biases are determined from a network of reference stations over a longer timescale and then provided to the mobile user for PPP. The time to reliable integer ambiguity resolution is so far in the order of a few minutes. The large wavelength of the optimized multi-frequency code carrier linear combinations enables a significantly shorter time to ambiguity resolution also for PPP. Therefore, a code carrier combination and a code-only combination shall be

again consider in this chapter for PPP, i.e.

$$
\begin{aligned}
&\begin{bmatrix} \sum_{m=1}^{M} \left(\alpha_m \lambda_m \Delta(\tilde{\boldsymbol{\phi}}_{u,m}(t_i) - \Delta \boldsymbol{b}_{\phi_{u,m}}) + \beta_m (\Delta \tilde{\boldsymbol{\rho}}_{u,m}(t_i) - \Delta \boldsymbol{b}_{\rho_{u,m}}) \right) \\ \sum_{m=1}^{M} \left(\gamma_m (\Delta \tilde{\boldsymbol{\rho}}_{u,m}(t_i) - \boldsymbol{b}_{\rho_{u,m}}) \right) \end{bmatrix} \\
&= \sum_{m=1}^{M} (\alpha_m + \beta_m) \left[\begin{array}{c|c|c} (\Delta \boldsymbol{e}_u^{1K}(t_i))^T & \Delta m_{\mathrm{w},u}^{1K}(t_i) & 1 \\ \vdots & \vdots & \vdots \\ (\Delta \boldsymbol{e}_u^{K-1,K}(t_i))^T & \Delta m_{\mathrm{w},u}^{(K-1,K)}(t_i) & 1 \\ \hline (\Delta \boldsymbol{e}_u^{1K}(t_i))^T & \Delta m_{\mathrm{w},u}^{1K}(t_i) & 1 \\ \vdots & \vdots & \vdots \\ (\Delta \boldsymbol{e}_u^{K-1,K}(t_i))^T & \Delta m_{\mathrm{w},u}^{(K-1,K)}(t_i) & 1 \end{array}\right] \begin{bmatrix} \boldsymbol{x}_u(t_i) \\ T_{\mathrm{z,w},u}(t_i) \\ c\delta\tau_u(t_i) \end{bmatrix} \\
&+ \sum_{m=1}^{M} (\alpha_m + \beta_m) \begin{bmatrix} (\boldsymbol{e}_u^1)^T \boldsymbol{\varepsilon}_{\hat{\boldsymbol{x}}^1}(t_i) - (\boldsymbol{e}_u^K)^T \boldsymbol{\varepsilon}_{\hat{\boldsymbol{x}}^K}(t_i) + c(\varepsilon_{\delta\hat{\tau}^1} - \varepsilon_{\delta\hat{\tau}^K}) \\ \vdots \\ (\boldsymbol{e}_u^{K-1})^T \boldsymbol{\varepsilon}_{\hat{\boldsymbol{x}}^{K-1}}(t_i) - (\boldsymbol{e}_u^K)^T \boldsymbol{\varepsilon}_{\hat{\boldsymbol{x}}^K}(t_i) + c(\varepsilon_{\delta\hat{\tau}^{K-1}} - \varepsilon_{\delta\hat{\tau}^K}) \\ (\boldsymbol{e}_u^1)^T \boldsymbol{\varepsilon}_{\hat{\boldsymbol{x}}^1}(t_i) - (\boldsymbol{e}_u^K)^T \boldsymbol{\varepsilon}_{\hat{\boldsymbol{x}}^K}(t_i) + c(\varepsilon_{\delta\hat{\tau}^1} - \varepsilon_{\delta\hat{\tau}^K}) \\ \vdots \\ (\boldsymbol{e}_u^{K-1})^T \boldsymbol{\varepsilon}_{\hat{\boldsymbol{x}}^{K-1}}(t_i) - (\boldsymbol{e}_u^K)^T \boldsymbol{\varepsilon}_{\hat{\boldsymbol{x}}^K}(t_i) + c(\varepsilon_{\delta\hat{\tau}^{K-1}} - \varepsilon_{\delta\hat{\tau}^K}) \end{bmatrix} \\
&+ \left[\begin{array}{ccc} \lambda & & \\ & \ddots & \\ & & \lambda \\ \hline 0 & \dots & 0 \\ \vdots & \ddots & \vdots \\ 0 & \dots & 0 \end{array}\right] \left[\sum_{m=1}^{M} j_m \Delta \boldsymbol{N}_{u,m} \right] + \begin{bmatrix} \sum_{m=1}^{M} \left(\alpha_m \lambda_m \Delta \boldsymbol{\varepsilon}_{\tilde{\phi}_{u,m}}(t_i) + \beta_m \Delta \boldsymbol{\varepsilon}_{\tilde{\rho}_{u,m}}(t_i) \right) \\ \sum_{m=1}^{M} \left(\gamma_m \Delta \boldsymbol{\varepsilon}_{\tilde{\rho}_{u,m}}(t_i) \right) \end{bmatrix},
\end{aligned}
\tag{3.7}
$$

with

$$
\begin{aligned}
\tilde{\boldsymbol{\rho}}_{u,m}(t_i) &= \begin{bmatrix} \tilde{\rho}_{u,m}^1(t_i) - \tilde{\rho}_{u,m}^K(t_i) \\ \vdots \\ \tilde{\rho}_{u,m}^{K-1}(t_i) - \tilde{\rho}_{u,m}^K(t_i) \end{bmatrix} \\
\tilde{\boldsymbol{\phi}}_{u,m}(t_i) &= \begin{bmatrix} \tilde{\phi}_{u,m}^1(t_i) - \tilde{\rho}_{u,m}^K(t_i) \\ \vdots \\ \tilde{\phi}_{u,m}^{K-1}(t_i) - \tilde{\rho}_{u,m}^K(t_i) \end{bmatrix}.
\end{aligned}
\tag{3.8}
$$

This measurement model can be again written in a more compact form as

$$
\boldsymbol{\Psi} = \boldsymbol{H}\boldsymbol{\xi} + \boldsymbol{A}\boldsymbol{N} + \boldsymbol{n}, \qquad \boldsymbol{\xi} \in \mathbb{R}^5, \quad \boldsymbol{N} \in \mathbb{Z}^{K-1}, \tag{3.9}
$$

which can be easily extended to include measurements from further epochs. This chapter also includes a section on bias estimation with a Kalman filter. No linear combinations

will be used so that the user can compute any linear combination.

The unknown $\boldsymbol{\xi}$ and $\boldsymbol{N}$ are obtained by the integer least-squares estimation, i.e.

$$\min_{\boldsymbol{\xi},\boldsymbol{N}} \|\boldsymbol{\Psi} - \boldsymbol{H}\boldsymbol{\xi} - \boldsymbol{A}\boldsymbol{N}\|^2_{\boldsymbol{\Sigma}^{-1}}, \tag{3.10}$$

which has been decomposed by Teunissen in [62] into three terms using a partitioned system of normal equations [29]. Introducing the orthogonal projection on $\boldsymbol{H}$ by

$$\boldsymbol{P}_H^{\perp} = \boldsymbol{I} - \boldsymbol{P}_H \quad \text{with} \quad \boldsymbol{P}_H = \boldsymbol{H}(\boldsymbol{H}^T\boldsymbol{\Sigma}^{-1}\boldsymbol{H})^{-1}\boldsymbol{H}^T\boldsymbol{\Sigma}^{-1}, \tag{3.11}$$

enables us to rewrite (3.10) as

$$\begin{aligned}
\min_{\boldsymbol{\xi},\boldsymbol{N}} \|\boldsymbol{\Psi} - \boldsymbol{H}\boldsymbol{\xi} - \boldsymbol{A}\boldsymbol{N}\|^2_{\boldsymbol{\Sigma}^{-1}} &= \min_{\boldsymbol{\xi},\boldsymbol{N}} \|\boldsymbol{P}_H\left(\boldsymbol{\Psi} - \boldsymbol{H}\boldsymbol{\xi} - \boldsymbol{A}\boldsymbol{N}\right) + \boldsymbol{P}_H^{\perp}\left(\boldsymbol{\Psi} - \boldsymbol{H}\boldsymbol{\xi} - \boldsymbol{A}\boldsymbol{N}\right)\|^2_{\boldsymbol{\Sigma}^{-1}} \\
&= \min_{\boldsymbol{N}} \Big(\|\boldsymbol{P}_H^{\perp}\left(\boldsymbol{\Psi} - \boldsymbol{A}\boldsymbol{N}\right)\|^2_{\boldsymbol{\Sigma}^{-1}} \\
&\quad + \min_{\boldsymbol{\xi}} \|\boldsymbol{P}_H\left(\boldsymbol{\Psi} - \boldsymbol{A}\boldsymbol{N}\right) - \boldsymbol{H}\boldsymbol{\xi}\|^2_{\boldsymbol{\Sigma}^{-1}}\Big).
\end{aligned} \tag{3.12}$$

The notation is simplified by defining an auxiliary matrix $\overline{\boldsymbol{A}}$ as

$$\overline{\boldsymbol{A}} = \boldsymbol{P}_H^{\perp}\boldsymbol{A}, \tag{3.13}$$

which enables us to write the least-squares float ambiguity estimates as

$$\hat{\boldsymbol{N}} = \left(\overline{\boldsymbol{A}}^T\boldsymbol{\Sigma}^{-1}\overline{\boldsymbol{A}}\right)^{-1}\overline{\boldsymbol{A}}^T\boldsymbol{\Sigma}^{-1}\boldsymbol{P}_H^{\perp}\boldsymbol{\Psi} = \left(\overline{\boldsymbol{A}}^T\boldsymbol{\Sigma}^{-1}\overline{\boldsymbol{A}}\right)^{-1}\overline{\boldsymbol{A}}^T\boldsymbol{\Sigma}^{-1}\boldsymbol{\Psi}, \tag{3.14}$$

with the transformed bias

$$\boldsymbol{b}_{\hat{\boldsymbol{N}}} = \left(\overline{\boldsymbol{A}}^T\boldsymbol{\Sigma}^{-1}\overline{\boldsymbol{A}}\right)^{-1}\overline{\boldsymbol{A}}^T\boldsymbol{\Sigma}^{-1}\boldsymbol{b}. \tag{3.15}$$

The orthogonal projection on $\overline{\boldsymbol{A}}$ is given by

$$\boldsymbol{P}_{\overline{A}}^{\perp} = \boldsymbol{I} - \boldsymbol{P}_{\overline{A}} \quad \text{with} \quad \boldsymbol{P}_{\overline{A}} = \overline{\boldsymbol{A}}(\overline{\boldsymbol{A}}^T\boldsymbol{\Sigma}^{-1}\overline{\boldsymbol{A}})^{-1}\overline{\boldsymbol{A}}^T\boldsymbol{\Sigma}^{-1}, \tag{3.16}$$

and used to rewrite the second term of (3.12) as

$$\begin{aligned}
\|\boldsymbol{P}_H^{\perp}\left(\boldsymbol{\Psi} - \boldsymbol{A}\boldsymbol{N}\right)\|^2_{\boldsymbol{\Sigma}^{-1}} &= \|\boldsymbol{P}_{\overline{\boldsymbol{A}}}\boldsymbol{P}_H^{\perp}\left(\boldsymbol{\Psi} - \boldsymbol{A}\boldsymbol{N}\right)\|^2_{\boldsymbol{\Sigma}^{-1}} + \|\boldsymbol{P}_{\overline{\boldsymbol{A}}}^{\perp}\boldsymbol{P}_H^{\perp}\left(\boldsymbol{\Psi} - \boldsymbol{A}\boldsymbol{N}\right)\|^2_{\boldsymbol{\Sigma}^{-1}} \\
&= \|\overline{\boldsymbol{A}}\hat{\boldsymbol{N}} - \overline{\boldsymbol{A}}\boldsymbol{N}\|^2_{\boldsymbol{\Sigma}^{-1}} + \|\boldsymbol{P}_{\overline{\boldsymbol{A}}}^{\perp}\boldsymbol{P}_H^{\perp}\boldsymbol{\Psi}\|^2_{\boldsymbol{\Sigma}^{-1}} \\
&= \|\hat{\boldsymbol{N}} - \boldsymbol{N}\|^2_{\boldsymbol{\Sigma}^{-1}_{\hat{\boldsymbol{N}}}} + \|\boldsymbol{P}_{\overline{\boldsymbol{A}}}^{\perp}\boldsymbol{P}_H^{\perp}\boldsymbol{\Psi}\|^2_{\boldsymbol{\Sigma}^{-1}},
\end{aligned} \tag{3.17}$$

with

$$\boldsymbol{\Sigma}_{\hat{\boldsymbol{N}}} = \left(\overline{\boldsymbol{A}}^T\boldsymbol{\Sigma}^{-1}\overline{\boldsymbol{A}}\right)^{-1}. \tag{3.18}$$

Combining (3.12) and (3.17) yields

$$\min_{\boldsymbol{\xi},\boldsymbol{N}} \|\boldsymbol{\Psi} - \boldsymbol{H}\boldsymbol{\xi} - \boldsymbol{A}\boldsymbol{N}\|^2_{\boldsymbol{\Sigma}^{-1}} = \min_{\boldsymbol{\xi},\boldsymbol{N}} \Big(\|\boldsymbol{P}_H \left(\boldsymbol{\Psi} - \boldsymbol{A}\boldsymbol{N}\right) - \boldsymbol{H}\boldsymbol{\xi}\|^2_{\boldsymbol{\Sigma}^{-1}} + \|\hat{\boldsymbol{N}} - \boldsymbol{N}\|^2_{\boldsymbol{\Sigma}^{-1}_{\hat{N}}} + \|\boldsymbol{P}^{\perp}_{\overline{\boldsymbol{A}}} \boldsymbol{P}^{\perp}_{H} \boldsymbol{\Psi}\|^2_{\boldsymbol{\Sigma}^{-1}} \Big), \tag{3.19}$$

where the second term is independent of $\boldsymbol{\xi}$, i.e. the ambiguity resolution can be separated from the baseline estimation. The fixed baseline estimate $\check{\boldsymbol{\xi}}$ is given by

$$\check{\boldsymbol{\xi}} = \left(\boldsymbol{H}^T \boldsymbol{\Sigma}^{-1} \boldsymbol{H}\right)^{-1} \boldsymbol{H}^T \boldsymbol{\Sigma}^{-1} \left(\boldsymbol{\Psi} - \boldsymbol{A}\boldsymbol{N}\right), \tag{3.20}$$

and used to rewrite the first term of (3.19) as

$$\begin{aligned} \|\boldsymbol{P}_H \left(\boldsymbol{\Psi} - \boldsymbol{A}\boldsymbol{N}\right) - \boldsymbol{H}\boldsymbol{\xi}\|^2_{\boldsymbol{\Sigma}^{-1}} &= \|\boldsymbol{H} \left(\boldsymbol{H}^T \boldsymbol{\Sigma}^{-1} \boldsymbol{H}\right)^{-1} \boldsymbol{H}^T \boldsymbol{\Sigma}^{-1} \left(\boldsymbol{\Psi} - \boldsymbol{A}\boldsymbol{N}\right) - \boldsymbol{H}\boldsymbol{\xi}\|^2_{\boldsymbol{\Sigma}^{-1}} \\ &= \|\boldsymbol{H}\check{\boldsymbol{\xi}}(\boldsymbol{N}) - \boldsymbol{H}\boldsymbol{\xi}\|^2_{\boldsymbol{\Sigma}^{-1}} = \|\check{\boldsymbol{\xi}}(\boldsymbol{N}) - \boldsymbol{\xi}\|^2_{\boldsymbol{\Sigma}^{-1}_{\check{\xi}(N)}}, \end{aligned} \tag{3.21}$$

which becomes 0 for $\boldsymbol{\xi} = \check{\boldsymbol{\xi}}(\boldsymbol{N})$. The weighting is given by

$$\boldsymbol{\Sigma}_{\check{\xi}(N)} = \left(\boldsymbol{H}^T \boldsymbol{\Sigma}^{-1} \boldsymbol{H}\right)^{-1}. \tag{3.22}$$

The last term in (3.19) denotes the irreducible error which does not depend on $\boldsymbol{N}$ and $\boldsymbol{\xi}$ and, thus, is irrelevant for the minimization. It has been stated by Teunissen in [29] that this irreducible error can be expressed also as a function of the float ambiguity and baseline estimates:

$$\|\boldsymbol{P}^{\perp}_{\overline{\boldsymbol{A}}} \boldsymbol{P}^{\perp}_{H} \boldsymbol{\Psi}\|^2_{\boldsymbol{\Sigma}^{-1}} = \|\boldsymbol{\Psi} - \boldsymbol{A}\hat{\boldsymbol{N}} - \boldsymbol{H}\hat{\boldsymbol{\xi}}\|^2_{\boldsymbol{\Sigma}^{-1}}, \tag{3.23}$$

This equivalence is proven by replacing the float baseline solution by

$$\hat{\boldsymbol{\xi}} = \left(\overline{\boldsymbol{H}}^T \boldsymbol{\Sigma}^{-1} \overline{\boldsymbol{H}}\right)^{-1} \overline{\boldsymbol{H}}^T \boldsymbol{\Sigma}^{-1} \boldsymbol{\Psi} \quad \text{with} \quad \overline{\boldsymbol{H}} = \boldsymbol{P}^{\perp}_{A} \boldsymbol{H}, \tag{3.24}$$

and by using $\hat{\boldsymbol{N}}$ of (3.14), i.e.

$$\begin{aligned} &\|\boldsymbol{\Psi} - \boldsymbol{A}\hat{\boldsymbol{N}} - \boldsymbol{H}\hat{\boldsymbol{\xi}}\|^2_{\boldsymbol{\Sigma}^{-1}} \\ &= \|\boldsymbol{\Psi} - \boldsymbol{A} \left(\overline{\boldsymbol{A}}^T \boldsymbol{\Sigma}^{-1} \overline{\boldsymbol{A}}\right)^{-1} \overline{\boldsymbol{A}}^T \boldsymbol{\Sigma}^{-1} \boldsymbol{\Psi} - \boldsymbol{H} \left(\overline{\boldsymbol{H}}^T \boldsymbol{\Sigma}^{-1} \overline{\boldsymbol{H}}\right)^{-1} \overline{\boldsymbol{H}}^T \boldsymbol{\Sigma}^{-1} \boldsymbol{\Psi}\|^2_{\boldsymbol{\Sigma}^{-1}} \\ &= \|\boldsymbol{P}^{\perp}_{H} \boldsymbol{\Psi} + \boldsymbol{P}_H \boldsymbol{\Psi} - \boldsymbol{A} \left(\overline{\boldsymbol{A}}^T \boldsymbol{\Sigma}^{-1} \overline{\boldsymbol{A}}\right)^{-1} \overline{\boldsymbol{A}}^T \boldsymbol{\Sigma}^{-1} \boldsymbol{\Psi} - \boldsymbol{H} \left(\overline{\boldsymbol{H}}^T \boldsymbol{\Sigma}^{-1} \overline{\boldsymbol{H}}\right)^{-1} \overline{\boldsymbol{H}}^T \boldsymbol{\Sigma}^{-1} \boldsymbol{\Psi}\|^2_{\boldsymbol{\Sigma}^{-1}} \\ &= \|\boldsymbol{P}^{\perp}_{\overline{A}} \boldsymbol{P}^{\perp}_{H} \boldsymbol{\Psi} + \boldsymbol{P}_{\overline{A}} \boldsymbol{P}^{\perp}_{H} \boldsymbol{\Psi} + \boldsymbol{P}_H \boldsymbol{\Psi} - \boldsymbol{A} \left(\overline{\boldsymbol{A}}^T \boldsymbol{\Sigma}^{-1} \overline{\boldsymbol{A}}\right)^{-1} \overline{\boldsymbol{A}}^T \boldsymbol{\Sigma}^{-1} \boldsymbol{\Psi} \\ &\quad - \boldsymbol{H} \left(\overline{\boldsymbol{H}}^T \boldsymbol{\Sigma}^{-1} \overline{\boldsymbol{H}}\right)^{-1} \overline{\boldsymbol{H}}^T \boldsymbol{\Sigma}^{-1} \boldsymbol{\Psi}\|^2_{\boldsymbol{\Sigma}^{-1}}. \end{aligned} \tag{3.25}$$

Replacing $\boldsymbol{\Psi}$ by (3.6) in the third and fourth term gives

$$\begin{aligned}\boldsymbol{P}_H\boldsymbol{\Psi} - \boldsymbol{A}\left(\overline{\boldsymbol{A}}^T\boldsymbol{\Sigma}^{-1}\overline{\boldsymbol{A}}\right)^{-1}\overline{\boldsymbol{A}}^T\boldsymbol{\Sigma}^{-1}\boldsymbol{\Psi}&\\ = \boldsymbol{P}_H\boldsymbol{A}\boldsymbol{N} + \boldsymbol{H}\boldsymbol{\xi} + \boldsymbol{P}_H\boldsymbol{\eta} - \boldsymbol{A}\boldsymbol{N} - \boldsymbol{A}\left(\overline{\boldsymbol{A}}^T\boldsymbol{\Sigma}^{-1}\overline{\boldsymbol{A}}\right)^{-1}\overline{\boldsymbol{A}}^T\boldsymbol{\Sigma}^{-1}\boldsymbol{\eta}&\\ = -\overline{\boldsymbol{A}}\boldsymbol{N} + \boldsymbol{H}\boldsymbol{\xi} + \boldsymbol{P}_H\boldsymbol{\eta} - \boldsymbol{A}\left(\overline{\boldsymbol{A}}^T\boldsymbol{\Sigma}^{-1}\overline{\boldsymbol{A}}\right)^{-1}\overline{\boldsymbol{A}}^T\boldsymbol{\Sigma}^{-1}\boldsymbol{\eta}.&\end{aligned} \tag{3.26}$$

Similarly, the second and fifth term are expanded into

$$\begin{aligned}\boldsymbol{P}_{\overline{A}}\boldsymbol{P}_H^{\perp}\boldsymbol{\Psi} - \boldsymbol{H}\left(\overline{\boldsymbol{H}}^T\boldsymbol{\Sigma}^{-1}\overline{\boldsymbol{H}}\right)^{-1}\overline{\boldsymbol{H}}^T\boldsymbol{\Sigma}^{-1}\boldsymbol{\Psi}&\\ = \overline{\boldsymbol{A}}\boldsymbol{N} + \boldsymbol{P}_{\overline{A}}\boldsymbol{P}_H^{\perp}\boldsymbol{\eta} - \boldsymbol{H}\boldsymbol{\xi} - \boldsymbol{H}\left(\overline{\boldsymbol{H}}^T\boldsymbol{\Sigma}^{-1}\overline{\boldsymbol{H}}\right)^{-1}\overline{\boldsymbol{H}}^T\boldsymbol{\Sigma}^{-1}\boldsymbol{\eta}&\end{aligned} \tag{3.27}$$

Combining (3.25)-(3.27) yields

$$\begin{aligned}\|\boldsymbol{\Psi} - \boldsymbol{A}\hat{\boldsymbol{N}} - \boldsymbol{H}\hat{\boldsymbol{\xi}}\|^2_{\boldsymbol{\Sigma}^{-1}} &= \|\boldsymbol{P}_{\overline{A}}^{\perp}\boldsymbol{P}_H^{\perp}\boldsymbol{\Psi} + \boldsymbol{P}_H\boldsymbol{\eta} - \boldsymbol{A}\left(\overline{\boldsymbol{A}}^T\boldsymbol{\Sigma}^{-1}\overline{\boldsymbol{A}}\right)^{-1}\overline{\boldsymbol{A}}^T\boldsymbol{\Sigma}^{-1}\boldsymbol{\eta} + \boldsymbol{P}_{\overline{A}}\boldsymbol{P}_H^{\perp}\boldsymbol{\eta}\\ &\quad -\boldsymbol{H}\left(\overline{\boldsymbol{H}}^T\boldsymbol{\Sigma}^{-1}\overline{\boldsymbol{H}}\right)^{-1}\overline{\boldsymbol{H}}^T\boldsymbol{\Sigma}^{-1}\boldsymbol{\eta}\|^2_{\boldsymbol{\Sigma}^{-1}}.\end{aligned} \tag{3.28}$$

Replacing the projections by their definitions results in

$$\begin{aligned}\|\boldsymbol{\Psi} - \boldsymbol{A}\hat{\boldsymbol{N}} - \boldsymbol{H}\hat{\boldsymbol{\xi}}\|^2_{\boldsymbol{\Sigma}^{-1}} &= \|\boldsymbol{P}_{\overline{A}}^{\perp}\boldsymbol{P}_H^{\perp}\boldsymbol{\Psi} + \boldsymbol{H}(\boldsymbol{H}^T\boldsymbol{\Sigma}^{-1}\boldsymbol{H})^{-1}\boldsymbol{H}^T\boldsymbol{\Sigma}^{-1}\boldsymbol{\eta}\\
&\quad - \boldsymbol{A}\left(\boldsymbol{A}^T\boldsymbol{\Sigma}^{-1}\boldsymbol{A} - \boldsymbol{A}^T\boldsymbol{\Sigma}^{-1}\boldsymbol{H}(\boldsymbol{H}^T\boldsymbol{\Sigma}^{-1}\boldsymbol{H})^{-1}\boldsymbol{H}^T\boldsymbol{\Sigma}^{-1}\boldsymbol{A}\right)^{-1}\\
&\quad\cdot(\boldsymbol{A}^T - \boldsymbol{A}^T\boldsymbol{\Sigma}^{-1}\boldsymbol{H}(\boldsymbol{H}^T\boldsymbol{\Sigma}^{-1}\boldsymbol{H})^{-1}\boldsymbol{H}^T)\boldsymbol{\Sigma}^{-1}\boldsymbol{\eta}\\
&\quad + (\boldsymbol{A} - \boldsymbol{H}(\boldsymbol{H}^T\boldsymbol{\Sigma}^{-1}\boldsymbol{H})^{-1}\boldsymbol{H}^T\boldsymbol{\Sigma}^{-1}\boldsymbol{A})\left(\boldsymbol{A}^T\boldsymbol{\Sigma}^{-1}\boldsymbol{A} - \boldsymbol{A}^T\boldsymbol{\Sigma}^{-1}\boldsymbol{H}(\boldsymbol{H}^T\boldsymbol{\Sigma}^{-1}\boldsymbol{H})^{-1}\boldsymbol{H}^T\boldsymbol{\Sigma}^{-1}\boldsymbol{A}\right)^{-1}\\
&\quad\cdot(\boldsymbol{A}^T - \boldsymbol{A}^T\boldsymbol{\Sigma}^{-1}\boldsymbol{H}(\boldsymbol{H}^T\boldsymbol{\Sigma}^{-1}\boldsymbol{H})^{-1}\boldsymbol{H}^T)\boldsymbol{\Sigma}^{-1}(\mathbf{1} - \boldsymbol{H}(\boldsymbol{H}^T\boldsymbol{\Sigma}^{-1}\boldsymbol{H})^{-1}\boldsymbol{H}^T\boldsymbol{\Sigma}^{-1})\boldsymbol{\eta}\\
&\quad - \boldsymbol{H}\left(\boldsymbol{H}^T\boldsymbol{\Sigma}^{-1}\boldsymbol{H} - \boldsymbol{H}^T\boldsymbol{\Sigma}^{-1}\boldsymbol{A}(\boldsymbol{A}^T\boldsymbol{\Sigma}^{-1}\boldsymbol{A})^{-1}\boldsymbol{A}^T\boldsymbol{\Sigma}^{-1}\boldsymbol{H}\right)^{-1}\\
&\quad\cdot(\boldsymbol{H}^T - \boldsymbol{H}^T\boldsymbol{\Sigma}^{-1}\boldsymbol{A}(\boldsymbol{A}^T\boldsymbol{\Sigma}^{-1}\boldsymbol{A})^{-1}\boldsymbol{A}^T)\boldsymbol{\Sigma}^{-1}\boldsymbol{\eta}\|^2_{\boldsymbol{\Sigma}^{-1}}.\end{aligned} \tag{3.29}$$

The inversion of a sum of matrices is performed with the Sherman-Morrison-Woodbury equation that is derived by Henderson and Searle in [54]. Let $\boldsymbol{G}$, $\boldsymbol{U}$ be invertible $n \times n$ matrices, and let $\boldsymbol{Y}$, $\boldsymbol{Z}$ be $n \times s$ matrices with $n \geq s$, then

$$(\boldsymbol{U} + \boldsymbol{Y}\boldsymbol{G}\boldsymbol{Z}^T)^{-1} = \boldsymbol{U}^{-1} - \boldsymbol{U}^{-1}\boldsymbol{Y}(\boldsymbol{G}^{-1} + \boldsymbol{Z}^T\boldsymbol{U}^{-1}\boldsymbol{Y})^{-1}\boldsymbol{Z}^T\boldsymbol{U}^{-1}. \tag{3.30}$$

The application of this theorem gives

$$\begin{aligned}&\left(\boldsymbol{H}^T\boldsymbol{\Sigma}^{-1}\boldsymbol{H} - \boldsymbol{H}^T\boldsymbol{\Sigma}^{-1}\boldsymbol{A}(\boldsymbol{A}^T\boldsymbol{\Sigma}^{-1}\boldsymbol{A})^{-1}\boldsymbol{A}^T\boldsymbol{\Sigma}^{-1}\boldsymbol{H}\right)^{-1}\\
&\quad= (\boldsymbol{H}^T\boldsymbol{\Sigma}^{-1}\boldsymbol{H})^{-1} + (\boldsymbol{H}^T\boldsymbol{\Sigma}^{-1}\boldsymbol{H})^{-1}\boldsymbol{H}^T\boldsymbol{\Sigma}^{-1}\boldsymbol{A}\\
&\quad\quad\cdot\left(\boldsymbol{A}^T\boldsymbol{\Sigma}^{-1}\boldsymbol{A} - \boldsymbol{A}^T\boldsymbol{\Sigma}^{-1}\boldsymbol{H}(\boldsymbol{H}^T\boldsymbol{\Sigma}^{-1}\boldsymbol{H})^{-1}\boldsymbol{H}^T\boldsymbol{\Sigma}^{-1}\boldsymbol{A}\right)^{-1}\boldsymbol{A}^T\boldsymbol{\Sigma}^{-1}(\boldsymbol{H}^T\boldsymbol{\Sigma}^{-1}\boldsymbol{H})^{-1},\end{aligned} \tag{3.31}$$

which requires the same matrix inversion as the remaining terms of (3.29). The notation is simplified by introducing

$$\boldsymbol{J} = \left(\boldsymbol{A}^T\boldsymbol{\Sigma}^{-1}\boldsymbol{A} - \boldsymbol{A}^T\boldsymbol{\Sigma}^{-1}\boldsymbol{H}(\boldsymbol{H}^T\boldsymbol{\Sigma}^{-1}\boldsymbol{H})^{-1}\boldsymbol{H}^T\boldsymbol{\Sigma}^{-1}\boldsymbol{A}\right)^{-1}, \tag{3.32}$$

to rewrite (3.29) as

$$\begin{aligned}\|\boldsymbol{\Psi} - \boldsymbol{A}\hat{\boldsymbol{N}} - \boldsymbol{H}\hat{\boldsymbol{\xi}}\|^2_{\boldsymbol{\Sigma}^{-1}} = \|&\boldsymbol{P}^{\perp}_{\boldsymbol{A}}\boldsymbol{P}^{\perp}_{\boldsymbol{H}}\boldsymbol{\Psi} + \boldsymbol{H}(\boldsymbol{H}^T\boldsymbol{\Sigma}^{-1}\boldsymbol{H})^{-1}\boldsymbol{H}^T\boldsymbol{\Sigma}^{-1}\boldsymbol{\eta}\\
&- \boldsymbol{A}\boldsymbol{J}(\boldsymbol{A}^T - \boldsymbol{A}^T\boldsymbol{\Sigma}^{-1}\boldsymbol{H}(\boldsymbol{H}^T\boldsymbol{\Sigma}^{-1}\boldsymbol{H})^{-1}\boldsymbol{H}^T)\boldsymbol{\Sigma}^{-1}\boldsymbol{\eta}\\
&+ (\boldsymbol{A} - \boldsymbol{H}(\boldsymbol{H}^T\boldsymbol{\Sigma}^{-1}\boldsymbol{H})^{-1}\boldsymbol{H}^T\boldsymbol{\Sigma}^{-1}\boldsymbol{A})\boldsymbol{J}\\
&\quad (\boldsymbol{A}^T - \boldsymbol{A}^T\boldsymbol{\Sigma}^{-1}\boldsymbol{H}(\boldsymbol{H}^T\boldsymbol{\Sigma}^{-1}\boldsymbol{H})^{-1}\boldsymbol{H}^T)\boldsymbol{\Sigma}^{-1}(\boldsymbol{1} - \boldsymbol{H}(\boldsymbol{H}^T\boldsymbol{\Sigma}^{-1}\boldsymbol{H})^{-1}\boldsymbol{H}^T\boldsymbol{\Sigma}^{-1})\boldsymbol{\eta}\\
&- \boldsymbol{H}\boldsymbol{J}(\boldsymbol{H}^T - \boldsymbol{H}^T\boldsymbol{\Sigma}^{-1}\boldsymbol{A}(\boldsymbol{A}^T\boldsymbol{\Sigma}^{-1}\boldsymbol{A})^{-1}\boldsymbol{A}^T)\boldsymbol{\Sigma}^{-1}\boldsymbol{\eta}\|^2_{\boldsymbol{\Sigma}^{-1}},\end{aligned} \tag{3.33}$$

which can be further simplified to

$$\begin{aligned}\|\boldsymbol{\Psi} - \boldsymbol{A}\hat{\boldsymbol{N}} - \boldsymbol{H}\hat{\boldsymbol{\xi}}\|^2_{\boldsymbol{\Sigma}^{-1}} &= \|\boldsymbol{P}^{\perp}_{\boldsymbol{A}}\boldsymbol{P}^{\perp}_{\boldsymbol{H}}\boldsymbol{\Psi} - \boldsymbol{H}(\boldsymbol{H}^T\boldsymbol{\Sigma}^{-1}\boldsymbol{H})^{-1}\boldsymbol{H}^T\boldsymbol{\Sigma}^{-1}\boldsymbol{A}\boldsymbol{J}\boldsymbol{A}^T\boldsymbol{\Sigma}^{-1}\boldsymbol{\eta}\\
&\quad +\boldsymbol{H}(\boldsymbol{H}^T\boldsymbol{\Sigma}^{-1}\boldsymbol{H})^{-1}\boldsymbol{H}^T\boldsymbol{\Sigma}^{-1}\boldsymbol{A}(\boldsymbol{A}^T\boldsymbol{\Sigma}^{-1}\boldsymbol{A})^{-1}\boldsymbol{A}^T\boldsymbol{\Sigma}^{-1}\boldsymbol{\eta}\\
&\quad +\boldsymbol{H}(\boldsymbol{H}^T\boldsymbol{\Sigma}^{-1}\boldsymbol{H})^{-1}\boldsymbol{H}^T\boldsymbol{\Sigma}^{-1}\boldsymbol{A}\boldsymbol{J}\boldsymbol{A}^T\boldsymbol{\Sigma}^{-1}\boldsymbol{H}(\boldsymbol{H}^T\boldsymbol{\Sigma}^{-1}\boldsymbol{H})^{-1}\boldsymbol{H}^T\\
&\quad\quad \boldsymbol{\Sigma}^{-1}\boldsymbol{A}(\boldsymbol{A}^T\boldsymbol{\Sigma}^{-1}\boldsymbol{A})^{-1}\boldsymbol{A}^T\boldsymbol{\Sigma}^{-1}\boldsymbol{\eta}\|^2_{\boldsymbol{\Sigma}^{-1}}\\
&= \|\boldsymbol{P}^{\perp}_{\boldsymbol{A}}\boldsymbol{P}^{\perp}_{\boldsymbol{H}}\boldsymbol{\Psi} + \boldsymbol{H}(\boldsymbol{H}^T\boldsymbol{\Sigma}^{-1}\boldsymbol{H})^{-1}\boldsymbol{H}^T\boldsymbol{\Sigma}^{-1}\boldsymbol{A}(\boldsymbol{A}^T\boldsymbol{\Sigma}^{-1}\boldsymbol{A})^{-1}\boldsymbol{A}^T\boldsymbol{\Sigma}^{-1}\boldsymbol{\eta}\\
&\quad -\boldsymbol{H}(\boldsymbol{H}^T\boldsymbol{\Sigma}^{-1}\boldsymbol{H})^{-1}\boldsymbol{H}^T\boldsymbol{\Sigma}^{-1}\boldsymbol{A}\boldsymbol{J}\\
&\quad\quad \left(\boldsymbol{A}^T\boldsymbol{\Sigma}^{-1} - \boldsymbol{A}^T\boldsymbol{\Sigma}^{-1}\boldsymbol{H}(\boldsymbol{H}^T\boldsymbol{\Sigma}^{-1}\boldsymbol{H})^{-1}\boldsymbol{H}^T\right.\\
&\quad\quad \left.\boldsymbol{\Sigma}^{-1}\boldsymbol{A}(\boldsymbol{A}^T\boldsymbol{\Sigma}^{-1}\boldsymbol{A})^{-1}\boldsymbol{A}^T\boldsymbol{\Sigma}^{-1}\right)\boldsymbol{\eta}\|^2_{\boldsymbol{\Sigma}^{-1}}\end{aligned} \tag{3.34}$$

The last component can be multiplied by the projection $\boldsymbol{P}_A$ without changing its value, i.e.

$$\begin{aligned}&\boldsymbol{J}\left(\boldsymbol{A}^T\boldsymbol{\Sigma}^{-1} - \boldsymbol{A}^T\boldsymbol{\Sigma}^{-1}\boldsymbol{H}(\boldsymbol{H}^T\boldsymbol{\Sigma}^{-1}\boldsymbol{H})^{-1}\boldsymbol{H}^T\boldsymbol{\Sigma}^{-1}\boldsymbol{A}(\boldsymbol{A}^T\boldsymbol{\Sigma}^{-1}\boldsymbol{A})^{-1}\boldsymbol{A}^T\boldsymbol{\Sigma}^{-1}\right)\\
&\quad = \boldsymbol{J}\left(\boldsymbol{A}^T\boldsymbol{\Sigma}^{-1} - \boldsymbol{A}^T\boldsymbol{\Sigma}^{-1}\boldsymbol{H}(\boldsymbol{H}^T\boldsymbol{\Sigma}^{-1}\boldsymbol{H})^{-1}\boldsymbol{H}^T\boldsymbol{\Sigma}^{-1}\boldsymbol{A}(\boldsymbol{A}^T\boldsymbol{\Sigma}^{-1}\boldsymbol{A})^{-1}\boldsymbol{A}^T\boldsymbol{\Sigma}^{-1}\right)\\
&\quad\quad \boldsymbol{A}(\boldsymbol{A}^T\boldsymbol{\Sigma}^{-1}\boldsymbol{A})^{-1}\boldsymbol{A}^T\boldsymbol{\Sigma}^{-1} = \boldsymbol{J}\boldsymbol{J}^{-1} = \boldsymbol{1},\end{aligned} \tag{3.35}$$

which simplifies (3.34) to

$$\|\boldsymbol{\Psi} - \boldsymbol{A}\hat{\boldsymbol{N}} - \boldsymbol{H}\hat{\boldsymbol{\xi}}\|^2_{\boldsymbol{\Sigma}^{-1}} = \|\boldsymbol{P}^{\perp}_{\boldsymbol{A}}\boldsymbol{P}^{\perp}_{\boldsymbol{H}}\boldsymbol{\Psi}\|^2_{\boldsymbol{\Sigma}^{-1}}, \tag{3.36}$$

and concludes our proof and enables us to rewrite the minimization problem of (3.10) as

$$\begin{aligned}\min_{\boldsymbol{\xi},\boldsymbol{N}}\|\boldsymbol{\Psi} - \boldsymbol{H}\boldsymbol{\xi} - \boldsymbol{A}\boldsymbol{N}\|^2_{\boldsymbol{\Sigma}^{-1}} &= \min_{\boldsymbol{N}}\left(\|\hat{\boldsymbol{N}} - \boldsymbol{N}\|^2_{\boldsymbol{\Sigma}^{-1}_{\hat{N}}} + \min_{\boldsymbol{\xi}}\|\check{\boldsymbol{\xi}}(\boldsymbol{N}) - \boldsymbol{\xi}\|^2_{\boldsymbol{\Sigma}^{-1}_{\hat{\xi}(N)}}\right)\\
&\quad +\|\boldsymbol{\Psi} - \boldsymbol{A}\hat{\boldsymbol{N}} - \boldsymbol{H}\hat{\boldsymbol{\xi}}\|^2_{\boldsymbol{\Sigma}^{-1}}.\end{aligned} \tag{3.37}$$

3.1.1 Rounding

The most simple integer ambiguity estimator is the rounding of the float solution $\hat{\boldsymbol{N}}$. Its success rate is given by the multivariate cumulative Gaussian distribution

$$P_{\mathrm{s}} = \frac{1}{\sqrt{|\boldsymbol{\Sigma}_{\hat{\boldsymbol{N}}}|(2\pi)^K}} \cdot \int_{N_1-0.5}^{N_1+0.5} \dots \int_{N_K-0.5}^{N_K+0.5} e^{-\frac{1}{2}(\hat{\boldsymbol{N}}-\boldsymbol{N}-\boldsymbol{b}_{\hat{\boldsymbol{N}}})^T \boldsymbol{\Sigma}_{\hat{\boldsymbol{N}}}^{-1}(\hat{\boldsymbol{N}}-\boldsymbol{N}-\boldsymbol{b}_{\hat{\boldsymbol{N}}})} d\hat{N}_1 \dots d\hat{N}_K, \quad (3.38)$$

with $\hat{\boldsymbol{N}} \sim \mathcal{N}\left(\boldsymbol{N} + \boldsymbol{b}_{\hat{\boldsymbol{N}}}, \boldsymbol{\Sigma}_{\hat{\boldsymbol{N}}}\right)$. Substituting $\hat{\boldsymbol{N}} - \boldsymbol{N} - \boldsymbol{b}_{\hat{\boldsymbol{N}}}$ by $\boldsymbol{\varepsilon}_{\hat{\boldsymbol{N}}}$ yields

$$P_{\mathrm{s}} = \frac{1}{\sqrt{|\boldsymbol{\Sigma}_{\hat{\boldsymbol{N}}}|(2\pi)^K}} \cdot \int_{-0.5-b_1}^{+0.5-b_1} \dots \int_{-0.5-b_K}^{+0.5-b_K} e^{-\frac{1}{2}\boldsymbol{\varepsilon}_{\hat{\boldsymbol{N}}}^T \boldsymbol{\Sigma}_{\hat{\boldsymbol{N}}}^{-1} \boldsymbol{\varepsilon}_{\hat{\boldsymbol{N}}}} \, d\varepsilon_{\hat{N}_1} \dots d\varepsilon_{\hat{N}_K}. \quad (3.39)$$

Genz suggested three sequential transformations in [55] to transform this integral into an integral over a unit hyper-cube which can then be evaluated by standard multidimensional numerical integration. First, the Cholesky decomposition $\boldsymbol{\Sigma}_{\hat{\boldsymbol{N}}} = \boldsymbol{C}\boldsymbol{C}^T$ is used to diagonalize the noise vector, i.e. $\boldsymbol{e}_{\hat{\boldsymbol{N}}} = \boldsymbol{C}^{-1}\boldsymbol{\varepsilon}_{\hat{\boldsymbol{N}}}$. The integration limits

$$-0.5 - b_k \leq \varepsilon_{\hat{N}_k} = \sum_{j=1}^{k} C_{kj} e_{\hat{N}_j} \leq +0.5 - b_k, \quad (3.40)$$

are transformed using the lower triangular structure of $\boldsymbol{C}$, i.e.

$$l_k = \frac{-0.5 - b_k - \sum_{j=1}^{k-1} C_{kj} e_{\hat{N}_j}}{C_{kk}} \leq e_{\hat{N}_k} \leq u_k = \frac{+0.5 - b_k - \sum_{j=1}^{k-1} C_{kj} e_{\hat{N}_j}}{C_{kk}}. \quad (3.41)$$

Thus, the multivariate integral becomes

$$P_{\mathrm{s}} = \frac{1}{\sqrt{(2\pi)^K}} \int_{l_1}^{u_1} e^{-\frac{e_{\hat{N}_1}^2}{2}} \int_{l_2(e_{\hat{N}_1})}^{u_2(e_{\hat{N}_1})} e^{-\frac{e_{\hat{N}_2}^2}{2}} \dots \int_{l_K(e_{\hat{N}_1},\dots,e_{\hat{N}_{K-1}})}^{u_K(e_{\hat{N}_1},\dots,e_{\hat{N}_{K-1}})} e^{-\frac{e_{\hat{N}_K}^2}{2}} de_{\hat{N}_1} de_{\hat{N}_2} \dots de_{\hat{N}_{K-1}}. \quad (3.42)$$

Genz's second transformation is given by

$$z_k = \Phi(e_{\hat{N}_k}) \quad (3.43)$$

with the normalized cumulative normal distribution

$$\Phi(\nu) = \frac{1}{\sqrt{2\pi}} \int_{-\infty}^{\nu} e^{-\frac{1}{2}\theta^2} d\theta. \quad (3.44)$$

The transformation can be applied separately to each $e_{\hat{N}_k}$ in (3.42), i.e.

$$P_{\mathrm{s}} = \int_{l_1'}^{u_1'} \int_{l_2'(z_1)}^{u_2'(z_1)} \dots \int_{l_K'(z_1,\dots,z_{K-1})}^{u_K'(z_1,\dots,z_{K-1})} dz_1 dz_2 \dots dz_K, \quad (3.45)$$

with the integration limits

$$\begin{aligned} l'_k &= \Phi\left(\left(-0.5 - b_k - \sum_{j=1}^{k-1} C_{kj}\Phi^{-1}(z_j)\right)/C_{kk}\right) \\ u'_k &= \Phi\left(\left(+0.5 - b_k - \sum_{j=1}^{k-1} C_{kj}\Phi^{-1}(z_j)\right)/C_{kk}\right). \end{aligned} \tag{3.46}$$

Finally, the transformation

$$w_k = \frac{z_k - l'_k}{u'_k - l'_k} \tag{3.47}$$

puts the integral into a constant limit form, i.e.

$$P_{\mathrm{s}} = (u'_1 - l'_1)\int_0^1 (u'_2 - l'_2)\int_0^1 \ldots (u'_K - l'_K)\int_0^1 dw_1 dw_2 \ldots dw_K. \tag{3.48}$$

with

$$\begin{aligned} l'_k &= \Phi\left(\left(-0.5 - b_k - \sum_{j=1}^{k-1} C_{kj}\Phi^{-1}(l'_j + w_k(u'_j - l'_j))\right)/C_{kk}\right) \\ u'_k &= \Phi\left(\left(+0.5 - b_k - \sum_{j=1}^{k-1} C_{kj}\Phi^{-1}(l'_j + w_k(u'_j - l'_j))\right)/C_{kk}\right). \end{aligned} \tag{3.49}$$

Eq. (3.48) can be rewritten by regarding w_k as a uniformly distributed random variable between 0 and 1, i.e.

$$P_{\mathrm{s}} = (u'_1 - l'_1)\int_0^1 (u'_2 - l'_2) f(w_1)\int_0^1 \ldots (u'_K - l'_K) f(w_{K-1})\int_0^1 f(w_K) dw_1 dw_2 \ldots dw_K, \tag{3.50}$$

which is equivalent to

$$P_{\mathrm{s}} = \mathrm{E}_{w_1,\ldots,w_K}\left\{\prod_{k=1}^{K}(u'_k(w_1,\ldots,w_K) - l'_k(w_1,\ldots,w_K))\right\} \quad \text{with} \quad w_k \sim \mathcal{U}(0,1). \tag{3.51}$$

The success rate of (3.51) can be efficiently computed using Monte-Carlo simulation or more advanced numerical integration techniques, e.g. the subregion adaptive method as discussed by Genz in [55].

An analytic lower bound on the success rate has been suggested by Teunissen in [57]: It neglects the correlation between float ambiguities and is given by

$$P_{\mathrm{s}} \geq \prod_{k=1}^{K} P_{\mathrm{s}}^k \quad \text{with} \quad P_{\mathrm{s}}^k = \int_{-0.5}^{+0.5} \frac{1}{\sqrt{2\pi\sigma^2_{\hat{N}_k}}} e^{-\frac{(\hat{N}_k - N_k - b_k)^2}{2\sigma^2_{\hat{N}_k}}} d\hat{N}_k. \tag{3.52}$$

It can be proven from the cumulative bivariate normal distribution that can be lower bounded by another cumulative bivariate normal distribution with equal variances but a different cross-correlation coefficient ρ between $\varepsilon_{\hat{N}_1}$ and $\varepsilon_{\hat{N}_2}$, i.e.

$$\begin{aligned}&\frac{1}{\sqrt{2\pi|\boldsymbol{\Sigma}_{\hat{N}}|}}\int_{-0.5}^{+0.5}\int_{-0.5}^{+0.5} e^{-\frac{1}{2}\boldsymbol{\varepsilon}_{\hat{N}}^T\boldsymbol{\Sigma}_{\hat{N}}^{-1}\boldsymbol{\varepsilon}_{\hat{N}}}d\varepsilon_{\hat{N}_1}d\varepsilon_{\hat{N}_2}\\ &\geq \min_{\rho}\left(\frac{1}{\sqrt{2\pi|\boldsymbol{\Sigma}_{\hat{N}}(\rho)|}}\int_{-0.5}^{+0.5}\int_{-0.5}^{+0.5} e^{-\frac{1}{2}\boldsymbol{\varepsilon}_{\hat{N}}^T\boldsymbol{\Sigma}_{\hat{N}}^{-1}(\rho)\boldsymbol{\varepsilon}_{\hat{N}}}d\varepsilon_{\hat{N}_1}d\varepsilon_{\hat{N}_2}\right).\end{aligned} \tag{3.53}$$

As the total integral over a bivariate normal distribution is always equal to 1 and as the Gaussian distribution is monotonously decreasing from the center in all directions, the minimization of (3.53) is equivalent to a min-max-optimization of the variance of $\tilde{\varepsilon}_{\hat{N}_1}$:

$$\min_{\rho}\left(\frac{1}{\sqrt{2\pi|\boldsymbol{\Sigma}_{\hat{N}}(\rho)|}}\int_{-0.5}^{+0.5}\int_{-0.5}^{+0.5} e^{-\frac{1}{2}\boldsymbol{\varepsilon}_{\hat{N}}^T\boldsymbol{\Sigma}_{\hat{N}}^{-1}(\rho)\boldsymbol{\varepsilon}_{\hat{N}}}d\varepsilon_{\hat{N}_1}d\varepsilon_{\hat{N}_2}\right) = \max_{\rho}\min_{\boldsymbol{R}}\left(\sigma^2_{\tilde{\varepsilon}_{\hat{N}_1}}\right), \tag{3.54}$$

where $\tilde{\varepsilon}_{\hat{N}_1}$ is obtained through the coordinate transformation

$$\begin{bmatrix}\tilde{\varepsilon}_{\hat{N}_1}\\ \tilde{\varepsilon}_{\hat{N}_2}\end{bmatrix} = \boldsymbol{R}\begin{bmatrix}\varepsilon_{\hat{N}_1}\\ \varepsilon_{\hat{N}_2}\end{bmatrix} \quad \text{with} \quad \boldsymbol{R} = \begin{bmatrix}\mu_{11} & \mu_{12}\\ \mu_{21} & \mu_{22}\end{bmatrix}. \tag{3.55}$$

As only $\boldsymbol{\mu} = [\mu_{11},\ \mu_{12}]^T$ affects $\tilde{\varepsilon}_{\hat{N}_1}$, the minimization over $\boldsymbol{R}$ simplifies to

$$\min_{\boldsymbol{\mu}}\left(\sigma^2_{\tilde{\varepsilon}_{\hat{N}_1}}\right) = \min_{\boldsymbol{\mu}}\left(\boldsymbol{\mu}^T\boldsymbol{\Sigma}_{\hat{N}}\boldsymbol{\mu}\right) \quad \text{s. t.} \quad \boldsymbol{\mu}^T\boldsymbol{\mu} = 1, \tag{3.56}$$

where the constraint is a property of $\boldsymbol{R}$. Eq. (3.56) can be rewritten as a Lagrange optimization:

$$\min_{\boldsymbol{\mu}}\left(\boldsymbol{\mu}^T\boldsymbol{\Sigma}_{\hat{N}}\boldsymbol{\mu} - \lambda\left(\boldsymbol{\mu}^T\boldsymbol{\mu} - 1\right)\right), \tag{3.57}$$

with the Lagrange multiplier λ. Setting the derivative w.r.t. $\boldsymbol{\mu}$ equal to zero yields

$$\boldsymbol{\Sigma}_{\hat{N}}\boldsymbol{\mu} = \lambda\boldsymbol{\mu} \quad \Rightarrow \quad \sigma^2_{\tilde{\varepsilon}_{\hat{N}_1}} = \lambda = \boldsymbol{\mu}^T\boldsymbol{\Sigma}_{\hat{N}}\boldsymbol{\mu} \tag{3.58}$$

which is the classical eigenvalue problem. The lower eigenvalue of $\boldsymbol{\Sigma}_{\hat{N}}$ is given by

$$\lambda = \frac{1}{2}(\sigma^2_{\hat{N}_1} + \sigma^2_{\hat{N}_2}) - \frac{1}{2}\sqrt{\left(\sigma^2_{\hat{N}_1} + \sigma^2_{\hat{N}_2}\right)^2 - 4\left(\sigma^2_{\hat{N}_1}\sigma^2_{\hat{N}_2} - \rho^2\sigma^2_{\hat{N}_1}\sigma^2_{\hat{N}_2}\right)}, \tag{3.59}$$

which has its minimum for $\rho = 0$ and, thus, concludes the proof. Note that this equivalent to minimizing the probability density at the coordinate center:

$$\partial/\partial\rho\left(P\left(\varepsilon_{\hat{N}_1} = 0, \varepsilon_{\hat{N}_2} = 0\right)\right) = 0. \tag{3.60}$$

3.1.2 Sequential ambiguity fixing

Blewitt suggested a sequential ambiguity fixing (also called bootstrapping) in [58]. This conditional fixing corrects for the difference between float and fixed ambiguities, i.e. the second conditional ambiguity is given by

$$\hat{N}_{2|1} = \hat{N}_2 - \gamma \cdot (\hat{N}_1 - [\hat{N}_1]), \tag{3.61}$$

where $[\cdot]$ denotes the rounding and γ is chosen such that the uncertainty about $\hat{N}_{2|1}$ is minimized (e.g. Teunissen [59]):

$$\min_{\gamma} \sigma_{\hat{N}_{2|1}}. \tag{3.62}$$

All currently known sequential fixing methods assume a correct rounding of $\hat{N}_1$ for the computation of γ. However, this is not always fulfilled. Therefore, the rounding has to be evaluated which is computationally also feasible. The solution of (3.62) is given by

$$\gamma_{\text{opt}} = \frac{\sigma_{\hat{N}_1\hat{N}_2} - \sigma_{[\hat{N}_1]\hat{N}_2}}{\sigma^2_{\hat{N}_1} - 2\sigma_{\hat{N}_1[\hat{N}_1]} + \sigma^2_{[\hat{N}_1]}}, \tag{3.63}$$

which requires the evaluation of the pseudo-covariances $\sigma_{[\hat{N}_1][\hat{N}_1]}$, $\sigma_{[\hat{N}_1]\hat{N}_1}$ and $\sigma_{[\hat{N}_1]\hat{N}_2}$. Let us introduce $\varepsilon_{\hat{N}_1} = \hat{N}_1 - N_1$ and $\varepsilon_{\hat{N}_2} = \hat{N}_2 - N_2$ with the Gaussian probability distributions $f(\varepsilon_{\hat{N}_1})$, $f(\varepsilon_{\hat{N}_2})$ and $f(\varepsilon_{\hat{N}_1}, \varepsilon_{\hat{N}_2})$, then the three pseudo-covariances are given by

$$\begin{aligned}
\sigma_{\hat{N}_1[\hat{N}_1]} &= \int_{-\infty}^{\infty} \varepsilon_{\hat{N}_1}[\varepsilon_{\hat{N}_1}] f(\varepsilon_{\hat{N}_1}) d\varepsilon_{\hat{N}_1} \\
&= \sum_{k=-\infty}^{\infty} k \int_{k-0.5}^{k+0.5} \varepsilon_{\hat{N}_1} f(\varepsilon_{\hat{N}_1}) d\varepsilon_{\hat{N}_1} = \frac{1}{\sqrt{2\pi}} \sum_{k=-\infty}^{\infty} k\sigma_{\hat{N}_1} \left(e^{-\frac{(k-0.5)^2}{2\sigma^2_{\hat{N}_1}}} - e^{-\frac{(k+0.5)^2}{2\sigma^2_{\hat{N}_1}}} \right) \\
\sigma^2_{[\hat{N}_1]} &= \int_{-\infty}^{\infty} \left([\varepsilon_{\hat{N}_1}] \right)^2 f(\varepsilon_{\hat{N}_1}) d\varepsilon_{\hat{N}_1} = \sum_{k=-\infty}^{\infty} k^2 \cdot \int_{k-0.5}^{k+0.5} f(\varepsilon_{\hat{N}_1}) d\varepsilon_{\hat{N}_1} \\
&= \sum_{k=-\infty}^{\infty} k^2 \cdot \left(\Phi\left(\frac{k+0.5}{\sigma_{\hat{N}_1}} \right) - \Phi\left(\frac{k-0.5}{\sigma_{\hat{N}_1}} \right) \right) \qquad (3.64) \\
\sigma_{[\hat{N}_1]\hat{N}_2} &= \int_{-\infty}^{\infty} \int_{-\infty}^{\infty} [\varepsilon_{\hat{N}_1}] \varepsilon_{\hat{N}_2} f(\varepsilon_{\hat{N}_1}, \varepsilon_{\hat{N}_2}) d\varepsilon_{\hat{N}_1} d\varepsilon_{\hat{N}_2} \\
&= \sum_{k=-\infty}^{\infty} k \cdot \int_{k-0.5}^{k+0.5} \int_{-\infty}^{\infty} \varepsilon_{\hat{N}_2} f(\varepsilon_{\hat{N}_1}, \varepsilon_{\hat{N}_2}) d\varepsilon_{\hat{N}_1} d\varepsilon_{\hat{N}_2}. \qquad (3.65)
\end{aligned}$$

The inner integration with the joint probability density $f(\varepsilon_{\hat{N}_1}, \varepsilon_{\hat{N}_2})$ is given by

$$\int_{-\infty}^{\infty} \varepsilon_{\hat{N}_2} f(\varepsilon_{\hat{N}_1}, \varepsilon_{\hat{N}_2}) d\varepsilon_{\hat{N}_2} = \int_{-\infty}^{\infty} \varepsilon_{\hat{N}_2} \frac{1}{2\pi\sqrt{|\boldsymbol{\Sigma}|}} \exp\left(-\frac{1}{2} \begin{bmatrix} \varepsilon_{\hat{N}_1} \\ \varepsilon_{\hat{N}_2} \end{bmatrix}^T \boldsymbol{\Sigma}^{-1} \begin{bmatrix} \varepsilon_{\hat{N}_1} \\ \varepsilon_{\hat{N}_2} \end{bmatrix} \right) d\varepsilon_{\hat{N}_2}, \tag{3.66}$$

with

$$\mathbf{\Sigma} = \begin{bmatrix} \sigma^2_{\hat{N}_1} & \sigma_{\hat{N}_1\hat{N}_2} \\ \sigma_{\hat{N}_1\hat{N}_2} & \sigma^2_{\hat{N}_2} \end{bmatrix}. \tag{3.67}$$

Expanding the exponent and rearranging yields

$$\begin{aligned}
\int_{-\infty}^{\infty} \varepsilon_{\hat{N}_2} f(\varepsilon_{\hat{N}_1}, \varepsilon_{\hat{N}_2}) d\varepsilon_{\hat{N}_2} &= \int_{-\infty}^{\infty} \varepsilon_{\hat{N}_2} \frac{1}{2\pi\sqrt{|\mathbf{\Sigma}|}} e^{-\frac{1}{2|\mathbf{\Sigma}|}\left(\varepsilon^2_{\hat{N}_1}\sigma^2_{\hat{N}_2} - 2\sigma_{\hat{N}_1\hat{N}_2}\varepsilon_{\hat{N}_1}\varepsilon_{\hat{N}_2} + \varepsilon^2_{\hat{N}_2}\sigma^2_{\hat{N}_1}\right)} d\varepsilon_{\hat{N}_2} \\
&= \int_{-\infty}^{\infty} \varepsilon_{\hat{N}_2} \frac{1}{2\pi\sqrt{|\mathbf{\Sigma}|}} e^{-\frac{\sigma^2_{\hat{N}_1}}{2|\mathbf{\Sigma}|}\left(\varepsilon_{\hat{N}_2} - \frac{\sigma_{\hat{N}_1\hat{N}_2}}{\sigma^2_{\hat{N}_1}}\varepsilon_{\hat{N}_1}\right)^2 + \frac{\sigma^2_{\hat{N}_1}}{2|\mathbf{\Sigma}|}\cdot\frac{\sigma^2_{\hat{N}_1\hat{N}_2}}{\sigma^4_{\hat{N}_1}}\varepsilon^2_{\hat{N}_1} - \frac{\sigma^2_{\hat{N}_1}}{2|\mathbf{\Sigma}|}\cdot\frac{\sigma^2_{\hat{N}_2}}{\sigma^2_{\hat{N}_1}}\varepsilon^2_{\hat{N}_1}} d\varepsilon_{\hat{N}_2} \\
&= e^{-\frac{\varepsilon^2_{\hat{N}_1}}{2\sigma^2_{\hat{N}_1}}} \cdot \int_{-\infty}^{\infty} \varepsilon_{\hat{N}_2} \frac{1}{2\pi\sqrt{|\mathbf{\Sigma}|}} e^{-\frac{\sigma^2_{\hat{N}_1}}{2|\mathbf{\Sigma}|}\left(\varepsilon_{\hat{N}_2} - \frac{\sigma_{\hat{N}_1\hat{N}_2}}{\sigma^2_{\hat{N}_1}}\varepsilon_{\hat{N}_1}\right)^2} d\varepsilon_{\hat{N}_2} \\
&= \frac{1}{2\pi\sqrt{|\mathbf{\Sigma}|}} e^{-\frac{\varepsilon^2_{\hat{N}_1}}{2\sigma^2_{\hat{N}_1}}} \int_{-\infty}^{\infty} \left(\varepsilon_{\hat{N}_2} - \frac{\sigma_{\hat{N}_1\hat{N}_2}}{\sigma^2_{\hat{N}_1}}\varepsilon_{\hat{N}_1}\right) e^{-\frac{\sigma^2_{\hat{N}_1}}{2|\mathbf{\Sigma}|}\left(\varepsilon_{\hat{N}_2} - \frac{\sigma_{\hat{N}_1\hat{N}_2}}{\sigma^2_{\hat{N}_1}}\varepsilon_{\hat{N}_1}\right)^2} d\varepsilon_{\hat{N}_2} \\
&\quad + \frac{1}{2\pi\sqrt{|\mathbf{\Sigma}|}} e^{-\frac{\varepsilon^2_{\hat{N}_1}}{2\sigma^2_{\hat{N}_1}}} \int_{-\infty}^{\infty} \frac{\sigma_{\hat{N}_1\hat{N}_2}}{\sigma^2_{\hat{N}_1}}\varepsilon_{\hat{N}_1} e^{-\frac{\sigma^2_{\hat{N}_1}}{2|\mathbf{\Sigma}|}\left(\varepsilon_{\hat{N}_2} - \frac{\sigma_{\hat{N}_1\hat{N}_2}}{\sigma^2_{\hat{N}_1}}\varepsilon_{\hat{N}_1}\right)^2} d\varepsilon_{\hat{N}_2}
\end{aligned} \tag{3.68}$$

The first component vanishes and the second one can be simplified by substitution, i.e.

$$\begin{aligned}
\int_{-\infty}^{\infty} \varepsilon_{\hat{N}_2} f(\varepsilon_{\hat{N}_1}, \varepsilon_{\hat{N}_2}) d\varepsilon_{\hat{N}_1} &= \frac{1}{2\pi\sqrt{|\mathbf{\Sigma}|}} e^{-\frac{\varepsilon^2_{\hat{N}_1}}{2\sigma^2_{\hat{N}_1}}} \int_{-\infty}^{\infty} \frac{\sigma_{\hat{N}_1\hat{N}_2}}{\sigma^2_{\hat{N}_1}}\varepsilon_{\hat{N}_1} \sqrt{2\pi\frac{|\mathbf{\Sigma}|}{\sigma^2_{\hat{N}_1}}} \frac{1}{\sqrt{2\pi\frac{|\mathbf{\Sigma}|}{\sigma^2_{\hat{N}_1}}}} e^{-\frac{t^2}{2|\mathbf{\Sigma}|}\sigma^2_{\hat{N}_1}} dt \\
&= \frac{1}{2\pi\sqrt{|\mathbf{\Sigma}|}} e^{-\frac{\varepsilon^2_{\hat{N}_1}}{2\sigma^2_{\hat{N}_1}}} \frac{\sigma_{\hat{N}_1\hat{N}_2}}{\sigma^2_{\hat{N}_1}}\varepsilon_{\hat{N}_1} \sqrt{2\pi\frac{|\mathbf{\Sigma}|}{\sigma^2_{\hat{N}_1}}}.
\end{aligned} \tag{3.69}$$

Thus, $\sigma_{[\hat{N}_1]\hat{N}_2}$ of Eq. (3.65) can be rewritten as

$$\begin{aligned}
\sigma_{[\hat{N}_1]\hat{N}_2} &= \frac{1}{2\pi\sqrt{|\mathbf{\Sigma}|}} \sum_{k=-\infty}^{+\infty} k \int_{k-0.5}^{k+0.5} e^{-\frac{1}{2\sigma^2_{\hat{N}_1}}\varepsilon^2_{\hat{N}_1}} \frac{\sigma_{\hat{N}_1\hat{N}_2}}{\sigma^2_{\hat{N}_1}}\varepsilon_{\hat{N}_1} \sqrt{2\pi\frac{|\mathbf{\Sigma}|}{\sigma^2_{\hat{N}_1}}} d\varepsilon_{\hat{N}_1} \\
&= \frac{1}{2\pi\sqrt{|\mathbf{\Sigma}|}} \frac{\sigma_{\hat{N}_1\hat{N}_2}}{\sigma^2_{\hat{N}_1}} \sqrt{2\pi\frac{|\mathbf{\Sigma}|}{\sigma^2_{\hat{N}_1}}} \sum_{k=-\infty}^{+\infty} k \int_{k-0.5}^{k+0.5} e^{-\frac{1}{2\sigma^2_{\hat{N}_1}}\varepsilon^2_{\hat{N}_1}} \varepsilon_{\hat{N}_1} d\varepsilon_{\hat{N}_1} \\
&= \frac{1}{2\pi\sqrt{|\mathbf{\Sigma}|}} \frac{\sigma_{\hat{N}_1\hat{N}_2}}{\sigma^2_{\hat{N}_1}} \sqrt{2\pi\frac{|\mathbf{\Sigma}|}{\sigma^2_{\hat{N}_1}}} \sum_{k=-\infty}^{+\infty} k \cdot (-\sigma^2_{\hat{N}_1}) \left(e^{-\frac{(k+0.5)^2}{2\sigma^2_{\hat{N}_1}}} - e^{-\frac{(k-0.5)^2}{2\sigma^2_{\hat{N}_1}}} \right) \\
&= -\frac{1}{\sqrt{2\pi\sigma^2_{\hat{N}_1}}} \sigma_{\hat{N}_1\hat{N}_2} \sum_{k=-\infty}^{+\infty} k \left(e^{-\frac{(k+0.5)^2}{2\sigma^2_{\hat{N}_1}}} - e^{-\frac{(k-0.5)^2}{2\sigma^2_{\hat{N}_1}}} \right),
\end{aligned} \tag{3.70}$$

which depends on $\sigma^2_{\hat{N}_1}$ and $\sigma_{\hat{N}_1\hat{N}_2}$ but is independent of $\sigma^2_{\hat{N}_2}$. Clearly, the infinite sum can be well approximated by a finite sum over $|k| \leq 10$.

Fig. 3.1 shows the optimal weighting γ_{opt} of (3.63) as a function of the correlation coefficient $\rho = \frac{\sigma_{\hat{N}_1\hat{N}_2}}{\sigma_{\hat{N}_1} \cdot \sigma_{\hat{N}_2}}$. The additional consideration of the fixing errors in (3.61) results in a smaller weight than the traditional $\gamma = \sigma_{\hat{N}_2\hat{N}_1}\sigma^{-2}_{\hat{N}_1} = \rho$. A lower weight γ turns into a smaller conditional variance $\sigma^2_{\hat{N}_{2|1}}$ and, thus, a lower probability of wrong fixing.

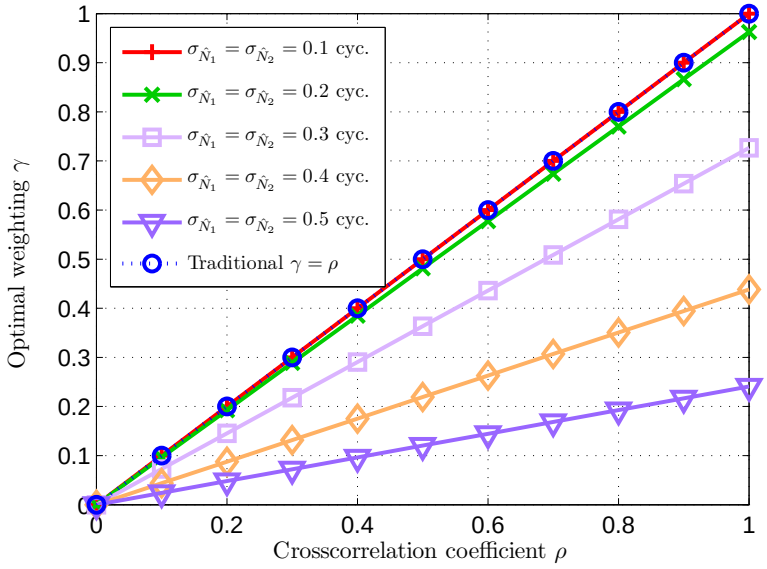

Figure 3.1: Optimal weighting γ_{opt} for bootstrapping: The additional consideration of the fixing errors in $[\hat{N}_1]$ result in a smaller weight than the traditional $\gamma = \sigma_{\hat{N}_2\hat{N}_1}\sigma^{-2}_{\hat{N}_1} = \rho$.

The traditional derivation of the bootstrapped estimator neglects the terms $\sigma_{\varepsilon_{\hat{N}_1}[\varepsilon_{\hat{N}_1}]}$, $\sigma^2_{[\varepsilon_{\hat{N}_1}]}$ and $\sigma_{[\varepsilon_{\hat{N}_1}]\varepsilon_{\hat{N}_2}}$ of (3.64). In this case, the optimum γ simplifies to

$$\gamma = \sigma_{\hat{N}_2\hat{N}_1}\sigma^{-2}_{\hat{N}_1}. \tag{3.71}$$

Replacing γ in (3.61) by (3.71) yields in accordance with Teunissen [60]

$$\hat{N}_{2|1} = \hat{N}_2 - \sigma_{\hat{N}_2\hat{N}_1}\sigma^{-2}_{\hat{N}_1} \cdot (\hat{N}_1 - [\hat{N}_1]), \tag{3.72}$$

which is uncorrelated to $\hat{N}_1$ if $[\hat{N}_1]$ is deterministic, i.e.

$$\sigma_{\hat{N}_1\hat{N}_{2|1}} = 0. \tag{3.73}$$

The variance of $\hat{N}_{2|1}$ is obtained from (3.72) under the assumption of correct rounding as

$$\sigma^2_{\hat{N}_{2|1}} = \sigma^2_{\hat{N}_2} - \sigma^2_{\hat{N}_2\hat{N}_1}\sigma^{-2}_{\hat{N}_1}, \tag{3.74}$$

which is lower than $\sigma^2_{\hat{N}_2}$. Once the second ambiguity is fixed, the third one can be corrected, i.e.

$$\hat{N}_{3|2,1} = \hat{N}_3 - \sigma_{\hat{N}_3\hat{N}_1}\sigma^{-2}_{\hat{N}_1} \cdot (\hat{N}_1 - [\hat{N}_1]) - \sigma_{\hat{N}_3\hat{N}_{2|1}}\sigma^{-2}_{\hat{N}_{2|1}} \cdot (\hat{N}_{2|1} - [\hat{N}_{2|1}]) \tag{3.75}$$

with the conditional variance

$$\sigma^2_{\hat{N}_{3|2,1}} = \sigma^2_{\hat{N}_3} - \sigma^2_{\hat{N}_3\hat{N}_1}\sigma^{-2}_{\hat{N}_1} - \sigma^2_{\hat{N}_3\hat{N}_{2|1}}\sigma^{-2}_{\hat{N}_{2|1}}, \tag{3.76}$$

and the covariance between $\hat{N}_3$ and $\hat{N}_{3|2,1}$ that is obtained from (3.75) as

$$\sigma_{\hat{N}_3\hat{N}_{2|1}} = \sigma_{\hat{N}_3\hat{N}_2} - \sigma_{\hat{N}_2\hat{N}_1}\sigma^{-2}_{\hat{N}_1}\sigma_{\hat{N}_1\hat{N}_3}. \tag{3.77}$$

The sequential adjustment is repeated for the remaining ambiguities, i.e. the k-th conditional ambiguity is given by

$$\hat{N}_{k|1,\ldots,k-1} = \hat{N}_k - \sum_{j=1}^{k-1} \sigma_{\hat{N}_k\hat{N}_{j|1,\ldots,j-1}}\sigma^{-2}_{\hat{N}_{j|1,\ldots,j-1}}(\hat{N}_{j|1,\ldots,j-1} - [\hat{N}_{j|1,\ldots,j-1}]), \tag{3.78}$$

with the conditional variance

$$\sigma^2_{\hat{N}_{k|1,\ldots,k-1}} = \sigma^2_{\hat{N}_k} - \sum_{j=1}^{k-1} \sigma^2_{\hat{N}_k\hat{N}_{j|1,\ldots,j-1}}\sigma^{-2}_{\hat{N}_{j|1,\ldots,j-1}}, \tag{3.79}$$

and the covariance between the unconditional and conditional float ambiguities

$$\sigma_{\hat{N}_k\hat{N}_{j|1,\ldots,j-1}} = \sigma_{\hat{N}_k\hat{N}_j} - \sum_{i=1}^{j-1} \sigma_{\hat{N}_j\hat{N}_{i|1,\ldots,i-1}}\sigma^{-2}_{\hat{N}_{i|1,\ldots,i-1}}\sigma_{\hat{N}_k\hat{N}_{i|1,\ldots,i-1}}. \tag{3.80}$$

Clearly, both the conditional variances and the covariances depend on the order of fixings. It can be shown from (3.78) that the conditional ambiguity estimates are uncorrelated, i.e.

$$\sigma_{\hat{N}_{k|1,\ldots,k-1},\hat{N}_{l|1,\ldots,l-1}} = 0 \quad \forall\, k \neq l \tag{3.81}$$

The k-th fixed (bootstrapped) ambiguity is denoted by

$$\check{N}_{\mathrm{B}_k} = \left[\hat{N}_{k|1,\ldots,k-1}\right], \tag{3.82}$$

which enables us to write (3.78) in matrix-vector notation, i.e.

$$\begin{bmatrix} \hat{N}_1 - \check{N}_{\mathrm{B}_1} \\ \hat{N}_2 - \check{N}_{\mathrm{B}_2} \\ \vdots \\ \hat{N}_K - \check{N}_{\mathrm{B}_K} \end{bmatrix} = \begin{bmatrix} 1 & 0 & \cdots & 0 \\ \sigma_{\hat{N}_2\hat{N}_1}\sigma^{-2}_{\hat{N}_1} & 1 & & \\ \vdots & & \ddots & \vdots \\ \sigma_{\hat{N}_K\hat{N}_1}\sigma^{-2}_{\hat{N}_1} & \sigma_{\hat{N}_K\hat{N}_{2|1}}\sigma^{-2}_{\hat{N}_{2|1}} & \cdots & 1 \end{bmatrix} \cdot \begin{bmatrix} \hat{N}_1 - \check{N}_{\mathrm{B}_1} \\ \hat{N}_{2|1} - \check{N}_{\mathrm{B}_2} \\ \vdots \\ \hat{N}_{K|1,\ldots,K-1} - \check{N}_{\mathrm{B}_K} \end{bmatrix}. \tag{3.83}$$

For fixed $\check{N}_{\mathrm{B}_k}$, the covariance matrix $\boldsymbol{\Sigma}_{\hat{N}}$ can be derived from (3.83) as

$$\boldsymbol{\Sigma}_{\hat{N}} = \boldsymbol{L}\boldsymbol{D}\boldsymbol{L}^T \tag{3.84}$$

with

$$L_{i,j} = \left\{ \begin{array}{l} \sigma_{\hat{N}_i \hat{N}_{j|1,\ldots,j-1}} \sigma^{-2}_{\hat{N}_{j|1,\ldots,j-1}} \\ 1 \\ 0 \end{array} \right\} \quad \text{for} \quad \left\{ \begin{array}{l} i > j \\ i = j \\ i < j \end{array} \right\} \tag{3.85}$$

and the diagonal matrix $\boldsymbol{D}$ with $D_{j,j} = \sigma^2_{\hat{N}_{j|1,\ldots,j-1}}$. For correct $\check{N}_{\mathrm{B}_k}$, Teunissen computed the biases in the conditional ambiguities $\hat{N}_{j|1,\ldots,j-1}$ from the biases in the float ambiguities [56], i.e.

$$\begin{bmatrix} b_{\hat{N}_1} \\ b_{\hat{N}_{2|1}} \\ \vdots \\ b_{\hat{N}_{K|1,\ldots,K-1}} \end{bmatrix} = \boldsymbol{L}^{-1} \begin{bmatrix} b_{\hat{N}_1} \\ b_{\hat{N}_2} \\ \vdots \\ b_{\hat{N}_K} \end{bmatrix}. \tag{3.86}$$

As the conditional variances are uncorrelated, the success rate of sequential ambiguity resolution can be efficiently computed (e.g. Teunissen [61]) as

$$P_{\mathrm{s}} = \prod_{k=1}^{K} \int_{-0.5}^{+0.5} \frac{1}{\sqrt{2\pi\sigma^2_{\hat{N}_{k|1,\ldots,k-1}}}} \cdot \exp\left(-\frac{(\hat{N}_{k|1,\ldots,k-1} - b_{\hat{N}_{k|1,\ldots,k-1}})^2}{2\sigma^2_{\hat{N}_{k|1,\ldots,k-1}}} \right) d\hat{N}_{k|1,\ldots,k-1}. \tag{3.87}$$

The ambiguity resolution can also be described graphically by pull-in regions $S_{\check{N}_k}$ that are defined as the set of float ambiguities which are mapped to $\check{N}_k$, i.e.

$$S_{\check{N}_k} = \left\{ \hat{\boldsymbol{N}} \in \mathbb{R}^K | \check{\boldsymbol{N}}_k = S(\hat{\boldsymbol{N}}) \right\}, \quad \check{\boldsymbol{N}}_k \in \mathbb{Z}^K. \tag{3.88}$$

For bootstrapping, the map S is obtained from (3.83) which can be rewritten as

$$\begin{bmatrix} \varepsilon_{\hat{N}_1} \\ \varepsilon_{\hat{N}_{2|1}} \\ \vdots \\ \varepsilon_{\hat{N}_{K|1,\ldots,K-1}} \end{bmatrix} = \boldsymbol{L}^{-1} \begin{bmatrix} \varepsilon_{\hat{N}_1} \\ \varepsilon_{\hat{N}_2} \\ \vdots \\ \varepsilon_{\hat{N}_K} \end{bmatrix}. \tag{3.89}$$

The conditional errors $\varepsilon_{\hat{N}_{k|1,\ldots,k-1}}$ shall be bounded by $\pm 1/2$ which enables us to write the bootstrapped pull-in regions as

$$S_{\mathrm{B},\check{N}_k} = \left\{ \hat{\boldsymbol{N}} \in \mathbb{R}^K \left| \left| \boldsymbol{c}_i^T \boldsymbol{L}^{-1} \left(\hat{\boldsymbol{N}} - \check{\boldsymbol{N}}_k \right) \right| \leq \frac{1}{2}, \quad i \in \{1, \ldots, K\} \right. \right\}, \quad \check{\boldsymbol{N}}_k \in \mathbb{Z}^K, \tag{3.90}$$

where $\boldsymbol{c}_i$ is a column vector with a 1 at the i-th entry and 0 elsewhere. Eq. (3.90) represents a parallelepiped which is shown for an exemplary two- and three-dimensional covariance matrix in Fig. 3.2. The optimal fixing order is achieved if the orientation of

the ellipsoid corresponds to the orientation of the parallelepiped.

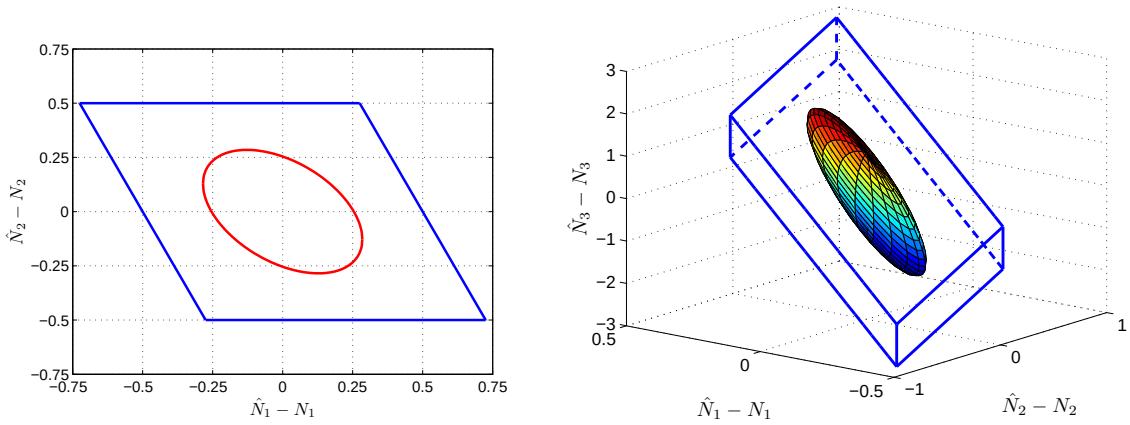

Figure 3.2: Two- and three-dimensional pull-in regions for bootstrapping: The correlation between the float ambiguity estimates results in parallelepiped pull-in regions for an ellipsoidal search space. The optimal fixing order is achieved if the orientation of the parallelepiped corresponds to the orientation of the ellipsoid.

3.1.3 Integer least-squares estimation

The integer least-squares estimate is given by

$$\check{\boldsymbol{N}} = \arg \min_{\boldsymbol{N} \in \mathbb{Z}^K} \left(\hat{\boldsymbol{N}} - \boldsymbol{N} \right)^T \boldsymbol{\Sigma}_{\hat{N}}^{-1} \left(\hat{\boldsymbol{N}} - \boldsymbol{N} \right), \tag{3.91}$$

and efficiently computed by the Least-squares Ambiguity Decorrelation Adjustment (LAMBDA) method of Teunissen in [62] and [63]. The implementation aspects are described by de Jonge and Tiberius in [64]. The LAMBDA method consists of two steps: a grid-preserving ambiguity transformation $\boldsymbol{Z}$ and a search $\mathcal{S}$. Thus, the integer least-squares estimate can be written as

$$\check{\boldsymbol{N}} = \boldsymbol{Z}^{-1} \mathcal{S} \left(\boldsymbol{Z} \hat{\boldsymbol{N}} \right), \tag{3.92}$$

where the back-transformation $\boldsymbol{Z}^{-1}$ has to be integer valued to keep the integer property of the fixed ambiguities. This is the case if $\det(\boldsymbol{Z}) = 1$ and all entries of $\boldsymbol{Z}$ are integer valued. This ambiguity transformation has been introduced by Teunissen for two objectives: the search space shall be decorrelated to improve the efficiency of the search, and, the variance of the first ambiguity shall be minimized as all other conditional ambiguity estimates depend on it. The ambiguity transformation is built from an alternating sequence of integer decorrelations and permutations.

In the first step, the first and second ambiguities are integer decorrelated by

$$\hat{\boldsymbol{N}}_1' = \boldsymbol{Z}_1 \hat{\boldsymbol{N}}, \tag{3.93}$$

with

$$\boldsymbol{Z}_1 = \begin{bmatrix} 1 & 0 & 0 & \cdots \\ -\mu & 1 & 0 & \\ 0 & 0 & 1 & \\ \vdots & & & \ddots \end{bmatrix}, \tag{3.94}$$

where $\mu = [L_{2,1}]$ is computed from the triangular decomposition of (3.84). The covariance matrix becomes

$$\boldsymbol{\Sigma}_{\hat{\boldsymbol{N}}_1'} = \boldsymbol{Z}_1 \boldsymbol{\Sigma}_{\hat{\boldsymbol{N}}} \boldsymbol{Z}_1^T = \boldsymbol{Z}_1 \boldsymbol{L}\boldsymbol{D}\boldsymbol{L}^T \boldsymbol{Z}_1^T = \tilde{\boldsymbol{L}}_1' \boldsymbol{D} \tilde{\boldsymbol{L}}_1'^T. \tag{3.95}$$

Note that the integer decorrelation matrix has the same lower triangular structure as $\boldsymbol{L}$ and, thus, does not change the conditional variances $\sigma_{\hat{N}_{j|1,\ldots,j-1}} = \sqrt{D_{j,j}}$. In the second step, a permutation of the first and second ambiguity is performed if the variance of the first one can be lowered. The permutation matrix is given by

$$\boldsymbol{P}_1 = \begin{bmatrix} 0 & 1 & 0 & \cdots \\ 1 & 0 & 0 & \\ 0 & 0 & 1 & \\ \vdots & & & \ddots \end{bmatrix}, \tag{3.96}$$

and used to permute $\hat{\boldsymbol{N}}_1'$, i.e.

$$\hat{\boldsymbol{N}}_1 = \boldsymbol{P}_1 \hat{\boldsymbol{N}}_1' = \boldsymbol{P}_1 \boldsymbol{Z}_1 \hat{\boldsymbol{N}}. \tag{3.97}$$

The covariance matrix of the permuted ambiguities is given by

$$\boldsymbol{\Sigma}_{\hat{\boldsymbol{N}}_1} = \boldsymbol{P}_1 \boldsymbol{\Sigma}_{\hat{\boldsymbol{N}}_1'} \boldsymbol{P}_1^T = \boldsymbol{P}_1 \tilde{\boldsymbol{L}}_1' \boldsymbol{D} \tilde{\boldsymbol{L}}_1'^T \boldsymbol{P}_1^T = \tilde{\boldsymbol{L}}_1 \tilde{\boldsymbol{D}}_1 \tilde{\boldsymbol{L}}_1^T, \tag{3.98}$$

i.e. the permutation changes both $\tilde{\boldsymbol{L}}_1'$ and $\boldsymbol{D}$ as $\boldsymbol{P}_1$ is not a lower triangular matrix. If the reordering was successful (i.e. it reduces the variance of the first ambiguity), the permuted ambiguities are again decorrelated. Otherwise, the second and third ambiguity are decorrelated and swapped if the conditional variance of the second one can be lowered.

These alternating decorrelations and permutations are repeated until no further permutation is possible. The transformed ambiguities are given by

$$\hat{\boldsymbol{N}}_{\Theta_{\text{it}}} = \boldsymbol{Z}\hat{\boldsymbol{N}} = \left(\prod_{\theta_{\text{it}}=1}^{\Theta_{\text{it}}} \boldsymbol{P}_{\Theta_{\text{it}}-(\theta_{\text{it}}-1)} \boldsymbol{Z}_{\Theta_{\text{it}}-(\theta_{\text{it}}-1)} \right) \hat{\boldsymbol{N}}, \tag{3.99}$$

where Θ_{it} denotes the number of iterations. Note that in each iteration, admissible permutations are only swaps between ambiguities i and $i+1$. This constraint might prevent an order which minimizes the variance of the first ambiguity or minimizes the correlation. However, the degradation is small and there is the benefit of a substantially reduced computational burden.

Once the ambiguities are decorrelated, a search of $\boldsymbol{N}$ is performed, i.e.

$$\left(\hat{\boldsymbol{N}}_{\Theta_{\mathrm{it}}} - \boldsymbol{N}\right)^T \boldsymbol{\Sigma}^{-1}_{\hat{\boldsymbol{N}}_{\Theta_{\mathrm{it}}}} \left(\hat{\boldsymbol{N}}_{\Theta_{\mathrm{it}}} - \boldsymbol{N}\right) \leq \chi^2, \tag{3.100}$$

where χ denotes a threshold on the quadratic error. The further analysis of the search is always based on decorrelated measurements such that the notation can be simplified by omitting the index Θ_{it}. The inverse covariance matrix $\boldsymbol{\Sigma}^{-1}_{\hat{\boldsymbol{N}}}$ is decomposed into

$$\boldsymbol{\Sigma}^{-1}_{\hat{\boldsymbol{N}}} = \boldsymbol{L}^T \boldsymbol{D} \boldsymbol{L} \tag{3.101}$$

to rewrite (3.100) as

$$\sum_{i=1}^{K} D_{i,i} \left(\left(\hat{N}_i - N_i\right) + \sum_{j=1}^{i-1} L_{i,j} \left(\hat{N}_j - N_j\right) \right)^2 \leq \chi^2. \tag{3.102}$$

Inversion of (3.101) yields

$$\boldsymbol{\Sigma}_{\hat{\boldsymbol{N}}} = \tilde{\boldsymbol{L}} \tilde{\boldsymbol{D}} \tilde{\boldsymbol{L}}^T \quad \text{with} \quad \tilde{\boldsymbol{L}} = \boldsymbol{L}^{-1} \quad \text{and} \quad \tilde{\boldsymbol{D}} = \boldsymbol{D}^{-1}, \tag{3.103}$$

where $D^{-1}_{i,i} = \sigma^2_{\hat{N}_{i|1,\ldots,i-1}}$ can be interpreted with (3.83) and (3.84) as conditional variance. Solving (3.83) for $\hat{N}_{i|1,\ldots,i-1}$ gives

$$\begin{bmatrix} \hat{N}_1 \\ \hat{N}_{2|1} \\ \vdots \\ \hat{N}_{K|1,\ldots,K-1} \end{bmatrix} = \boldsymbol{L}^{-1} \begin{bmatrix} \hat{N}_1 - \check{N}_{\mathrm{B}_1} \\ \hat{N}_2 - \check{N}_{\mathrm{B}_2} \\ \vdots \\ \hat{N}_K - \check{N}_{\mathrm{B}_K} \end{bmatrix} + \begin{bmatrix} \check{N}_{\mathrm{B}_1} \\ \check{N}_{\mathrm{B}_2} \\ \vdots \\ \check{N}_{\mathrm{B}_K} \end{bmatrix}. \tag{3.104}$$

Thus, the search of (3.102) can be rewritten as sequential conditional adjustment:

$$\sum_{i=1}^{K} \frac{\left(N_i - \hat{N}_{i|1,\ldots,i-1}\right)^2}{\sigma^2_{\hat{N}_{i|1,\ldots,i-1}}} \leq \chi^2. \tag{3.105}$$

Rearranging this inequality gives

$$\begin{aligned} \frac{\left(N_i - \hat{N}_{i|1,\ldots,i-1}\right)^2}{\sigma^2_{\hat{N}_{i|1,\ldots,i-1}}} &\leq \chi^2 - \sum_{l=1}^{i-1} \frac{\left(N_l - \hat{N}_{l|1,\ldots,l-1}\right)^2}{\sigma^2_{\hat{N}_{l|1,\ldots,l-1}}} - \sum_{l=i+1}^{K} \frac{\left(N_l - \hat{N}_{l|1,\ldots,l-1}\right)^2}{\sigma^2_{\hat{N}_{l|1,\ldots,l-1}}} \\ &\leq \chi^2 - \sum_{l=1}^{i-1} \frac{\left(N_l - \hat{N}_{l|1,\ldots,l-1}\right)^2}{\sigma^2_{\hat{N}_{l|1,\ldots,l-1}}}, \end{aligned} \tag{3.106}$$

which depends only on the fixed ambiguities $N_1, \ldots N_{i-1}$ and enables a sequential search.

Thus, the candidates of N_i are given by

$$|N_i - \hat{N}_{i|1,\ldots,i-1}| \leq \sigma_{\hat{N}_{i|1,\ldots,i-1}} \sqrt{\chi^2 - \sum_{l=1}^{i-1} \frac{\left(N_l - \hat{N}_{l|1,\ldots,l-1}\right)^2}{\sigma^2_{\hat{N}_{l|1,\ldots,l-1}}}}. \tag{3.107}$$

An efficient way to determine χ is to round the decorrelated ambiguities to their closest integers, compute the error norm $(\hat{\boldsymbol{N}}-\check{\boldsymbol{N}})^T\boldsymbol{\Sigma}^{-1}_{\hat{\boldsymbol{N}}}(\hat{\boldsymbol{N}}-\check{\boldsymbol{N}})$, and use it as χ. This will ensure that the search space includes at least one integer vector. Rounding all ambiguities but one to their closest integers and one to the next nearest integer will ensure that the search space includes at least two candidates. Obviously, the search criterion $\min_{\boldsymbol{N}} \|\hat{\boldsymbol{N}}-\boldsymbol{N}\|^2_{\boldsymbol{\Sigma}^{-1}_{\hat{N}}}$ becomes sub-optimal in the presence of biases. It should be extended to

$$\min_{\boldsymbol{N}} \max_{\boldsymbol{b}_{\hat{N}}} \|\hat{\boldsymbol{N}} - \boldsymbol{N} - \boldsymbol{b}_{\hat{N}}\|^2_{\boldsymbol{\Sigma}^{-1}_{\hat{N}}} \quad \text{s.t.} \quad |b_{\hat{N}^k}| < b_{\max} \quad \forall\, k, \tag{3.108}$$

where $b_{\max}$ is an upper bound on the ambiguity bias. The efficiency of the search depends on the shape of the search space. The eigenvalue decomposition of the covariance matrix of the integer decorrelated ambiguities is given by

$$\boldsymbol{Q}\boldsymbol{\Lambda}\boldsymbol{Q}^T = \boldsymbol{\Sigma}_{\hat{\boldsymbol{N}}}, \tag{3.109}$$

and used to determine the elongation of the search space. It is defined as the ratio between the largest eigenvalue $\lambda_{\max}$ and the smallest eigenvalue $\lambda_{\min}$, i.e.

$$e = \frac{\lambda_{\max}}{\lambda_{\min}}, \tag{3.110}$$

which is reduced by several orders of magnitude by the integer decorrelation transformation. Another parameter of the ellipsoidal search space is its volume which depends on the threshold χ and has been derived by Apostel in [65] as

$$E = \chi^K \cdot \sqrt{|\boldsymbol{Z}\boldsymbol{\Sigma}_{\hat{\boldsymbol{N}}}\boldsymbol{Z}^T|} \cdot V_K = \chi^K \cdot \left(\prod_{i=1}^{K} \sigma_{\hat{N}_{i|1,\ldots,i-1}}\right) \cdot V_K, \tag{3.111}$$

with the volume V_K of the K-dimensional unit sphere given by

$$V_K = \frac{2}{K} \cdot \frac{\pi^{\frac{K}{2}}}{\Gamma(\frac{K}{2})}, \tag{3.112}$$

and the gamma function $\Gamma(x) = \int_0^\infty e^{-t}t^{x-1}dt$ for $x > 0$.

Fig. 3.3 visualizes the benefit of the integer decorrelation transformation for a three-dimensional ambiguity search space. If no decorrelation is applied, the strong correlations in the float solution result in a largely elongated search space and, thus, an inefficient search. This elongation is reduced stepwise by integer approximated decorrelation

transforms which preserve the integer grid and decorrelate the search space. An almost spherical search space is achieved within a few iterations.

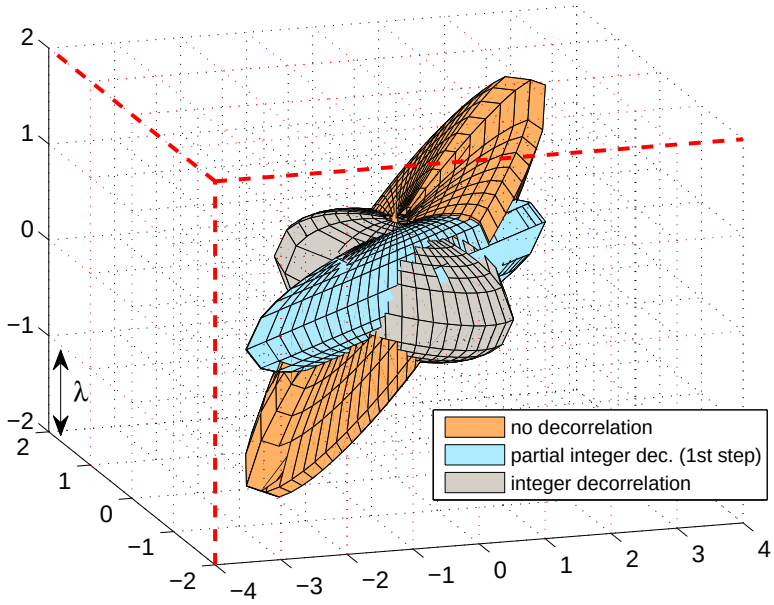

Figure 3.3: Integer ambiguity search space: The strong correlations in the float solution result in a largely elongated search space and, thus, an inefficient search. This elongation is reduced by an integer decorrelation transform which preserves the integer grid and decorrelates the search space.

3.1.4 Integer Aperture estimation

The traditional integer least-squares estimation (e.g. LAMBDA) can be visualized graphically as a mapping of float ambiguities to integer ambiguities according to a map S. The amount of float solutions that are mapped to a common integer vector $\check{\boldsymbol{N}}_k$ form the subset $S_{\check{\boldsymbol{N}}_k}$, i.e.

$$S_{\check{\boldsymbol{N}}_k} = \{\hat{\boldsymbol{N}} \in \mathbb{R}^K | \check{\boldsymbol{N}}_k = S(\hat{\boldsymbol{N}})\}, \quad \check{\boldsymbol{N}}_k \in \mathbb{Z}^K, \tag{3.113}$$

where the subset is also called pull-in region. An integer estimator fulfills the three properties

$$\begin{aligned}
&(1) \quad \bigcup_{\check{\boldsymbol{N}}_k \in \mathbb{Z}^K} S_{\check{\boldsymbol{N}}_k} = \mathbb{R}^K \\
&(2) \quad S_{\check{\boldsymbol{N}}_1} \bigcap S_{\check{\boldsymbol{N}}_2} = \emptyset \quad \forall \{\check{\boldsymbol{N}}_1, \check{\boldsymbol{N}}_2\} \in \mathbb{Z}^K, \check{\boldsymbol{N}}_1 \neq \check{\boldsymbol{N}}_2 \\
&(3) \quad S_{\check{\boldsymbol{N}}_k} = \check{\boldsymbol{N}}_k + S_{\boldsymbol{0}},
\end{aligned} \tag{3.114}$$

where the first constraint ensures that each float vector is mapped to an integer one, the second constraint prevents an overlapping of the pull-in regions, and the third constraint is referred as integer remove-restore technique and enables us to consider only the fractional part. In [66], Teunissen gave up the first constraint to introduce a new

class of integer estimators called Integer Aperture (IA) estimation. It includes integer least-squares estimation as a special case and is defined by the mapping

$$\check{\boldsymbol{N}}(\hat{\boldsymbol{N}}) = \hat{\boldsymbol{N}} + \sum_{\check{\boldsymbol{N}} \in \mathbb{Z}^K} (\check{\boldsymbol{N}} - \hat{\boldsymbol{N}}) \omega_{\check{\boldsymbol{N}}}(\hat{\boldsymbol{N}}), \tag{3.115}$$

where $\omega_{\check{\boldsymbol{N}}}(\hat{\boldsymbol{N}})$ is an indicator function which is 1 if $\hat{\boldsymbol{N}}$ lies in the aperture pull-in region of $\check{\boldsymbol{N}}$ and 0 otherwise.

There are three possible outcomes of an IA estimation: the correct integer solution, a wrong integer solution, and a float solution. The latter one is chosen if a fixing can not be performed reliably enough. The ellipsoidal IA (EIA) estimator of Verhagen [67] uses ellipsoidal pull-in regions that are given by

$$S_{\check{\boldsymbol{N}}_k} = \{\hat{\boldsymbol{N}} \in \mathbb{R}^K | \, \|\hat{\boldsymbol{N}} - \check{\boldsymbol{N}}_k\|^2_{\boldsymbol{\Sigma}^{-1}_{\hat{\boldsymbol{N}}}} \leq \mu^2\}, \quad \forall \, \check{\boldsymbol{N}}_k \in \mathbb{Z}^K, \tag{3.116}$$

where μ denotes the threshold used for hypothesis testing. As the squared norm of Gaussian distributed errors is χ^2 distributed, the EIA probabilities of failure, success and undecided fixing can be efficiently computed [67]:

$$P_{\mathrm{w}} = \sum_{\check{\boldsymbol{N}}_k \in \mathbb{Z}^K \setminus \{\boldsymbol{N}\}} P\left(\|\hat{\boldsymbol{N}} - \check{\boldsymbol{N}}_k\|^2_{\boldsymbol{\Sigma}^{-1}_{\hat{\boldsymbol{N}}}} \leq \mu^2\right) = \sum_{\check{\boldsymbol{N}}_k \in \mathbb{Z}^K \setminus \{\boldsymbol{N}\}} \int_0^{\mu^2} P_{\chi^2(K, \lambda_{\check{\boldsymbol{N}}_k})}(x) dx \tag{3.117}$$

and

$$\begin{aligned} P_{\mathrm{s}} &= \int_0^{\mu^2} P_{\chi^2(K,0)}(x) dx \\ P_{\mathrm{u}} &= 1 - P_{\mathrm{s}} - P_{\mathrm{w}}, \end{aligned} \tag{3.118}$$

where $P_{\chi^2(K, \lambda_{\check{\boldsymbol{N}}_k})}(x)$ denotes the non-central χ^2 distribution with K degrees of freedom and non-centrality parameter $\lambda_{\check{\boldsymbol{N}}_k} = \|\check{\boldsymbol{N}}_k - \boldsymbol{N}\|^2_{\boldsymbol{\Sigma}^{-1}_{\hat{\boldsymbol{N}}}}$.

Fig. 3.4 shows the pull-in regions for the integer least-squares and ellipsoidal IA estimators. The additional hypothesis of undecided ambiguities reduces the probability of wrong fixing at the price of a lower probability of correct fixing. The failure rate can be controlled by the choice of μ. The hexagonal shape of the pull in region for the ILS estimation can be obtained by equating the norm of two neighbored pull-in regions, i.e.

$$\left[\begin{array}{c} \hat{N}_1 - N_1 \\ \hat{N}_2 - N_2 \end{array} \right]^2_{\boldsymbol{\Sigma}^{-1}_{\hat{N}}} = \left[\begin{array}{c} \hat{N}_1 - (N_1 + k) \\ \hat{N}_2 - (N_2 + l) \end{array} \right]^2_{\boldsymbol{\Sigma}^{-1}_{\hat{N}}}, \tag{3.119}$$

which can be simplified to

$$(\hat{N}_1 - N_1)(k\sigma^2_{\hat{N}_2} - l\sigma_{\hat{N}_{12}}) + (\hat{N}_2 - N_2)(l\sigma^2_{\hat{N}_1} - k\sigma_{\hat{N}_{12}}) - \frac{1}{2}(k^2\sigma^2_{\hat{N}_2} - 2kl\sigma_{\hat{N}_{12}} + l^2\sigma^2_{\hat{N}_1}) = 0, \tag{3.120}$$

and represents a linear equation.

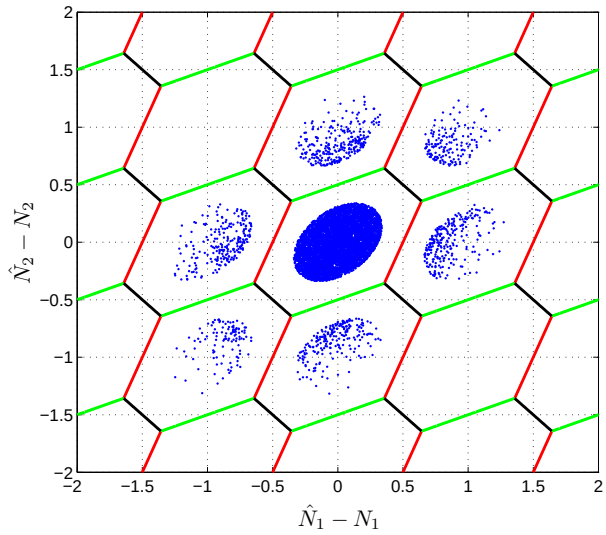

Figure 3.4: Integer Aperture Estimation: A float solution is mapped either to the correct integer vector, to a wrong integer vector, or it is kept as float solution if a decision is not reliably enough. Therefore, the aperture pull-in regions do not cover the complete search space. A mapping to an integer solution is performed only if $\|\hat{\boldsymbol{N}} - \check{\boldsymbol{N}}\|^2_{\boldsymbol{\Sigma}_{\hat{\boldsymbol{N}}}^{-1}} \leq \mu^2$. The probability of wrong fixing is lower than for integer least-squares estimation.

3.1.5 Baseline constrained ambiguity resolution

The reliability of ambiguity resolution can be further improved by some a priori information, e.g. the baseline length $l = \|\boldsymbol{\xi}\|_{I_3}$. The constrained integer least-squares problem has been formulated by Teunissen in [68] as

$$\min_{\boldsymbol{\xi},\boldsymbol{N}} \|\boldsymbol{\Psi} - \boldsymbol{H}\boldsymbol{\xi} - \boldsymbol{A}\boldsymbol{N}\|^2_{\boldsymbol{\Sigma}^{-1}}, \quad \boldsymbol{\xi} \in \mathbb{R}^3, \quad \boldsymbol{N} \in \mathbb{Z}^K, \quad \text{s.t.} \quad \|\boldsymbol{\xi}\|_{I_3} = l. \tag{3.121}$$

The baseline is reparametrized in spherical coordinates, i.e.

$$\boldsymbol{\xi}(\gamma) = l \begin{bmatrix} \cos(\alpha)\cos(\beta) \\ \cos(\alpha)\sin(\beta) \\ \sin(\alpha) \end{bmatrix} \quad \text{with} \quad \boldsymbol{\gamma} = \begin{bmatrix} \alpha \\ \beta \end{bmatrix}, \tag{3.122}$$

which allows to transform the constrained integer least-squares problem in an unconstrained one, i.e.

$$\min_{\boldsymbol{\gamma},\boldsymbol{N}} \|\boldsymbol{\Psi} - \boldsymbol{H}\boldsymbol{\xi}(\boldsymbol{\gamma}) - \boldsymbol{A}\boldsymbol{N}\|^2_{\boldsymbol{\Sigma}^{-1}}, \quad \boldsymbol{\gamma} \in \mathbb{R}^2, \quad \boldsymbol{N} \in \mathbb{Z}^K, \tag{3.123}$$

which is nonlinear in $\boldsymbol{\gamma}$. A linearization of the baseline vector with respect to some approximate angles $\boldsymbol{\gamma}_0 = [\alpha_0,\ \beta_0]^T$ gives

$$\boldsymbol{\xi}(\boldsymbol{\gamma}) = \boldsymbol{\xi}(\boldsymbol{\gamma}_0) + \boldsymbol{C}(\gamma_0)\boldsymbol{\Delta\gamma}, \tag{3.124}$$

with

$$\boldsymbol{C}(\boldsymbol{\gamma}_0) = l \cdot \begin{bmatrix} -\sin(\alpha_0)\cos(\beta_0) & -\cos(\alpha_0)\sin(\beta_0) \\ -\sin(\alpha_0)\sin(\beta_0) & \cos(\alpha_0)\cos(\beta_0) \\ \cos(\alpha_0) & 0 \end{bmatrix}, \tag{3.125}$$

and $\boldsymbol{\Delta\gamma} = \boldsymbol{\gamma} - \boldsymbol{\gamma}_0$. Substituting $\boldsymbol{\xi}(\boldsymbol{\gamma})$ in (3.123) by (3.124) gives an unconstrained, linearized integer least-squares problem:

$$\min_{\boldsymbol{\Delta\gamma},\boldsymbol{N}} \|\boldsymbol{\Delta\Psi} - \boldsymbol{H}\boldsymbol{C}(\boldsymbol{\gamma}_0)\boldsymbol{\Delta\gamma} - \boldsymbol{A}\boldsymbol{N}\|^2_{\boldsymbol{\Sigma}^{-1}}, \quad \boldsymbol{\Delta\gamma} \in \mathbb{R}^2, \quad \boldsymbol{N} \in \mathbb{Z}^K, \tag{3.126}$$

with $\boldsymbol{\Delta\Psi} = \boldsymbol{\Psi} - \boldsymbol{H}\boldsymbol{\xi}(\boldsymbol{\gamma}_0)$. The minimization problem of (3.126) has the same structure as the integer least-squares problem without the baseline a priori information and, thus, can be solved with the Least-squares Ambiguity Decorrelation Adjustment method. The approximate angles $\boldsymbol{\gamma}_0$ can be obtained from an external attitude determination method (IMU) or from the float solution. However, in the latter case, the estimation of $\boldsymbol{\gamma}_0$ requires a large number of epochs for very small baselines.

Alternatively, the constrained integer least-squares problem of (3.121) is rewritten as

$$\min_{\boldsymbol{N}} \left(\|\hat{\boldsymbol{N}} - \boldsymbol{N}\|^2_{\boldsymbol{\Sigma}^{-1}_{\hat{N}}} + \min_{\check{\boldsymbol{\xi}}(\boldsymbol{N}),\|\check{\boldsymbol{\xi}}(\boldsymbol{N})\|=l} \|\hat{\boldsymbol{\xi}}(\boldsymbol{N}) - \check{\boldsymbol{\xi}}(\boldsymbol{N})\|^2_{\boldsymbol{\Sigma}^{-1}_{\hat{\xi}(N)}} \right), \tag{3.127}$$

where the second term can no longer be made to zero due to the baseline constraint. However, it can be rewritten as a Lagrange optimization problem, i.e.

$$f(\lambda) = \left(\hat{\boldsymbol{\xi}}(\boldsymbol{N}) - \check{\boldsymbol{\xi}}(\boldsymbol{N})\right)^T \boldsymbol{\Sigma}^{-1}_{\hat{\boldsymbol{\xi}}(\boldsymbol{N})} \left(\hat{\boldsymbol{\xi}}(\boldsymbol{N}) - \check{\boldsymbol{\xi}}(\boldsymbol{N})\right) + \lambda \cdot (\check{\boldsymbol{\xi}}(\boldsymbol{N})^T\check{\boldsymbol{\xi}}(\boldsymbol{N}) - l^2), \tag{3.128}$$

with the Lagrange multiplier λ. Computing the derivative with respect to $\boldsymbol{\xi}$ gives

$$\check{\boldsymbol{\xi}}(\boldsymbol{N}) = \left(\boldsymbol{\Sigma}^{-1}_{\hat{\boldsymbol{\xi}}(\boldsymbol{N})} - \lambda\mathbf{1}\right)^{-1} \boldsymbol{\Sigma}^{-1}_{\hat{\boldsymbol{\xi}}(\boldsymbol{N})}\hat{\boldsymbol{\xi}}(\boldsymbol{N}), \tag{3.129}$$

and setting it into the constraint $\|\check{\boldsymbol{\xi}}(\boldsymbol{N})\|^2 = l^2$ gives

$$\hat{\boldsymbol{\xi}}^T(\boldsymbol{N})\boldsymbol{\Sigma}^{-1}_{\hat{\boldsymbol{\xi}}(\boldsymbol{N})} \left(\boldsymbol{\Sigma}^{-1}_{\hat{\boldsymbol{\xi}}(\boldsymbol{N})} - \lambda\mathbf{1}\right)^{-1} \left(\boldsymbol{\Sigma}^{-1}_{\hat{\boldsymbol{\xi}}(\boldsymbol{N})} - \lambda\mathbf{1}\right)^{-1} \boldsymbol{\Sigma}^{-1}_{\hat{\boldsymbol{\xi}}(\boldsymbol{N})}\hat{\boldsymbol{\xi}}(\boldsymbol{N}) - l^2 = 0. \tag{3.130}$$

As there does not exist an analytical solution for λ, a line (one-dimensional) search is required. The iterative bisection method is used as it efficiently finds the root of a function without requiring its gradient. The method starts with two candidate solutions with functional values of opposite signs and then converges to a solution by halving the interval in each iteration (Fig. 3.5). The obtained estimate is then used in (3.129) to compute the baseline vector.

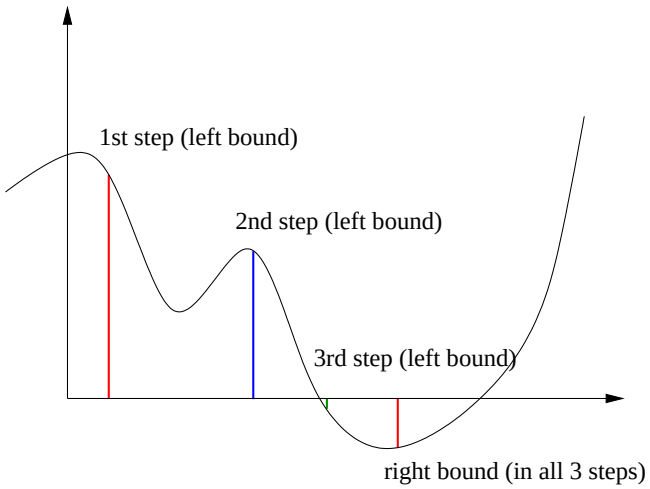

Figure 3.5: Integer least-squares estimation with constrained baseline length: The Lagrange optimization requires the root finding of a nonlinear function. It can be found efficiently by the iterative bisection method which only requires the evaluation of the function. The method starts with two candidate solutions and then converges to a solution by halving the interval in each iteration.

The baseline constrained ambiguity resolution is validated with a Septentrio PolaRx3G receiver that is connected to the institute's Nav NCS Galileo signal simulator of IFEN. Fig. 3.6 shows the measurement equipment, i.e. a notebook on the left side for setting the parameters of receiver location and movement, atmospheric errors, satellite clocks and orbits, etc. The notebook is connected to the signal constellation simulator which provides a high frequency signal that is fed into the Septentrio receiver. The receiver settings and the data logging are done from the small remote PC. In the following analysis, a stationary baseline with a length of 30.583 m was simulated with a standard atmospheric setting, i.e. the Klobuchar model for the ionosphere and the WAAS MOPS model for the troposphere.

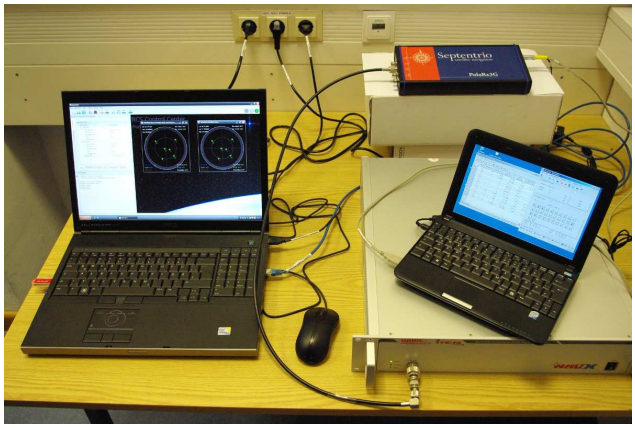

Figure 3.6: Measurement equipment for baseline constrained ambiguity resolution: The NavX NCS Galileo signal simulator of IFEN is connected to the dual frequency PolaRx3G receiver of Septentrio which tracks six Galileo satellites on E1 and E5a. Two different receiver locations are simulated to verify differential integer ambiguity resolution.

Fig. 3.7 shows the achievable accuracy for the estimation of E1-E5a widelane float ambiguities on a single epoch basis. All float ambiguity estimates are close to integers with a noise level varying between one tenth and one third of a cycle. This enables extremely reliable integer ambiguity resolution.

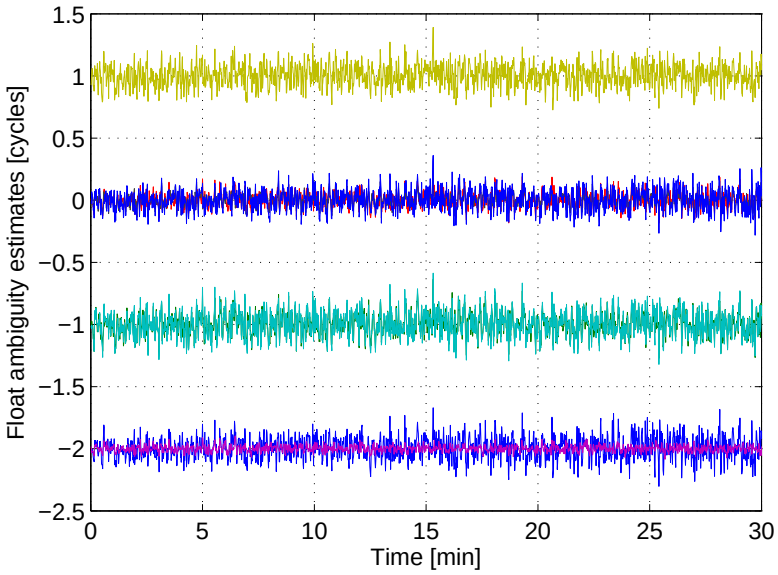

Figure 3.7: Analysis of float ambiguity solution: The baseline and the widelane double difference ambiguities are estimated on a single epoch basis. The E1 and E5a double difference measurements were combined into an ionosphere-free code-only combination and the traditional phase-only widelane combination with a wavelength of 75.1cm. The measurements were generated with the NavX-NCS Galileo signal simulator of IFEN.

Fig. 3.8 shows a comparison of the code-only, the float and the fixed solution of the unconstrained baseline estimation. The large code noise is substantially reduced by the widelane float solution, and further reduced to the millimeter level by the fixed solution. The small bias in the unconstrained fixed solution will be eliminated in the baseline constrained estimation. Fig. 3.9 shows that the ambiguity fixing reduces the range residuals by more than one order of magnitude.

The search of the integer ambiguities is also affected by the baseline constraint, i.e. the integer search space is given by

$$\Omega(\chi^2) = \{\boldsymbol{N} \in \mathbb{Z}^K | \quad \|\hat{\boldsymbol{N}} - \boldsymbol{N}\|^2_{\boldsymbol{\Sigma}^{-1}_{\hat{N}}} + \|\hat{\boldsymbol{\xi}}(\boldsymbol{N}) - \check{\boldsymbol{\xi}}(\boldsymbol{N})\|^2_{\boldsymbol{\Sigma}^{-1}_{\hat{\xi}(N)}} \leq \chi^2\}, \tag{3.131}$$

where $\hat{\boldsymbol{\xi}}(\boldsymbol{N})$ denotes the unconstrained fixed baseline estimate and $\check{\boldsymbol{\xi}}(\boldsymbol{N})$ is the solution of the Lagrange optimization (3.129). Giorgi et al. have extended this baseline constrained integer least-squares estimation to multiple baselines in [69], and observed an additional reduction in the probability of wrong fixing.

It is suggested to perform the search in two steps, i.e. first to search the Ξ integer

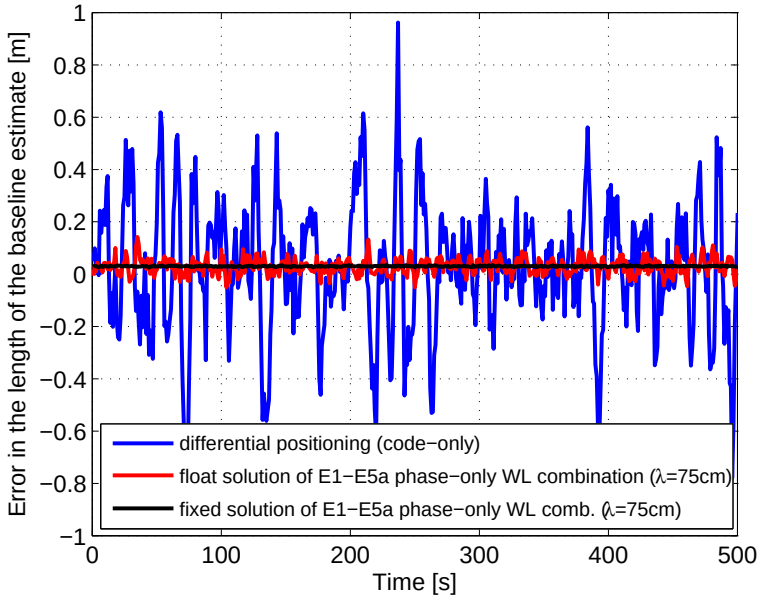

Figure 3.8: Error in length of unconstrained baseline estimation: The code-only solution suffers from the large code noise which is substantially reduced by the widelane float solution. The fixed solution keeps the noise at the millimeter level. The small bias in the unconstrained fixed solution is eliminated in the baseline constrained solution.

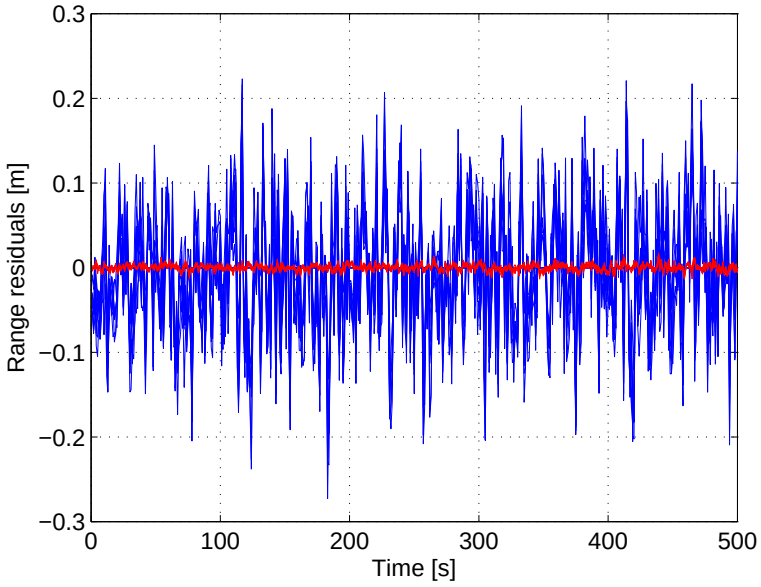

Figure 3.9: Range residuals: The ambiguity fixing reduces the range residuals by more than one order of magnitude.

candidates of lowest $\|\hat{\boldsymbol{N}} - \boldsymbol{N}\|^2_{\boldsymbol{\Sigma}^{-1}_{\hat{N}}}$ and then to select the candidate which minimizes (3.131). The number Ξ of candidates required for the search of the global minimum is

given by the inequality

$$\|\hat{\boldsymbol{N}} - \boldsymbol{N}_\Xi\|^2_{\boldsymbol{\Sigma}^{-1}_{\hat{N}}} \geq \min_{i\in\{1,\ldots,\Xi-1\}} \left(\|\hat{\boldsymbol{N}} - \boldsymbol{N}_i\|^2_{\boldsymbol{\Sigma}^{-1}_{\hat{N}}} + \|\hat{\boldsymbol{\xi}}(\boldsymbol{N}_i) - \check{\boldsymbol{\xi}}(\boldsymbol{N}_i)\|^2_{\boldsymbol{\Sigma}^{-1}_{\hat{\xi}(N)}} \right), \tag{3.132}$$

where the set of integer candidates minimizing the unconstrained error norm is given by $S_{\boldsymbol{\Sigma}_{\hat{N}}} \in \{\boldsymbol{N}_1, \ldots, \boldsymbol{N}_\Xi\}$, with $\boldsymbol{N}_1$ having the lowest and $\boldsymbol{N}_\Xi$ the largest error norm.

In many applications, the length of the baseline is not known exactly. For example, turbulence can change the distance between two receivers on the wings of an aircraft. Therefore, the tightly constrained integer ambiguity resolution shall be replaced by a soft constrained ambiguity resolution for reliable attitude determination. The baseline and integer ambiguities are again determined jointly by minimizing the cost function

$$C(\boldsymbol{N}, \boldsymbol{\xi}) = \|\boldsymbol{\Psi} - \boldsymbol{H}\boldsymbol{\xi} - \boldsymbol{A}\boldsymbol{N}\|^2_{\boldsymbol{\Sigma}^{-1}} + \mu \cdot (\|\boldsymbol{\xi}\| - l)^2, \tag{3.133}$$

where the first term denotes the weighted range residuals and the second term describes the difference between the length of the estimated baseline and its a priori knowledge l. A certain weighting μ was introduced to control the confidence in the a priori knowledge, i.e. a small μ is chosen if one can trust less in l and vice versa. Fig. 3.10 shows a comparison of unconstrained, loosely constrained and tight constrained ambiguity resolution as a function of the a priori information. If it is correct, the tight constraint outperforms the unconstrained fixing by two orders of magnitude. If the a priori information is biased by more than 1 m, the tight constraint results in a poorer performance than the unconstrained fixing but the soft constrained still outperforms it by more than one order of magnitude.

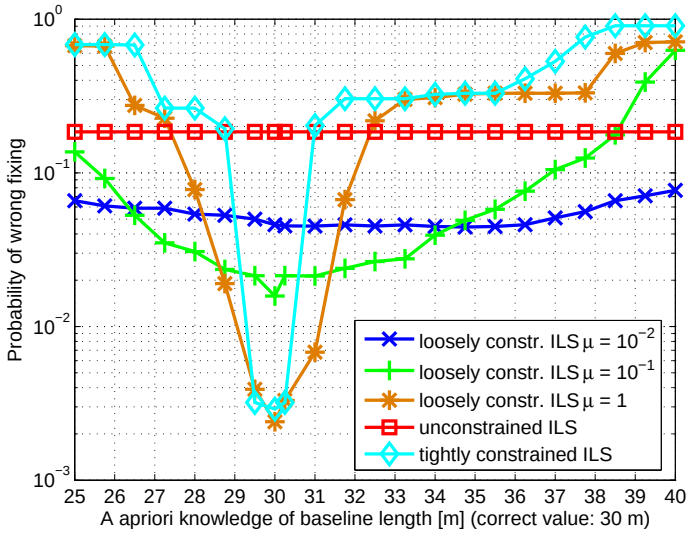

Figure 3.10: Comparison of probability of wrong fixing between unconstrained, loosely and tightly constrained integer least-squares estimation: The tight constraint reduces the unconstrained failure rate by two orders of magnitude if the a priori knowledge is correct. The loose constraint is especially beneficial if the a priori information is erroneous, e.g. it lowers the unconstrained failure rate by one order of magnitude for a 1 m length bias.

3.2 Ambiguity spectrum for multi-frequency combinations

Teunissen showed in [62], [63] and [70] that the conditional standard deviations of the first and last ambiguity differ by several orders of magnitude due to a discontinuity between the third and fourth ambiguity. The spectrum of ambiguities is the graphical representation of the conditional standard deviations $\sigma_{\hat{N}_{k|1,\ldots,k-1}}$ as a function of the ambiguity index k. The discontinuity in the spectrum can be easily explained: Once three ambiguities are fixed, the unknown baseline can be determined with an accuracy that is comparable to the one of carrier phase measurements. This allows us to determine the remaining ambiguities with such a high precision, i.e. the order of magnitude of the remaining conditional standard deviations has to be equal to the one of the carrier phase noise.

In [72], Teunissen et al. analyzed the impact of satellite redundancy, two frequencies, multiple epochs and additional code measurements on the spectrum of ambiguities. The first two extensions do not change the spectrum significantly as each satellite or frequency adds a new ambiguity. A similar observation has been made for the use of additional measurements that have been taken one minute after the first ones: The small change in satellite geometry does not provide sufficient redundancy to improve the spectrum significantly.

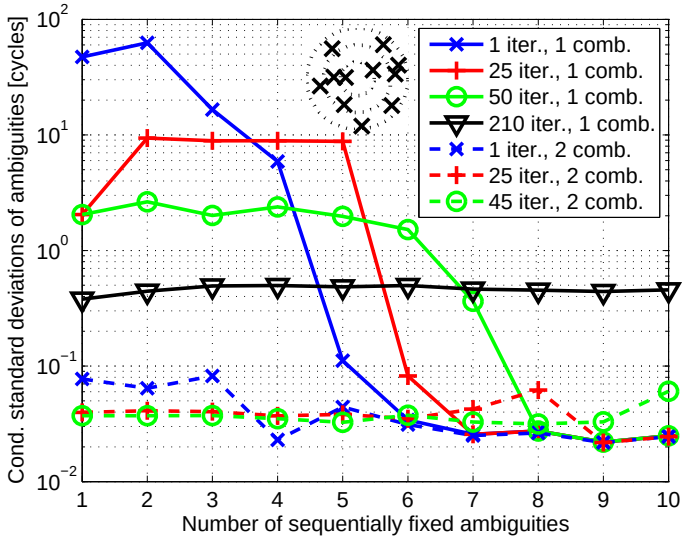

Figure 3.11: Spectrum of ambiguities for precise point positioning: A flat spectrum is achieved by full integer decorrelation. The use of two optimized linear combinations enables an almost flat spectrum even without integer decorrelation. An E1-E5 GP-IF code-carrier combination of maximum discrimination and a code-only combination are computed from satellite-satellite SD measurements of 10 s to estimate the position (once per epoch), ambiguities and tropospheric zenith delay (once per epoch).

Finally, the fourth source of redundancy arises from the code measurements which are

much noisier than the carrier phase measurements. Teunissen et al. assumed a phase noise standard deviation of 3 mm and a code noise standard deviation of 60 cm. This results in an ill-conditioned system of equations which motivated Teunissen to introduce the integer decorrelation transformation to flatten the ambiguity spectrum.

Fig. 3.11 shows a discontinuity by more than two orders of magnitude if no integer decorrelation is used. The GP-IF E1-E5 mixed code-carrier combination of Tab. 2.5 is applied to satellite-satellite SD measurements for precise point positioning [71]. The discontinuity occurs between the 4-th and 5-th ambiguity as the tropospheric zenith delay is estimated in addition to the position. The ambiguity transformation of (3.99) flattens the spectrum within 210 iterations. The use of an additional GP-IF code-only combination enables an almost flat spectrum even without integer decorrelation [45]. Moreover, the code-only combination also reduces the conditional standard deviations by one order of magnitude. This is due to the low code noise of Galileo and the zero-correlation between both combinations which improves the conditioning of the system of equations.

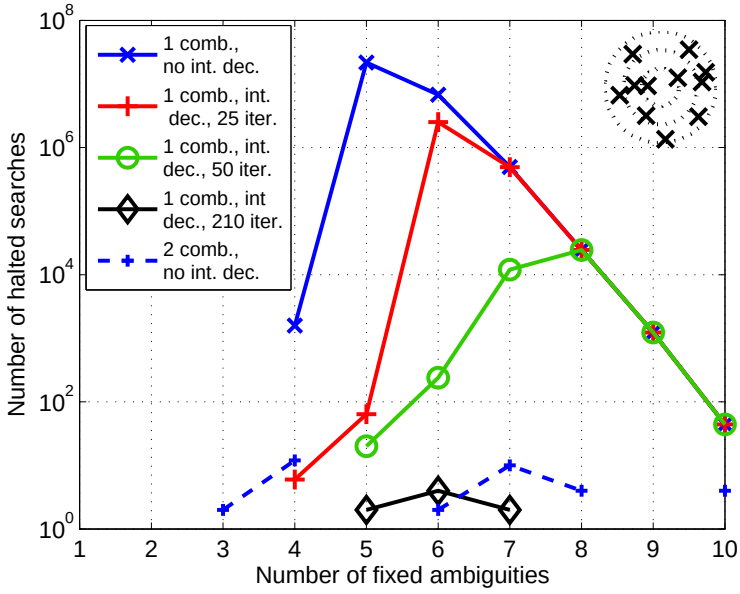

Figure 3.12: Number of halted searches for precise point positioning: The first four ambiguities can be fixed easily due to the four degrees of freedom for position and tropospheric wet zenith delay. The extremely low conditional variances of the fifth and further ambiguities result in frequent halted searches. The flattening of the ambiguity spectrum by integer decorrelation or two linear combinations improves the efficiency dramatically. An E1-E5 GP-IF code-carrier combination of maximum discrimination and a code-only combination of satellite-satellite SD meas. have been considered over 10 s to estimate the position (once per epoch), ambiguities and tropospheric zenith delay (once per epoch).

The discontinuity in the spectrum causes a large elongation of the search space and a large number of halted searches. Fig. 3.12 shows that frequent halts can be avoided either by an integer decorrelation with 210 iterations or a second code-only combination.

3.3 Benefit of multi-frequency linear combinations for ambiguity fixing

The optimized mixed code-carrier widelane combinations of Chapter 2 eliminate the ionosphere and maximize the ambiguity discrimination. The large wavelength of several meters increases the robustness to orbital and clock errors but also results in an increased noise level. If the ambiguities can be resolved without linear combinations, the noise amplification is avoided and a higher positioning accuracy can be expected. However, the estimation of the ionospheric delay is required for each satellite and the small wavelength prevents reliable ambiguity resolution. Moreover, the ambiguity fixing of uncombined measurements is rather sensitive to orbital and clock errors.

Linear combinations enable a trade-off between a higher reliability of ambiguity resolution and a lower positioning accuracy than uncombined carrier phase measurements. Fig. 3.13 shows a comparison of the probability of wrong fixing with and without combinations. The use of two GP-IF E1-E5 combinations (mixed code-carrier comb. of Tab. 2.4 and code-only comb.) results in a probability of wrong fixing of less than 10^{-9} which is more than 9 orders of magnitude lower than in the case of uncombined measurements.

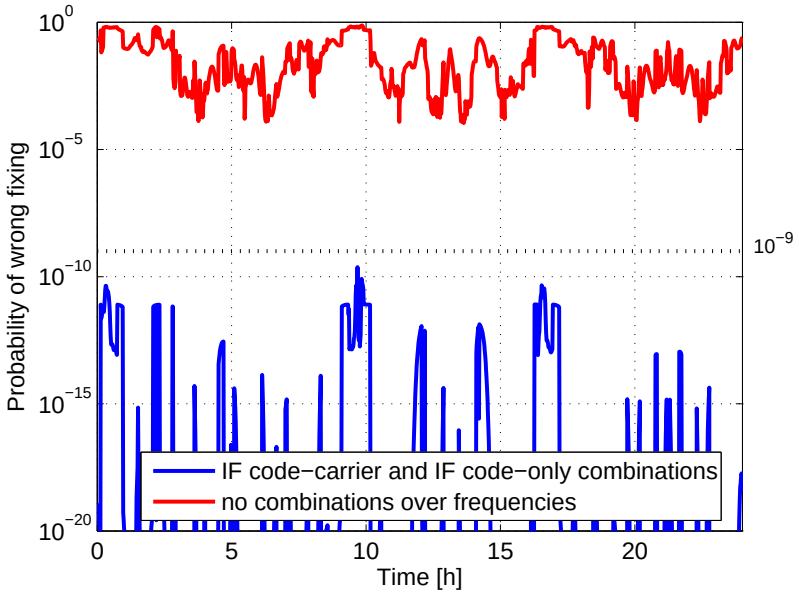

Figure 3.13: Benefit of geometry-preserving, ionosphere-free linear combinations for ambiguity resolution: Double difference measurements on E1 and E5 are considered on 3 consecutive epochs (rate 1 Hz) for Wide-Area RTK. The following parameters are estimated: the baseline (once per epoch), the integer ambiguities (using bootstrapping with integer decorrelation), the tropospheric wet zenith delay (of first epoch), the temporal gradient of the tropospheric wet zenith delay, the ionospheric delays for all satellites (of first epoch), the temporal gradient of ionospheric delays for all satellites. The latter two parameters do not have to be estimated in the case of IF linear combinations.

Double difference measurements have been considered for Wide-Area RTK to eliminate the clock offsets, receiver and satellite biases. The float solution is determined by least-squares estimation of the baseline (once per epoch), the ambiguities, the tropospheric wet zenith delay (of first epoch), the temporal gradient of the tropospheric wet zenith delay, the ionospheric delays for all satellites (of first epoch) and the temporal gradient of ionospheric delays for all satellites. The ambiguities are resolved in both cases with bootstrapping after integer decorrelation.

Fig. 3.14 shows the pull-in regions for the previous RTK scenario at a good satellite geometry. Subfigure (a) refers to the estimation of the E1 integers and subfigure (b) to the widelane ambiguities. Obviously, the increase in wavelength from 19 cm to 3.285 m substantially increases the size of the pull-in regions. Both figures also the include the error ellipse given by $\|\hat{\boldsymbol{N}}-\boldsymbol{N}\|^2_{\boldsymbol{\Sigma}^{-1}_{\hat{N}}}=3$. Its size is larger than the size of the pull-in region for uncombined ambiguities but significantly smaller than the size of the widelane pull-in regions. This is another indication for extremely reliable ambiguity resolution with our linear combinations.

Fig. 3.15 shows the benefit of geometry-free, ionosphere-free (GF-IF) E1-E5b-E5a linear combinations ($j_1=1$, $j_2=-5$, $j_3=4$) over no linear combinations for kinematic differential ambiguity resolution. Receiver-receiver single difference measurements are considered for a baseline of 20 km to suppress the ephemeris errors and to eliminate the satellite clock offsets. The elimination of the range, clock offsets, ionospheric and tropospheric delays improves the robustness over modeling errors. However, the GF-IF condition also means that the satellite redundancy is not taken into account and that the noise level is increased. Ambiguity resolution without linear combinations benefits from the satellite redundancy and the low noise level of the phase measurements but suffers from the small wavelengths and the large number of unknown parameters including the clock offset, ionospheric delays, ionospheric gradients, tropospheric zenith delay and tropospheric zenith delay gradient. The probability of wrong fixing using GF-IF combinations shows negligible temporal variations as it depends only on the number of satellites and the assumed noise statistics. The lowest error rate is achieved for the minimum number of visible satellites. If no linear combinations are used, an opposite behavior can be observed: The probability of wrong fixing (using bootstrapping with integer decorrelation) varies by more than 10 orders of magnitude with the highest values for a poor satellite geometry.

For precise point positioning, multipath, orbital errors and especially satellite clock offsets limit the reliability of ambiguity resolution. The biases in the conditional decorrelated ambiguity estimates are obtained from (3.15), (3.99) and (3.86) as

$$\begin{bmatrix} b_{\hat{N}_1} \\ b_{\hat{N}_{2|1}} \\ \vdots \\ b_{\hat{N}_{K|1,\ldots,K-1}} \end{bmatrix} = \boldsymbol{L}^{-1}\boldsymbol{Z}(\overline{\boldsymbol{A}}^T\boldsymbol{\Sigma}^{-1}\overline{\boldsymbol{A}})^{-1}\overline{\boldsymbol{A}}^T\boldsymbol{\Sigma}^{-1}\begin{bmatrix} \boldsymbol{b}^{(1)} \\ \boldsymbol{b}^{(2)} \end{bmatrix}, \tag{3.134}$$

where $\boldsymbol{b}^{(1)}$ denotes the biases for the code-carrier combinations and $\boldsymbol{b}^{(2)}$ the biases for the

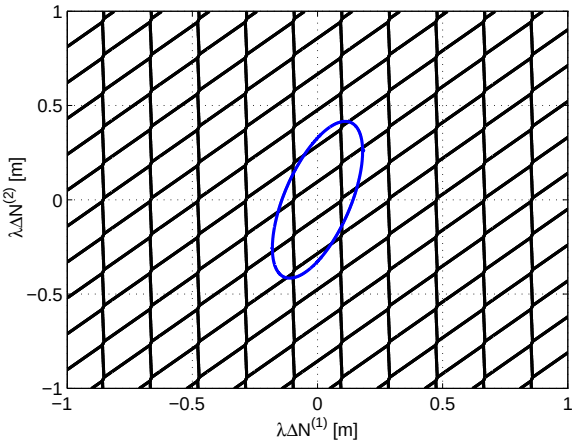

(a) E1 pull-in regions with $\lambda = 19.0$ cm

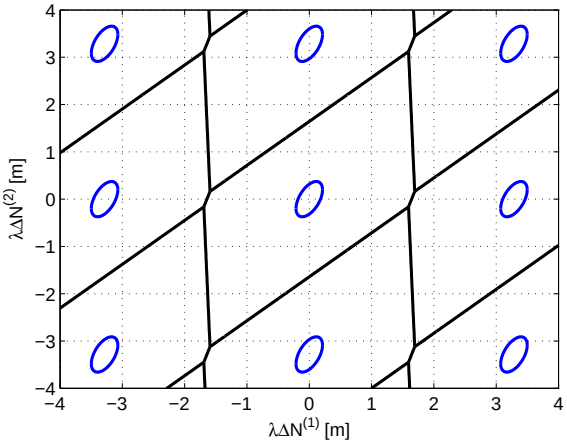

(b) Widelane pull-in regions with $\lambda = 3.285$ m

Figure 3.14: Increase of pull-in regions with multi-frequency linear combinations

code-only combinations. Both bias vectors can be split into orbital errors, satellite clock offsets and satellite hardware biases, i.e.

$$\begin{aligned}
\boldsymbol{b}^{(1)} &= \begin{bmatrix} (\boldsymbol{e}^{1,T}\delta\boldsymbol{x}^1 - \boldsymbol{e}^{2,T}\delta\boldsymbol{x}^2) - c\Delta\delta\tau^{12} \\ \vdots \\ (\boldsymbol{e}^{1,T}\delta\boldsymbol{x}^1 - \boldsymbol{e}^{K,T}\delta\boldsymbol{x}^K) - c\Delta\delta\tau^{1K} \end{bmatrix} + \begin{bmatrix} \sum_{m=1}^{M} \left(\alpha_m\lambda_m\Delta b_{\phi_m}^{12} + \beta_m\Delta b_{\rho_m}^{12}\right) \\ \vdots \\ \sum_{m=1}^{M} \left(\alpha_m\lambda_m\Delta b_{\phi_m}^{1K} + \beta_m\Delta b_{\rho_m}^{1K}\right) \end{bmatrix} \\
\boldsymbol{b}^{(2)} &= \begin{bmatrix} (\boldsymbol{e}^{1,T}\delta\boldsymbol{x}^1 - \boldsymbol{e}^{2,T}\delta\boldsymbol{x}^2) - c\Delta\delta\tau^{12} \\ \vdots \\ (\boldsymbol{e}^{1,T}\delta\boldsymbol{x}^1 - \boldsymbol{e}^{K,T}\delta\boldsymbol{x}^K) - c\Delta\delta\tau^{1K} \end{bmatrix} + \begin{bmatrix} \sum_{m=1}^{M} b_m\Delta b_{\rho_m}^{12} \\ \vdots \\ \sum_{m=1}^{M} b_m\Delta b_{\rho_m}^{1K} \end{bmatrix},
\end{aligned} \tag{3.135}$$

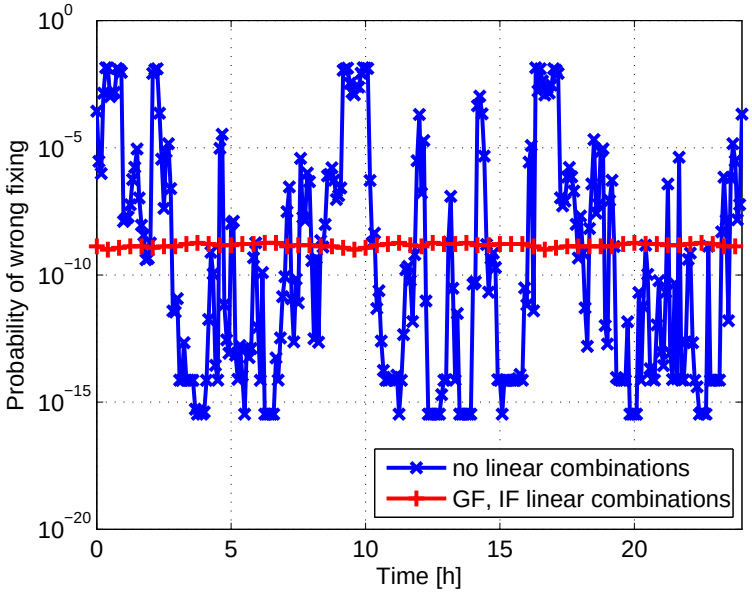

Figure 3.15: Benefit of geometry-free, ionosphere-free linear combinations over no linear combinations for ambiguity resolution: The combinations increase the wavelength to 1 m and eliminate the range, clock offsets, tropospheric and ionospheric delays. The respective success rate depends only on the number of visible satellites, i.e. the combinations are particulary useful for poor satellite geometries. Ambiguity resolution of the uncombined carrier phases is advantageous for geometries with a large number of visible satellites, i.e. the redundancy is sufficiently high to estimate the additional parameters.

where Δ denotes the single difference between satellites 1 and $k = \{2, \ldots, K\}$. After simplification of the notation by introducing

$$\boldsymbol{S} = \boldsymbol{L}^{-1}\boldsymbol{Z}(\overline{\boldsymbol{A}}^T\boldsymbol{\Sigma}^{-1}\overline{\boldsymbol{A}})^{-1}\overline{\boldsymbol{A}}^T\boldsymbol{\Sigma}^{-1}, \tag{3.136}$$

we can rewrite the k-th conditional bias $b_{\hat{N}_{k|\boldsymbol{k}}}$ as

$$\begin{aligned} b_{\hat{N}_{k|\boldsymbol{k}}} &= \sum_{j=1}^{K-1}\left(\boldsymbol{S}_{kj} + \boldsymbol{S}_{k,j+(K-1)}\right)\cdot\left((\boldsymbol{e}^{1,T}\delta\boldsymbol{x}^1 - \boldsymbol{e}^{1+j,T}\delta\boldsymbol{x}^{1+j}) - c\Delta\delta\tau^{1,1+j}\right) \\ &\quad + \sum_{m=1}^{M}\left(\sum_{j=1}^{K-1}\boldsymbol{S}_{kj}\alpha_m\lambda_m\cdot\Delta b_{\phi_m}^{1,1+j} + \sum_{j=1}^{K-1}\left(\boldsymbol{S}_{kj}\beta_m + \boldsymbol{S}_{k,j+(K-1)}b_m\right)\cdot\Delta b_{\rho_m}^{1,1+j}\right) \\ &\leq \sum_{j=1}^{K-1}|\boldsymbol{S}_{kj} + \boldsymbol{S}_{k,j+(K-1)}|\cdot\left(|\boldsymbol{e}^{1,T}\delta\boldsymbol{x}^1| + |\boldsymbol{e}^{1+j,T}\delta\boldsymbol{x}^{1+j}| + |c\Delta\delta\tau^{1,1+j}|\right) \\ &\quad + \sum_{m=1}^{M}\left(\sum_{j=1}^{K-1}|\boldsymbol{S}_{kj}\alpha_m\lambda_m|\cdot|\Delta b_{\phi_m}^{1,1+j}| + \sum_{j=1}^{K-1}|\boldsymbol{S}_{kj}\beta_m + \boldsymbol{S}_{k,j+(K-1)}b_m|\cdot|\Delta b_{\rho_m}^{1,1+j}|\right). \end{aligned} \tag{3.137}$$

This worst-case accumulation of biases has to be considered for Safety-of-Life critical applications. The latter two components are frequency dependant and include multipath. As low elevation satellites are more affected by ground reflections than satellites at high elevation, an elevation-dependant exponential delay profile [73] is used for phase and code biases, i.e.

$$\begin{aligned} \Delta b^{1,1+j}_{\phi_{m,\max}}(E^{1+j}) &= \Delta b_{\phi_{m,\max}}(E=0^\circ)\cdot e^{-E^{(1+j)}/\zeta_{\phi m}} \\ \Delta b^{1,1+j}_{\rho_{m,\max}}(E^{1+j}) &= \Delta b_{\rho_{m,\max}}(E=0^\circ)\cdot e^{-E^{(1+j)}/\zeta_{\rho m}}, \end{aligned} \tag{3.138}$$

with the elevation angle E and the decay constants ζ_{ϕ_m} and ζ_{ρ_m}. Fig. 3.16 shows the probability of wrong fixing for PPP with the combinations of Tab. 3.1. The first one is geometry-preserving and benefits from a larger ambiguity discrimination. The ambiguity resolution additionally benefits from the satellite redundancy but it also suffers from the clock offsets and orbital errors. The latter combination in Tab. 3.1 is geometry-free so that the fixing benefits from the elimination of clock offsets and orbital errors.

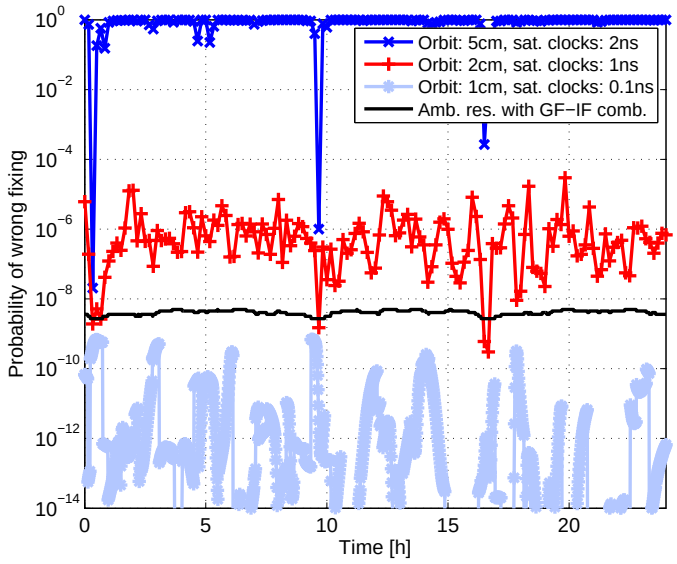

Figure 3.16: Integer ambiguity resolution for Precise Point Positioning: A geometry-preserving and a geometry-free approach are compared for worst-case superposition of orbital and satellite clock errors. The GP approach benefits from a larger discrimination and the satellite redundancy but suffers from the orbital and satellite clock errors while the GF approach behaves vice versa.

	$\{\alpha_1,\alpha_2,\alpha_3\}$, $\{\alpha'_1,\alpha'_2,\alpha'_3\}$	$\{\beta_1,\beta_2,\beta_3\}$	λ	σ_{sm} ($\tau=10$ s)	D
GP	18.57, −71.15, 55.47 1.89, 3.30, −4.19	−0.24, −0.81, −0.85	3.53m	11.0cm	16.1
GF	5.26, −20.13, 15.70 −0.12, 1.07, −0.95	−0.72, −0.14, 0.03	1.00m	8.0cm	6.2

Table 3.1: Carrier smoothed IF combinations with $j_1=1$, $j_2=-5$ and $j_3=4$.

In this case, the reliability of ambiguity resolution depends only on the number of visible satellites and the combination properties. The ambiguity resolution is adapted to the kind of combination: For GP combinations, bootstrapping is performed based on the least-squares solution of the position, float ambiguities and tropospheric wet zenith delay. In the case of GF combinations, the ambiguities are directly provided by the smoothing. For the currently available ultra-rapid (half predicted) IGS orbits with an accuracy of 5 cm for the orbits and of 2 ns for the satellite clocks, the worst-case bias accumulation over all satellites results in a probability of wrong fixing which is close to 1 if the geometry-preserving combination is used. Note that the accuracy of the satellite clocks is about one order of magnitude lower than for the orbits. The GF-IF combination is strongly recommended as it achieves a probability of wrong fixing of less than 10^{-8} for any geometry. The standard deviations of the undifferenced code measurements were set to 3Γ to include multipath. The differential biases $\Delta b_{\phi_m}^{1,1+j}$ and $\Delta b_{\rho_m}^{1,1+j}$ are neglected. A higher accuracy of the orbits and satellite clock offsets will reduce the probability of wrong fixing based on the GP-IF linear combinations. If the standard deviation of the orbits is reduced to 1 cm and of the satellite clocks to 0.1 ns in the future, the GP-IF linear combination will achieve a lower probability of wrong fixing than the GF-IF linear combination as the satellite redundancy more than compensates for the degradation due to orbital errors and clock offsets.

3.4 Comparison of integer ambiguity estimation methods

In this section, the probability of wrong fixing of rounding, bootstrapping and integer least-squares estimation is compared for both unbiased and biased measurements with worst-case bias accumulation [74]. Rounding achieves the lowest success rate for unbiased measurements as it does not consider the correlation between ambiguities.

Fig. 3.17 shows that sequential fixing reduces the probability of wrong fixing of rounding by one order of magnitude for a smoothing period of 10 s and the assumption of unbiasedness. Bootstrapping with integer decorrelation benefits from an even lower probability of wrong fixing as the ambiguity transformation optimizes both the order of fixings and the integer decorrelation. The integer-least squares (ILS) estimation includes a search which results in an even higher success rate. The two orders of magnitude between the probabilities of wrong fixing of rounding and ILS estimation are quite substantial as the chosen two E1-E5 carrier smoothed GP-IF linear combinations (code-only and code-carrier of maximum discrimination) already flatten the ambiguity spectrum significantly. Note that the probability of wrong fixing of ILS estimation can be reduced to an arbitrary value by ellipsoidal integer aperture (EIA) estimation with sufficiently small pull-in regions.

For WA-RTK with double difference measurements, multipath is one of the most critical error sources. The introduction of an elevation-dependant exponential bias profile with worst-case bias accumulation obviously increases the probability of wrong fixing for all estimators. However, the sorting of the fixing methods w.r.t. their failure rates becomes inverse, i.e. rounding achieves the lowest error rate and ILS the largest one. The integer

decorrelation is no longer beneficial as it amplifies the worst-case biases. The parameters of the considered exponential bias profile are $\Delta b_{\rho_{m,\max}}(E) = \{1, \ldots, 10\}$ cm and $\Delta b_{\phi_{m,\max}}(E) = \{0.01, \ldots, 0.1\}$ cycles for $E \in \{0, \ldots, 90°\}$. The signs of the measurement biases were chosen such the degradation in the success rate becomes maximal, i.e. the bias of the sequential decorrelated ambiguity estimates was maximized for bootstrapping. For ILS, the biases in the decorrelated float ambiguity estimates were maximized as they are the basis for the integer search of (3.100). The poor performance of ILS estimation is caused by the ambiguity transformation $\boldsymbol{Z}$ of (3.99) which amplifies the measurement biases as well as by the suboptimal search criterion of (3.100). However, an improved bias bounding can be found by considering the sequential form of the search as described in (3.107). In this case, the worst-case biases are kept at the same level as for sequential fixing and the degradation is only caused by the suboptimal search criterion. Fig. 3.17 shows a significant reduction of the error rate in this case. The success rate of bootstrapping lies between the success rates of rounding and ILS estimation for both unbiased and biased measurements, and has the advantage that it can be expressed in closed form.

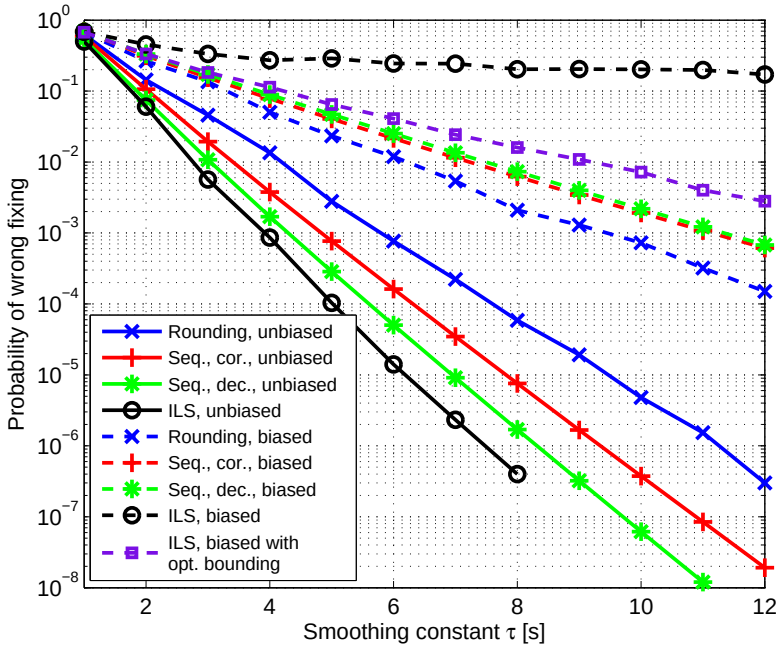

Figure 3.17: Comparison of different ambiguity resolution methods for WA-RTK with unbiased and biased measurements: The sequential conditioning, the integer decorrelation and the search reduce the error rate for unbiased measurements but also increase the sensitivity w.r.t. biases.

There exist several approaches to reduce the probability of wrong fixing in the presence of biases: One of them is RAIM which enables the detection and exclusion of worst-case combination biases. It is shown later that the minimum undetectable conditional ambiguity biases result in a substantially lower probability of wrong fixing. Another option is partial ambiguity fixing to remove the low elevation satellites with the largest bias contributions.

3.5 Partial integer decorrelation for biased carrier phase positioning

The integer decorrelation transformation substantially increases the magnitude of the elements of $\boldsymbol{S}$ of (3.136), and thus, amplifies the conditional ambiguity biases for worst-case bias accumulation. Ambiguity resolution techniques that include an integer decorrelation and/or a search process are more sensitive to biases than simple rounding. The bias amplification due to integer decorrelation compensates for the gain obtained from the variance reduction. Therefore, Henkel et al. have suggested a partial integer decorrelation to achieve the optimum trade-off between variance reduction and bias amplification in [45] and [74]. The partial integer decorrelation is obtained from (3.99) by a reduced number of permutation and decorrelation steps N_{it}. Note that the worst-case bias accumulation becomes less likely but especially severe with a large number of visible satellites.

Fig. 3.18 shows the benefit of partial integer decorrelation for sequential bootstrapping in the presence of biases. If no phase biases are present, a complete integer decorrelation with $\Theta_{\text{it}} = 248$ iterations achieves the lowest error rate. However, for SD phase biases of only 0.05 cycles, a partial integer decorrelation with a single step $\Theta_{\text{it}} = 1$ achieves a probability of wrong fixing that is more than 15 orders of magnitude smaller than in the case of a complete integer decorrelation.

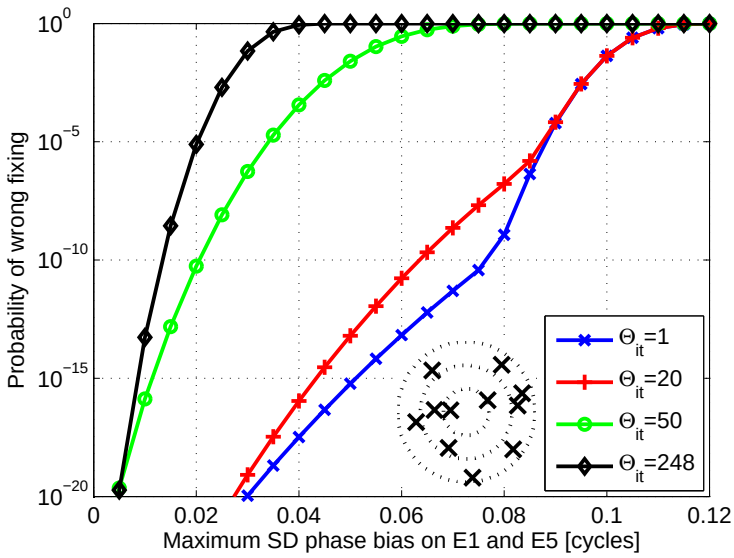

Figure 3.18: Benefit of partial integer decorrelation for sequential bootstrapping in the presence of biases: An exponential bias profile with $\{\Delta b_{\rho_{1,\max}}(E), \Delta b_{\rho_{2,\max}}(E)\} = \{1, \ldots 10\}$ cm and $\{\Delta b_{\phi_{1,\max}}(E), \Delta b_{\phi_{2,\max}}(E)\} = \{0.01, \ldots 0.1\}$ cycles has been assumed for the satellite-satellite SD measurements. The probabilities of wrong fixing are computed for a positive accumulation of all measurement biases, i.e. a worst-case scenario. A reduced number of decorrelation steps improves the reliability of precise point positioning with smoothed ($\tau = 30$ s) E1-E5 code-carrier and code-only combinations.

The probabilities in Fig. 3.18 are upper bounds on the probability of wrong fixing that are only fulfilled in the case of worst-case bias accumulation. An exponential bias profile with $\{\Delta b_{\rho_{1,\max}}(E), \Delta b_{\rho_{2,\max}}(E)\} = \{1, \ldots 10\}$ cm and $\{\Delta b_{\phi_{1,\max}}(E), \Delta b_{\phi_{2,\max}}(E)\} = \{0.01, \ldots 0.1\}$ cycles has been assumed for the satellite-satellite SD measurements. The non-dispersive ephemeris errors and satellite clock offsets of (3.137) have been mapped to the frequency dependant SD biases.

3.6 Cascaded ambiguity resolution with mixed code-carrier combinations

The large ratio between chip and carrier frequencies prevents a direct resolution of carrier phase ambiguities with code measurements. Therefore, Hatch has proposed a Cascaded integer resolution (CIR) in [75] for triple frequency measurements. It is also called Three Carrier Ambiguity Resolution (TCAR) and has been applied to double difference measurements with a short baseline by Forssell et al. [76], Jung [77] and Jung et al. [78].

In the first step, the L2-L5 extra-widelane (EWL) ambiguities with a wavelength of $\lambda = 5.86$m are estimated with the help of the L5 code measurements, i.e.

$$\check{N}_{\mathrm{EWL}} = \left[\phi_{\mathrm{EWL}} - \frac{\rho_{\mathrm{L5}}}{\lambda_{\mathrm{EWL}}} \right], \tag{3.139}$$

with $\phi_{\mathrm{EWL}} = \phi_{\mathrm{L2}} - \phi_{\mathrm{L5}}$. Eq. (3.139) can also be regarded as a geometry-free linear combination of L5 code measurements and L1 and L5 carrier phase measurements, i.e. the ambiguity estimation is not affected by the differential tropospheric delay. In a second step, the L1-L2 widelane (WL) ambiguities with a wavelength of $\lambda = 86.2$cm are fixed:

$$\check{N}_{\mathrm{WL}} = \left[\phi_{\mathrm{WL}} - \frac{\lambda_{\mathrm{EWL}}}{\lambda_{\mathrm{WL}}} (\phi_{\mathrm{EWL}} - \check{N}_{\mathrm{EWL}}) \right], \tag{3.140}$$

with $\phi_{\mathrm{WL}} = \phi_{\mathrm{L1}} - \phi_{\mathrm{L2}}$. In a third step, the L1-L5 mediumlane (ML) ambiguities are determined from the sum of the L1-L2 WL and L2-L5 EWL ambiguities. Finally, an L1 ambiguity estimate is given by

$$\check{N}_{\mathrm{L1}} = \left[\phi_{\mathrm{L1}} - \frac{\lambda_{\mathrm{ML}}}{\lambda_{\mathrm{L1}}} (\phi_{\mathrm{ML}} - \check{N}_{\mathrm{ML}}) \right]. \tag{3.141}$$

This traditional TCAR (or CIR) scheme uses only geometry-free combinations that weight the phase measurements either by -1 or $+1$. Henkel and Günther have suggested a full-geometry approach in [79] that benefits from the satellite redundancy and combines triple frequency combinations with integer least-squares ambiguity resolution. The weighting of linear phase combinations has been generalized to non-binary values which enables a substantial reduction of the probability of wrong fixing.

The previously mentioned CIR approaches have in common that the pure carrier phase combinations slightly amplify the differential ionospheric delay, e.g. the L1-L5 widelane

combination with $\lambda = 75.1$cm scales differential ionospheric delay by a factor of 1.34. Jung et al. have shown in [78] that instantaneous widelane ambiguity resolution with a probability of wrong fixing of less than 10^{-8} is only possible for a baseline of 6.9 km if the carrier phase multipath and receiver errors are within 1% of the wavelength, and the ionospheric delay gradient can be bounded by 2mm/km. In ionospheric storms, gradients of up to 425mm/km have been observed by Pullen et al. in [24] which reduces the maximum service coverage to a few tens of meters.

Therefore, an alternative cascaded ambiguity resolution scheme with geometry-preserving, ionosphere-free (GP-IF) code-carrier linear combinations shall be suggested here. Tab. 3.2 shows the optimized CIR scheme for dual frequency E1-E5 measurements. Three types of linear combinations are considered: a code-only combination, a mixed code-carrier widelane combination of maximum discrimination (first row of Tab. 2.5), and a mixed code-carrier narrowlane combination of minimum noise. A search over all integer coefficients j_m revealed that there is no GP-IF linear combination with a reasonable noise level and wavelength between the selected widelane and narrowlane combinations. Therefore, a $\tau = 60$s smoothing is applied to the first two combinations to overcome the "wavelength gap". A noise level of $\sigma_\phi = 2$mm and $\sigma_{\rho_m} = 3 \cdot \Gamma_m$ has been assumed to include multipath.

Table 3.2: Cascaded ambiguity resolution with GP-IF E1-E5 linear combinations: A $\tau = 60$s smoothing is applied to the first two combinations to overcome the "wavelength gap" between widelane and narrowlane combinations. A noise level of $\sigma_\phi = 2$mm and $\sigma_{\rho_m} = 3 \cdot \Gamma_m$ has been assumed.

Step	GP-IF combination type	j_1	j_2	λ [m]	σ_n [cm]	$\sigma_\mathrm{n,sm}$ [cm]
1	code-only				78.5	7.2
2	widelane code-carrier of max. discr.	+1	−1	3.285	19.0	1.8
3	narrowlane code-carrier of min. noise	+4	−3	0.108	0.5	

For precise point positioning, the three linear combinations of satellite-satellite SD measurements are processed jointly, i.e.

$$\begin{bmatrix} \boldsymbol{\rho} \\ \lambda_\mathrm{WL}\boldsymbol{\phi}_\mathrm{WL} \\ \lambda_\mathrm{NL}\boldsymbol{\phi}_\mathrm{NL} \end{bmatrix} = \boldsymbol{H}\boldsymbol{\xi} + \boldsymbol{A}\boldsymbol{N} + \boldsymbol{\eta}, \tag{3.142}$$

with the unknowns $\boldsymbol{\xi} = [\boldsymbol{x}^T, T_\mathrm{z}]^T$ and $\boldsymbol{N} = [\boldsymbol{N}_\mathrm{WL}^T, \boldsymbol{N}_\mathrm{NL}^T]^T$, and

$$\boldsymbol{H} = \mathbf{1}^{3\times 1} \otimes \boldsymbol{H}_0,\ \boldsymbol{H}_0 = \begin{bmatrix} \Delta\boldsymbol{e}^{12,T} & m_\mathrm{w}(E^1) - m_\mathrm{w}(E^2) \\ \vdots & \vdots \\ \Delta\boldsymbol{e}^{1K,T} & m_\mathrm{w}(E^1) - m_\mathrm{w}(E^K) \end{bmatrix} \text{ and } \boldsymbol{A} = \begin{bmatrix} \mathbf{0} & \mathbf{0} \\ \lambda_\mathrm{WL}\mathbf{1} & \mathbf{0} \\ \mathbf{0} & \lambda_\mathrm{NL}\mathbf{1} \end{bmatrix}. \tag{3.143}$$

Fig. 3.19 shows the temporal evolution of the number of fixable ambiguities with $P_\mathrm{w} \leq 10^{-7}$ and of the positioning accuracy. Bootstrapping with integer decorrelation has been used for fixing. Fig. 3.20 refers to the steady state performance of the smoothing filter.

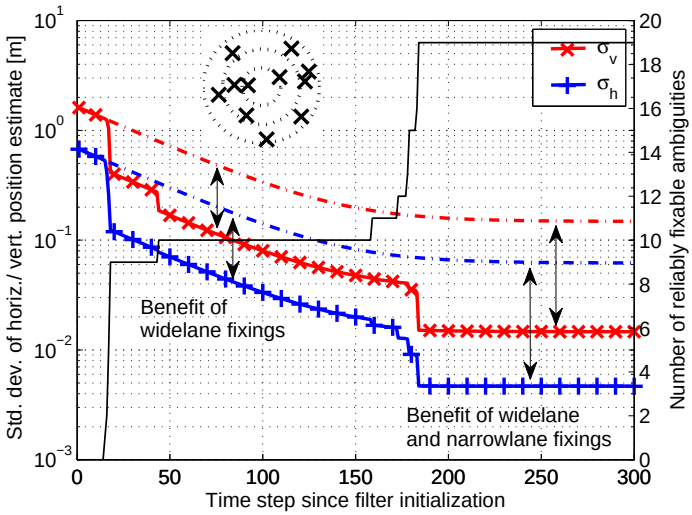

Figure 3.19: Cascaded ambiguity resolution for precise point positioning: The carrier smoothing requires a certain time since filter initialization to enable reliable ambiguity fixing with an overall probability of wrong fixing of less than 10^{-7}. The fixing of widelane ambiguities reduces the position errors by a factor of 4. The fixing of both widelane and narrowlane ambiguities (Tab. 3.2) results in position errors that are one order of magnitude lower than of the non-fixed float solution. The fixing has been performed with sequential bootstrapping after integer decorrelation.

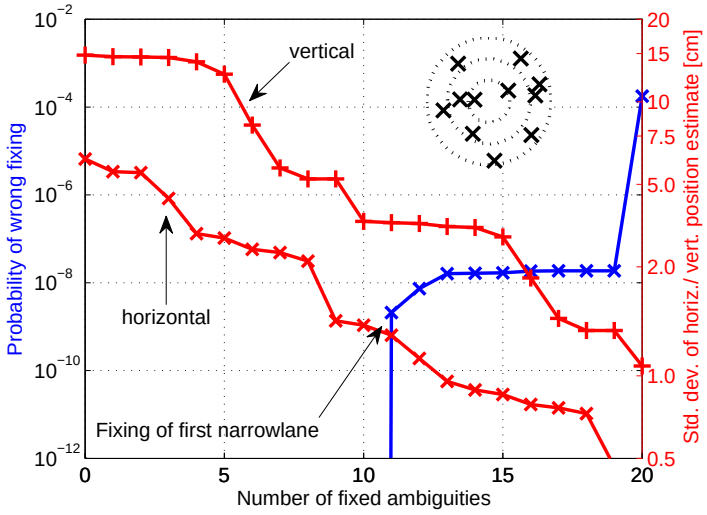

Figure 3.20: Cascaded ambiguity resolution for precise point positioning: The widelane ambiguities can be fixed extremely reliable. All except one narrowlane ambiguities can be fixed with an overall probability of wrong fixing of less than 10^{-7}. The fixing reduces the standard deviation of both horizontal and vertical position by one order of magnitude. The integer ambiguities of both code-carrier combinations of Tab. 3.2 have been fixed with sequential bootstrapping after integer decorrelation.

3.7 Partial ambiguity fixing in the presence of biases

In a severe multipath environment, instantaneous fixing of all ambiguities becomes challenging. However, a subset of ambiguities can still be fixed reliably.

Teunissen et al. have suggested a geometry-free partial ambiguity fixing in [80]. In their notation "geometry-free" means that the satellite redundancy is not taken into account which does not necessarily mean that the range is eliminated by a linear combination. The geometry-free model of single epoch double difference measurements is given by

$$\begin{bmatrix} \Delta\phi_1 \\ \vdots \\ \Delta\phi_M \\ \Delta\rho_1 \\ \vdots \\ \Delta\rho_M \end{bmatrix} = \begin{bmatrix} 1 & q_{11}^2 \\ \vdots & \vdots \\ 1 & q_{13}^2 \\ 1 & -q_{11}^2 \\ \vdots & \vdots \\ 1 & -q_{13}^2 \end{bmatrix} \begin{bmatrix} \Delta r \\ \Delta I_1 \end{bmatrix} + \begin{bmatrix} \lambda_1 & & \\ & \ddots & \\ & & \lambda_M \\ 0 & \cdots & 0 \\ \vdots & & \vdots \\ 0 & \cdots & 0 \end{bmatrix} \begin{bmatrix} \Delta N_1 \\ \vdots \\ \Delta N_M \end{bmatrix} + \begin{bmatrix} \Delta\varepsilon_1 \\ \vdots \\ \Delta\varepsilon_M \\ \Delta\eta_1 \\ \vdots \\ \Delta\eta_M \end{bmatrix}, \quad (3.144)$$

where the DD range Δr also includes the differential tropospheric delay. In [80], Teunissen computed a float solution of the DD range, ionospheric delay and ambiguities, and applied an integer decorrelation to the float ambiguities, i.e.

$$\Delta\hat{\boldsymbol{N}}' = \boldsymbol{Z}\Delta\hat{\boldsymbol{N}} \quad \text{with} \quad \boldsymbol{\Sigma}_{\Delta\hat{\boldsymbol{N}}'} = \boldsymbol{Z}\boldsymbol{\Sigma}_{\Delta\hat{N}}\boldsymbol{Z}^T. \quad (3.145)$$

He has then chosen the decorrelated ambiguity of lowest variance. It can be rewritten as a linear combination, i.e.

$$\Delta\hat{N}' = \sum_{m=1}^{M} j_m \cdot \Delta\hat{N}_m, \quad (3.146)$$

where $j_m = Z_{l,m}$ and l is the row in $\Delta\hat{\boldsymbol{N}}'$ that corresponds to the ambiguity of minimum variance. Tab. 3.3 shows that this method results in widelane combinations with binary weighting.

Table 3.3: Linear combinations of ambiguities: The combinations are determined with the LAMBDA ambiguity transformation for a geometry-free model. The smallest uncertainty is achieved by the traditional widelane combinations. A noise level of $\sigma_\phi = 2$mm and $\sigma_{\rho_m} = 3 \cdot \Gamma_m$ has been assumed.

E1	E5	E5b	E5a
j_1	j_2	j_3	j_4
1	−1		
0		1	−1

The computation of decorrelated ambiguities of minimum variance is repeated for the remaining double differences. The N_p most accurate ambiguity combinations are then selected for partial fixing. Cao et al. [81] have considered a full-geometry approach for

partial ambiguity fixing. A Kalman filter is used to estimate the float solution for a short baseline, i.e. atmospheric errors are neglected. The traditional widelane combinations with binary weighting have been computed and the fixing has been performed with bootstrapping after integer decorrelation. The results of Cao et al. show the temporal evolution of the probability of incorrect fixes, the number of fixed ambiguities and the achievable positioning accuracy for unbiased measurements.

In [74], Henkel and Günther have analyzed partial ambiguity fixing in the presence of biases. As the integer decorrelation transformation results in a poor performance for biased measurements with worst-case bias accumulation, it is omitted and the optimal fixing order is determined by a search. The traditional sequential fixing of Blewitt [58] performs a pure forward search: First, the ambiguity of largest P_s^k is fixed. Then, the float solution is updated and the most reliable ambiguity is selected among the remaining ones. This process is repeated until the probability of wrong fixing exceeds a certain threshold or all ambiguities are fixed. This efficient search requires the testing of at most $K + (K-1) + \ldots + 1 = \frac{K(K+1)}{2}$ candidates.

However, the maximization of the reliability of the first ambiguity does not necessarily maximize the number of fixable ambiguities. An exhaustive search of this order would require the evaluation of $K!$ search branches. It has been shown by Henkel et al. in [45] that the number of search branches can be reduced to a few hundreds if a constraint on the probability of wrong fixing is evaluated at each step. Moreover, a constraint on the geometry of fixings further reduces the search effort without much affecting the number of fixable ambiguities. Fig. 3.21 shows a search tree for the fixing order that maximizes the number of fixable ambiguities. The search includes both forward and backward steps.

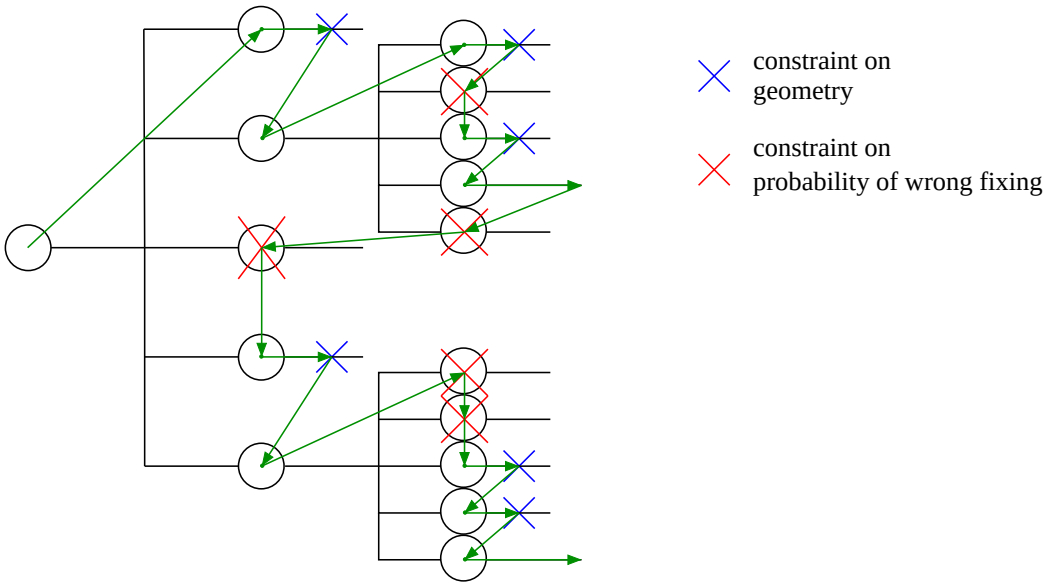

Figure 3.21: Search of the optimal fixing order in the presence of biases: An exhaustive search with constraints on the maximum probability of wrong fixing and the fixing geometry is used to find the order which maximizes the number of fixable ambiguities.

Fig. 3.22 shows that the maximization of N_p enables the reliable fixing of 6 ambiguities compared to 3 ambiguities for the order that maximizes the reliability of the first fix. Two GP-IF E1-E5 linear combinations (a code-only and a code-carrier of max. discrimination) of sat.-sat. SD measurements have been smoothed over 20 s. An exponential bias profile (code biases: 10 cm for $E = 0°$, 1 cm for $E = 90°$; phase biases: 0.1 cycles for $E = 0°$, 0.01 cycles for $E = 90°$) with worst-case bias accumulation has been assumed. Note that the optimization depends on the threshold probability which has been set to 10^{-9}. Fig. 3.23 shows the temporal evolution of N_p for both fixing orders.

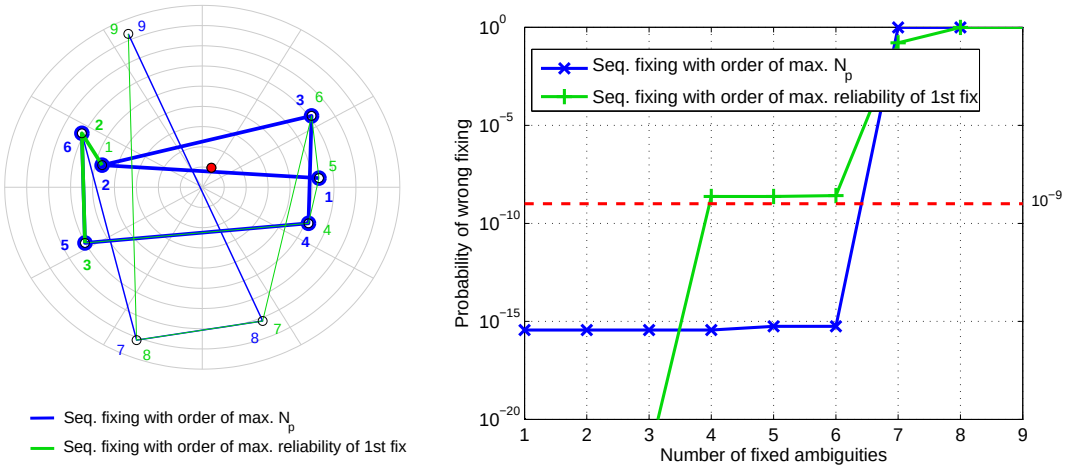

Figure 3.22: Skyplot for two sequential fixing orders: The maximization of the reliability of the first fix results in a fixing order with three ambiguities below the threshold of 10^{-9}. The allowance of larger error rates for the first fixes enables a larger number of reliably fixable ambiguities. In both cases, an exponential bias profile with worst-case bias accumulation has been assumed.

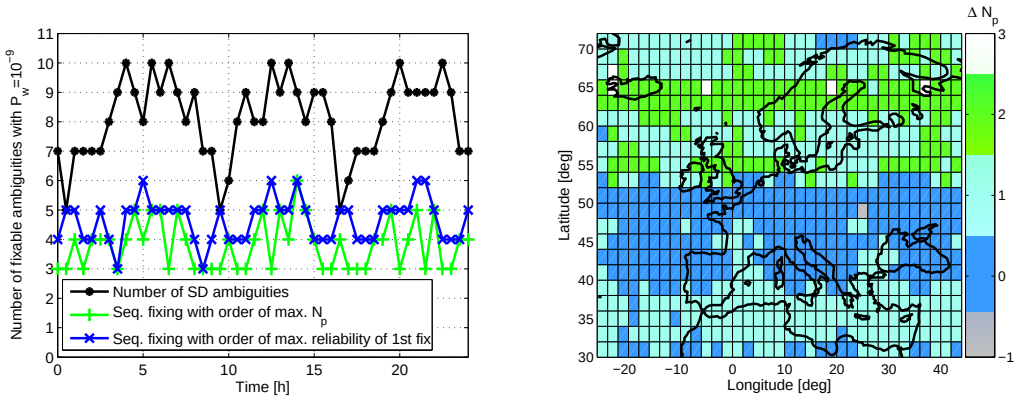

(a) Receiver location: 48.1507° N, 11.5690° E (b) Time of minimum N_p

Figure 3.23: Comparison of two sequential ambiguity fixing schemes in the presence of biases: The right graph is the result of a minmax-optimization, i.e. it shows the benefit of maximizing N_p for the most critical time instant.

Fig. 3.17 showed that sequential fixing is more sensitive to biases than rounding. However, sequential fixing enables a larger number of fixable ambiguities even in the presence of biases with worst-case bias accumulation if an optimized order is used. It can be searched exhaustively based on the bias profile and correlation between float ambiguities. Fig. 3.24 and 3.25 show the optimized order of fixings, the probabilities of wrong fixing and the temporal evolution of the number of fixable ambiguities for rounding and sequential fixing.

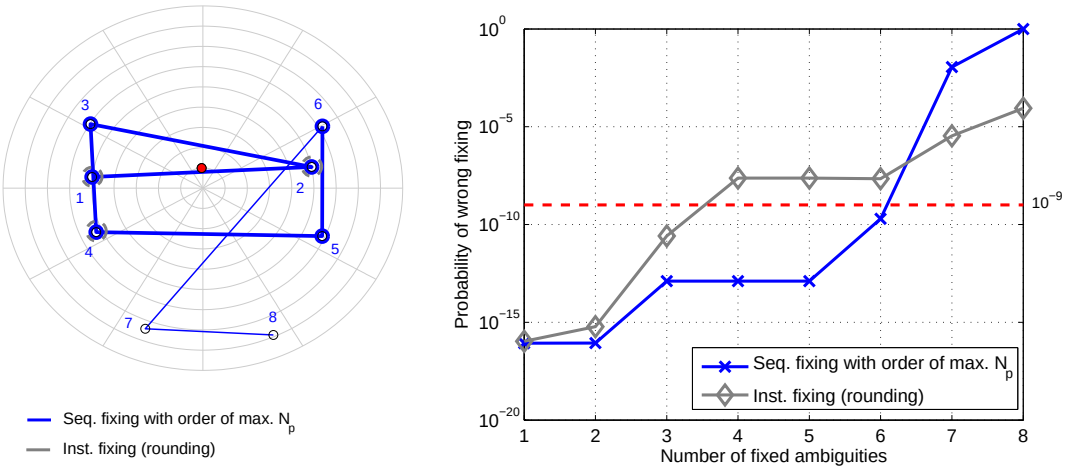

Figure 3.24: Comparison between instantaneous fixing (rounding) and sequential fixing with an order of maximum N_p for a given geometry: The combined forward-backward search based on the bias profile and correlation between float ambiguities enable the fixing of 6 instead of 3 ambiguities.

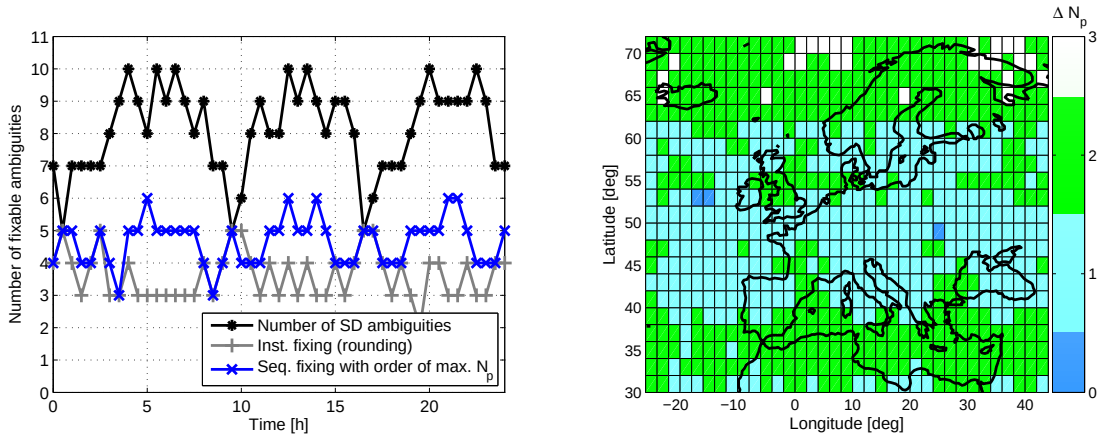

(a) Receiver location: 48.1507° N, 11.5690° E

(b) Time of minimum N_p

Figure 3.25: Benefit of sequential fixing with order of maximum N_p over instantaneous rounding for an exponential bias profile: (a) shows the temporal evolution of the numbers of fixable ambiguities for a fixed location and (b) shows the difference in the numbers of fixable ambiguities between both methods for the worst-case time instant.

3.8 Fault detection with multiple mixed code-carrier combinations

Several multi-frequency combinations are required to determine the measurement ambiguities from the combination ambiguities. The mapping of measurement into combination ambiguities can be described by a matrix $\boldsymbol{M}$ which has to be of full rank and integer valued to enable fixing in the transformed domain. The inverse mapping from the decorrelated combined into the measurement ambiguities is given by

$$\begin{bmatrix} \check{N}_1 \\ \vdots \\ \check{N}_M \end{bmatrix} = \boldsymbol{M}^{-1}\boldsymbol{Z}^{-1} \begin{bmatrix} \check{N}'_1 \\ \vdots \\ \check{N}'_M \end{bmatrix} \overset{!}{\in} \mathbb{Z}^{M\times 1}, \tag{3.147}$$

where $\boldsymbol{M}^{-1}$ does not have to be integer valued. The mapping matrix $\boldsymbol{M}$ can be chosen such that the most likely integer errors are mapped to real-valued ambiguities by $\boldsymbol{M}^{-1}$ and, thus, can be detected as failures. In [82] and [83], $\boldsymbol{M}$ is determined such that the probability of the most likely undetectable ambiguity error is minimized, i.e.

$$P_{\mathrm{MLUO}} = \min_{\boldsymbol{M}} \max_{\Delta\check{\boldsymbol{N}}'|\left(\boldsymbol{M}^{-1}\boldsymbol{Z}^{-1}\Delta\check{\boldsymbol{N}}'\right)\in\mathbb{Z}} P(\Delta\check{\boldsymbol{N}}'), \tag{3.148}$$

where the probability of an integer error vector $\Delta\check{\boldsymbol{N}}'$ is given by

$$P(\Delta\check{\boldsymbol{N}}') = \prod_{m=1}^{M} \int_{\Delta\check{N}'_m-0.5}^{\Delta\check{N}'_m+0.5} p^{(m)}(x)dx, \tag{3.149}$$

with $p^{(m)}(x) \sim \mathcal{N}(0, \sigma^2_{\hat{N}_{m|1,\ldots,m-1}})$. The optimization in (3.148) is constrained by the requirements on the rank, the geometry and the ionospheric delay of the combinations.

In the following analysis, the search of $\boldsymbol{M}$ is split into two steps: First, an exhaustive search of GF-IP E1-E5a-E5b code-carrier combinations of minimum noise is performed. In a second step, the subset of three combinations with minimum P_{MLUO} and full rank $\boldsymbol{M}$ is searched. The complexity of the second step is reduced by considering only combinations with a discrimination of at least two. Fig. 3.26 shows the integer ambiguity grid and error ellipsoid that is given by

$$P\left(\sum_{m=1}^{M} \frac{\varepsilon^2_{\hat{N}_{m|1,\ldots,m-1}}}{\sigma^2_{\hat{N}_{m|1,\ldots,m-1}}} \leq \mu\right) = \int_0^{\mu} p_{\chi^2_M}(x)dx \overset{!}{=} 10^{-7} \tag{3.150}$$

where $p_{\chi^2_M}(x)$ denotes the χ^2 distribution with M degrees of freedom. The integer errors that can be detected by the back-transformation are marked with an 'x' and the remaining one with an 'o'. All integer errors in the ellipsoid are detectable; the most likely undetectable offset is $[0, 1, -1]$ and occurs with a probability of $1.2 \cdot 10^{-14}$. The optimization has been constraint to a maximum integer weight of $j_{\max} = 10$.

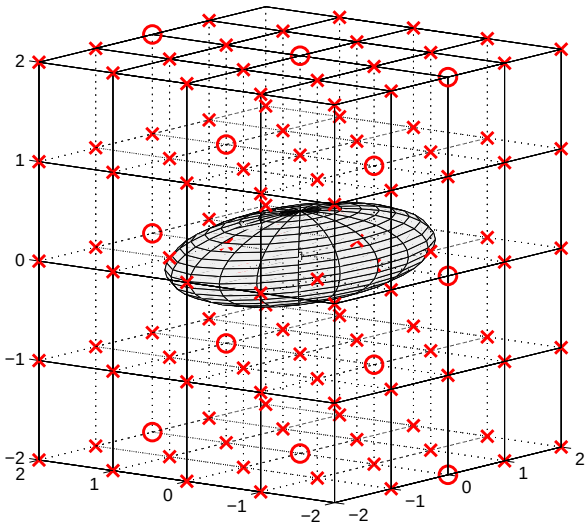

Figure 3.26: Integer ambiguity grid and error ellipsoid for $P(\sum_{m=1}^{M} \frac{\varepsilon^2_{\check{N}_{m|1,\ldots,m-1}}}{\sigma^2_{\check{N}_{m|1,\ldots,m-1}}} \leq \mu) = 10^{-7}$: A set of triple frequency geometry-free, ionosphere-preserving code-carrier combinations has been chosen such that the fault detection capacity is maximized, i.e. the probability of the most likely undetectable offset is minimized. All integer errors in the ellipsoid are detectable; the most likely undetectable offset is $[0, 1, -1]$ and occurs with a probability of $1.2 \cdot 10^{-14}$. The optimization has been constraint to a max. integer weight of $j_{\max} = 10$. Measurements were simulated for 7 epochs with $\sigma_{\rho_m} = 3 \cdot \Gamma_m$ and $\sigma_\phi = 2$mm.

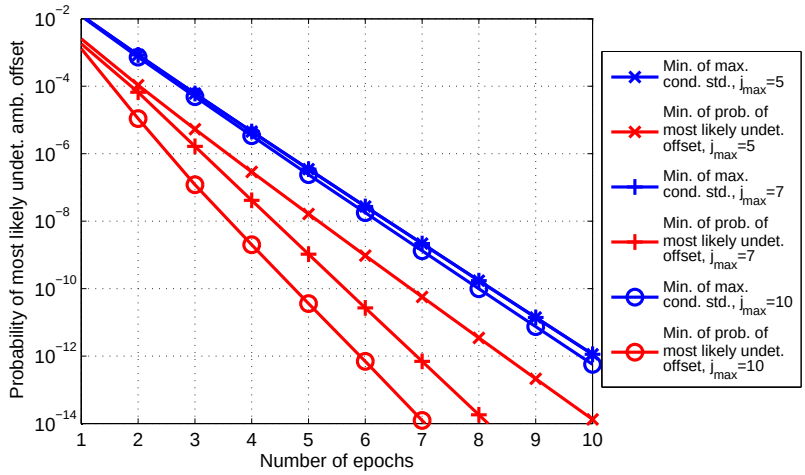

Figure 3.27: Comparison of two criteria for the design of combination sets: a.) Minimization of the maximum conditional standard deviation, and b.) minimization of the probability of the most likely undetectable integer offset. The latter approach results in a real-valued $\boldsymbol{M}^{-1}$ which enables the detection of integer estimation errors. The fault detection capacity further improves for larger values of $j_{\max}$. In both criteria, bootstrapping with integer decorrelation has been used for ambiguity resolution.

Traditionally, the set of combinations has been chosen such that the maximum conditional standard deviation is minimized over all combinations, i.e.

$$\min_{\boldsymbol{M}} \max_{m} \sigma_{\hat{N}_{m|1,\ldots,m-1}}, \tag{3.151}$$

with the same constraints on the rank, geometry and ionosphere as in the optimization of (3.148). Fig. 3.27 shows that the fault detection optimization of (3.148) enables a substantially lower P_{MLUO} than the minimization of the maximum conditional standard deviation of (3.151). The fault detection capability depends on the maximum allowed integer values $j_{\max}$ of $\boldsymbol{M}$, i.e. a larger $j_{\max}$ means more prime numbers in $\boldsymbol{M}$, and thus a better fault detection by $\boldsymbol{M}^{-1}$. On the contrary, the min-max-optimization of (3.151) does not benefit of an increased $j_{\max}$.

3.9 Integrity risk of carrier phase positioning

Traditionally, the reliability of carrier phase positioning is measured by the probability of wrong fixing. However, a large number of wrong fixings results in position errors that are acceptable for many applications and do not violate integrity. For example, the RTCA has defined horizontal and vertical alert limits of 17 m (56 ft) and 10 m (33 ft) for GBAS Service Level F (CAT IIIb) in [97]. The most stringent vertical alert limit in aviation is 5.3 m for CAT IIIc [1].

Therefore, Khanafseh and Pervan have considered the impact of erroneous fixings on the positioning accuracy in [98]. The integrity risk is substantially reduced by omitting the conservative assumption that each wrong fixing results in an integrity risk. The derivation is briefly introduced here and starts with the rules of Bayes, i.e.

$$\begin{aligned} I_{\mathrm{H}_0} &= P(|\hat{x}_{\mathrm{v}} - x_{\mathrm{v}}| > VAL) \\ &= P(|\hat{x}_{\mathrm{v}} - x_{\mathrm{v}}| > VAL|_{\mathrm{CF}}) \cdot P_{\mathrm{CF}} + P(|\hat{x}_{\mathrm{v}} - x_{\mathrm{v}}| > VAL|_{\mathrm{IF}}) \cdot P_{\mathrm{IF}}, \end{aligned} \tag{3.152}$$

where $\hat{x}_{\mathrm{v}}$ and x_{v} are the estimated and the true vertical position, VAL denotes the Vertical Alarm Limit and P_{CF} and P_{IF} denote the probabilities of correct and incorrect fixing of the ambiguities. The latter term in (3.152) is rewritten to consider all integer error vectors individually, and to group these error vectors into a set of more likely errors and a set of less likely ones, i.e.

$$\begin{aligned} P(|\hat{x}_{\mathrm{v}} - x_{\mathrm{v}}| > VAL|_{\mathrm{IF}}) \cdot P_{\mathrm{IF}} &= \sum_{n=1}^{r} P(|\hat{x}_{\mathrm{v}} - x_{\mathrm{v}}| > VAL|_{\mathrm{IF}_n}) \cdot P_{\mathrm{IF}_n} \\ &\quad + \sum_{n=r+1}^{\infty} \underbrace{P(|\hat{x}_{\mathrm{v}} - x_{\mathrm{v}}| > VAL|_{\mathrm{IF}_n})}_{\approx 1} \cdot P_{\mathrm{IF}_n}, \end{aligned} \tag{3.153}$$

where r is number of integer error vectors with probabilities larger than P_{th}, i.e. $P_{\mathrm{IF}_n} > P_{\mathrm{th}}$. For the less likely error vectors, the conditional probability of an integrity risk is

bounded by 1 so that the second sum simplifies to

$$\sum_{n=r+1}^{\infty} P_{\mathrm{IF}_n} = 1 - P_{\mathrm{CF}} - \sum_{n=1}^{r} P_{\mathrm{IF}_n}. \tag{3.154}$$

Combining (3.152)-(3.154) yields

$$\begin{aligned} I_{\mathrm{H}_0} &= 1 - (1 - P(|\hat{x}_{\mathrm{v}} - x_{\mathrm{v}}| > VAL|_{\mathrm{CF}})) \cdot P_{\mathrm{CF}} \\ &\quad - \sum_{n=1}^{r} ((1 - P(|\hat{x}_{\mathrm{v}} - x_{\mathrm{v}}| > VAL|_{\mathrm{IF}_n})) \cdot P_{\mathrm{IF}_n}. \end{aligned} \tag{3.155}$$

Traditionally, the probability $P(|\hat{x}_{\mathrm{v}} - x_{\mathrm{v}}| > VAL|_{\mathrm{IF}_n})$ is bounded by 1 so that the latter term drops out. However, the negative sign of this term motivates the evaluation of the position errors due to each fixing error especially for large r.

The four probability terms in (3.155) can be determined efficiently for sequential bootstrapping. Teunissen has computed the probability of the n-th incorrect fix in [56], i.e.

$$P_{\mathrm{IF}_n} = \prod_{k=1}^{K} \left(\Phi\left(\frac{1 - 2 \cdot \boldsymbol{l}_k^T \Delta \boldsymbol{N}_n}{2 \cdot \sigma_{k|1,\ldots,k-1}} \right) + \Phi\left(\frac{1 + 2 \cdot \boldsymbol{l}_k^T \Delta \boldsymbol{N}_n}{2 \cdot \sigma_{k|1,\ldots,k-1}} \right) - 1 \right), \tag{3.156}$$

where $\boldsymbol{l}_k^T$ represents the k-th row of $\boldsymbol{L}^{-1}$ that results from the $\boldsymbol{LDL}^T$ decomposition of the decorrelated ambiguity covariance matrix. $\Delta \boldsymbol{N}_n$ denotes the n-th integer error vector in the decorrelated search space. The conditional probability for the vertical position error is obtained similarly as

$$P(|\hat{x}_{\mathrm{v}} - x_{\mathrm{v}}| > VAL|_{\mathrm{IF}_n}) = \Phi\left(\frac{-\mathrm{VAL} - b_{\mathrm{v},n}}{\sigma_{\mathrm{v}}} \right) + \Phi\left(\frac{-\mathrm{VAL} + b_{\mathrm{v},n}}{\sigma_{\mathrm{v}}} \right), \tag{3.157}$$

where the vertical position bias $b_{\mathrm{v},n}$ due to the n-th integer estimation error is given by Khanafseh and Pervan in [98] as

$$b_{\mathrm{v},n} = \boldsymbol{s}^T \left(\boldsymbol{X}^T \boldsymbol{\Sigma}^{-1} \boldsymbol{X} \right)^{-1} \boldsymbol{X}^T \boldsymbol{\Sigma}^{-1} \boldsymbol{A} \boldsymbol{Z}^{-1} \Delta \boldsymbol{N}_n, \tag{3.158}$$

with $\boldsymbol{s} = [0,\ 0,\ 1,\ 0]^T$.

The integer error vectors $\Delta \boldsymbol{N}_n$ with $P_{\mathrm{IF}_n} > P_{\mathrm{th}}$ can be computed iteratively for bootstrapping. Khanafseh and Pervan have suggested an efficient method for the computation of a candidate matrix $\boldsymbol{C}$ whose columns represent the integer error vectors with $P_{\mathrm{IF}_n} > P_{\mathrm{th}}$: First, $\boldsymbol{C}$ is initialized by the row vector $\boldsymbol{C}_1 = [-d, -d+1, \ldots, -1, +1, \ldots, d-1, d]$ which includes all possible fixing errors for the first ambiguity up to an arbitrary integer bound d. Then, the matrix $\boldsymbol{C}$ is sequentially updated for the ambiguities $k \in \{2, \ldots, K\}$, i.e.

$$\boldsymbol{C}_k = \begin{bmatrix} \boldsymbol{C}_{k-1} & \ldots & \boldsymbol{C}_{k-1} & \ldots & \boldsymbol{C}_{k-1} & 0 & \ldots & 0 & 0 & \ldots & 0 \\ -\boldsymbol{d}^T & \ldots & \boldsymbol{0}^T & \ldots & \boldsymbol{d}^T & -d & \ldots & -1 & 1 & \ldots & d \end{bmatrix}, \tag{3.159}$$

where $\boldsymbol{d}$ is a column vector with all of its elements equal to d. As this unconstrained computation would result in $(2d+1)^K - 1$ integer error vectors, P_{IF_n} is computed in each update step for each error vector, and only the relevant candidates with $P_{\mathrm{IF}_n} > P_{\mathrm{th}}$ are kept. As the large computational burden remains the main limitation even with this constraint, Kanafseh and Pervan have used an integer decorrelation transformation to reduce the search space and number of integer error candidates. The use of a code carrier linear combination with a large wavelength further reduces the search space such that $d = 1$ becomes sufficient for most geometries.

Fig. 3.28 shows the integrity risk and the number of integer error candidates as a function of the threshold probability P_{th}. Removing the worst-case assumption (a wrong fixing results in a positioning error above the alert limit) reduces the integrity risk by more than two orders of magnitude if $P_{\mathrm{th}} < 10^{-12}$. A vertical alert limit of 5.3 m has been assumed. A code carrier combination of maximum discrimination (Tab. 2.5, $\lambda = 4.309$m) and a code-only combination of satellite-satellite single difference measurements on E1 and E5a have been smoothed over $\tau = 5$ s. Both linear combinations are used for sequential least-squares estimation of position, tropospheric delay and ambiguities.

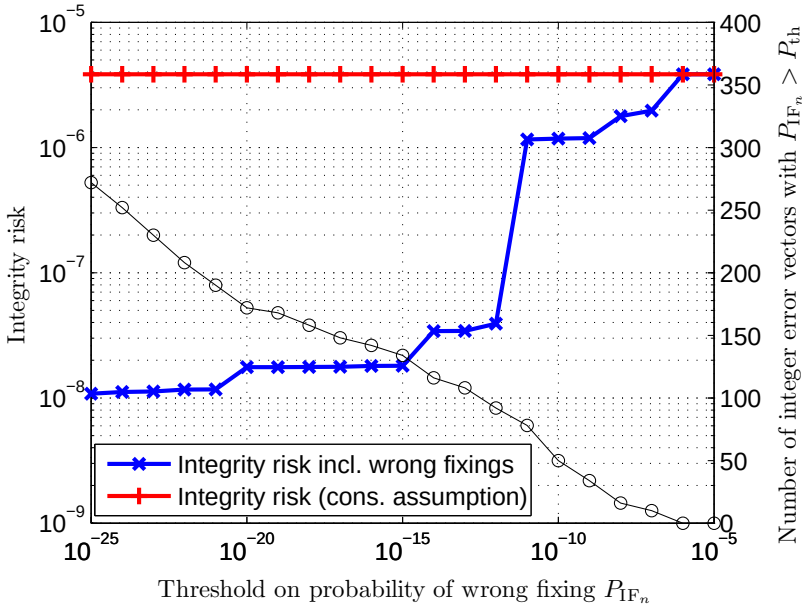

Figure 3.28: Integrity risk of carrier phase positioning: A conservative assumption is that each erroneous fixing is an integrity threat. The computation of the position errors due to the most likely integer error vectors reduces the integrity risk by more than two orders of magnitude. Satellite-satellite single differences on E1 and E5a have been used for a code carrier combination of maximum discrimination and a code-only combination. Both combinations are smoothed over $\tau = 5$s. The position, tropospheric delay and ambiguities are estimated by sequential least-squares with integer decorrelation. A vertical alert limit of 5.3 m has been assumed.

4

Multi-frequency, multi-satellite Vector Phase Locked Loop

Current GNSS receivers use independent Phase Locked Loops (PLLs) for each satellite and frequency. The introduction of new GPS signals on L5 and the development of new satellite constellations (Galileo, Compass) will increase the number of PLLs in each receiver and, thus, the probability of a loss of lock of one PLL. This probability becomes critical especially during ionospheric scintillations with frequent deep amplitude fades of more than 20 dB. Another threat are jammers with random frequency hopping that continuously interfere at least one frequency. The outage of a PLL on one frequency prevents the computation of an ionosphere-free combination at this instant and, thus, degrades the positioning accuracy. The joint tracking of multiple satellites has attracted a lot of attention over the last years as it enables a substantial improvement in both accuracy and robustness of code and carrier tracking. This section summarizes our developments for joint carrier phase tracking and then discusses a method for mitigating wideband ionospheric effects for both code and carrier phase measurements.

For traditional GPS receivers with a bandwidth of 2 MHz, the ionospheric dispersion within the L1 band can be neglected. However, the Galileo E5 band has a bandwidth of 90 MHz, which results in a substantial difference between the ionospheric delay at the upper and lower edges of the frequency band. This delay corresponds to a phase shift in frequency domain. Therefore, the received signal model of (1.3) shall be further expanded with the help of the Fourier transform:

$$\tilde{r}(t) = \sum_{k=1}^{K} \sum_{m=1}^{M} \mathcal{F}^{-1}\{\mathcal{F}\{r_m^k(t)\} \cdot e^{-j2\pi f \tau_{\mathrm{I},m}^k(f)}\}, \tag{4.1}$$

where $\tau^k_{\mathrm{I},m}(f)$ denotes the frequency dependant ionospheric delay (in units of seconds) and $\mathcal{F}(\cdot)$ is the Fourier transform. As the carriers are sinusoidal signals, the ionospheric dispersion is limited to the inphase and quadrature components, i.e.

$$\begin{aligned}\tilde{r}(t) &= \sum_{k=1}^{K}\sum_{m=1}^{M}\left(\alpha^k_m \tilde{s}^k_{\mathrm{I},m}(t)\cos\left((\omega_{\mathrm{c},m}-\omega^k_{\mathrm{D},m}(t))(t-\tau^k_m(t))+\phi^k_m(t)\right)\right.\\ &\quad \left.+j\cdot\alpha^k_m\tilde{s}^k_{\mathrm{Q},m}(t)\sin\left((\omega_{\mathrm{c},m}-\omega^k_{\mathrm{D},m}(t))(t-\tau^k_m(t))+\phi^k_m(t)\right)+\tilde{n}^k_m(t)\right). \quad (4.2)\end{aligned}$$

with

$$\tilde{s}^k_{\{\mathrm{I,Q}\},m}(t)=\mathcal{F}^{-1}\{\mathcal{F}\{s^k_{\{\mathrm{I,Q}\},m}(t)\}\cdot e^{-j2\pi f\tau^k_{\mathrm{I},m}(f)}\}. \quad (4.3)$$

The navigation bit can be assumed constant during the integration time such that the ionospheric dispersion is limited to the code chips of the inphase and quadrature components, i.e.

$$\tilde{s}^k_{\{\mathrm{I,Q}\},m}(t)=\sqrt{\mathcal{P}^k_{\{\mathrm{I,Q}\},m}}b^k_{\{\mathrm{I,Q}\},m}(t-\tau^k_{0,m})\mathcal{F}^{-1}\{\mathcal{F}\{c^k_{\{\mathrm{I,Q}\},m}(t-\tau^k_{0,m})\}\cdot e^{-j2\pi f\tau^k_{\mathrm{I},m}(f)}\}. \quad (4.4)$$

The inphase and quadrature components of $\tilde{r}(t)$ are multiplied by the receiver generated signal $\cos\left(\omega^{k'}_{r,m'}(t-\tau^{k'}_{r,m'})+\phi^{k'}_{r,m'}\right)$, i.e.

$$\begin{aligned}&\sum_{k=1}^{K}\sum_{m=1}^{M}\tilde{r}^k_{\mathrm{I},m}(t)\cdot\cos\left(\omega^{k'}_{r,m'}(t-\tau^{k'}_{r,m'})+\phi^{k'}_{r,m'}\right)\\ &\quad=\frac{1}{2}\alpha^{k'}_{m'}\tilde{s}^{k'}_{\mathrm{I},m'}(t)\cos(\Delta\omega^{k'}_{m'}(t-\tau^{k'}_{r,m'})-\omega^{k'}_{m'}\Delta\tau^{k'}_{m'}+\Delta\phi^{k'}_{m'})+\tilde{n}^{k'}_{\mathrm{I},m'}(t)\\ &\qquad+\frac{1}{2}\sum_{k=1,k\neq k'}^{K}\sum_{m=1,m\neq m'}^{M}\tilde{r}^k_{\mathrm{I},m}(t)\cdot\cos\left(\omega^{k'}_{r,m'}(t-\tau^{k'}_{r,m'})+\phi^{k'}_{r,m'}\right)+\mathcal{O}(\omega^k_m+\omega^k_{r,m})\\ &\sum_{k=1}^{K}\sum_{m=1}^{M}\tilde{r}^k_{\mathrm{Q},m}(t)\cdot\cos\left(\omega^{k'}_{r,m'}(t-\tau^{k'}_{r,m'})+\phi^{k'}_{r,m'}\right)\\ &\quad=\frac{1}{2}\alpha^{k'}_{m'}\tilde{s}^{k'}_{\mathrm{Q},m'}(t)\sin(\Delta\omega^{k'}_{m'}(t-\tau^{k'}_{r,m'})-\omega^{k'}_{m'}\Delta\tau^{k'}_{m'}+\Delta\phi^{k'}_{m'})+\tilde{n}^{k'}_{\mathrm{Q},m'}(t)\\ &\qquad+\frac{1}{2}\sum_{k=1,k\neq k'}^{K}\sum_{m=1,m\neq m'}^{M}\tilde{r}^k_{\mathrm{Q},m}(t)\cdot\cos\left(\omega^{k'}_{r,m'}(t-\tau^{k'}_{r,m'})+\phi^{k'}_{r,m'}\right)+\mathcal{O}(\omega^k_m+\omega^k_{r,m}) \quad (4.5)\end{aligned}$$

with $\omega^{k'}_{m'}=\omega_{\mathrm{c},m'}-\omega^{k'}_{\mathrm{D},m'}$ and the following unknown offsets in frequency, code delay and phase:

$$\Delta\omega^{k'}_{m'}=\omega^{k'}_{m'}-\omega^{k'}_{r,m'},\quad \Delta\tau^{k'}_{m'}=\tau^{k'}_{m'}-\tau^{k'}_{r,m'},\quad \text{and}\quad \Delta\phi^{k'}_{m'}=\phi^{k'}_{m'}-\phi^{k'}_{r,m'}. \quad (4.6)$$

The result of (4.5) is lowpass filtered, then multiplied (4.5) by the locally generated code $c^{k'}_{\{\mathrm{I,Q}\},m'}(t-\tau^{k'}_{r,m'})$ and integrated over the interval $[nT_i+\tau_r,(n+1)T_i+\tau^{k'}_{r,m'}]$ of duration

$T_i = \nu N T_c$:

$$\begin{aligned}
\tilde{C}^k_{\mathrm{I},m} &= \frac{1}{2}\int_{nT_i+\tau^k_{r,m}}^{(n+1)T_i+\tau^k_{r,m}} \alpha^k_m \tilde{s}^k_{\mathrm{I},m}(t) c^k_{\mathrm{I},m}(t-\tau^k_{r,m}) \\
&\quad \cdot \cos(\Delta\omega^k_m(t-\tau^k_{r,m}) - \omega^k_m \Delta\tau^k_m + \Delta\phi^k_m) + \tilde{n}^k_{\mathrm{I},m}(t)dt \\
\tilde{C}^k_{\mathrm{Q},m} &= \frac{1}{2}\int_{nT_i+\tau^k_{r,m}}^{(n+1)T_i+\tau^k_{r,m}} \alpha^k_m \tilde{s}^k_{\mathrm{Q},m}(t) c^k_{\mathrm{Q},m}(t-\tau^k_{r,m}) \\
&\quad \cdot \sin(\Delta\omega^k_m(t-\tau^k_{r,m}) - \omega^k_m \Delta\tau^k_m + \Delta\phi^k_m) + \tilde{n}^k_{\mathrm{Q},m}(t)dt, \qquad (4.7)
\end{aligned}$$

where k' and m' were replaced by k and m as the signals from satellites $k \neq k'$ are eliminated by the de-spreading. It is shown by Günther in [1] that the complex correlation result $\tilde{C}^k_m = \tilde{C}^k_{\mathrm{I},m} + j\tilde{C}^k_{\mathrm{Q},m}$ can be well approximated by

$$\tilde{C}^k_m \approx \sqrt{\mathcal{P}^k_m} \cdot T_i \cdot R(\Delta\tau^k_m) \cdot \mathrm{sinc}\left(\frac{\Delta\omega^k_m T_i}{2}\right) \cdot e^{j\left((n+\frac{1}{2})\Delta\omega^k_m T_i - \omega^k_m \Delta\tau^k_m + \Delta\phi^k_m\right)} + \tilde{n}^k_m, \qquad (4.8)$$

where $R(\Delta\tau^k_m)$ denotes the distorted code autocorrelation function which is given by

$$R(\Delta\tau^k_m) = \frac{1}{T_c}\int_0^{T_c} \mathcal{F}^{-1}\{\mathcal{F}\{c^k_{\{\mathrm{I,Q}\},m}(t)\} \cdot e^{-j2\pi f \tau^k_{\mathrm{I},m}(f)}\} \cdot c^k_{\{\mathrm{I,Q}\},m}(t+\Delta\tau^k_m)dt, \qquad (4.9)$$

which simplifies for rectangular pulses and negligible ionospheric intra-band dispersion to

$$R(\Delta\tau^k_m) = \begin{cases} 1 - \frac{|\Delta\tau^k_m|}{T_c} & \text{if } |\Delta\tau^k_m| \leq T_c \\ 0 & \text{otherwise.} \end{cases} . \qquad (4.10)$$

Obviously, increasing the integration time T_i improves the correlation result $\tilde{C}^k_m$ as long as the frequency error $\Delta\omega^k_m T_i$ remains sufficiently small. A phase discriminator extracts the phase from the correlation result. It is generally assumed that both the Delay Locked Loop (DLL) and the Frequency Locked Loop (FLL) are in lock, i.e. $\Delta\tau^k_m \ll 1$, $\Delta\omega^k_m \ll 1$ and, thus, $R(\Delta\tau^k_m) \approx 1$. In this case, the correlation result simplifies to

$$\tilde{C}^k_m \approx \sqrt{\mathcal{P}^k_m} \cdot T_i \cdot e^{j\Delta\phi^k_m} + \tilde{n}^k_m. \qquad (4.11)$$

A widely used phase discriminator is the classical Costas' product discriminator which is independent of the data bit and described by Kaplan and Hegarty in [28] as

$$\Delta\phi^k_{\mathrm{prod},m}(t_i) = \frac{1}{(\sqrt{\mathcal{P}^k_m} \cdot T_i)^2} \cdot \tilde{C}^k_{\mathrm{I},m}(t_i)\tilde{C}^k_{\mathrm{Q},m}(t_i) = \Delta\phi^k_m(t_i) + \eta_{\phi^k_{\mathrm{prod},m}}(t_i), \qquad (4.12)$$

For high and low SNR, the maximum likelihood phase estimator is the four-quadrant arctangent discriminator [28], i.e.

$$\Delta\phi_{\mathrm{atan}}(t_i) = \mathrm{atan}_2(\tilde{C}_{\mathrm{Q},m}(t_i), \tilde{C}_{\mathrm{I},m}(t_i)) = \Delta\phi^k_m(t_i) + \eta_{\phi^k_{\mathrm{atan},m}}(t_i). \qquad (4.13)$$

4.1 Vector phase locked loops

The joint tracking of all satellites goes back to Sennott and Senfer [10] and Spilker [11] who have developed the Vector Delay Locked Loop (DLL) of Fig. 4.1. The tracking errors are transformed into position domain by weighted least-squares estimation. The position errors and receiver clock offset errors are then individually filtered, back-transformed to range domain and integrated. The main benefit of this VDLL is the adaptive weighting of satellites, i.e. the stronger signals help to track the weaker signals. The filtered least-squares position corrections can also be directly integrated to obtain an estimate of the receiver position.

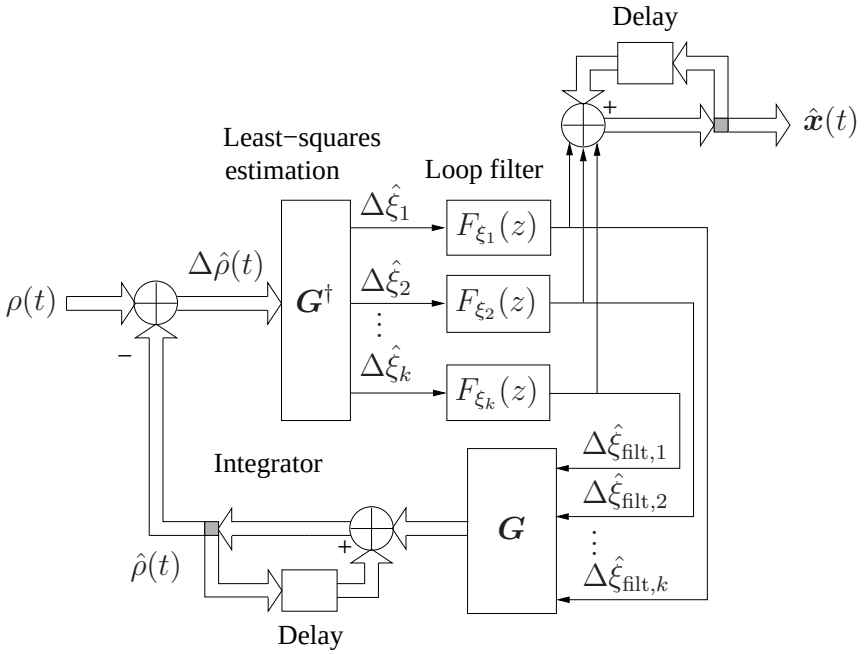

Figure 4.1: Vector Delay Locked Loop as proposed by Spilker in [11]: The pseudorange errors $\Delta\hat{\rho}(t)$ from K satellites are transformed into position domain, then filtered, inverse-transformed into range domain, and integrated. The filtered least-squares position corrections can also be directly integrated to obtain an estimate of the receiver position.

Note that the estimation of atmospheric errors was not included in the least-squares estimation of [10] and [11]. A possible reason might be that the authors worried about the noise amplification due to the estimation of additional parameters. However, these atmospheric errors are projected by the least-squares estimation and the back-transformation into

$$\begin{aligned} \Delta\tilde{\boldsymbol{I}} &= \boldsymbol{H}(\boldsymbol{H}^T\boldsymbol{\Sigma}^{-1}\boldsymbol{H})^{-1}\boldsymbol{H}^T\boldsymbol{\Sigma}^{-1}\Delta\boldsymbol{I} \\ \Delta\tilde{\boldsymbol{T}} &= \boldsymbol{H}(\boldsymbol{H}^T\boldsymbol{\Sigma}^{-1}\boldsymbol{H})^{-1}\boldsymbol{H}^T\boldsymbol{\Sigma}^{-1}\Delta\boldsymbol{T}. \end{aligned} \tag{4.14}$$

The estimation of $\Delta\boldsymbol{I}$ and $\Delta\boldsymbol{T}$ after the tracking loop becomes much more difficult as a separation into a mapping function and a zenith delay is no longer feasible. Therefore, Henkel et al. have suggested the inclusion of atmospheric delays in the least-squares

estimation in the tracking loop in [16] and [23]. The vector tracking of carrier phase is more challenging due to its higher precision and the existence of an unknown integer ambiguity for each satellite and frequency. It is described in the next section.

4.1.1 Co-Op tracking

Zhodzishsky, Yudanov, Veitsel and Ashjaee have first applied vector tracking to carrier phase in [21]. The phase offsets provided by the discriminators were transformed into position and receiver clock offsets by least-squares estimation. The estimates were then filtered and transformed back to range domain. As ambiguities, atmospheric delays and biases were neglected in the least-squares estimation, Zhodzishsky et al. also used individual loop filters, and combined the filtered ranges of individual and joint filters in the oscillators. This "Co-Op tracking" led to a substantial reduction of the tracking errors in Javad receivers [21].

Fig. 4.2 shows an extended version of Zhodzishsky's vector tracking [22]. The upper part includes the vector tracking of the carrier phases and the lower one refers to the joint tracking of the Doppler shifts. The incoming signal is first multiplied with the NCO generated signal, then correlated with the receiver generated code, and fed into a discriminator for extracting the phase (Costa's discriminator, (1.10)) or Doppler shift. The extracted phases are the basis for the joint tracking of the carrier phases on multiple frequencies. The following model is used for the discriminator outputs:

$$\begin{bmatrix} \lambda_1 \Delta\phi_1^k(t_i) \\ \vdots \\ \lambda_M \Delta\phi_M^k(t_i) \end{bmatrix} = \underbrace{\begin{bmatrix} 1 & q_{11}^2 \\ \vdots & \vdots \\ 1 & q_{1M}^2 \end{bmatrix}}_{\boldsymbol{X}} \begin{bmatrix} \Delta\tilde{r}^k(t_i) \\ \Delta\tilde{I}^k(t_i) \end{bmatrix} + \begin{bmatrix} \Delta\varepsilon_1^k(t_i) \\ \vdots \\ \Delta\varepsilon_M^k(t_i) \end{bmatrix}, \tag{4.15}$$

where $\Delta\tilde{r}^k(t_i)$ includes the time-difference in the true range and all non-dispersive error sources (clock offsets, troposphere offset) and $\Delta\tilde{I}^k(t_i)$ describes the time-difference in the ionospheric slant delay. The least-squares estimates of $\Delta\tilde{r}^k(t_i)$ and $\Delta\tilde{I}^k(t_i)$ are given by

$$\begin{bmatrix} \Delta\hat{\tilde{r}}^k(t_i) \\ \Delta\hat{\tilde{I}}^k(t_i) \end{bmatrix} = (\boldsymbol{X}^T \boldsymbol{\Sigma}^{-1}(t_i) \boldsymbol{X})^{-1} \boldsymbol{X}^T \boldsymbol{\Sigma}^{-1}(t_i) \begin{bmatrix} \lambda_1 \Delta\phi_1^k(t_i) \\ \vdots \\ \lambda_M \Delta\phi_M^k(t_i) \end{bmatrix}, \tag{4.16}$$

with the weighting matrix $\boldsymbol{\Sigma}_i(t_i)$. It is in general diagonal and adapted with time according to the noise characteristics. For the Costa's discriminator, the variances of the discriminator outputs were derived in (1.12). Note that the least-squares estimation does not require any knowledge about the satellite geometry and, thus, is not affected by orbital errors and satellite clock offsets. The multi-carrier VPLL is initialized by independent PLLs to avoid the estimation of integer ambiguities, atmospheric delays, and biases. Once at least two individual PLLs are in lock, the joint tracking is switched on.

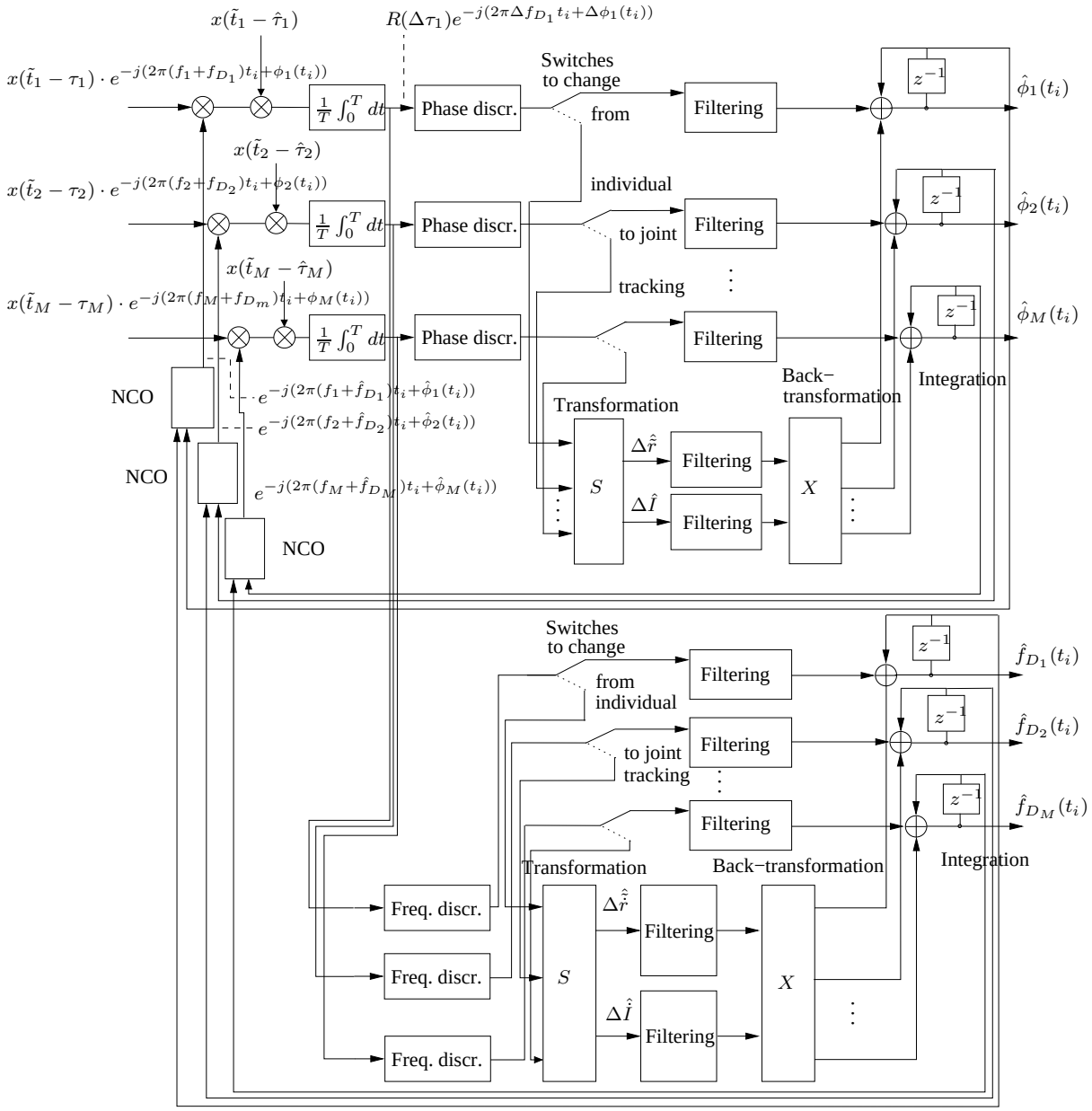

Figure 4.2: Functional diagram of Multicarrier Vector Phase and Frequency Locked Loop (MC-VPLL/FLL): The complex correlation results are the basis for the joint tracking of the carrier phases and Doppler shifts. The phase discriminators provide the phase tracking errors, which are transformed into range and ionospheric errors, then filtered, transformed back, and integrated. The Doppler shifts are determined similarly from the frequency discriminators. The obtained phases and Doppler shifts are then used to steer the NCOs. The joint tracking is initialized by independent PLLs to avoid the estimation of integer ambiguities and biases. Once at least two PLLs are in lock, the joint tracking is switched on.

Fig. 4.3 shows the carrier phase range residuals for time-differenced Galileo measurements on E1, E5a and E5b. The small magnitude confirms the validity of our model. Note that the residuals on E5a and E5b are larger than the ones on E1, which is a consequence of the small distance between the E5a and E5b frequencies. The small variations on E5a and E5b are caused by carrier phase multipath.

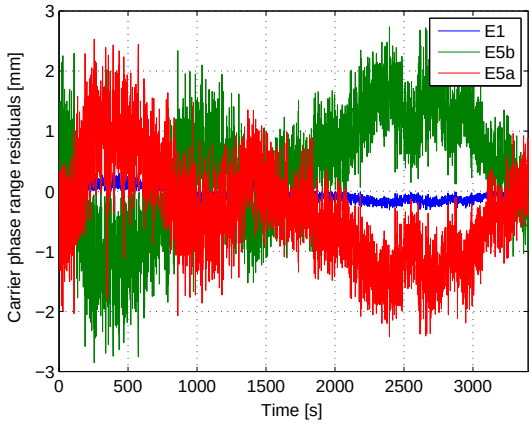

Figure 4.3: Carrier phase range residuals for time-differenced measurements: The small magnitude of the range residuals confirms the validity of our measurement model. The variations in the residuals of the E5a and E5b carrier phases indicate some multipath.

The joint tracking has been further expanded to include measurements from multiple satellites by Giger et al. in [12] and [13]. The spectral and spatial correlation between the carrier phases is exploited in a Kalman filter and a linear controller.

4.1.2 Multi-Carrier VPLL performance during ionospheric scintillations

This subsection shows the benefit of the VPLL during ionospheric scintillations that arise from random fluctuations of electron density in the E and F regions of the ionosphere. These scintillations result in frequent deep fades in amplitude and a substantial increase in phase noise. The VPLL suppresses the peaks in tracking errors as deep fades in amplitude do not occur at all satellites simultaneously.

Let us consider the following model for the received signal:

$$s(t) = A(t)e^{j\phi(t)} = A_0(t)\delta A(t)e^{j(\phi_0(t)+\delta\phi(t))}, \tag{4.17}$$

with the nominal amplitude $A_0(t)$ and phase $\phi(t)$ (without scintillation) and its variations $\delta A(t)$, $\delta\phi(t)$ due to scintillations. Pullen et al. modeled the intensity variations $\delta I(t) = \delta A(t)^2$ by a Nakagami distribution in [31], i.e.

$$p(\delta I) = \frac{m(m\delta I)^{m-1}}{(m-1)!}e^{-m\delta I}, \tag{4.18}$$

with $m = 1/S_4^2$ and the scintillation intensity index $S_4 = \sigma(\delta I)/\mathrm{E}\{\delta I\}$. Scintillation samples $\delta A[i]$ and $\delta\phi[i]$ are generated according to the wideband model described by Pullen et al. in [31] and by Hegarty et al. in [30]. First, two statistically independent sequences $\delta\tilde{I} \sim \mathcal{N}(0, \sigma_I^2)$ and $\delta\tilde{\phi} \sim \mathcal{N}(0, 1)$ of white Gaussian noise are computed. Then, a linear transformation is performed to introduce correlation between amplitude and phase scintillations, i.e.

$$\begin{bmatrix} \delta I \\ \delta\phi \end{bmatrix} = \begin{bmatrix} 1 & 0 \\ \rho_{\delta\phi\delta I}\sigma_{\delta\phi}/\sigma_{\delta I} & \sigma_{\delta\phi}\sqrt{1-\sigma^2_{\delta\phi\delta I}} \end{bmatrix} \begin{bmatrix} \delta\tilde{I} \\ \delta\tilde{\phi} \end{bmatrix}, \tag{4.19}$$

where $\sigma_{\delta\phi\delta I}$ denotes the correlation coefficient between intensity and phase scintillations. A set of cascaded band-pass, low-pass and high-pass Butterworth filters is then applied to introduce time correlation and the desired power spectral density of the form $P_\phi(f) = K \cdot f^{-p}$ with a unitless slope of $p = \{2, \ldots, 5.5\}$. The transfer function of the cascaded filters is given by Pullen et al. in [31] as

$$|H(f)|^2 = K \cdot \frac{f^{2m_h}}{f^{2m_h} + c^{2m_h}} \cdot \frac{d^{2m_l}}{f^{2m_l} + d^{2m_l}} \cdot \frac{f^2 + a_0^2}{f^2 + b_0^2} \cdot \frac{f^2 + a_1^2}{f^2 + b_1^2} \cdot \ldots \cdot \frac{f^2 + a_n^2}{f^2 + b_n^2}, \tag{4.20}$$

where the filter orders m_h, m_l and the corner frequencies c, d, $a_0, \ldots, a_n$ and $b_0, \ldots, b_n$ are chosen to best fit the strong scintillation data of Basu [32]. Note that the integral $\int_0^\infty |H(f)|^2 df = 1$ is normalized by the gain K and that different filters are used for intensity and phase scintillations. After spectral shaping, the scintillation samples are transformed from a Gaussian to the Gamma/Nakagami distribution of (4.18). The carrier to noise power ratio $C_m/N_0(t_i)$ is linear proportional to the scintillation intensity δI which is generated for each satellite independently.

Fig. 4.4 shows the achievable tracking performance of the multicarrier, multisatellite VPLL compared to independent PLLs for moderate ionospheric scintillations [23].

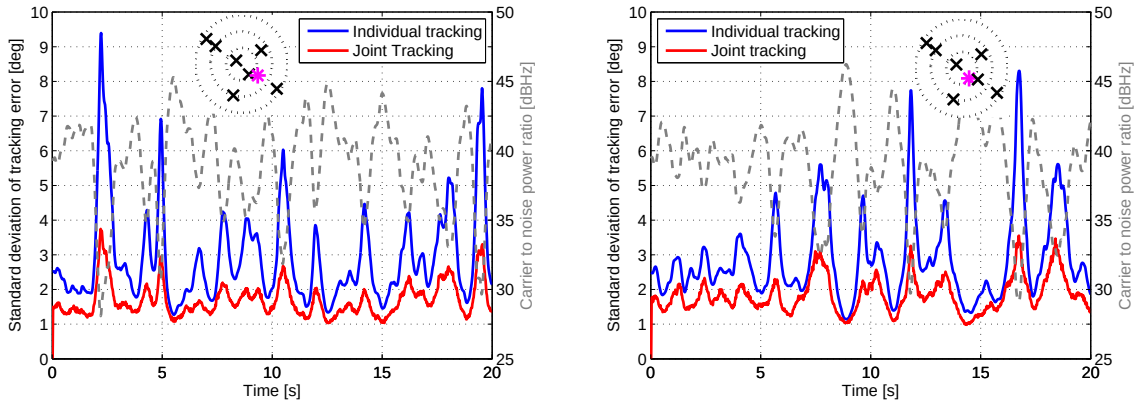

(a) Tracking of moderate elevation satellite

(b) Tracking of high elevation satellite

Figure 4.4: Benefit of multicarrier, multisatellite VPLL over independent tracking of eight Galileo satellites on three frequencies for moderate ionospheric scintillations ($S_4 = 0.7$ on all satellites) and $B_\mathrm{L} = 10$Hz. Two of the eight tracked satellites are shown.

A weighted least-squares estimation was used to transform the carrier tracking errors of the discriminators into range, clock offset, ionospheric and tropospheric errors. The dashed lines refer to the carrier to noise power ratios that vary substantially due to scintillations. The skyplots indicate the Galileo geometry (as seen from TUM) and the scintillation intensity, i.e. signals from 8 satellites that are affected by moderate scintillations ($S_4 = 0.7$) with deep fades up to 15 dB. The same scintillation intensity has been assumed for all frequencies (E1, E5a, E5b) which corresponds to a worst-case assumption. A filter bandwidth of $B_\mathrm{L} = 10$ Hz, a pre-detection integration time of $T_i = 20$ ms and an average carrier to noise power ratio of $C/N_0 = 45$ dB-Hz has been chosen. The joint tracking of all satellites reduces the peaks in tracking errors by up to 4 dB.

4.2 Compensation of ionospheric wideband effects

The main lobe and the first two side lobes of the Galileo E5 signal have together a bandwidth of 51 MHz which is more than 25 times the bandwidth of the GPS C/A code and results in a substantial reduction of the noise level. Gao et al. have shown in [34] that the ionospheric dispersion within the wideband Galileo signals is not negligible. It causes ripples in the code signal that result in a power shift in correlation result from the real part to the imaginary part. If no wideband correction is applied, the phase tracked by an independent PLL is biased by $14°/100\,\mathrm{TECU}$, and this bias can not be mapped to the ionospheric delay. Therefore, an efficient method for the suppression of wideband ionospheric effects is described in this section.

4.2.1 Introduction to ionospheric wideband effects

The derivation of the code correlation result $\tilde{C}_m^k$ in (4.1)-(4.8) includes the distortion due to a dispersive delay. For the ionosphere, the dispersive delay is given by

$$\tau_{\mathrm{I},m}^k(f) = \frac{40.3 \cdot \mathrm{TEC}^k}{f_m^2 \cdot c}, \tag{4.21}$$

where TEC^k represents the total electron content. The distortion of $\tilde{C}_m^k$ is caused by the distortion of the chip, that can be determined from

$$\tilde{c}_{\{\mathrm{I,Q}\},m}^k(t) = \mathcal{F}^{-1}\{\mathcal{F}\{c_{\{\mathrm{I,Q}\},m}^k(t)\} \cdot e^{-j2\pi f \tau_{\mathrm{I},m}^k(f)}\}. \tag{4.22}$$

As the transmit signals are bandlimited, the Fourier transform has to be evaluated only for $|f| \leq \mathrm{BW}$.

Fig. 4.5 and 4.6 show the impact of the receiver bandwidth on the signal deformation of a BPSK modulated signal (E5a). The signal that is not affected by the ionosphere is depicted as a reference in blue. The dispersive ionosphere delays the signal (100 TECU) and shifts some power from the real part (shown in red) to the imaginary part (shown in green). For BW = 20 MHz, the ripples due to the Gibb's phenomenon are dominating over the ripples due the ionospheric dispersion within the E5a band.

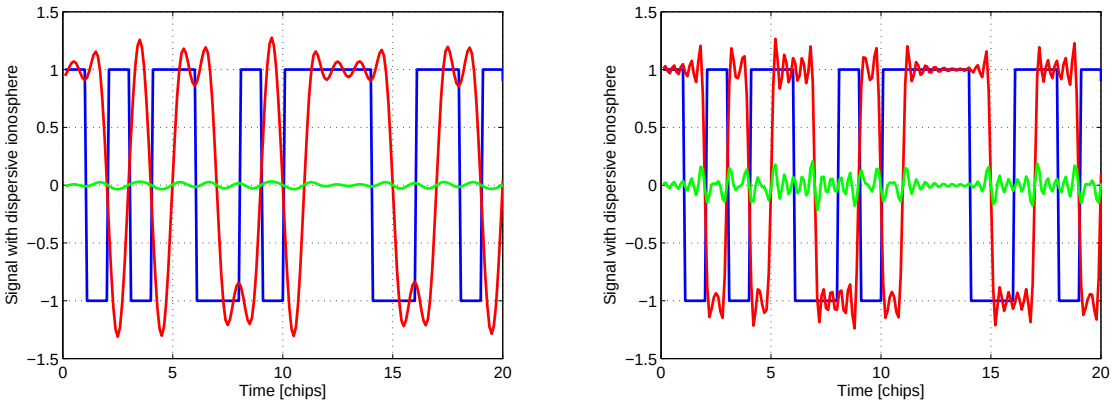

(a) E5a BPSK signal with 20 MHz bandwidth (b) E5a BPSK signal with 50 MHz bandwidth

Figure 4.5: Signal distortion by wideband iono. effects (100 TEC) and band limitation

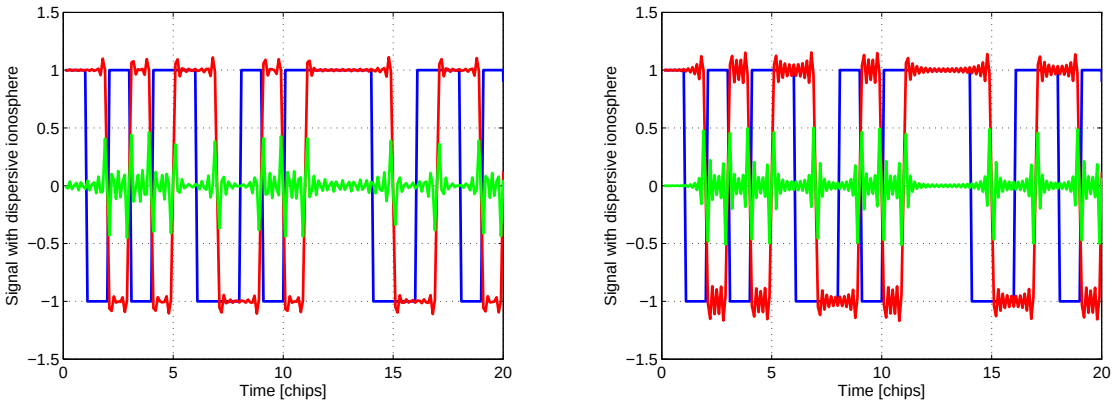

(a) E5a BPSK signal with 75 MHz bandwidth (b) E5a BPSK signal with 100 MHz bandwidth

Figure 4.6: Signal distortion by wideband iono. effects (100 TEC) and band limitation

The degradation of correlation and tracking results remains negligible for this modulation and bandwidth. Increasing the bandwidth reduces the Gibb's phenomenon but increases the ionospheric dispersion. For the real part of the signal, the smallest ripples can be observed for a bandwidth of 75 MHz. For the imaginary part of the signal, the amplitude of the ripples increases monotonously with the bandwidth.

Fig. 4.7 shows that the ionospheric dispersion is much more critical for the AltBOC E5 signal as a significant part of the power is allocated at the edges of the E5 band with a bandwidth of 50 MHz. The Gibb's phenomenon is also more pronounced due to the use of a subcarrier which increases the number of chip transitions. Thus, the chips can no longer be recognized from the degraded signal shape.

Fig. 4.8 shows the correlation result. A reduced real-valued correlation peak can be observed for the AltBOC E5 signal as some part of the power is shifted from the real part to the imaginary part. Moreover, the correlation function is smoother compared to a non-

dispersive ionospheric delay. The temporal shift of the correlation function corresponds to the ionospheric delay on the carrier frequency, i.e. the dispersion within the E5 band does not cause any additional delay for the code measurements.

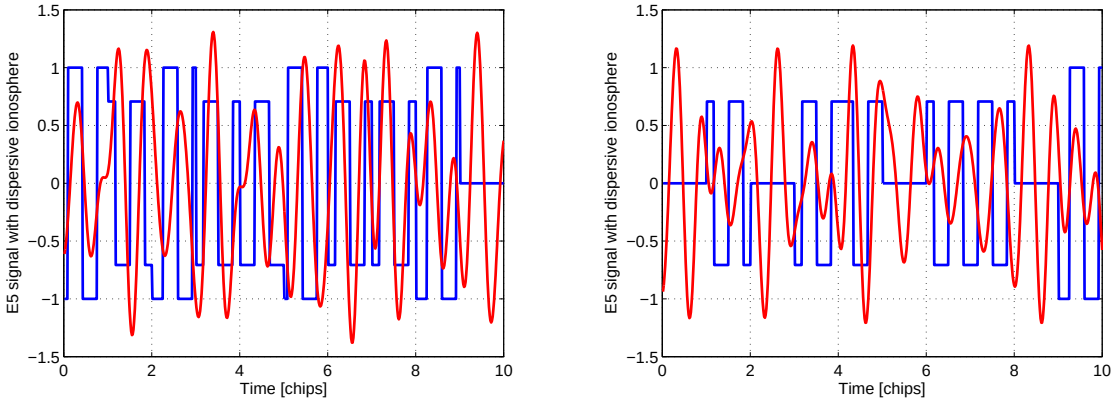

(a) E5 AltBOC signal: real part (b) E5 AltBOC signal: imaginary part

Figure 4.7: Signal distortion by wideband ionospheric effects for 100 TECU

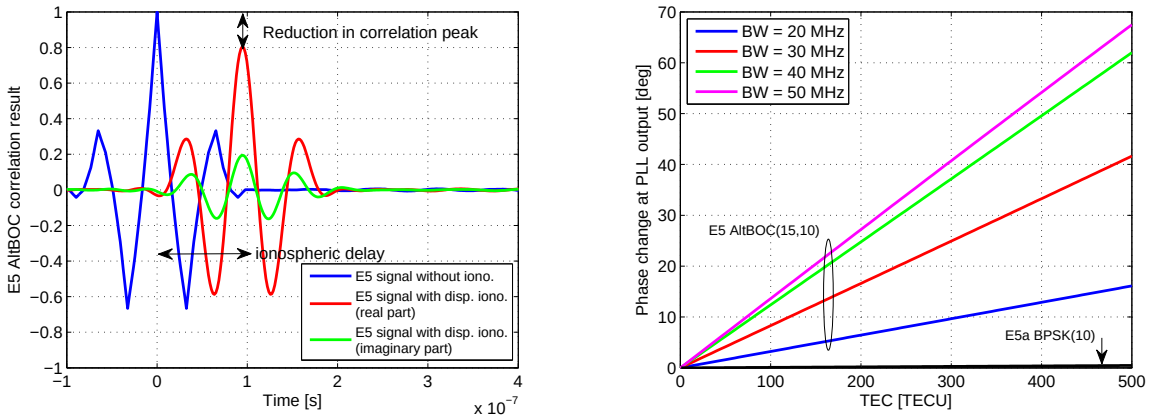

(a) E5 correlation result for 100 TECU (b) Phase bias of PLL output

Figure 4.8: Impact of wideband ionospheric effects on correlation and carrier tracking

The complex correlation function $R\left(\Delta\tau_m^k\right)$ results in a PLL tracking error given by

$$\Delta\phi_m^k(\Delta\tau_{m,\max}^k) = \operatorname{atan}\left(\frac{\Im\left(R(\Delta\tau_{m,\max}^k)\right)}{\Re\left(R(\Delta\tau_{m,\max}^k)\right)}\right) \quad \text{with} \quad \Delta\tau_{m,\max}^k = \arg\max_{\Delta\tau_m^k} |R(\Delta\tau_m^k)|, \tag{4.23}$$

It is shown for different TEC^k and filter bandwidths in Fig. 4.8b. The PLL tracking error $\Delta\phi_m^k$ increases linear with TEC but remains less than 0.5° for the E5a/E5b signals even during an active ionosphere. However, a phase offset of 15° can be observed for AltBOC(15,10) tracking during normal ionospheric conditions and of up to 70° during ionospheric storms.

4.2.2 Ionospheric wideband correction for carrier tracking

The wideband ionospheric effects can be equalized in frequency domain by multiplication with the conjugate complex of $e^{-j2\pi f \tau^k_{\mathrm{I},m} \tau(f)}$, i.e.

$$\hat{r}^k(t) = \mathcal{F}^{-1}\{\mathcal{F}\{\tilde{r}^k(t)\} e^{+j2\pi f \hat{\tau}^k_{\mathrm{I},m}(f)}\}, \tag{4.24}$$

which requires some knowledge about the ionospheric delay $I^k_m = \tau^k_{\mathrm{I},m}$ at carrier frequency f_m. As the intra-band ionospheric dispersion does not change the code delay, an estimate $\hat{I}^k_m$ can be obtained by combining code measurements on two frequencies in a geometry-free, ionosphere-preserving linear combination. Replacing $\tilde{r}^k(t)$ by (4.1) in (4.24) yields

$$\hat{r}^k(t) = \mathcal{F}^{-1}\{\mathcal{F}\{r^k(t)\} e^{-j2\pi f (\tau^k_{\mathrm{I},m}(f) - \hat{\tau}^k_{\mathrm{I},m}(f))}\}, \tag{4.25}$$

i.e. the remaining distortion equals the one corresponding to $\tau^k_{\mathrm{I},m} - \hat{\tau}^k_{\mathrm{I},m}$. Fig. 4.8 shows that an accuracy of 10 TECU is sufficient to suppress the phase bias due to wideband ionospheric effects to less than 1°.

This method requires an FFT of the downconverted signal and an IFFT after the application of the wideband correction. Alternatively, a phase correction can be determined from a look-up table (e.g. Fig. 4.8b) and applied directly to the tracked carrier phases. The equalization in frequency domain is omitted, which improves the efficiency of this method as it does not require the FFT and IFFT.

5

Estimation of phase and code biases

5.1 Estimation of phase and code biases

Ambiguity resolution for precise point positioning requires the precise knowledge of satellite phase and code biases on each frequency. These biases can be determined by a network of reference stations. The following model shall be used for undifferenced phase and code measurements of satellite k, receiver r and epoch t_n:

$$\begin{aligned}
\lambda_1\phi^k_{1,r}(t_n) &= g^k_r(t_n) - I^k_{1,r}(t_n) + \lambda_1 N^k_{1,r} + \beta_{1,r} + \beta^k_1 + p^k_1(t_n) + \varepsilon^k_{1,r}(t_n) \\
\lambda_2\phi^k_{2,r}(t_n) &= g^k_r(t_n) - q^2_{12} I^k_{1,r}(t_n) + \lambda_2 N^k_{2,r} + \beta_{2,r} + \beta^k_2 + p^k_2(t_n) + \varepsilon^k_{2,r}(t_n) \\
\rho^k_{1,r}(t_n) &= g^k_r(t_n) + I^k_{1,r}(t_n) + b_{1,r} + b^k_1 + \eta^k_{1,r}(t_n) \\
\rho^k_{2,r}(t_n) &= g^k_r(t_n) + q^2_{12} I^k_{1,r}(t_n) + b_{2,r} + b^k_2 + \eta^k_{2,r}(t_n), \qquad (5.1)
\end{aligned}$$

where g_r denotes the range including clock errors and tropospheric delay, $\beta_{m,r}$ is the receiver phase bias, β^k_m is the satellite phase bias, $b_{m,r}$ is the receiver code bias, b^k_m is the satellite code bias, p^k_m is the satellite antenna phase center variation, $\eta^k_{m,r}$ is the code noise, and $\varepsilon^k_{m,r}$ is the phase noise on frequency $m = \{1, 2\}$. Multipath errors are included in the phase and code noise.

A dynamical model is used for the geometry term $g^k_r(t_n)$ which can be split into the range r^k_r, the clock offsets $c\delta\tau_r$ and $c\delta\tau^k$ and tropospheric delays T^k_r, i.e.

$$g^k_r(t_n) = g^k_r(t_{n-1}) + \Delta t \cdot \dot{g}^k_r(t_{n-1}) + w_{g^k_r}(t_n) = r^k_r(t_n) + c \cdot (\delta\tau_r(t_n) - \delta\tau^k) + T^k_r(t_n),$$

where $w_{g_r^k}(t_n) \sim \mathcal{N}(0, \sigma^2_{w_{g_r^k}})$ denotes the process noise to model accelerations. The slant ionospheric delay $I^k_{1,r}$ is modeled as $I^k_{1,r}(t_n) = m_{\mathrm{I}}(E^k_r(t_n)) \cdot I_{\mathrm{v}}(t_n)$ with the vertical ionospheric delay I_{v} at the ionospheric pierce point (IPP) and the mapping function m_{I} that is given by

$$m_{\mathrm{I}}(E^k_r(t_n)) = \frac{1}{\sqrt{1 - \frac{\cos^2(E^k_r(t_n))}{(1+h/R_{\mathrm{e}})^2}}}, \tag{5.2}$$

with the elevation angle $E^k_r(t_n)$ and the height h of the ionospheric shell above the ground.

The carrier phase measurements are also affected by time-variant antenna phase center variations $p^k_m(t_n)$ which are caused by a shift of $(\Delta x, \Delta y)$ between the actual and original phase center of the satellite antenna pattern. Fig. 5.1 shows the relationship between p^k_m, Δx_m and Δy_m as suggested by Schmid et al. in [85]. The latter two are extremely stable in time if a coordinate system is chosen where the z-axis points towards the center of the earth, the y-axis corresponds to the rotation axis of the solar panels and the x-axis completes the right-hand system. The time dependency of p^k_m is introduced by the azimuth α and the nadir angle z'.

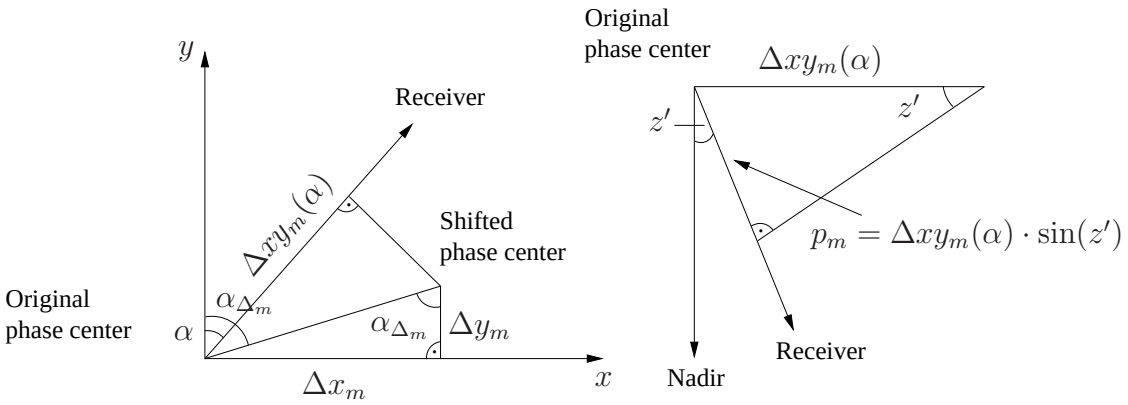

Figure 5.1: Relationship between horizontal offset, azimuth direction and nadir angle: The coordinate system is chosen such the y-axis corresponds to the rotation axis of the solar panels, the z-axis points towards the earth and the x-axis completes the coordinate system.

Receiver measurements in azimuth direction α are affected by

$$\Delta xy_m(\alpha) = \sqrt{\Delta x_m^2 + \Delta y_m^2} \cdot \cos(\alpha_{\Delta_m} - \alpha), \tag{5.3}$$

which reaches its maximum for $\alpha = \alpha_{\Delta_m}$. The right subfigure shows the impact of the nadir angle z' which causes a maximum phase bias for $z' = 14°$. The combined effect of azimuth and nadir-dependent phase center variations is given by

$$p^k_m(z'(t_n), \alpha(t_n)) = \sqrt{\Delta x_m^2 + \Delta y_m^2} \cdot \sin(z'(t_n)) \cdot \cos\left(\operatorname{atan}\left(\frac{\Delta x_m}{\Delta y_m}\right) - \alpha(t_n)\right). \tag{5.4}$$

Schmid et al. have suggested a fitting of these phase center variations p^k_m for a fixed nadir

angle z'_0 to the cosine function

$$f(\alpha) = A_m \cdot \cos(\alpha_{\Delta_m} - \alpha), \tag{5.5}$$

with the amplitude A_m and the phase shift α_{Δ_m}. The horizontal offsets Δx_m and Δy_m to be compensated for are then obtained from

$$\Delta x_m = \frac{A}{\sin(z'_0)} \cdot \sin(\alpha_{\Delta_m}) \quad \text{and} \quad \Delta y_m = \frac{A}{\sin(z'_0)} \cdot \cos(\alpha_{\Delta_m}). \tag{5.6}$$

Schmid et al. [85] and Schmid and Rothacher [86] processed double difference measurements from more than 150 IGS stations with the BERNESE software [87] to determine the ionosphere-free combination of these biases together with station coordinates, tropospheric parameters, orbit parameters and Earth rotation parameters. The PCVs were estimated with a 1 mm accuracy as a function of azimuth and nadir angles and confirmed the derived harmonic behaviour. They also observed an impressive day to day repeatability for the azimuthal PCV of block IIR satellites.

The phase and code noise is assumed to follow a zero mean white Gaussian distribution. The standard deviation $\sigma_{\rho^k_{m,r}}$ of the code tracking error has been set to the Cramer Rao bound which is given by

$$\Gamma_m = \frac{c}{\sqrt{\frac{E_s}{N_0} \cdot \frac{\int (2\pi f)^2 |S_m(f)|^2 df}{\int |S_m(f)|^2 df}}}, \tag{5.7}$$

with the speed of light c, the signal to noise power ratio $\frac{E_s}{N_0}$, and the power spectral density $S_m(f)$ that has been derived by Betz in [3] for binary offset carrier (BOC) modulated signals. Table 5.1 shows the Cramer Rao bound for the wideband Galileo signals at a signal to noise power ratio of 45dB [45]. The phase noise standard deviations $\sigma_{\phi^k_{m,r}}$ have been assumed to be 1 mm.

Table 5.1: Cramer Rao Bounds for $E_s/N_0 = 45$dB

	Signal	BW [MHz]	Γ [cm]
E1	MBOC	20	11.14
E5	AltBOC(15,10)	51	1.95
E5a	BPSK(10)	20	7.83
E5b	BPSK(10)	20	7.83

Ge et al. [89], Gabor and Nerem [88] and Laurichesse and Mercier [90] have tried to estimate L1 and L2 satellite-satellite single difference (SD) phase biases. The derivation is briefly introduced here and starts with the geometry-free, ionosphere-free Melbourne-Wübbena combination [91]. It combines the SD phase measurements $\Delta\phi^{kl}_{1,r}$, $\Delta\phi^{kl}_{2,r}$ and the SD code measurements $\Delta\rho^{kl}_{1,r}$, $\Delta\rho^{kl}_{2,r}$ on the frequencies f_1 and f_2 as

$$\left(\frac{f_1}{f_1 - f_2}\lambda_1 \Delta\phi^{kl}_{1,r} - \frac{f_2}{f_1 - f_2}\lambda_2 \Delta\phi^{kl}_{2,r}\right) - \left(\frac{f_1}{f_1 + f_2}\Delta\rho^{kl}_{1,r} + \frac{f_2}{f_1 + f_2}\Delta\rho^{kl}_{2,r}\right) = \lambda_w \Delta b^{kl}_{w,r} + \Delta\varepsilon^{kl}_{w,r}, \tag{5.8}$$

with the widelane wavelength

$$\lambda_{\mathrm{w}} = \frac{1}{\frac{1}{\lambda_1} - \frac{1}{\lambda_2}}, \tag{5.9}$$

the combined ambiguity/ bias term

$$\Delta b^{kl}_{\mathrm{w},r} = \Delta N^{kl}_{1,r} - \Delta N^{kl}_{2,r} + \Delta\beta^{kl}_1 - \Delta\beta^{kl}_2 - \frac{f_1 - f_2}{f_1 + f_2} \cdot \frac{\Delta b^{kl}_1}{\lambda_1} - \frac{f_1 - f_2}{f_1 + f_2} \cdot \frac{\Delta b^{kl}_2}{\lambda_2}, \tag{5.10}$$

with the SD ambiguities ΔN^{kl}_m, the SD phase biases $\Delta\beta^{kl}_m$ in units of cycles, the SD code biases Δb^{kl}_m in units of meters, and the combined phase and code noise $\Delta\varepsilon^{kl}_{\mathrm{w},r}$.

In a second step, the geometry-preserving, ionosphere-free phase only combination is computed, i.e.

$$\frac{f_1^2}{f_1^2 - f_2^2}\lambda_1\Delta\phi^{kl}_{1,r} - \frac{f_2^2}{f_1^2 - f_2^2}\lambda_2\Delta\phi^{kl}_{2,r} = \Delta g^{kl}_r + \Delta b^{kl}_{\mathrm{c},r} + \Delta\varepsilon^{kl}_{\mathrm{c},r}, \tag{5.11}$$

with the geometry term Δg^{kl}_r including the range and some non-dispersive errors that are introduced in the next section, and the combined ambiguity/ bias term

$$\Delta b^{kl}_{\mathrm{c},r} = \frac{f_1^2}{f_1^2 - f_2^2} \cdot \lambda_1(\Delta N^{kl}_{1,r} + \Delta\beta^{kl}_1) - \frac{f_2^2}{f_1^2 - f_2^2} \cdot \lambda_2(\Delta N^{kl}_{2,r} + \Delta\beta^{kl}_2). \tag{5.12}$$

The biases of the Melbourne-Wübbena combination and of the ionosphere-free combination are combined into

$$\frac{f_1 + f_2}{c} \cdot \Delta b^{kl}_{\mathrm{c},r} - \frac{f_2}{f_1 - f_2} \cdot \Delta b^{kl}_{\mathrm{w},r} = \Delta N^{kl}_{1,r} + \Delta\tilde{\beta}^{kl}_1, \tag{5.13}$$

with

$$\Delta\tilde{\beta}^{kl}_1 = \Delta\beta^{kl}_1 + \frac{f_2}{f_1 + f_2} \cdot \frac{\Delta b^{kl}_1}{\lambda_1} + \frac{f_2}{f_1 + f_2} \cdot \frac{\Delta b^{kl}_2}{\lambda_2}. \tag{5.14}$$

Similarly, an estimate of the phase bias on the second frequency can be obtained as

$$\Delta\tilde{\beta}^{kl}_2 = \Delta\beta^{kl}_2 + \frac{f_1}{f_1 + f_2} \cdot \frac{\Delta b^{kl}_1}{\lambda_1} + \frac{f_1}{f_1 + f_2} \cdot \frac{\Delta b^{kl}_2}{\lambda_2}. \tag{5.15}$$

The transmission of $\Delta\tilde{\beta}^{kl}_1$ and $\Delta\tilde{b}^{kl}_2$ enables an unbiased estimation of L1 and L2 integer ambiguities at the mobile receiver. However, these pseudo-phase biases can only be applied to linear combinations of the form

$$\alpha_1 \cdot \left(\lambda_1\Delta\phi^{kl}_1 + \frac{f_2}{f_1 + f_2}\Delta\rho^{kl}_1 + \frac{f_2\lambda_1}{f_1 + f_2}\frac{\Delta\rho^{kl}_2}{\lambda_2}\right) + \alpha_2 \cdot \left(\lambda_2\Delta\phi^{kl}_2 + \frac{f_1\lambda_2}{f_1 + f_2}\frac{\Delta\rho^{kl}_1}{\lambda_1} + \frac{f_1}{f_1 + f_2}\Delta\rho^{kl}_2\right),$$

which is an ionosphere-free combination for any α_1 and α_2. It is also geometry-preserving if

$$\alpha_1\frac{f_1 + f_2}{f_1} + \alpha_2\frac{f_1 + f_2}{f_2} = 1, \tag{5.16}$$

and integer-preserving if

$$\alpha_1 = \frac{j_1\lambda}{\lambda_1} \quad \text{and} \quad \alpha_2 = \frac{j_2\lambda}{\lambda_2} \quad \text{with} \quad \{j_1, j_2\} \overset{!}{\in} \mathbb{Z}. \tag{5.17}$$

Combining (5.16) and (5.17) yields the wavelength of the combination:

$$\lambda = \frac{1}{j_1 + j_2}\frac{c}{f_1 + f_2} \leq \frac{f_1}{f_1 + f_2}\lambda_1, \tag{5.18}$$

which means that the bias estimates of (5.14) and (5.14) are only applicable to ionosphere-free narrowlane combinations with a wavelength of at most 10.7 cm.

The next subsections describe an alternative approach for the estimation of undifferenced receiver and satellite phase biases which has been suggested in [92] and [93] to overcome the previous shortcomings.

5.1.1 Parameter mapping

The estimation of all biases in Eq. (5.1) is not feasible but also not required as some biases can not be separated from the remaining parameters. Additionally, the integer ambiguity resolution is simplified if the code biases are mapped to the ranges and ionospheric delays, i.e.

$$\begin{aligned} \rho^k_{1,r}(t_n) &= g^k_r(t_n) + q^2_{11} I^k_r(t_n) + b_{1,r} + b^k_1 + \eta^k_{1,r}(t_n) \\ &= \underbrace{\left(g^k_r(t_n) + b_{g_r} + b_{g^k}\right)}_{\tilde{g}^k_r(t_n)} + q^2_{11} \underbrace{\left(I^k_r(t_n) + b_{I_r} + b_{I^k}\right)}_{\tilde{I}^k_r(t_n)} + \eta^k_{1,r}(t_n) \end{aligned} \tag{5.19}$$

and

$$\begin{aligned} \rho^k_{2,r}(t_n) &= g^k_r(t_n) + q^2_{12} I^k_r(t_n) + b_{2,r} + b^k_2 + \eta^k_{2,r}(t_n) \\ &= \underbrace{\left(g^k_r(t_n) + b_{g_r} + b_{g^k}\right)}_{\tilde{g}^k_r(t_n)} + q^2_{12} \underbrace{\left(I^k_r(t_n) + b_{I_r} + b_{I^k}\right)}_{\tilde{I}^k_r(t_n)} + \eta^k_{2,r}(t_n). \end{aligned} \tag{5.20}$$

Equations (5.19) and (5.20) can be solved for the receiver dependant biases b_{g_r} and b_{I_r} which can be expressed as a function of $b_{1,r}$ and $b_{2,r}$, i.e.

$$b_{g_r} = \frac{b_{2,r} - q^2_{12} b_{1,r}}{1 - q^2_{12}}, \quad b_{I_r} = \frac{b_{1,r} - b_{2,r}}{1 - q^2_{12}}. \tag{5.21}$$

Similarly, the satellite dependant biases b^k_g and b^k_I are given by

$$b_{g^k} = \frac{b^k_2 - q^2_{12} b^k_1}{1 - q^2_{12}}, \quad b_{I^k} = \frac{b^k_1 - b^k_2}{1 - q^2_{12}}. \tag{5.22}$$

The mapping of code biases to ranges and ionospheric delays also effects the phase measurements which are rewritten as

$$\begin{aligned}\lambda_1\phi^k_{1,r}(t_n) &= \tilde{g}^k_r(t_n) - q^2_{11}\tilde{I}^k_{1,r}(t_n) + \lambda_1 N^k_{1,r} + \tilde{\beta}_{1,r} + \tilde{\beta}^k_1 + p^k_1(t_n) + \varepsilon^k_{1,r}(t_n)\\ \lambda_2\phi^k_{2,r}(t_n) &= \tilde{g}^k_r(t_n) - q^2_{12}\tilde{I}^k_{1,r}(t_n) + \lambda_2 N^k_{2,r} + \tilde{\beta}_{2,r} + \tilde{\beta}^k_2 + p^k_2(t_n) + \varepsilon^k_{2,r}(t_n),\end{aligned} \quad (5.23)$$

with

$$\begin{aligned}\tilde{\beta}_{1,r} &= \beta_{1,r} - b_{g_r} + q^2_{11} b_{I_r}, \quad \tilde{\beta}^k_1 = \beta^k_1 - b_{g^k} + q^2_{11} b_{I^k}\\ \tilde{\beta}_{2,r} &= \beta_{2,r} - b_{g_r} + q^2_{12} b_{I_r}, \quad \tilde{\beta}^k_2 = \beta^k_2 - b_{g^k} + q^2_{12} b_{I^k}.\end{aligned} \quad (5.24)$$

Moreover, the satellite phase biases of one satellite can be absorbed by the receiver phase biases, i.e.

$$\begin{aligned}\tilde{\tilde{\beta}}_{1,r} &= \tilde{\beta}_{1,r} + \tilde{\beta}^1_1, \quad \tilde{\tilde{\beta}}^k_1 = \tilde{\beta}^k_1 - \tilde{\beta}^1_1\\ \tilde{\tilde{\beta}}_{2,r} &= \tilde{\beta}_{2,r} + \tilde{\beta}^1_2, \quad \tilde{\tilde{\beta}}^k_2 = \tilde{\beta}^k_2 - \tilde{\beta}^1_2,\end{aligned} \quad (5.25)$$

which results in $R+K-1$ remaining phase biases $\tilde{\tilde{\beta}}_{m,r}$ and $\tilde{\tilde{\beta}}^k_m$ on each frequency. These phase biases are estimated from a global network of reference stations, e.g. the 37 Galileo Sensor Stations (GSS) that are shown in Fig. 5.2.

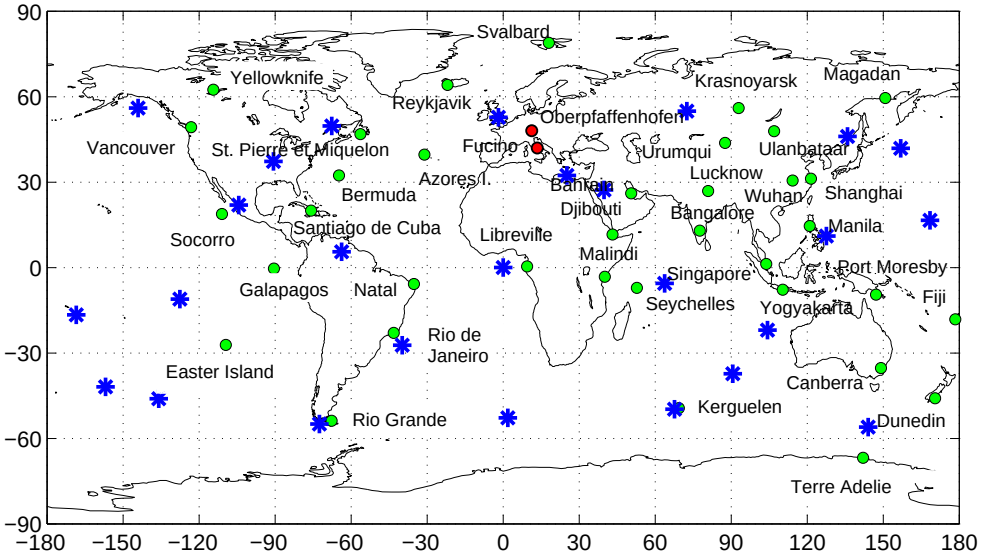

Figure 5.2: Bias estimation with global network of 37 Galileo Sensor Stations, the two control centers at Oberpfaffenhofen and Fucino, and the projection of 27 Galileo satellite positions for a single snapshot.

The phase biases of (5.25) can not be separated from the integer ambiguities and, thus, are mapped to a subset of $R+K-1$ ambiguities. Let $\boldsymbol{H}_{\tilde{\tilde{\beta}}_{m,r}}$, $\boldsymbol{H}_{\tilde{\tilde{\beta}}^k_m}$ and $\boldsymbol{H}_N$ describe the

mapping of receiver/ satellite phase biases and integer ambiguities to the measurements. Applying a Gaussian elimination to the combined coefficent matrices gives

$$\left(\prod_{i=1}^{N} \boldsymbol{P}_i\right) \left[\boldsymbol{H}_{\tilde{\tilde{\beta}}_{m,r}}, \quad \boldsymbol{H}_{\tilde{\tilde{\beta}}_m^k}, \quad \boldsymbol{H}_N\right] \begin{bmatrix} \tilde{\tilde{\boldsymbol{\beta}}}_{m,r} \\ \tilde{\tilde{\boldsymbol{\beta}}}_m^k \\ \boldsymbol{N} \end{bmatrix} = \boldsymbol{C} \begin{bmatrix} \tilde{\tilde{\boldsymbol{\beta}}}_{m,r} \\ \tilde{\tilde{\boldsymbol{\beta}}}_m^k \\ \boldsymbol{N} \end{bmatrix}, \tag{5.26}$$

where each $\boldsymbol{P}_i$ represents a step of the Gaussian elimination and $\boldsymbol{C}$ is the coefficient matrix in row canonical form.

Example for $R = 3$ receivers, $K = 3$ satellites and $s = \sum_{r=1}^{R} K_r = 9$ ambiguities:

$$\begin{bmatrix} \tilde{\tilde{\boldsymbol{\beta}}}_{\boldsymbol{m,r}} \\ \tilde{\tilde{\boldsymbol{\beta}}}_m^{\boldsymbol{k}} \\ \boldsymbol{N} \end{bmatrix} = \left[\tilde{\tilde{\beta}}_{m,1},\ \tilde{\tilde{\beta}}_{m,2},\ \tilde{\tilde{\beta}}_{m,3},\ \tilde{\tilde{\beta}}_m^2,\ \tilde{\tilde{\beta}}_m^3,\ N_{m,1}^1,\ N_{m,1}^2,\ N_{m,1}^3, \ldots, N_{m,3}^1,\ N_{m,3}^2,\ N_{m,3}^3\right]^T$$

$$\left[\boldsymbol{H}_{\tilde{\tilde{\beta}}_{m,r}},\ \boldsymbol{H}_{\tilde{\tilde{\beta}}_m^k},\ \boldsymbol{H}_N\right] =$$

$$\left[\begin{array}{ccc|cc|ccccccccc} 1 & 0 & 0 & 0 & 0 & \lambda_m & 0 & 0 & 0 & 0 & 0 & 0 & 0 & 0 \\ 1 & 0 & 0 & 1 & 0 & 0 & \lambda_m & 0 & 0 & 0 & 0 & 0 & 0 & 0 \\ 1 & 0 & 0 & 0 & 1 & 0 & 0 & \lambda_m & 0 & 0 & 0 & 0 & 0 & 0 \\ 0 & 1 & 0 & 0 & 0 & 0 & 0 & 0 & \lambda_m & 0 & 0 & 0 & 0 & 0 \\ 0 & 1 & 0 & 1 & 0 & 0 & 0 & 0 & 0 & \lambda_m & 0 & 0 & 0 & 0 \\ 0 & 1 & 0 & 0 & 1 & 0 & 0 & 0 & 0 & 0 & \lambda_m & 0 & 0 & 0 \\ 0 & 0 & 1 & 0 & 0 & 0 & 0 & 0 & 0 & 0 & 0 & \lambda_m & 0 & 0 \\ 0 & 0 & 1 & 1 & 0 & 0 & 0 & 0 & 0 & 0 & 0 & 0 & \lambda_m & 0 \\ 0 & 0 & 1 & 0 & 1 & 0 & 0 & 0 & 0 & 0 & 0 & 0 & 0 & \lambda_m \end{array}\right]$$

and after Gaussian elimination

$$\boldsymbol{C} = \left[\begin{array}{ccc|cc|ccccccccc} 1 & 0 & 0 & 0 & 0 & 0 & 0 & * & 0 & 0 & * & * & * & * \\ 0 & 1 & 0 & 0 & 0 & 0 & 0 & * & 0 & 0 & * & * & * & * \\ 0 & 0 & 1 & 0 & 0 & 0 & 0 & * & 0 & 0 & * & * & * & * \\ 0 & 0 & 0 & 1 & 0 & 0 & 0 & * & 0 & 0 & * & * & * & * \\ 0 & 0 & 0 & 0 & 1 & 0 & 0 & * & 0 & 0 & * & * & * & * \\ \hline 0 & 0 & 0 & 0 & 0 & \mathbf{1} & 0 & * & 0 & 0 & * & * & * & * \\ 0 & 0 & 0 & 0 & 0 & 0 & \mathbf{1} & * & 0 & 0 & * & * & * & * \\ 0 & 0 & 0 & 0 & 0 & 0 & 0 & 0 & \mathbf{1} & 0 & * & * & * & * \\ 0 & 0 & 0 & 0 & 0 & 0 & 0 & 0 & 0 & \mathbf{1} & * & * & * & * \end{array}\right] \tag{5.27}$$

where the columns marked by $(*)$ are linear dependent on the other columns. The mapping of ambiguities to biases is given by

$$\tilde{\tilde{\beta}}_{m,r} = \tilde{\tilde{\beta}}_{m,r} + \sum_{r'=1}^{R} \sum_{k=1}^{K_{r'}} \boldsymbol{C}_{r,R+K-1+(\sum_{r''=1}^{r'-1} K_{r''})+k} \cdot N_{m,r'}^k \quad \forall\, r \in \{1, \ldots, R\}, \tag{5.28}$$

$$\tilde{\tilde{\beta}}_m^k = \tilde{\tilde{\beta}}_m^k + \sum_{r=1}^{R} \sum_{k'=1}^{K_r} \boldsymbol{C}_{R+k,R+K-1+(\sum_{r'=1}^{r-1} K_{r'})+k'} \cdot N_{m,r}^{k'} \quad \forall\, k \in \{1,\ldots,K\}. \tag{5.29}$$

and the mapping of ambiguities to ambiguities is given by the lower part of $\boldsymbol{C}$. The pivot element in the $R+K-1+l$-th row with $l \in \{1,\ldots,s-(K+R-1)\}$ represents the ambiguity of receiver $r_\mu(l)$ and satellite $k_\mu(l)$. Thus, the mapping of ambiguities to ambiguities is given by

$$\tilde{N}_{m,r(l)}^{k(l)} = N_{m,r(l)}^{k_\mu(l)} + \sum_{r=r_\mu(l)}^{R} \sum_{k=k(l)+1}^{K_r} \boldsymbol{C}_{R+K-1+l,R+K-1+(\sum_{r'=1}^{r-1} K_{r'})+k} \cdot N_{m,r}^{k}. \tag{5.30}$$

Fig. 5.3 shows the set of K_r visible satellites for each of the 37 GSS at a certain epoch. As the number of all ambiguities s exceeds the number of biases, the ambiguities are subdivided into two subsets: One subset which includes float valued ambiguities due to the absorption of biases, and one which includes integer valued ambiguities. The latter one is in general much larger than the first one. The choice of the subset of integer ambiguities offers some additional degrees of freedom. This subset is chosen such that the error in the bias estimation is minimized.

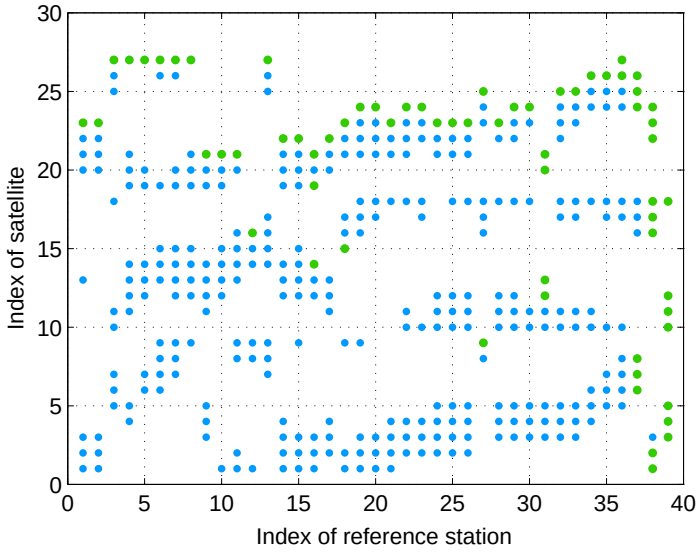

Figure 5.3: Integer ambiguities for the network of 37 Galileo Sensor Stations and the two control centers for a snapshot of 27 Galileo satellites: Each column shows the visible satellites for a particular reference station. The blue dots refer to ambiguities that have to be estimated while the green ones are absorbed in the biases. The green dots include the ambiguities with the largest satellite index for each reference station as well as the largest reference station index for each satellite. As 5 ambiguities fulfill both criteria simultaneously, four additional ambiguities have to be removed for a full rank measurement sensitivity matrix.

5.1.2 Estimation of code and carrier phase biases

The precise estimation of receiver and satellite biases requires a network of reference stations and measurements from a few hundred epochs which motivates a recursive state estimation, e.g. by a Kalman filter [95]. The state vector includes the ranges, range rates, range accelerations, ionospheric delays, receiver and satellite phase biases and ambiguities, i.e.

$$\boldsymbol{x}_n = \left[\tilde{\boldsymbol{g}}^T(t_n),\, \dot{\boldsymbol{g}}^T(t_n),\, \ddot{\boldsymbol{g}}^T(t_n),\, \tilde{\boldsymbol{I}}^T(t_n),\, \tilde{\boldsymbol{\beta}}_{\mathrm{R}}^T,\, \tilde{\boldsymbol{\beta}}_{\mathrm{S}}^T, \boldsymbol{N}\right]^T, \tag{5.31}$$

with

$$\tilde{\boldsymbol{g}}(t_n) = \begin{bmatrix} \tilde{g}_1^1(t_n) \\ \vdots \\ \tilde{g}_1^{K_1}(t_n) \\ \vdots \\ \tilde{g}_R^{K_R}(t_n) \end{bmatrix}, \quad \dot{\boldsymbol{g}}(t_n) = \begin{bmatrix} \dot{g}_1^1(t_n) \\ \vdots \\ \dot{g}_1^{K_1}(t_n) \\ \vdots \\ \dot{g}_R^{K_R}(t_n) \end{bmatrix}, \quad \ddot{\boldsymbol{g}}(t_n) = \begin{bmatrix} \ddot{g}_1^1(t_n) \\ \vdots \\ \ddot{g}_1^{K_1}(t_n) \\ \vdots \\ \ddot{g}_R^{K_R}(t_n) \end{bmatrix} \tag{5.32}$$

and

$$\tilde{\boldsymbol{I}}(t_n) = \begin{bmatrix} \tilde{I}_1^1(t_n) \\ \vdots \\ \tilde{I}_1^{K_1}(t_n) \\ \vdots \\ \tilde{I}_R^{K_R}(t_n) \end{bmatrix}, \quad \tilde{\boldsymbol{\beta}}_{\mathrm{R}} = \begin{bmatrix} \tilde{\beta}_{1,1} \\ \vdots \\ \tilde{\beta}_{1,R} \\ \tilde{\beta}_{2,1} \\ \vdots \\ \tilde{\beta}_{2,R} \end{bmatrix}, \quad \tilde{\boldsymbol{\beta}}_{\mathrm{S}} = \begin{bmatrix} \tilde{\beta}_1^2 \\ \vdots \\ \tilde{\beta}_1^K \\ \tilde{\beta}_2^2 \\ \vdots \\ \tilde{\beta}_2^K \end{bmatrix} \tag{5.33}$$

and the subset of integer valued ambiguities $\boldsymbol{N}$. The phase and code measurements of Eq. (5.1) are written in matrix-vector notation as

$$\begin{aligned} \boldsymbol{z}_n &= \left[\phi_{1,1}^1(t_n), \ldots, \phi_{1,R}^{K_R}(t_n), \ldots, \phi_{2,R}^{K_R}(t_n), \rho_{1,1}^1(t_n), \ldots, \rho_{1,R}^{K_R}(t_n), \ldots, \rho_{2,R}^{K_R}(t_n)\right]^T, \\ &= \boldsymbol{H}_n^{(1)}\boldsymbol{x}_n + \boldsymbol{v}_n, \end{aligned} \tag{5.34}$$

where $\boldsymbol{H}_n^{(1)}$ is implicitly given by Eq. (5.1), (5.2), (5.19), (5.20), (5.25), (5.31) and (5.32) and depends only on λ_1 and λ_2. The measurement noise is assumed to be uncorrelated between satellites and zero-mean white Gaussian distributed, i.e. $\boldsymbol{v}_n \sim \mathcal{N}(\boldsymbol{0}, \boldsymbol{\Sigma}_{\mathrm{v}})$ with the variances $\sigma^2_{\phi^k_{m,r}}$ and $\sigma^2_{\rho^k_{m,r}}$. The state space model for $\boldsymbol{x}_n$ is given by

$$\boldsymbol{x}_n = \boldsymbol{\Phi}\boldsymbol{x}_{n-1} + \boldsymbol{w}_n, \tag{5.35}$$

with the process noise $\boldsymbol{w}_n$ and the state transition matrix $\boldsymbol{\Phi}$ that is obtained from the dynamic model of (5.2):

$$\boldsymbol{\Phi} = \begin{bmatrix} \boldsymbol{1}^{s\times s} & \Delta t \cdot \boldsymbol{1}^{s\times s} & \frac{1}{2}\Delta t^2 \cdot \boldsymbol{1}^{s\times s} & \boldsymbol{0} \\ \boldsymbol{0} & \boldsymbol{1}^{s\times s} & \Delta t \cdot \boldsymbol{1}^{s\times s} & \boldsymbol{0} \\ \boldsymbol{0} & \boldsymbol{0} & \boldsymbol{1}^{s\times s} & \boldsymbol{0} \\ \boldsymbol{0} & \boldsymbol{0} & \boldsymbol{0} & \boldsymbol{1}^{3s\times 3s} \end{bmatrix}, \tag{5.36}$$

where Δt represents the interval between two measurement epochs. A random walk process is assumed for the ranges: The third derivatives of the ranges are assumed to be zero mean white Gaussian noise with variance S_p. The range accelerations, range rates and ranges are then obtained through integration. The variances and covariances of the ranges and their derivatives are obtained as (see e.g. Brown and Hwang in [95])

$$\begin{aligned}
\mathrm{E}\left\{\ddot{x}(\Delta t)\ddot{x}(\Delta t)\right\} &= \mathrm{E}\left\{\int_0^{\Delta t} n(u)du \cdot \int_0^{\Delta t} n(v)dv\right\} = \mathrm{E}\left\{\int_0^{\Delta t}\int_0^{\Delta t} n^2(u)\delta(u-v)dudv\right\} \\
&= \int_0^{\Delta t}\int_0^{\Delta t} S_p \cdot 1 \cdot 1 \cdot \delta(u-v)dudv = S_p \cdot \Delta t \\
\mathrm{E}\{\dot{x}(\Delta t)\ddot{x}(\Delta t)\} &= \int_0^{\Delta t}\int_0^{\Delta t} S_p \cdot u \cdot 1 \cdot \delta(u-v)dudv = \frac{1}{2}S_p \cdot \Delta t^2 \\
\mathrm{E}\{x(\Delta t)\ddot{x}(\Delta t)\} &= \int_0^{\Delta t}\int_0^{\Delta t} S_p \cdot \frac{1}{2}u^2 \cdot 1 \cdot \delta(u-v)dudv = \frac{1}{6}S_p \cdot \Delta t^3 \\
\mathrm{E}\{\dot{x}(\Delta t)\dot{x}(\Delta t)\} &= \int_0^{\Delta t}\int_0^{\Delta t} S_p \cdot u \cdot v \cdot \delta(u-v)dudv = \frac{1}{3}S_p \cdot \Delta t^3 \\
\mathrm{E}\{x(\Delta t)\dot{x}(\Delta t)\} &= \int_0^{\Delta t}\int_0^{\Delta t} S_p \cdot \frac{1}{2}u^2 \cdot v \cdot \delta(u-v)dudv = \frac{1}{8}S_p \cdot \Delta t^4 \\
\mathrm{E}\{x(\Delta t)x(\Delta t)\} &= \int_0^{\Delta t}\int_0^{\Delta t} S_p \cdot \frac{1}{2}u^2 \cdot \frac{1}{2}v^2 \cdot \delta(u-v)dudv = \frac{1}{20}S_p \cdot \Delta t^5, \qquad (5.37)
\end{aligned}$$

which gives the state covariance matrix of range, range-rate and range-acceleration related errors:

$$\boldsymbol{\Sigma}_{\mathrm{w},\tilde{g}\dot{\tilde{g}}\ddot{\tilde{g}}} = S_p\Delta t \cdot \begin{bmatrix} \frac{1}{20}\cdot\Delta t^4 & \frac{1}{8}\cdot\Delta t^3 & \frac{1}{6}\cdot\Delta t^2 \\ \frac{1}{8}\cdot\Delta t^3 & \frac{1}{3}\cdot\Delta t^2 & \frac{1}{2}\cdot\Delta t \\ \frac{1}{6}\cdot\Delta t^2 & \frac{1}{2}\cdot\Delta t & 1 \end{bmatrix} \otimes \mathbf{1}^{s\times s}, \qquad (5.38)$$

which is used to model the covariance matrix of the whole state vector as

$$\boldsymbol{\Sigma}_{\mathrm{w}} = \begin{bmatrix} \boldsymbol{\Sigma}_{\mathrm{w},\tilde{g}\dot{\tilde{g}}\ddot{\tilde{g}}} & & \\ & \boldsymbol{\Sigma}_{\mathrm{w},I} & \\ & & \boldsymbol{\Sigma}_{\mathrm{w},b} \end{bmatrix}, \qquad (5.39)$$

with

$$\boldsymbol{\Sigma}_{\mathrm{w},I} = \sigma_{\mathrm{I}}^2 \cdot \mathbf{1}^{s\times s} \quad \text{and} \quad \boldsymbol{\Sigma}_{\mathrm{w},b} = \mathbf{0}^{2s\times 2s}, \qquad (5.40)$$

i.e. no process noise is assumed for the biases and integer ambiguities. In the simulations, the third derivatives of the ranges are modeled as white Gaussian noise with variance $S_{\mathrm{p}} = 1\,(\mathrm{mm/s^2})^2\,\frac{1}{\mathrm{s}}$ m and $\sigma_I = 1$ cm.

The Kalman filter based estimation of $\boldsymbol{x}_n$ includes a prediction and an update step. The current state estimate $\hat{\boldsymbol{x}}_n^+$ is extrapolated with the state space model of (5.35), i.e.

$$\hat{\boldsymbol{x}}_{n+1}^- = \boldsymbol{\Phi}\hat{\boldsymbol{x}}_n^+. \qquad (5.41)$$

The covariance matrix of the predicted (a priori) state estimate follows as

$$\boldsymbol{P}_{\hat{x}_{n+1}^-} = \boldsymbol{\Phi}\boldsymbol{P}_{\hat{x}_n^+}\boldsymbol{\Phi}^T + \boldsymbol{\Sigma}_{\mathrm{w}}. \tag{5.42}$$

The predicted state is updated once the measurements of the next epoch are available, i.e. the a posteriori state estimate is given by

$$\hat{\boldsymbol{x}}_n^+ = \hat{\boldsymbol{x}}_n^- + \boldsymbol{K}_n\left(\boldsymbol{z}_n - \boldsymbol{H}_n^{(1)}\hat{\boldsymbol{x}}_n^-\right), \tag{5.43}$$

where $\boldsymbol{z}_n - \boldsymbol{H}_n^{(1)}\hat{\boldsymbol{x}}_n^-$ denotes the innovation or measurement residual and $\boldsymbol{K}_n$ is the Kalman gain. It is chosen such that

$$\min_{\boldsymbol{K}_n} \mathrm{E}\{\|\hat{\boldsymbol{x}}_n^+ - \boldsymbol{x}_n\|^2\} = \min_{\boldsymbol{K}_n} \mathrm{tr}(\boldsymbol{P}_{\hat{x}_n^+}), \tag{5.44}$$

where $\boldsymbol{P}_{\hat{x}_n^+}$ denotes the a posteriori state covariance matrix that is obtained from (5.43):

$$\boldsymbol{P}_{\hat{x}_n^+} = \boldsymbol{P}_{\hat{x}_n^-} - \boldsymbol{P}_{\hat{x}_n^-}\boldsymbol{H}_n^{(1),T}\boldsymbol{K}_n^T - \boldsymbol{K}_n\boldsymbol{H}_n^{(1)}\boldsymbol{P}_{\hat{x}_n^-} + \boldsymbol{K}_n(\boldsymbol{H}_n^{(1)}\boldsymbol{P}_{\hat{x}_n^-}\boldsymbol{H}_n^T + \boldsymbol{\Sigma}_{\mathrm{v}})\boldsymbol{K}_n^T. \tag{5.45}$$

Setting the matrix derivation $\partial\mathrm{tr}(\boldsymbol{P}_n^+)/\partial\boldsymbol{K}_n = \boldsymbol{0}$ and solving for $\boldsymbol{K}_n$ yields the optimal Kalman gain

$$\boldsymbol{K}_n = \boldsymbol{P}_{\hat{x}_n^-}\boldsymbol{H}_n^{(1),T}\left(\boldsymbol{H}_n^{(1)}\boldsymbol{P}_{\hat{x}_n^-}\boldsymbol{H}_n^{(1),T} + \boldsymbol{\Sigma}_{\mathrm{v}}\right)^{-1}, \tag{5.46}$$

which is used in (5.43) to obtain an a posteriori MMSE estimator. Equation (5.45) can be simplified by replacing the Kalman gain by (5.46), i.e.

$$\boldsymbol{P}_{\hat{x}_n^+} = \left(\boldsymbol{1} - \boldsymbol{K}_n\boldsymbol{H}_n^{(1)}\right)\boldsymbol{P}_{\hat{x}_n^-}. \tag{5.47}$$

Note that the estimation of integer ambiguities can be separated from the estimation of the real-valued ranges, range rates, ionospheric delays and biases by an orthogonal projection, i.e.

$$\tilde{\boldsymbol{z}}_n = \boldsymbol{P}_{\tilde{\boldsymbol{H}}^{(1)}}^{\perp}\boldsymbol{z}_n = \boldsymbol{P}_{\tilde{\boldsymbol{H}}^{(1)}}^{\perp}\left(\boldsymbol{A}\boldsymbol{N} + \boldsymbol{v}_n\right), \tag{5.48}$$

with

$$\boldsymbol{P}_{\tilde{H}^{(1)}}^{\perp} = \boldsymbol{1} - \tilde{\boldsymbol{H}}^{(1)}\left(\tilde{\boldsymbol{H}}^{(1),T}\boldsymbol{\Sigma}_{\mathrm{v}}^{-1}\tilde{\boldsymbol{H}}^{(1)}\right)^{-1}\tilde{\boldsymbol{H}}^{(1)}\boldsymbol{\Sigma}_{\mathrm{v}}^{-1}, \tag{5.49}$$

where $\tilde{\boldsymbol{H}}^{(1)}$ is obtained from $\boldsymbol{H}^{(1)}$ by removing the columns referring to the ambiguities. The Kalman filter based state estimation of (5.41)-(5.47) is then applied to the projected measurements. The obtained a posteriori float ambiguity estimates are then integer decorrelated and resolved by bootstrapping as described in (3.78) and (3.99). Once the ambiguities are resolved, the projection is omitted and the transformed receiver and satellite phase biases of (5.25) are estimated with a higher accuracy.

Benefit of ambiguity resolution

Fig. 5.4 shows the achievable accuracies for the receiver and satellite phase bias estimates using a network of $R = 20$ reference stations: Ranges, range rates, ionospheric delays, ambiguities, receiver and satellite phase biases are estimated by a Kalman filter. It is initialized by a least-squares solution from measurements of two epochs [93]. The float ambiguities are decorrelated and sequentially fixed after 200 epochs with an error rate of less than 10^{-9}. The fixing reduces the uncertainty in the bias estimates by a factor between 3 and 5. Dual frequency E1 and E5 code and carrier phase measurements from $K_r = 10$ satellites at R receivers have been simulated. As the bias estimation is performed on range domain, the achievable accuracy does not depend on the satellite geometry.

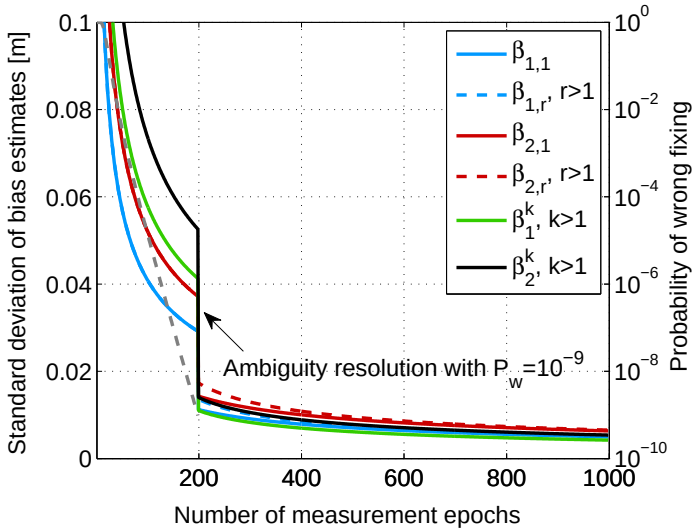

Figure 5.4: Achievable accuracies of receiver and satellite phase bias estimation with a Kalman filter: A network of $R = 20$ reference stations with $K_r = 10$ satellites has been simulated: The float ambiguities are decorrelated and sequentially fixed after 200 epochs with an error rate of less than 10^{-9}. The fixing reduces the standard deviations of the bias estimates by a factor between 3 and 5.

Benefit of a third frequency

Fig. 5.5 shows the benefit of measurements on a third frequency for bias estimation: If no ambiguities are fixed, the benefit of the third frequency for bias estimation remains negligible. However, the redundancy given by the third frequency enables an almost three times earlier ambiguity fixing, and, thus a higher accuracy of the bias estimates. Dual frequency E1-E5a and triple frequency E1-E5a-E5b measurements of $R = 20$ receivers and $K_r = 10$ satellites were simulated for the estimation of ranges, range rates, ionospheric delays, ambiguities, receiver and satellite phase biases.

Note that the code biases on the third frequency have to be estimated, as the ranges and ionospheric delays can absorb the code biases on only two frequencies. However,

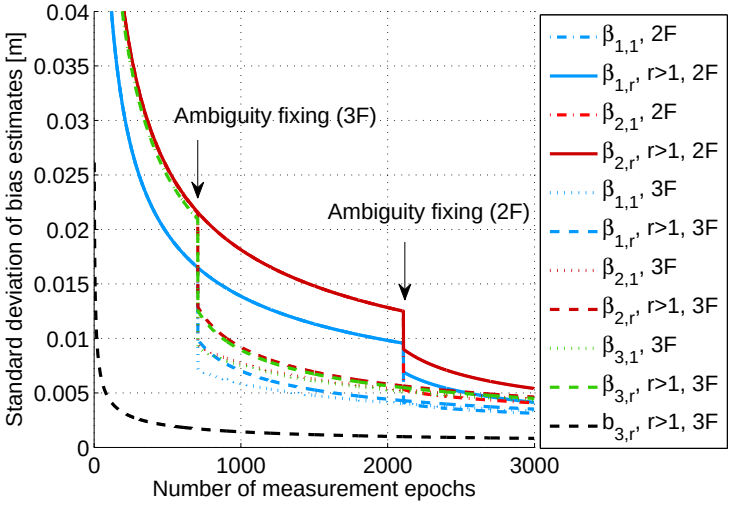

Figure 5.5: Bias estimation with dual frequency E1-E5a and triple frequency E1-E5a-E5b measurements: The redundancy given by the third frequency enables an almost three times earlier ambiguity fixing, and, thus a higher accuracy of the receiver phase bias estimates. The achievable accuracies are also shown for the code biases on the third frequency which have to be estimated as the ranges and ionospheric delays can absorb the code biases on only two frequencies.

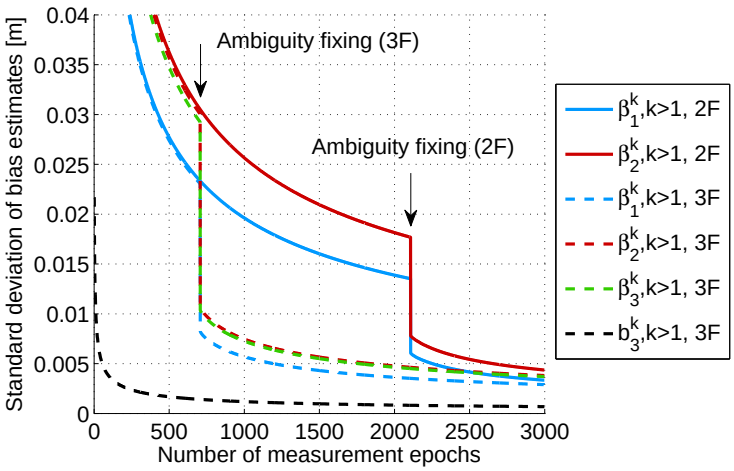

Figure 5.6: Benefit of measurements on a third frequency for bias estimation: The achievable accuracies refer to the satellite biases. The same scenario as in Fig. 5.5 has been assumed. The redundancy given by the third frequency results in an almost three times earlier ambiguity fixing with $P_{\mathrm{w}} = 10^{-9}$.

the absence of both ambiguities and biases on the other two code measurements (due to absorption by the range and ionospheric delay) enable a higher accuracy for the code bias estimates despite the increased code noise level.

Fig. 5.6 shows the achievable accuracies for the satellite phase and code bias estimates

for the same scenario. The satellite biases can be estimated with a slightly higher accuracy than the receiver biases once the ambiguities are fixed due to $R > K_r$. If no ambiguities are fixed, the receiver bias estimation benefits from the absorption of one satellite bias by the receiver biases.

Fig. 5.7 shows the impact of the network size R on the achievable bias accuracies. As long as no ambiguities are fixed, the bias estimation does not benefit from a large R as the number of ambiguities plus biases increases with KR. However, the gain in the bias estimation due to fixing depends on R and increases for larger networks due to the additional redundancy. The estimation of E5 satellite biases with $\sigma_{\hat{\beta}_2^k} = 1$ cm requires 325 epochs for $R = 20$, 750 epochs for $R = 8$ and several thousand epochs for $R = 2$.

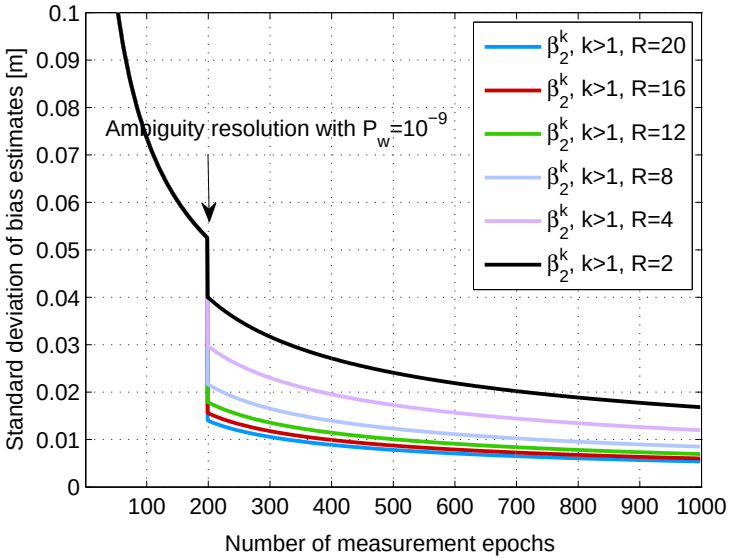

Figure 5.7: Benefit of large network for bias estimation: The fixing of ambiguities ($K_r = 10$) improves the satellite bias accuracy by a factor 4 for $R = 20$. The float ambiguity estimates are fixed sequentially with bootstrapping after integer decorrelation. The process noise is characterized by $S_p = 1$m and $\sigma_\mathrm{I} = 1$cm.

The estimation of receiver and satellite phase biases is validated with L1/ L2 GPS code and carrier phase measurements of the 37 geodetic SAPOS stations of the Landesamt für Vermessung u. Geoinformation in the next chapter. A sequential ambiguity fixing with integer decorrelation has been performed, i.e. the a posteriori float ambiguities of the Kalman filter were decorrelated into

$$\hat{\boldsymbol{N}}'^{+} = \boldsymbol{Z}\hat{\boldsymbol{N}}^{+}, \tag{5.50}$$

and the ambiguity to fix was chosen in each step by a minimization of the cost function

$$\min_{\hat{N}'^{,k,+}_{m,r}} w_1 \cdot |\hat{N}'^{,k,+}_{m,r} - [\hat{N}'^{k,+}_{m,r}]| + w_2 \cdot \sigma_{\hat{N}'^{,k,+}_{m,r}}, \tag{5.51}$$

which uses both the a posteriori statistical information $\sigma_{\hat{N}'^{,k,+}_{m,r}}$ of the Kalman filter and the actual deviation between the a posteriori estimate $\hat{N}'^{,k,+}_{m,r}$ and its rounded value $[\hat{N}'^{,k,+}_{m,r}]$. The coefficients w_1 and w_2 enable a certain weighting and where set in this work to 1.

As only a subset of ambiguities is fixed in each epoch, the decorrelated and partially fixed ambiguities are transformed back to the correlated search space in each epoch, i.e.

$$\hat{\boldsymbol{N}} = \boldsymbol{Z}^{-1}\hat{\hat{\boldsymbol{N}}}' = [\boldsymbol{\Lambda}_1,\ \boldsymbol{\Lambda}_2] \begin{bmatrix} \hat{\boldsymbol{N}}'_{\mathrm{A}} \\ \left[\hat{\boldsymbol{N}}'_{\mathrm{B}}\right] \end{bmatrix}, \tag{5.52}$$

which simplifies the system of equations $\boldsymbol{\Psi} = \boldsymbol{H}\boldsymbol{\xi} + \boldsymbol{A}\boldsymbol{N} + \boldsymbol{\varepsilon}$ to

$$\boldsymbol{\Psi} - \boldsymbol{A}\boldsymbol{\Lambda}_2\,[\boldsymbol{N}'_{\mathrm{B}}] = \boldsymbol{H}\boldsymbol{\xi} + \boldsymbol{A}\boldsymbol{\Lambda}_1\boldsymbol{N}'_{\mathrm{A}} + \boldsymbol{\varepsilon}. \tag{5.53}$$

Fig. **??** shows that the sequential fixing of L1 and L2 integer ambiguities substantially improves the phase bias estimates. The slight variations over time are caused by multipath of the reference stations. The second derivative of the ranges was additionally estimated to improve the stability of the satellite phase biases, i.e. the state vector of the Kalman filter includes the ranges, range rates, range accelerations, ionospheric delays, integer ambiguities, receiver and satellite phase biases.

Precise point positioning with integer ambiguity resolution requires precise estimates of the satellite phase biases $\tilde{\tilde{\beta}}^k_m$ and of the code biases b_{g^k}. As the latter one can not be separated from the clock offsets, the geometry term $\tilde{g}^k_r(t_n)$ of (5.19) is rewritten as

$$\tilde{g}^k_r(t_n) = \left(\boldsymbol{e}^k_r\right)^T \cdot \left(\boldsymbol{r}_r - \boldsymbol{r}^k(t_n)\right) + c \cdot \left(\delta\tilde{\tau}_r(t_n) - \delta\tilde{\tau}^k(t_n)\right) + m_{\mathrm{w}}(E^k_r(t_n)) \cdot T^k_{\mathrm{z},r}(t_n), \tag{5.54}$$

with

$$\begin{aligned} c\delta\tilde{\tau}_r(t_n) &= c\delta\tau_r(t_n) + b_{g_r} \\ c\delta\tilde{\tau}^k(t_n) &= c\delta\tau^k(t_n) - b^k_g. \end{aligned} \tag{5.55}$$

The station coordinates $\boldsymbol{r}_r$ shall be assumed known. A second Kalman filter is used to estimate the satellite positions $\boldsymbol{r}^k$, the satellite velocities $\dot{\boldsymbol{r}}^k$, the tropospheric zenith delays $T_{\mathrm{z},r}$ and the combined clock/bias terms $c\delta\tilde{\tau}_r$ and $c\delta\tilde{\tau}^k$ as states, i.e.

$$\boldsymbol{x}_n = \left[\boldsymbol{r}^{1,\mathrm{T}}, \ldots, \boldsymbol{r}^{K,\mathrm{T}}, \dot{\boldsymbol{r}}^{1,\mathrm{T}}, \ldots, \dot{\boldsymbol{r}}^{K,\mathrm{T}}, T_{\mathrm{z},1}, \ldots, T_{\mathrm{z},R}, c\delta\tilde{\tau}_1, \ldots, c\delta\tilde{\tau}_R, c\delta\tilde{\tau}^2, \ldots, c\delta\tilde{\tau}^K\right]^T, \tag{5.56}$$

As the $\boldsymbol{e}^k_r$ depend on the unknown satellite positions, the iterative Newton algorithm is integrated into the Kalman filter. Its a posteriori state estimates $\hat{\boldsymbol{x}}^+_n$ are computed from

the measurement vector $\boldsymbol{z}_n = \left[\tilde{g}_1^1(t_n), \ldots, \tilde{g}_R^K(t_n)\right]^T$, i.e.

$$\begin{aligned}
\hat{\boldsymbol{x}}_n^+ &= \hat{\boldsymbol{x}}_n^- + \boldsymbol{K}_n^{(2)}\left(\boldsymbol{z}_n - \boldsymbol{H}_n^{(2)}\hat{\boldsymbol{x}}_n^-\right) \\
&= \left(\mathbf{1} - \boldsymbol{K}_n^{(2)}\boldsymbol{H}_n^{(2)}\right)\hat{\boldsymbol{x}}_n^- + \boldsymbol{K}_n^{(2)}\boldsymbol{z}_n \\
&= \left(\mathbf{1} - \boldsymbol{K}_n^{(2)}\boldsymbol{H}_n^{(2)}\right)\boldsymbol{\Phi}\hat{\boldsymbol{x}}_{n-1}^+ + \boldsymbol{K}_n^{(2)}\boldsymbol{z}_n \\
&= \left(\mathbf{1} - \boldsymbol{K}_n^{(2)}\boldsymbol{H}_n^{(2)}\right)\boldsymbol{\Phi}\left(\mathbf{1} - \boldsymbol{K}_{n-1}^{(2)}\boldsymbol{H}_{n-1}^{(2)}\right)\hat{\boldsymbol{x}}_{n-1}^- \\
&\quad + \left(\mathbf{1} - \boldsymbol{K}_n^{(2)}\boldsymbol{H}_n^{(2)}\right)\boldsymbol{\Phi}\boldsymbol{K}_{n-1}^{(2)}\boldsymbol{z}_{n-1} + \boldsymbol{K}_n^{(2)}\boldsymbol{z}_n,
\end{aligned} \tag{5.57}$$

with the Kalman gain $\boldsymbol{K}_n^{(2)}$, the state transition matrix $\boldsymbol{\Phi}$ and the extended geometry matrix $\boldsymbol{H}_n^{(2)}$ which includes the unit vectors from the satellites to the receivers and a mapping function for transforming the tropospheric zenith delay into slant delays. Equation (5.57) can also be written in non-recursive form as

$$\hat{\boldsymbol{x}}_n^+ = \left[\prod_{l=1}^{n}(\mathbf{1} - \boldsymbol{K}_{n-l+1}\boldsymbol{H}_{n-l+1})\boldsymbol{\Phi}\right]\boldsymbol{\Phi}^{-1}\hat{\boldsymbol{x}}_1^- + \sum_{l=1}^{n}\left(\prod_{m=0}^{n-l-1}(\mathbf{1} - \boldsymbol{K}_{n-m}\boldsymbol{H}_{n-m})\boldsymbol{\Phi}\right)\boldsymbol{K}_l\boldsymbol{z}_l, \tag{5.58}$$

where the first term represents the impact of the state initialization and the second term describes the impact of the measurements on $\hat{\boldsymbol{x}}_n^+$.

5.1.3 Estimation of code biases and ionospheric grid

The code biases and the Grid Ionospheric Vertical Delays (GIVD) can be estimated also without integer ambiguity resolution. In this case, it is suggested to use the code measurements on at least two frequencies and two linear combinations of time-differenced carrier phase measurements: A geometry-preserving, ionosphere-free combination which makes the range rates observable, and a geometry-free, ionosphere-preserving combination which makes the ionospheric rates observable. The measurement model is written in matrix vector as

$$\boldsymbol{z}_n = \begin{bmatrix} \rho_1(t_n) \\ \rho_2(t_n) \\ \sum_{m=1}^{M}\alpha_m\lambda_m\left(\phi_m(t_{n+1}) - \phi_m(t_n)\right) \\ \sum_{m=1}^{M}\gamma_m\lambda_m\left(\phi_m(t_{n+1}) - \phi_m(t_n)\right) \end{bmatrix} = \underbrace{\begin{bmatrix} 1 & 0 & 1 & 0 \\ 1 & 0 & q_{12}^2 & 0 \\ 0 & \Delta t & 0 & 0 \\ 0 & 0 & 0 & \Delta t \end{bmatrix}}_{\mathbf{H}_n^{(2)}} \cdot \underbrace{\begin{bmatrix} \tilde{g}(t_n) \\ \dot{\tilde{g}}(t_n) \\ \tilde{I}(t_n) \\ \dot{\tilde{I}}(t_n) \end{bmatrix}}_{\mathbf{x}_n} + \mathbf{v}_n, \tag{5.59}$$

where α_m denote the weighing coefficients of the geometry-preserving, ionosphere-free combination and γ_m represent the weighting coefficients of the geometry-free, ionosphere-

preserving combination. Fig. 5.8 shows a 5° × 5° grid over Europe with the EGNOS RIMS stations (red circles) [96].

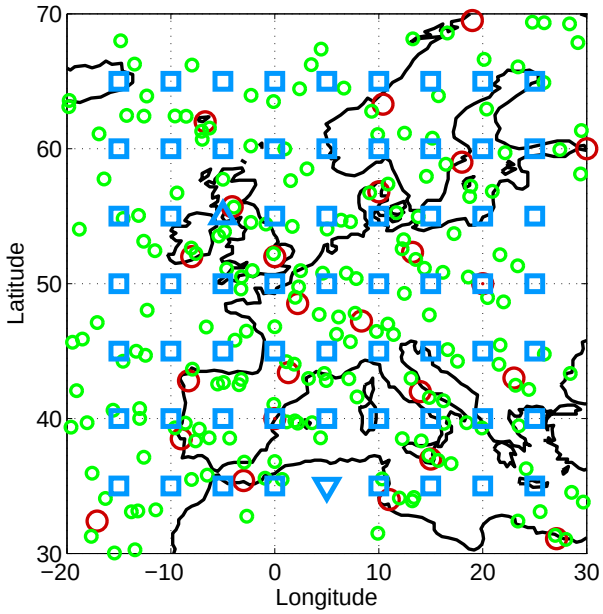

Figure 5.8: Ionospheric grid: Map of Europe with EGNOS RIMS stations (red circles), ionospheric pierce points (green circles) and ionospheric grid points (blue squares) of a 5° × 5° grid. The grid points for which the ionospheric delay can be estimated most and least accurately are also indicated.

The vertical ionospheric delays at the grid points (blue squares) shall be determined from the slant ionospheric delays at the pierce points (green circles). The latter ones are provided by a Kalman filter using the measurements of Eq. (5.59).

Let the vertical ionospheric delay at the ionospheric grid point (IGP) $(\lambda^{(l)}, \phi^{(l)})$ be denoted by $i_0^{(l)}$, the latitudinal gradient by $i_\phi^{(l)}$, the longitudinal gradient by $i_\lambda^{(l)}$ and its temporal gradients by $\dot{i}_0^{(l)}$, $\dot{i}_\phi^{(l)}$ and $\dot{i}_\lambda^{(l)}$. Then, the slant ionospheric delays in the surrounding of the IGP are modeled as

$$\begin{bmatrix} \tilde{I}_1^1 \\ \vdots \\ \tilde{I}_R^{K_R} \\ \dot{\tilde{I}}_1^1 \\ \vdots \\ \dot{\tilde{I}}_R^{K_R} \end{bmatrix} = \boldsymbol{M}\boldsymbol{H}_I \begin{bmatrix} i_0^{(l)} \\ i_\phi^{(l)} \\ i_\lambda^{(l)} \\ \dot{i}_0^{(l)} \\ \dot{i}_\phi^{(l)} \\ \dot{i}_\lambda^{(l)} \end{bmatrix} + \begin{bmatrix} \boldsymbol{H}_{b_{I_r}} & \boldsymbol{H}_{b_{I^k}} \end{bmatrix} \begin{bmatrix} b_{\mathrm{I}_1} \\ \vdots \\ b_{\mathrm{I}_R} \\ b_{\mathrm{I}^1} \\ \vdots \\ b_{\mathrm{I}^K} \end{bmatrix} + \boldsymbol{\eta}, \tag{5.60}$$

with the mapping matrix

$$\boldsymbol{M} = \begin{bmatrix} m_{\mathrm{I}}(E_1^1) & & \\ & \ddots & \\ & & m_{\mathrm{I}}(E_R^{K_R}) \end{bmatrix}, \tag{5.61}$$

the interpolation matrix

$$\boldsymbol{H}_I = \mathbf{1}^{2\times 2} \otimes \begin{bmatrix} 1 & \phi_1^1 - \phi^{(l)} & \lambda_1^1 - \lambda^{(l)} \\ \vdots & \vdots & \vdots \\ 1 & \phi_R^{K_R} - \phi^{(l)} & \lambda_R^{K_R} - \lambda^{(l)} \end{bmatrix}, \tag{5.62}$$

where ϕ_r^k and λ_r^k denote the latitude and longitude of the ionospheric pierce point with slant delay $\tilde{I}_r^k$. The receiver code bias coefficient matrix is given by

$$\boldsymbol{H}_{b_{I_r}} = \begin{bmatrix} \mathbf{1}^{K_1\times 1} & & \\ & \ddots & \\ & & \mathbf{1}^{K_R\times 1} \end{bmatrix}, \tag{5.63}$$

and the satellite code bias coefficient matrix is written as

$$\boldsymbol{H}_{b^k}\left[\sum_{r'=1}^{r-1} K_{r'} + k, j\right] = \begin{cases} 1, & \text{if} \quad j = \mu(k, \mathcal{S}_r). \\ 0, & \text{elsewhere.} \end{cases}, \tag{5.64}$$

where $\mu(k, \mathcal{S}_r)$ describes the position of the k-th satellite of subset

$$\mathcal{S}_r \triangleq \{k_{\mathcal{S}_r}^1, \ldots, k_{\mathcal{S}_r}^{K_r}\} \tag{5.65}$$

within the union set $\mathcal{S} = \{\mathcal{S}_1 \cup \mathcal{S}_2 \cup \ldots \cup \mathcal{S}_R\}$ containing all satellites that are visible from at least one reference station.

The ionospheric vertical delay $i_0^{(l)}$ at the l-th grid point is computed by a weighted least-squares fit of the slant ionospheric delays from the surrounding pierce points, i.e.

$$\min_{\begin{bmatrix} i_0^{(l)} \\ i_\phi^{(l)} \\ i_\lambda^{(l)} \\ \dot{i}_0^{(l)} \\ \dot{i}_\phi^{(l)} \\ \dot{i}_\lambda^{(l)} \end{bmatrix}, \begin{bmatrix} b_{\mathrm{I}_1} \\ \vdots \\ b_{\mathrm{I}_R} \\ b_{\mathrm{I}^2} \\ \vdots \\ b_{\mathrm{I}^K} \end{bmatrix}} \left\| \begin{bmatrix} \tilde{I}_1^1 \\ \vdots \\ \tilde{I}_R^K \\ \dot{\tilde{I}}_1^1 \\ \vdots \\ \dot{\tilde{I}}_R^K \end{bmatrix} - \boldsymbol{M}\boldsymbol{H}_I \begin{bmatrix} i_0^{(l)} \\ i_\phi^{(l)} \\ i_\lambda^{(l)} \\ \dot{i}_0^{(l)} \\ \dot{i}_\phi^{(l)} \\ \dot{i}_\lambda^{(l)} \end{bmatrix} - \begin{bmatrix} \boldsymbol{H}_{b_{I_r}} & \boldsymbol{H}_{b_{I^k}} \end{bmatrix} \begin{bmatrix} b_{\mathrm{I}_1} \\ \vdots \\ b_{\mathrm{I}_R} \\ b_{\mathrm{I}^2} \\ \vdots \\ b_{\mathrm{I}^K} \end{bmatrix} \right\|_{\boldsymbol{\Sigma}^{-1}}^2, \tag{5.66}$$

with the weighting matrix

$$\boldsymbol{\Sigma} = \begin{bmatrix} \frac{\sin(E_1^1)}{\|\boldsymbol{x}_{\mathrm{IPP}_1^1} - \boldsymbol{x}_{\mathrm{IGP}^{(l)}}\|} & & \\ & \ddots & \\ & & \frac{\sin(E_R^{K_R})}{\|\boldsymbol{x}_{\mathrm{IPP}_R^{K_R}} - \boldsymbol{x}_{\mathrm{IGP}^{(l)}}\|} \end{bmatrix}, \tag{5.67}$$

where $\boldsymbol{x}_{\mathrm{IPP}_r^k}$ is the position of the ionospheric pierce point IPP_r^k and $\boldsymbol{x}_{\mathrm{IGP}^{(l)}}$ is the position of the ionospheric grid point $\mathrm{IGP}^{(l)}$.

Note that the least-squares fitting of ionospheric slant delays in Eq. (5.66) should not use the measurements from all pierce points due to the irregular structure of the ionosphere. Typically, a bounding circle is drawn around each grid point to exclude farer points from the least-squares fitting. In this work, it has been set to 2000 km in the simulations and to 400 km in the analysis of real measurements.

Fig. 5.9 shows the achievable accuracy for the GIVDs. Obviously, this accuracy depends on the distribution of pierce points around the grid point. The most and least accurately computable vertical grid ionospheric delays are also indicated in Fig. 5.8.

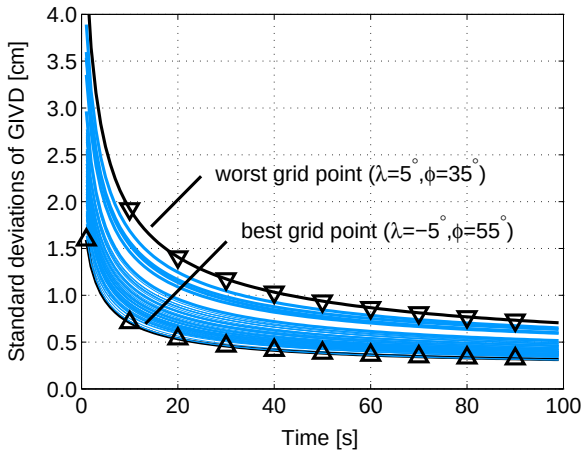

Figure 5.9: Achievable accuracies for GIVD: The code measurements on E1 and E5 and two combinations of time-differenced carrier phase measurements are used in a Kalman filter to estimate the GIVD and the code biases: The first combination is geometry-preserving and ionosphere-free, and the second one is geometry-free and ionosphere-preserving which make the range rates and ionospheric rates observable respectively. A least-squares fit has been used to estimate the vertical ionospheric delay for each grid point from the slant delays of the surrounding pierce points.

Fig. 5.10 and 5.11 show that the error in the bias estimates b_{I_r} and b_{I^k} drop below 1 cm within 300 epochs. Galileo code and carrier phase measurements on E1 and E5 were simulated for the 37 EGNOS RIMS stations.

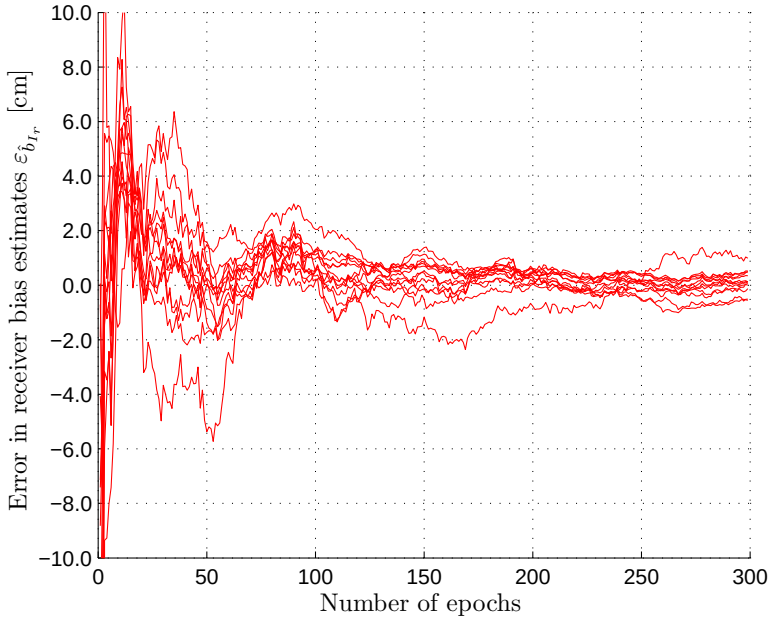

Figure 5.10: Error in receiver bias estimates based on simulated E1 and E5 Galileo measurements of the network of 37 EGNOS reference stations. The boundary circle for each grid point is set to 2000 km. After 300 epochs the errors in receiver bias estimates are reduced to less than 1 cm.

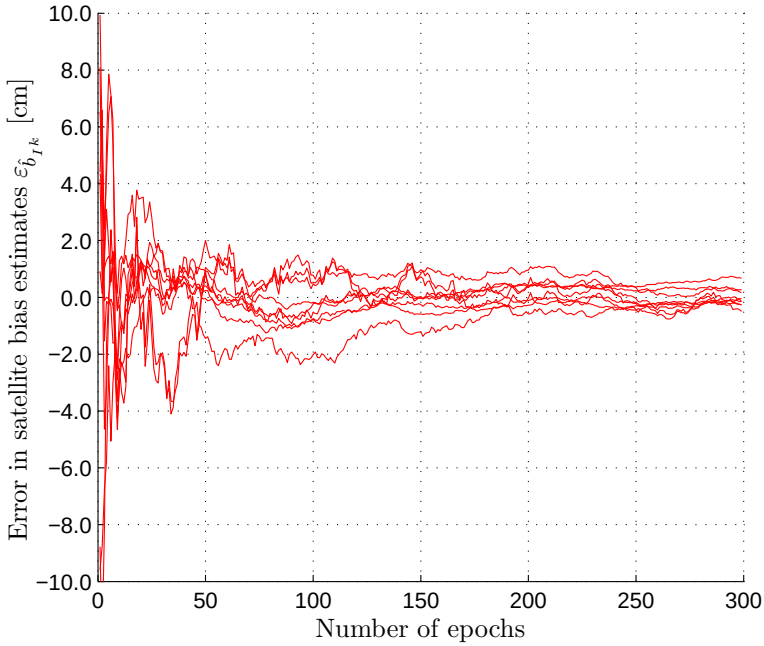

Figure 5.11: Error in satellite bias estimates using the same scenario as in Fig. 5.10. The errors are reduced to less than 1 cm within 300 epochs.

The slant ionospheric delay estimates are affected by both satellite and receiver biases. As these biases occur in the estimation of several ionospheric grid point delays, a joint estimation of the ionospheric grid point delays shall now be considered. Fig. 5.12 shows some ionospheric pierce points of which a few are included in the bounding circles of multiple ionospheric grid points.

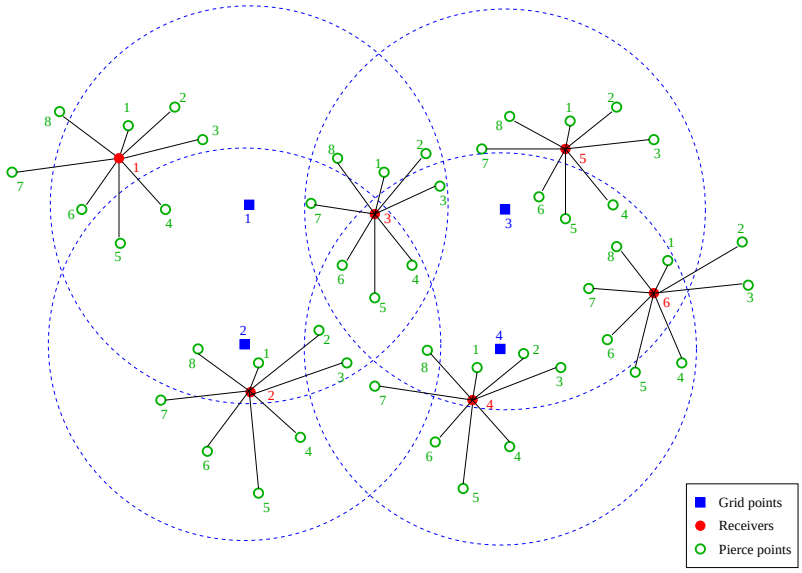

Figure 5.12: Illustration of overlapping ionospheric grid planes: Several satellites are visible from multiple receivers which motivates the joint estimation of multiple grid point delays.

The vertical ionospheric delay at the pierce point $\boldsymbol{x}_{\mathrm{IPP}_r^k}$ is represented by a linear combination of several grid point delays, i.e.

$$I_{\mathrm{v}}(\boldsymbol{x}_{\mathrm{IPP}_r^k}) = \sum_{l \in S_r^k} \alpha_r^{k,(l)} \cdot (i_0^{(l)} + i_\phi^{(l)}(\phi_r^k - \phi^{(l)}) + i_\lambda^{(l)}(\lambda_r^k - \lambda^{(l)})), \tag{5.68}$$

where S_r^k denotes the subset of ionospheric grid points that is given by

$$S_r^k = \{l \mid \|\boldsymbol{x}_{\mathrm{IGP}^{(l)}} - \boldsymbol{x}_{\mathrm{IPP}_r^k}\| < r_{\mathrm{bound}}\}, \tag{5.69}$$

with the radius of the boundary circle r_{bound} around the IPP. The weighting coefficients $\alpha_r^{k,(l)}$ are chosen such that

$$\min_{\alpha_r^{k,(l)}} \sum_{l \in S_r^k} \frac{(\alpha_r^{k,(l)})^2}{\frac{\sin E_r^k}{\|\boldsymbol{x}_{\mathrm{IPP}_r^k} - \boldsymbol{x}_{\mathrm{IGP}^{(l)}}\|}} \quad \text{s. t.} \quad \sum_{l \in S_r^k} \alpha_r^{k,(l)} = 1. \tag{5.70}$$

The ionospheric slant delays and their rates are modeled as

$$\begin{bmatrix} \tilde{\boldsymbol{I}} \\ \dot{\tilde{\boldsymbol{I}}} \end{bmatrix} = \boldsymbol{H}_I \left[(\boldsymbol{i}^{(1)})^T, \ldots, (\boldsymbol{i}^{(L)})^T, (\dot{\boldsymbol{i}}^{(1)})^T, \ldots, (\dot{\boldsymbol{i}}^{(L)})^T \right]^T + \begin{bmatrix} \boldsymbol{H}_{b_{I_r}} & \boldsymbol{H}_{b_{I^k}} \end{bmatrix} \begin{bmatrix} \boldsymbol{b}_{I_r} \\ \boldsymbol{b}_{I^k} \end{bmatrix} + \boldsymbol{\eta}, \tag{5.71}$$

with the combined ionospheric mapping and interpolation matrix

$$\boldsymbol{H}_I = \begin{bmatrix} \mathbf{1}^{2\times 2} \otimes \begin{bmatrix} \boldsymbol{A}_1^{(1)} \boldsymbol{M}_1 \boldsymbol{H}_{I_1}^{(1)} & \boldsymbol{A}_1^{(2)} \boldsymbol{M}_1 \boldsymbol{H}_{I_1}^{(2)} & \ldots & \boldsymbol{A}_1^{(L)} \boldsymbol{M}_1 \boldsymbol{H}_{I_1}^{(L)} \\ \vdots & & & \vdots \\ \boldsymbol{A}_R^{(1)} \boldsymbol{M}_R \boldsymbol{H}_{I_R}^{(1)} & \boldsymbol{A}_R^{(2)} \boldsymbol{M}_R \boldsymbol{H}_{I_R}^{(2)} & \ldots & \boldsymbol{A}_R^{(L)} \boldsymbol{M}_R \boldsymbol{H}_{I_R}^{(L)} \end{bmatrix} \end{bmatrix}, \tag{5.72}$$

the linear combination matrix

$$\boldsymbol{A}_r^{(l)} = \begin{bmatrix} \alpha_r^{1,(l)} & \ldots & \alpha_r^{1,(l)} \\ \vdots & \ddots & \vdots \\ \alpha_r^{K_r,(l)} & \ldots & \alpha_r^{K_r,(l)} \end{bmatrix}, \tag{5.73}$$

the ionospheric slant and grid point delays with their spatial and temporal gradients

$$\tilde{\boldsymbol{I}} = \begin{bmatrix} \tilde{I}_1^1 \\ \vdots \\ \tilde{I}_1^{K_1} \\ \hline \vdots \\ \tilde{I}_R^1 \\ \vdots \\ \tilde{I}_R^{K_R} \end{bmatrix}, \quad \dot{\tilde{\boldsymbol{I}}} = \begin{bmatrix} \dot{\tilde{I}}_1^1 \\ \vdots \\ \dot{\tilde{I}}_1^{K_1} \\ \hline \vdots \\ \dot{\tilde{I}}_R^1 \\ \vdots \\ \dot{\tilde{I}}_R^{K_R} \end{bmatrix}, \quad \boldsymbol{i}^{(l)} = \begin{bmatrix} i_0^{(l)} \\ i_\phi^{(l)} \\ i_\lambda^{(l)} \end{bmatrix}, \quad \dot{\boldsymbol{i}}^{(l)} = \begin{bmatrix} \dot{i}_0^{(l)} \\ \dot{i}_\phi^{(l)} \\ \dot{i}_\lambda^{(l)} \end{bmatrix}, \tag{5.74}$$

and the receiver and satellite biases

$$\boldsymbol{b}_{I_r} = [b_{I_1}, \ldots, b_{I_R}]^T, \quad \boldsymbol{b}_{I^k} = [b_{I^2}, \ldots, b_{I^K}]^T. \tag{5.75}$$

The ionospheric vertical delays $i_0^{(l)}$ at the l-th grid points are computed by a weighted least-squares fit of the slant ionospheric delays from the surrounding pierce points, i.e.

$$\begin{bmatrix} \boldsymbol{i}^{(1)} \\ \vdots \\ \boldsymbol{i}^{(L)} \end{bmatrix}, \begin{bmatrix} \dot{\boldsymbol{i}}^{(1)} \\ \vdots \\ \dot{\boldsymbol{i}}^{(L)} \end{bmatrix}, \begin{bmatrix} \boldsymbol{b}_{I_r} \\ \boldsymbol{b}_{I^k} \end{bmatrix} \min \left\| \begin{bmatrix} \tilde{\boldsymbol{I}} \\ \dot{\tilde{\boldsymbol{I}}} \end{bmatrix} - \boldsymbol{H}_I \begin{bmatrix} \boldsymbol{i}^{(1)} \\ \vdots \\ \boldsymbol{i}^{(L)} \\ \dot{\boldsymbol{i}}^{(1)} \\ \vdots \\ \dot{\boldsymbol{i}}^{(L)} \end{bmatrix} - \begin{bmatrix} \boldsymbol{H}_{b_{I_r}} & \boldsymbol{H}_{b_{I^k}} \end{bmatrix} \begin{bmatrix} \boldsymbol{b}_{I_r} \\ \boldsymbol{b}_{I^k} \end{bmatrix} \right\|^2_{\Sigma^{-1}}. \tag{5.76}$$

Estimation of ionospheric grid with measurements from CORS network

The method for joint estimation of code biases and grid ionospheric vertical delays is validated with real data from 7 CORS stations in Vermont, USA: (1) Middlebury: $\lambda = -73.15°$, $\phi = 44.00°$, (2) Montpelier: $\lambda = -72.58°$, $\phi = 44.26°$, (3) Randolph Center: $\lambda = -72.60°$, $\phi = 43.94°$, (4) Danby: $\lambda = -73.00°$, $\phi = 43.35°$, (5) Bradford: $\lambda = -72.11°$, $\phi = 44.01°$. (6) Derby: $\lambda = -72.09°$, $\phi = 44.57°$. (7) Brighton: $\lambda = -71.53°$, $\phi = 44.49°$. The maximum distance between these 7 stations is 140 km. The GPS L1/ L2 code and carrier phase measurements of February 7, 2010 have been chosen. The ionospheric grid point at $\lambda = -71°$, $\phi = 43°$ is considered. Fig. 5.13 shows the residuals of the ionospheric slant delays which are obtained from the grid estimation of Eq. (5.66), i.e.

$$r_I = \begin{bmatrix} \tilde{I}_1^1 \\ \vdots \\ \tilde{I}_R^{K_R} \\ \tilde{I}_1^1 \\ \vdots \\ \tilde{I}_R^{K_R} \end{bmatrix} - \boldsymbol{M}\boldsymbol{H}_I \begin{bmatrix} \hat{i}^{(l)} \\ \hat{i}^{(l)} \end{bmatrix} - \boldsymbol{H}_b \begin{bmatrix} \hat{b}_{\mathrm{I}_1} \\ \vdots \\ \hat{b}_{\mathrm{I}_R} \\ \hat{b}_{\mathrm{I}^2} \\ \vdots \\ \hat{b}_{\mathrm{I}^K} \end{bmatrix}. \tag{5.77}$$

Smaller residuals refer to the ionospheric pierce points that are closer to the grid point, and larger residuals can be observed for the ionospheric pierce points that are farer away. Consequently, these ionospheric residuals also indicate irregularities in the ionosphere.

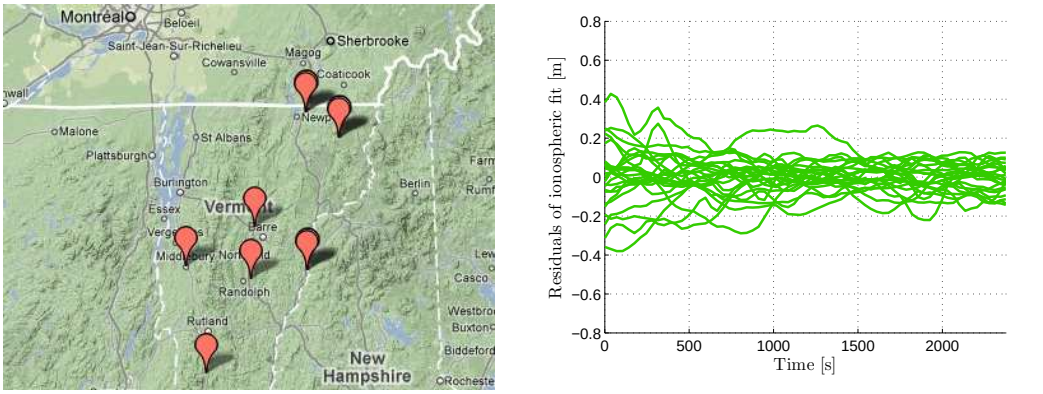

(a) Map of CORS stations in Vermont (b) Residuals of vertical ionospheric delays

Figure 5.13: Residuals of slant ionospheric delays: A least-squares fit has been used to estimate the vertical ionospheric delay for each grid point from the slant delays of the surrounding pierce points.

It is recommended that a satellite based augmentation system transmits the bias estimates $\hat{b}_{\mathrm{I}^k}$ in addition to the grid ionospheric vertical delays $\hat{i}_0^{(l)}$. A more detailed analysis of measurements from a larger network of 21 CORS stations is given in the next chapter.

5.1.4 Estimation of phase biases with SAPOS stations

The receiver and satellite phase biases shall now be estimated with real GPS measurements from 9 SAPOS stations (equipped with Leicca receivers) in northern Bavaria. The Kalman filter based approach with the modified cost function of (5.51) for sequential ambiguity resolution are reused. Fig. 5.14 and 5.14 shows a high temporal stability for the geometry-dependant part of the receiver and satellite phase biases. The drift varies between less than 1 cm and at most 5 cm within one hour.

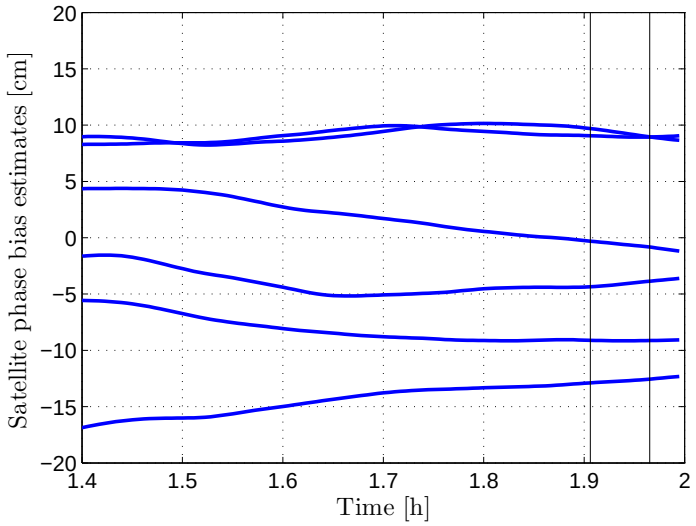

Figure 5.14: Estimation of satellite phase biases with a network of SAPOS stations: The geometry-dependant part of these biases is extremely stable over time.

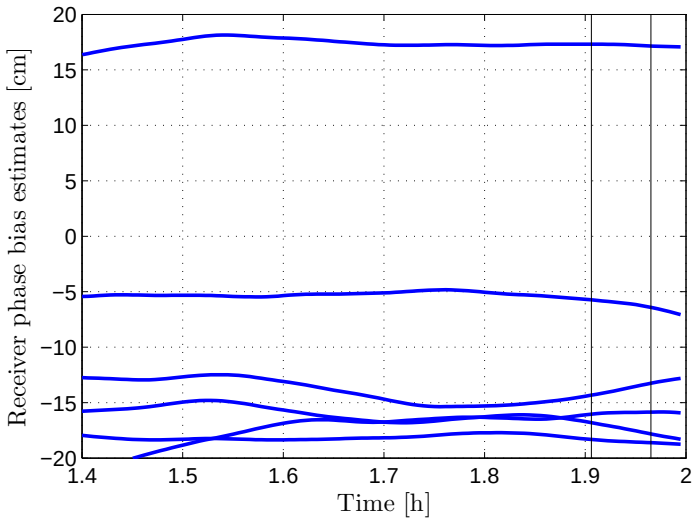

Figure 5.15: Estimation of receiver phase biases with a network of SAPOS stations: The geometry-dependant part of these biases is extremely stable over time.

6

Measurement analysis

In this chapter, some of the analyzed methods for differential carrier phase positioning are validated with real data.

First, a dual frequency carrier smoothing is analyzed for ionospheric delay estimation with geometry-free, ionosphere-preserving code and carrier phase linear combinations. A spectral analysis is performed to show the impact of multipath on the ionospheric delay estimates.

Secondly, the carrier phase integer ambiguities are resolved for both stationary and kinematic GPS L1/ L2 measurements from Javad receivers. An integer least-squares estimation with integer decorrelation (LAMBDA) is used to increase the efficiency of the search. The obtained baseline estimates are validated with laser ranging and agree up to 9 mm. A high reliability of the kinematic ambiguity resolution is observed as the range residuals were more than one order of magnitude lower than the widelane wavelength. The measurements were performed on a Beechcraft King Air 350 during a flight campaign of the institute.

Finally, the estimation of satellite biases is analyzed with GPS measurements from the SAPOS and CORS stations. A Kalman filter is used to compute a network solution. The integer ambiguities are sequentially fixed using a new cost function which includes both the a posteriori standard deviation of the Kalman filter and the actual deviation of the float ambiguities and their nearest integer numbers.

6.1 Smoothing algorithms

This section shows the benefit of carrier smoothing for ionospheric delay estimation. The measurements have been collected by the institute's Genesis-112 GPS/GLONASS L1/L2 receiver of Javad which has been mounted on top of the FCS building at Braunschweig on December 15, 2008.

Fig. 6.1 shows the instantaneous ionospheric delay estimates for a low elevation satellite which rises over the southern horizon at the beginning of the measurements. The code noise as well as the strong code multipath with a 100 s periodic structure are substantially reduced by the ionosphere-free smoothing. The benefit of the smoothing obviously increases for larger smoothing time constants. Moreover, one can observe a reduction in code multipath over time (especially after 30 min) due to the increase in satellite elevation.

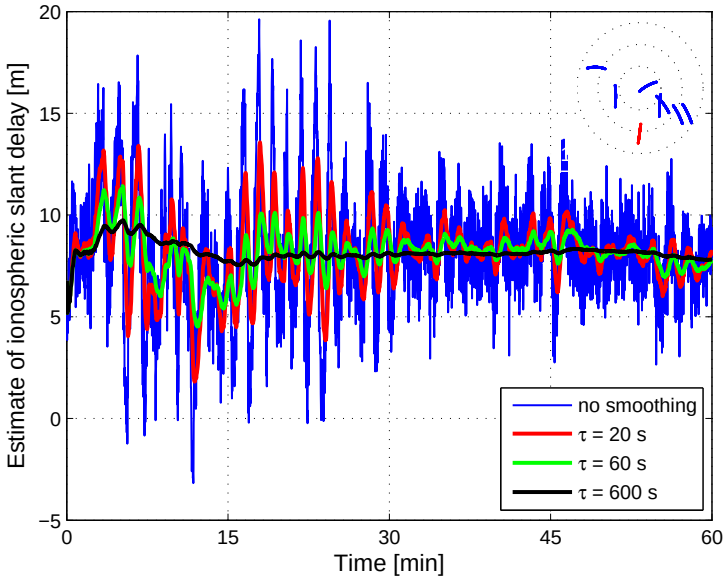

Figure 6.1: Ionospheric delay estimation from dual frequency measurements: The noise is substantially reduced by dual frequency ionosphere-free carrier smoothing. The somewhat regular variations in the beginning indicate multipath and are reduced as the elevation increases. The measurements have been collected by the institute's Genesis-112 GPS/GLONASS L1/L2 receiver of Javad at Braunschweig.

Fig. 6.2 includes a spectral analysis of the ionospheric delay estimates. A white Gaussian noise signal would result in a constant in the spectrum. As the measurements were collected during solar minimum and the ionosphere was in particular calm on the chosen day, a 10 min smoothing results almost in a constant delay estimate which turns into a peak for $f = 0$ Hz and negligible power at other frequencies. A comparison of the spectral density between a 10 min smoothing and no smoothing enables a separation of code multipath from noise. The side lobes at ± 0.01 Hz and ± 0.025 Hz are caused by multipath, and the spectral density for $|f| > 0.03$ Hz indicates the smoothed noise level.

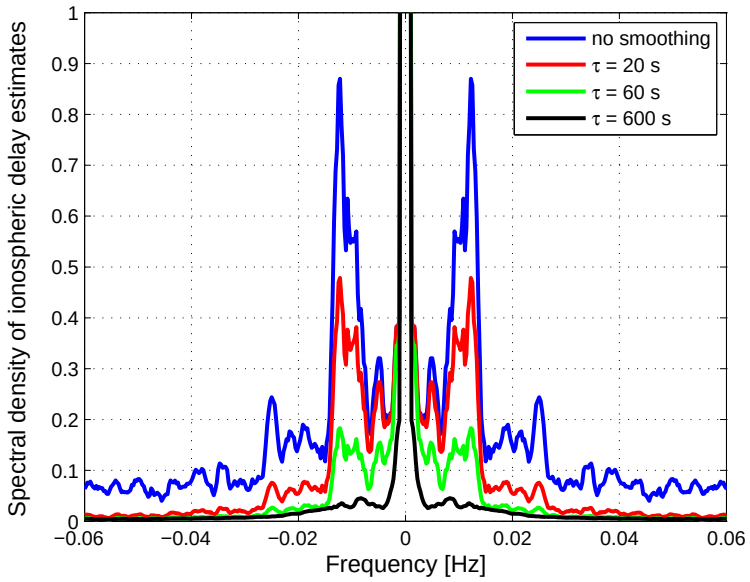

Figure 6.2: Spectral analysis of ionospheric delay estimation: The side lobes at 0.01 Hz are caused by multipath. The smoothing reduces both the multipath and the white Gaussian noise that corresponds to a constant in the spectrum. The measurements have been collected by the institute's Genesis-112 GPS/GLONASS L1/L2 receiver of Javad at Braunschweig.

6.2 Ambiguity resolution

In this section, the benefit of integer ambiguity resolution is analyzed for relative positioning. In a first part, a set of measurements from two stationary receivers are used and, in a second part, measurements from a flight campaign are considered.

6.2.1 Measurements from stationary receivers

A Leica and a Javad receiver have been positioned on top of the IAPG building at TUM with a fixed baseline of 133.541 m on August 28, 2008. The baseline estimation has been performed iteratively based on double difference measurements. The integer ambiguities have been resolved with the Least Squares Ambiguity Decorrelation Adjustment (LAMBDA) method. Fig. 6.3 shows an average deviation of 9 mm between the GPS based baseline estimation and the estimate obtained from laser ranging.

Fig. 6.4 shows the double difference range residuals after ambiguity resolution. Both the standard deviations and the biases of all 6 residuals are only a few millimeters which indicates a correct integer ambiguity resolution. The skyplot shows the satellite geometry with the satellite of highest elevation being chosen as reference satellite. Note that the range residuals require a certain number of iterations, i.e. the geometry matrix has to converge.

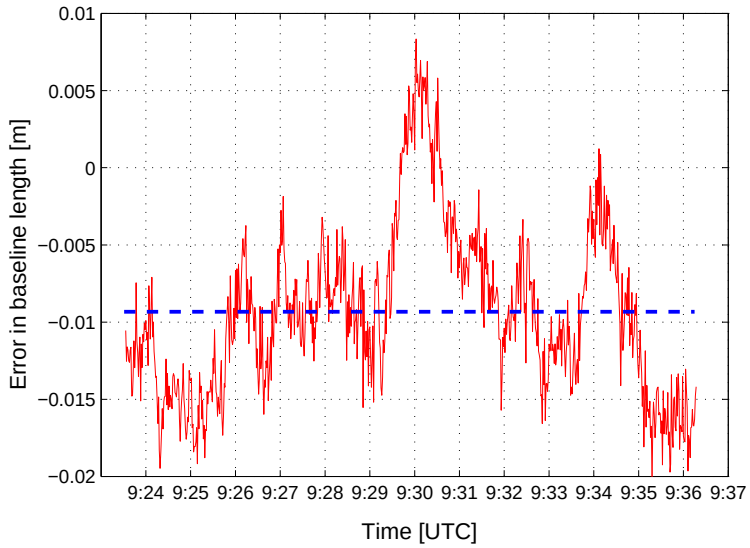

Figure 6.3: Baseline estimation with carrier phase ambiguity resolution: A Leica and Javad receiver have been positioned on top of the building of the IAPG at TUM on August 28, 2008. The iterative baseline estimation is based on double difference measurements and includes an integer search for ambiguity resolution. The baseline length has been verified by laser ranging. An error of 9 mm can be observed in the estimate of the 133.541 m long baseline which indicates a correct integer ambiguity resolution.

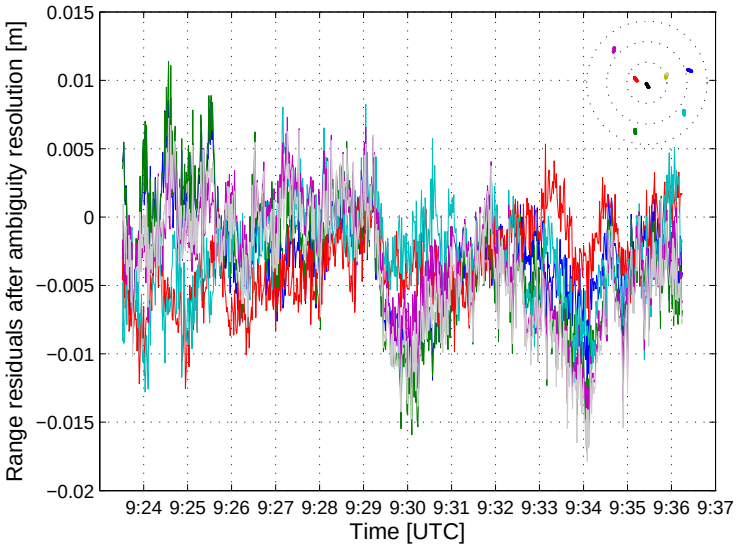

Figure 6.4: Range residuals of baseline estimation: The residuals have been obtained after 20 iterations and indicate a correct carrier phase ambiguity resolution. The skyplot shows the movement of the satellites including the reference satellite of highest elevation. The integer ambiguities have been determined by a search. The measurements have been collected with a Leica and Javad receiver positioned on top of the building of the IAPG at TUM on August 28, 2008.

Fig. 6.5 shows the convergence behaviour of the range residuals after ambiguity resolution: Residuals of less than 4 mm are obtained for all double differences after at least 13 iterations. Lower range residuals for a reduced number of iterations occur if the baseline estimate results in an overfitting of one or a few double differences.

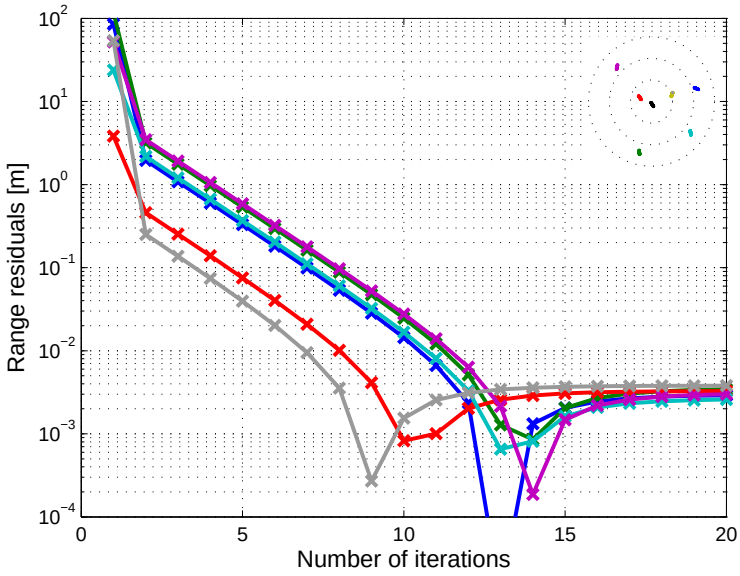

Figure 6.5: Convergence behaviour of range residuals after ambiguity resolution: Residuals of less than 4 mm are obtained for all double differences after at least 13 iterations. Lower range residuals for a reduced number of iterations occur if the baseline estimate results in an overfitting of one or a few double differences. The measurements have been collected with a Leica and Javad receiver positioned on top of the building of the IAPG at TUM on August 28, 2008.

Fig. 6.6 shows the convergence of the float ambiguity estimates to integer values. For single frequency measurements without integer decorrelation, the convergence is rather slow. Obviously, the ambiguity referring to the pair of satellites with highest elevation can be fixed correctly much earlier than of the low elevation satellites (violet, turquoise). A correlation can also be observed between the range residual convergence in Fig. 6.5 and the float ambiguity errors of Fig. 6.6: The two range residuals with fastest convergence correspond to two ambiguity estimates whose absolute errors converge fastest to less than $\pm 1/2$ cycle.

Fig. 6.7 shows the benefit of a priori knowledge for integer ambiguity fixing. In this case, the ambiguity of the highest elevation satellite is assumed to be known which results in one unambiguous carrier phase measurement. This a priori knowledge reduces the uncertainty in the float solution of all other ambiguities, and is especially beneficial for the resolution of a low elevation satellite ambiguity. This sequential fixing is done by a variety of integer estimators including bootstrapping and integer least-squares estimation.

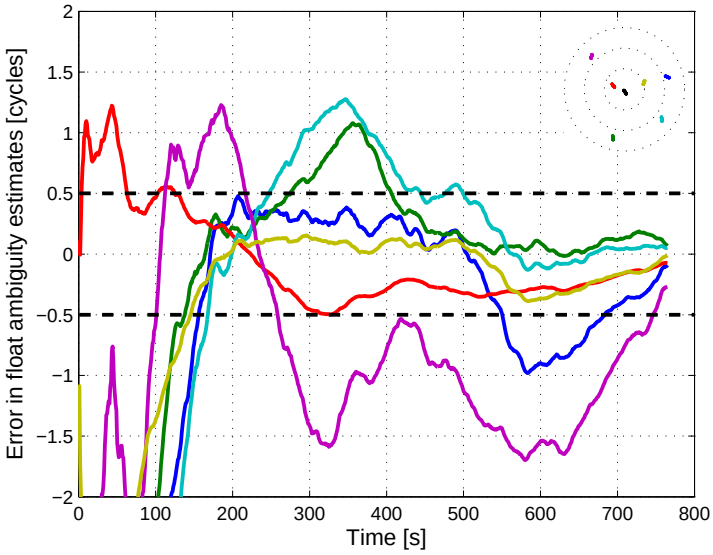

Figure 6.6: Errors in float ambiguity estimates before integer decorrelation: These errors are reduced to less than ±0.5 cycle within a few hundred epochs. The ambiguities of the high elevation satellites converge faster than of the low elevation satellites. The measurements have been collected with a Leica and Javad receiver positioned on top of the building of the IAPG at TUM on August 28, 2008.

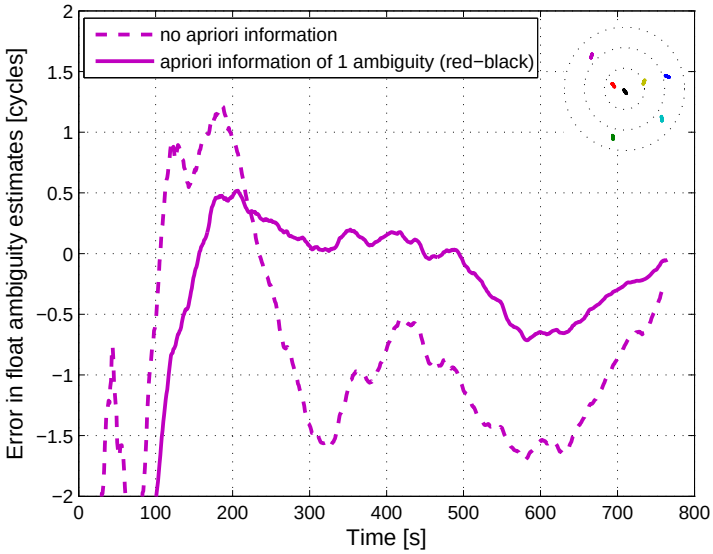

Figure 6.7: Impact of a priori integer knowledge on ambiguity resolution: The same measurements as in Fig. 6.6 are considered but the ambiguity of the double difference between the two satellites of highest elevation (red, black) is assumed to be known. The a priori knowledge reduces the errors in the most critical ambiguities that are referring to low elevation satellites (turquoise, violet).

6.2.2 Measurements from flight campaign

The first flight with kinematic carrier phase positioning based on both GPS L1/L2 and GIOVE E1/E5a signals was performed by the institute on December 15, 2008. The capability of reliable widelane ambiguity resolution for combined GPS and Galileo signals, and a new vector phase locked loop for joint satellite tracking were validated.

The flight was conducted with a Beechcraft King Air 350 of Flight Calibration Services, Braunschweig (Fig. 6.8). Two multi-frequency Galileo capable 42GO1116A2-XT-1 antennas of Antcom (with 743 ARINC configuration) were mounted on the aircraft.

Figure 6.8: Beechcraft King Air of Flight Calibration Services at runway of Braunschweig

The flight started with an en-route flight from Braunschweig to Innsbruck, followed by several touchdowns, low approaches and banking maneuvers in Alpine valleys. The flight path is shown in Fig. 6.9 and 6.10.

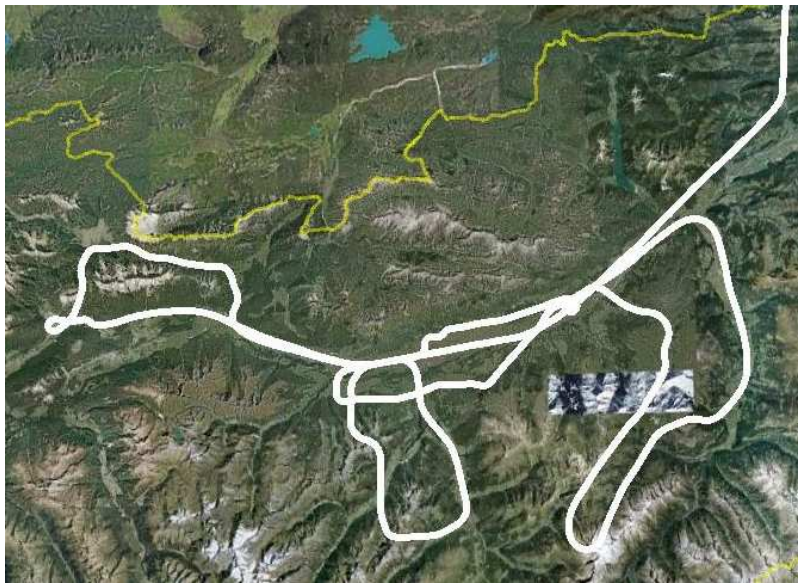

Figure 6.9: Overview of flight path through the Inn-, Leutasch-, Wipp-, Stubai- and Zillertal in the Austrian Alps: Several banking manoeuvres and steep circles have been flown with low approaches/ touch-downs at the airport of Innsbruck.

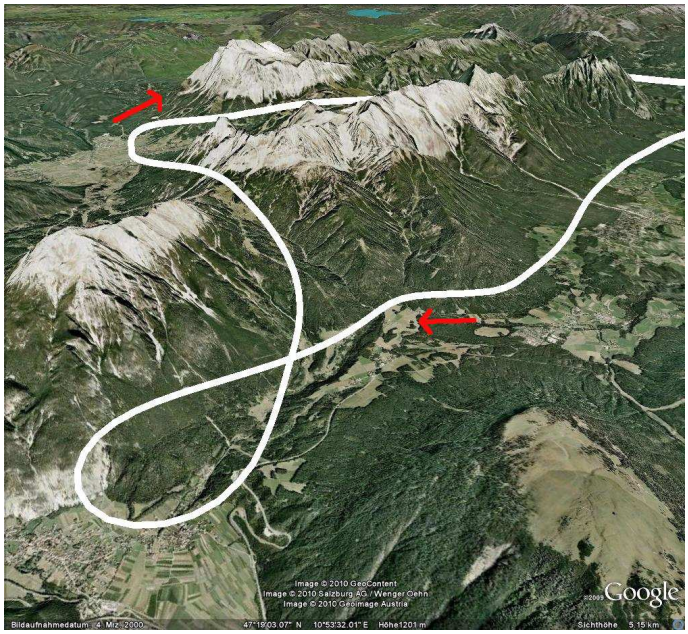

Figure 6.10: Flight path through the Austrian Alps: The path follows the valley of the Inn from Innsbruck to Imst. A steep bend of 270 degrees is then flown to approach the Marienbergjoch, and the basin of Ehrwald. The flight path then turns into the valley of the Leutasch between the Zugspitze in the north and the Mieminger Kette in the south.

Fig. 6.11 shows the onboard measurement equipment: Two multi-frequency, multi-constellation GNSS Triumph receivers of Javad, the Nordnav L1 frontend, and an antenna splitter were arranged in a rack. The commands for the receivers were sent from a remote PC which also stores the measurement data.

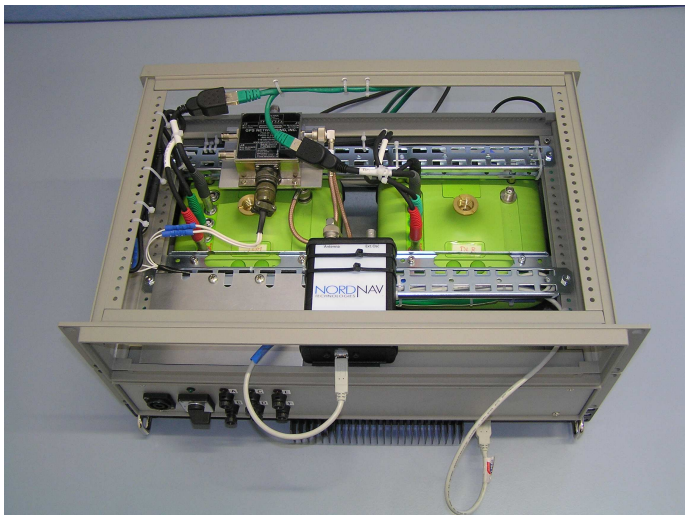

Figure 6.11: Measurement equipment for flight campaign: Two multi-frequency, multi-constellation GNSS Triumph receivers of Javad, the Nordnav L1 frontend, and an antenna splitter have been arranged in a rack. The commands for the receivers were sent from a remote PC which also stores the measurement data.

Fig. 6.12 shows the benefit of ambiguity resolution for the estimation of the 98.66 cm baseline between both Javad receivers. The fixing of the L1-L2 widelane ambiguities with a wavelength of $\lambda = 86.2$cm reduces the estimation error in the baseline height component by one to two orders of magnitude compared to the float solution. Note that the float solution has been computed on an epoch by epoch basis.

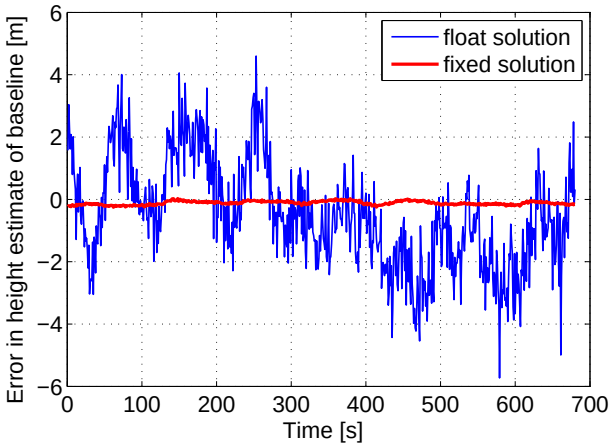

Figure 6.12: Error in height estimation between the antenna on the aircraft and the antenna of the reference station on top of the FCS building: The fixing of L1-L2 widelane ambiguities ($\lambda = 86.2$cm) reduces the variations in the height estimate by one to two orders of magnitude compared to the float solution.

Fig. 6.13 shows the range residuals of double difference widelane measurements after widelane ambiguity fixing. The range residuals are more than one order of magnitude smaller than the wavelength which indicates a correct integer ambiguity fixing.

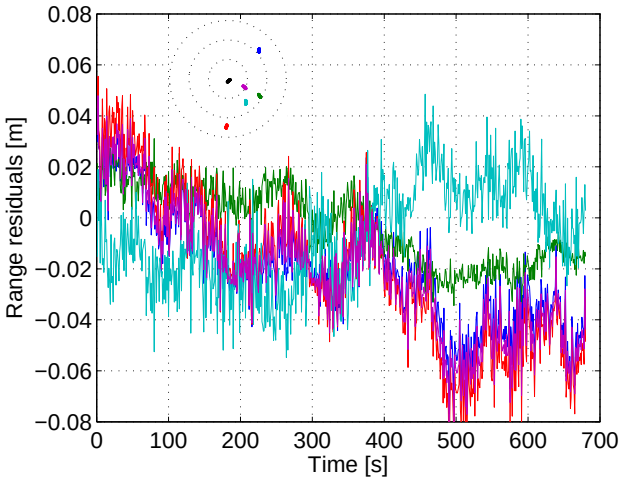

Figure 6.13: Range residuals after widelane ambiguity resolution: The range residuals are more than one order of magnitude smaller than the wavelength which indicates a correct integer ambiguity fixing.

7

Conclusion

In this work, the reliability of carrier phase positioning with multiple frequencies was substantially improved. This is especially important for safety of life critical applications (aviation) as well as for the positioning of reference stations in a local, continental or global network where a fixing of all ambiguities has been feasible only with a probability of wrong fixing of a few percent so far. It was even impossible during ionospheric storms in the past. The proposed integer ambiguity resolution is benefiting from the wideband Galileo signals with their large bandwidths and Binary Offset Carrier modulation which result in a code noise of only a few centimeters.

The carrier tracking has been improved by a vector phase locked loop which jointly tracks all signals and benefits from both the spectral and spatial correlation. For the Galileo wideband signals, the ionosphere causes not only a delay but also a distortion of the code correlation function which results in a phase bias of a few centimeters. Therefore, a method for equalizing the signal in spectral domain has been suggested.

New groups of multi-frequency mixed code carrier linear combinations were derived to improve the reliability of integer ambiguity resolution. The linear combination of code and carrier phase measurements has several advantages: It enables dual frequency widelane combinations that eliminate the ionospheric delay which is not possible with phase-only combinations. The inclusion of code measurements relaxes the integer constraint which enables larger wavelengths while the ionosphere is still eliminated. The large wavelength in relation to the geometry-preserving property substantially improves the robustness over orbital errors, satellite clock offsets and tropospheric modeling errors. The combination of code and carrier phase measurements also offers some additional degrees of freedom for the combination design: The geometry is either preserved or eliminated, the ionospheric delay of first order and/ or of second order are either preserved or eliminated, the

noise level is minimized, the wavelength is maximized, or the ambiguity discrimination is maximized. For example, a geometry-preserving, ionosphere-free dual frequency linear combination of Galileo E1 and E5 measurements with a wavelength of 3.285 m and a noise level of only a few centimeters has been found. The noise level of the code carrier combination was further reduced by carrier smoothing, and optimal combination design is based on a joint optimization of the phase-only combination and the code carrier combination. Moreover, constraints on biases were integrated into the combination computation, an ambiguity resolution based on geometry-free, ionosphere-free, carrier smoothed combinations was discussed, and linear combinations including next generation C-band signals were evaluated.

Integer ambiguity resolution can be performed either by direct rounding, by sequential conditional rounding (bootstrapping), by integer least-squares estimation (including a search), or by integer aperture estimation. In this work, these estimators were applied to both uncombined and combined double differenced, single differenced and undifferenced measurements. The optimal combinations with their large wavelength substantially improve the reliability of ambiguity resolution for both Wide Area Real Time Kinematics (RTK) and Precise Point Positioning (PPP) applications. Several contributions were made to further improve the success rate, e.g. a modified bootstrapping that uses slightly lower weights than the traditional bootstrapping to take the erroneous fixings into account. A partial integer decorrelation was suggested to find the optimum trade-off between variance reduction and worst-case bias amplification. The first cascaded ambiguity resolution scheme with three multi-frequency geometry-preserving, ionosphere-free code carrier combinations was derived. A new partial ambiguity fixing was obtained from a forward-backward search while current methods are using only a pure forward search. The optimal fixing order lead to a substantial increase in the number of reliably fixable ambiguities in the case of worst-case biases. The detection of erroneous fixings was improved by selecting a set of linear combinations where the most likely integer errors in the combined ambiguities result in non-integer valued errors for the uncombined ambiguities. Moreover, receiver and satellite code and phase biases and the vertical ionospheric grid were estimated with a Kalman filter and a network of reference station. The method was validated with simulated measurements from the global network of Galileo Sensor Stations and with real data from a few CORS stations as well as from the Bavarian network of SAPOS stations. The integrity risk is in general substantially lower than the probability of wrong fixing as a large number of erroneous fixings does not necessarily result in an integrity threat. It was evaluated for the CAT IIIc vertical alarm limit of 5.3 m using the optimized linear combinations of satellite-satellite single difference measurements on E1 and E5a.

The integer ambiguity resolution methods were validated with GPS measurements from a stationary baseline on top of the IAPG building of the Technische Universität München as well as with kinematic measurements from a flight campaign. Range residuals of less than 10 % of the wavelength were observed which indicate a quite reliable integer ambiguity resolution. This reliability will further improve with the next Galileo satellites.

Appendix

A1. Power spectral density of Binary Offset Carrier Modulated Signals

Betz has introduced the BOC spreading symbol as a sequence of alternating ±1 in [3], i.e. the spreading symbol for sine phasing is written as

$$q_{(m,n)}(t) = \sum_{l=0}^{k-1} (-1)^l \cdot p_{\frac{T_s}{2}} \left(t - l \cdot \frac{T_s}{2} \right), \tag{7.1}$$

where $p_{\frac{T_s}{2}}$ is a rectangular pulse of duration $\frac{T_s}{2}$ and $k = \frac{2m}{n}$ represents the number of subcarrier half cycles in one chip. The Fourier transformation of $p_{\frac{T_s}{2}}(t - l \cdot \frac{T_s}{2})$ is given by

$$\begin{aligned} \mathcal{F}\left(p_{\frac{T_s}{2}} \left(t - l \cdot \frac{T_s}{2} \right) \right) &= \int_{(l-\frac{1}{2})\frac{T_s}{2}}^{(l+\frac{1}{2})\frac{T_s}{2}} e^{-j2\pi f t} dt = -\frac{1}{j2\pi f} e^{-j2\pi f l \frac{T_s}{2}} \left(e^{-j2\pi f \frac{T_s}{4}} - e^{j2\pi f \frac{T_s}{4}} \right) \\ &= \frac{e^{-j2\pi l f \frac{T_s}{2}}}{\pi f} \sin\left(\pi f \frac{T_s}{2} \right). \end{aligned} \tag{7.2}$$

The Fourier transformation of a linear combination is equal to the linear combination of Fourier transforms, i.e. $\mathcal{F}(q_{(m,n)}(t))$ can be rewritten as

$$\mathcal{F}(q_{(m,n)}(t)) = \frac{\sin(\pi f \frac{T_s}{2})}{\pi f} \sum_{l=0}^{k-1} (-1)^l e^{-j2\pi f l \frac{T_s}{2}}. \tag{7.3}$$

For k even, pairing terms in the summation yields

$$\begin{aligned} \sum_{l=0}^{k-1} (-1)^l e^{-j2\pi l f \frac{T_s}{2}} &= 1 - e^{-j2\pi f \frac{T_s}{2}} + \cdots + e^{-j2\pi(k-2) f \frac{T_s}{2}} - e^{-j2\pi(k-1) f \frac{T_s}{2}} \\ &= \left(1 - e^{-j2\pi f \frac{T_s}{2}} \right) \cdot \sum_{l=0}^{k/2-1} e^{-j4\pi l f \frac{T_s}{2}} = 2j e^{-j\pi f \frac{T_s}{2}} \sin\left(\pi f \frac{T_s}{2} \right) \sum_{l=0}^{k/2-1} e^{-j4\pi l f \frac{T_s}{2}}. \end{aligned} \tag{7.4}$$

The geometric series $\sum_{l=0}^{k} x^l = \frac{x^{k+1}-1}{x-1}$ is used to obtain

$$\sum_{l=0}^{k-1}(-1)^l e^{-j2\pi l f\frac{T_\mathrm{s}}{2}} = 2je^{-j\pi f\frac{T_\mathrm{s}}{2}}\sin\left(\pi f\frac{T_\mathrm{s}}{2}\right)\cdot\left(\frac{e^{-j2\pi k f\frac{T_\mathrm{s}}{2}}-1}{e^{-j4\pi f\frac{T_\mathrm{s}}{2}}-1}\right), \tag{7.5}$$

which can be further simplified using trigonometric identities, i.e.

$$\begin{aligned}\sum_{l=0}^{k-1}(-1)^l e^{-j2\pi l f\frac{T_\mathrm{s}}{2}} &= 2je^{-j\pi f\frac{T_\mathrm{s}}{2}}\sin(\pi f\frac{T_\mathrm{s}}{2})\cdot\frac{e^{-j\pi k f\frac{T_\mathrm{s}}{2}}}{e^{-j2\pi f\frac{T_\mathrm{s}}{2}}}\cdot\frac{\sin(\pi k f\frac{T_\mathrm{s}}{2})}{\sin(2\pi f\frac{T_\mathrm{s}}{2})}\\ &= je^{-j\pi(k-1)f\frac{T_\mathrm{s}}{2}}\cdot\frac{\sin(\pi k f\frac{T_\mathrm{s}}{2})}{\cos(\pi f\frac{T_\mathrm{s}}{2})}.\end{aligned} \tag{7.6}$$

Substituting (7.6) in (7.2) and using the definition of the power spectral density results in

$$\begin{aligned}P_{\mathrm{sinb}_{(m,n)}}(f) &= \frac{1}{k\frac{T_\mathrm{s}}{2}}|\mathcal{F}(q_{(m,n)}(t))|^2 = \frac{1}{k\frac{T_\mathrm{s}}{2}}\cdot\left(\frac{\sin(\pi f\frac{T_\mathrm{s}}{2})\sin(\pi k f\frac{T_\mathrm{s}}{2})}{\pi f\cos(\pi f\frac{T_\mathrm{s}}{2})}\right)^2\\ &= \frac{1}{f_\mathrm{c}}\cdot\left(\frac{\sin\left(\frac{\pi f}{2f_\mathrm{s}}\right)\sin\left(\frac{\pi f}{f_\mathrm{c}}\right)}{\frac{\pi f}{f_\mathrm{c}}\cos\left(\frac{\pi f}{2f_\mathrm{s}}\right)}\right)^2 \quad (k \text{ even}).\end{aligned} \tag{7.7}$$

If k is an odd number, one additional term remains after the pairing in (7.4), i.e.

$$\sum_{l=0}^{k-1}(-1)^l e^{-j2\pi l f\frac{T_\mathrm{s}}{2}} = je^{-j\pi(k-2)f\frac{T_\mathrm{s}}{2}}\cdot\frac{\sin(\pi(k-1)f\frac{T_\mathrm{s}}{2})}{\cos(\pi f\frac{T_\mathrm{s}}{2})} + e^{-2(k-1)\pi f\frac{T_\mathrm{s}}{2}}. \tag{7.8}$$

The common terms are factored out, and real and imaginary components are grouped:

$$\begin{aligned}\sum_{l=0}^{k-1}(-1)^l e^{-j2\pi f l\frac{T_\mathrm{s}}{2}} &= e^{-j2(k-1)\pi f\frac{T_\mathrm{s}}{2}}\left(je^{jk\pi f\frac{T_\mathrm{s}}{2}}\left(\frac{\sin\left((k-1)\pi f\frac{T_\mathrm{s}}{2}\right)}{\cos\left(\pi f\frac{T_\mathrm{s}}{2}\right)}+1\right)\right)\\ &= e^{-j2(k-1)\pi f\frac{T_\mathrm{s}}{2}}\left(1-\sin\left(k\pi f\frac{T_\mathrm{s}}{2}\right)\frac{\sin((k-1)\pi f\frac{T_\mathrm{s}}{2})}{\cos(\pi f\frac{T_\mathrm{s}}{2})}\right.\\ &\quad\left.+j\cos\left(k\pi f\frac{T_\mathrm{s}}{2}\right)\frac{\sin\left((k-1)\pi f\frac{T_\mathrm{s}}{2}\right)}{\cos(\pi f\frac{T_\mathrm{s}}{2})}\right).\end{aligned} \tag{7.9}$$

which is rewritten with

$$\sin\left((k-1)\pi f\frac{T_\mathrm{s}}{2}\right) = \sin(k\pi f\frac{T_\mathrm{s}}{2})\cos(\pi f\frac{T_\mathrm{s}}{2}) - \cos(k\pi f\frac{T_\mathrm{s}}{2})\sin(\pi f\frac{T_\mathrm{s}}{2}) \tag{7.10}$$

as

$$\begin{aligned}\sum_{l=0}^{k-1}(-1)^l e^{-j2\pi f l\frac{T_\mathrm{s}}{2}} &= e^{-j2(k-1)\pi f\frac{T_\mathrm{s}}{2}}\left(1-\sin^2\left(k\pi f\frac{T_\mathrm{s}}{2}\right)+\frac{\sin(k\pi f\frac{T_\mathrm{s}}{2})\cos(k\pi f\frac{T_\mathrm{s}}{2})\sin(\pi f\frac{T_\mathrm{s}}{2})}{\cos(\pi f\frac{T_\mathrm{s}}{2})}\right.\\ &\qquad\left.+j\left(\sin\left(k\pi f\frac{T_\mathrm{s}}{2}\right)\cos\left(k\pi f\frac{T_\mathrm{s}}{2}\right)-\frac{\cos^2(k\pi f\frac{T_\mathrm{s}}{2})\sin(\pi f\frac{T_\mathrm{s}}{2})}{\cos(\pi f\frac{T_\mathrm{s}}{2})}\right)\right)\\ &= e^{-j2(k-1)\pi f\frac{T_\mathrm{s}}{2}}\left(\frac{\cos^2(k\pi f\frac{T_\mathrm{s}}{2})\cos(\pi f\frac{T_\mathrm{s}}{2})+\sin(k\pi f\frac{T_\mathrm{s}}{2})\cos(k\pi f\frac{T_\mathrm{s}}{2})\sin(\pi f\frac{T_\mathrm{s}}{2})}{\cos(\pi f\frac{T_\mathrm{s}}{2})}\right.\\ &\qquad\left.+j\frac{\sin(k\pi f\frac{T_\mathrm{s}}{2})\cos(k\pi f\frac{T_\mathrm{s}}{2})\cos(\pi f\frac{T_\mathrm{s}}{2})-\cos^2(k\pi f\frac{T_\mathrm{s}}{2})\sin(\pi f\frac{T_\mathrm{s}}{2})}{\cos(\pi f\frac{T_\mathrm{s}}{2})}\right).\end{aligned} \tag{7.11}$$

Factoring out the common terms and further simplifying yields

$$\begin{aligned}\sum_{l=0}^{k-1}(-1)^l e^{-j2\pi f l\frac{T_\mathrm{s}}{2}} &= e^{-j2(k-1)\pi f\frac{T_\mathrm{s}}{2}}\cdot\frac{\cos(k\pi f\frac{T_\mathrm{s}}{2})}{\cos(\pi f\frac{T_\mathrm{s}}{2})}\\ &\quad\cdot\left[\cos\left(k\pi f\frac{T_\mathrm{s}}{2}\right)\cos\left(\pi f\frac{T_\mathrm{s}}{2}\right)+\sin\left(k\pi f\frac{T_\mathrm{s}}{2}\right)\sin\left(\pi f\frac{T_\mathrm{s}}{2}\right)\right.\\ &\quad\left.+j\left(\sin\left(k\pi f\frac{T_\mathrm{s}}{2}\right)\cos\left(\pi f\frac{T_\mathrm{s}}{2}\right)-\cos\left(k\pi f\frac{T_\mathrm{s}}{2}\right)\sin\left(\pi f\frac{T_\mathrm{s}}{2}\right)\right)\right]\\ &= e^{-j2(k-1)\pi f\frac{T_\mathrm{s}}{2}}\cdot\frac{\cos(k\pi f\frac{T_\mathrm{s}}{2})}{\cos(\pi f\frac{T_\mathrm{s}}{2})}\cdot\left(\cos\left((k-1)\pi f\frac{T_\mathrm{s}}{2}\right)+j\sin\left((k-1)\pi f\frac{T_\mathrm{s}}{2}\right)\right)\\ &= e^{-j2(k-1)\pi f\frac{T_\mathrm{s}}{2}}\cdot\frac{\cos(k\pi f\frac{T_\mathrm{s}}{2})}{\cos(\pi f\frac{T_\mathrm{s}}{2})}\cdot e^{j(k-1)\pi f\frac{T_\mathrm{s}}{2}} = e^{-j(k-1)\pi f\frac{T_\mathrm{s}}{2}}\cdot\frac{\cos(k\pi f\frac{T_\mathrm{s}}{2})}{\cos(\pi f\frac{T_\mathrm{s}}{2})},\end{aligned} \tag{7.12}$$

which enables us to write the power spectral density of a sine phased BOC symbol with odd k as

$$P_{\mathrm{sinb}_{(m,n)}}(f) = \frac{1}{k\frac{T_\mathrm{s}}{2}}\cdot\left(\frac{\sin(\pi f\frac{T_\mathrm{s}}{2})\cos(k\pi f\frac{T_\mathrm{s}}{2})}{\pi f\cos(\pi f\frac{T_\mathrm{s}}{2})}\right)^2 = \frac{1}{f_\mathrm{c}}\cdot\left(\frac{\sin(\frac{\pi f}{2f_\mathrm{s}})\cos(\frac{\pi f}{f_\mathrm{c}})}{\frac{\pi f}{f_\mathrm{c}}\cos(\frac{\pi f}{2f_\mathrm{s}})}\right)^2. \tag{7.13}$$

For a cosine phased subcarrier, the derivation of the power spectral density is based on a $T_\mathrm{s}/4$ shifted version of (7.1) which results in

$$P_{\mathrm{cosb}_{(m,n)}}(f) = \begin{cases}\frac{1}{f_\mathrm{c}}\cdot\left(\frac{\left(\cos(\frac{\pi f}{2f_\mathrm{s}})-1\right)\sin(\frac{\pi f}{f_\mathrm{c}})}{\frac{\pi f}{f_\mathrm{c}}\cos(\frac{\pi f}{2f_\mathrm{s}})}\right)^2 \\ \frac{1}{f_\mathrm{c}}\cdot\left(\frac{\left(\cos(\frac{\pi f}{2f_\mathrm{s}})-1\right)\cos(\frac{\pi f}{f_\mathrm{c}})}{\frac{\pi f}{f_\mathrm{c}}\cos(\frac{\pi f}{2f_\mathrm{s}})}\right)^2\end{cases} \quad \text{if} \quad k\begin{cases}\text{even}\\ \text{odd.}\end{cases} \tag{7.14}$$

A2. Cramer Rao Bound of Galileo and GPS Signals

The Cramer Rao bound (CRB) is a lower bound on the estimation error of a real-valued parameter. It shall be derived according to Kay [9], Spilker [11] and Günther [1] and evaluated in this section for the Galileo and GPS code signals. Let τ be the unknown code delay and r be the received signal, then an unbiased estimator of τ is characterized by

$$\mathrm{E}\{\hat{\tau}(r)\} = \int \hat{\tau}(r) p(r|\tau) dr = \tau. \tag{7.15}$$

The CRB only exists if

$$\int \frac{\partial}{\partial \tau} p(r|\tau) dr = \frac{\partial}{\partial \tau} \int p(r|\tau) dr = 0, \tag{7.16}$$

i.e. the integration w.r.t. r and the differentiation w.r.t. τ have to be interchangeable. The derivation starts with

$$\begin{aligned} \int (\hat{\tau}(r) - \tau) \cdot \frac{\partial \log(p(r|\tau))}{\partial \tau} \cdot p(r|\tau) dr &= \int \hat{\tau}(r) \frac{\partial}{\partial \tau} p(r|\tau) dr - \int \tau \frac{\partial}{\partial \tau} p(r|\tau) dr \\ &= \frac{\partial}{\partial \tau} \int \hat{\tau}(r) p(r|\tau) dr - \tau \frac{\partial}{\partial \tau} \int p(r|\tau) dr = 1. \end{aligned} \tag{7.17}$$

Applying the Cauchy-Schwarz inequality yields

$$\begin{aligned} 1 &= \left| \int (\hat{\tau}(r) - \tau) \cdot \frac{\partial \log(p(r|\tau))}{\partial \tau} \cdot p(r|\tau) dr \right|^2 \\ &\leq \int |\hat{\tau}(r) - \tau|^2 p(r|\tau) dr \cdot \int |\frac{\partial}{\partial \tau} \log(p(r|\tau))|^2 p(r|\tau) dr, \end{aligned} \tag{7.18}$$

which gives the Cramer Rao bound as

$$\sigma^2_{\hat{\tau}(r)} \geq \frac{1}{\mathrm{E}_r\{|\frac{\partial}{\partial \tau} \log(p(r|\tau))|^2\}}, \tag{7.19}$$

which only depends on the conditional probability distribution of the received signal. For an AWGN-delay channel, $r(t)$ is given by

$$r(t) = \sqrt{P} s(t - \tau) + n(t), \tag{7.20}$$

with the transmit power P, the delay τ of the transmitted signal $s(t)$, and AWG noise $n(t) \sim \mathcal{N}(0, \sigma^2 = 2FN_0)$. As $s(t)$ has a limited bandwidth F, it is sufficient to sample the signal at times $t_n = n\Delta$ with $\Delta = 1/(2F)$ (Nyquist theorem), i.e.

$$r_n = r(n\Delta) = \sqrt{P} s(n\Delta - \tau). \tag{7.21}$$

A signal bandwidth of $F = 10$ MHz requires a sampling interval of at most 0.05μs which is short compared to the temporal variations in the code delay τ. Therefore, τ can be assumed constant over a certain number of samples N. The conditional probability distribution of $\boldsymbol{r} = [r_1, \ldots, r_N]^T$ for given τ is given by

$$p(\boldsymbol{r}|\tau) = \frac{1}{(2\pi\sigma^2)^N} e^{-\frac{1}{2\sigma^2}\sum_{i=1}^{N}\left(r_n - \sqrt{P}s(n\Delta-\tau)\right)^2}. \tag{7.22}$$

Computing the derivative with respect to τ yields

$$\frac{\partial}{\partial\tau}\log p(r|\tau) = \frac{\sqrt{P}}{\sigma^2}\sum_{i=1}^{N} n_i \frac{\partial s(i\Delta-\tau)}{\partial\tau}, \tag{7.23}$$

which enables us to determine the denominator of (7.19), i.e.

$$\mathrm{E}\{|\frac{\partial}{\partial\tau}\log p(r|\tau)|^2\} = \frac{P}{\sigma^4}\sum_{i,j}\mathrm{E}\{n_i^* n_j\}\frac{\partial s^*(i\Delta-\tau)}{\partial\tau}\frac{\partial s(j\Delta-\tau)}{\partial\tau} = \frac{P}{\sigma^2}\sum_{i=1}^{N}|\frac{\partial s(i\Delta-\tau)}{\partial\tau}|^2. \tag{7.24}$$

The term $\partial/\partial\tau(s(i\Delta-\tau))$ can also be expressed by the Fourier transform of $s(t)$, i.e.

$$\frac{\partial s(i\Delta-\tau)}{\partial\tau} = \int_{-F}^{F} S(f)(-j2\pi f)e^{j2\pi f(i\Delta-\tau)}df, \tag{7.25}$$

and the Parseval's theorem yields

$$\frac{P}{\sigma^2}\sum_{i=1}^{N}|\frac{\partial s(i\Delta-\tau)}{\partial\tau}|^2 = \frac{P}{\sigma^2}\int_{-F}^{F}|S(f)|^2(2\pi f)^2 df. \tag{7.26}$$

The Parseval's theorem is also used to compute the symbol energy from N samples as

$$E_\mathrm{s} = P\Delta\sum_{i=1}^{N}|s(i\Delta-\tau)|^2 = P\Delta\int_{-F}^{F}|S(f)|^2 df. \tag{7.27}$$

Combining (7.19), (7.26) and (7.27) gives the Cramer Rao bound (CRB) as a function of the power spectral density $S(f)$ and of the signal to noise ratio:

$$\sigma_{\hat{\tau}}^2 \geq \frac{\int|S(f)|^2 df}{\frac{E_\mathrm{s}}{N_0}\int|S(f)|^2(2\pi f)^2 df}. \tag{7.28}$$

The Binary Offset Carrier modulation shifts the power to higher frequencies which increases $\int|S(f)|^2(2\pi f)^2 df$ and, thus, results in a lower CRB. Tab. 1.2 and 1.3 show the CRBs for the Galileo and GPS signals for a signal to noise ratio of $E_\mathrm{s}/N_0 = 45$dB. Low cost GPS receivers use only a bandwidth of 2 MHz which results in a CRB of 78.29 cm for the BPSK(1) modulated L1 signal. A BOC(1,1) modulated signal with sine phasing and a bandwidth of 20 MHz benefits from a CRB of 14.81 cm, and the MBOC modulation

further reduces the CRB to 11.13 cm. The lowest noise level of only 1.62 cm is achieved by the AltBOC(15,10) modulated Galileo signal on E5 with a bandwidth of $90 \cdot 1.023$ MHz. This low code noise substantially improves the reliability of carrier phase integer ambiguity resolution.

The further analysis is restricted to the signals of the Open Service (OS), the Safety of Life (SoL) service and the Commercial Service (CS). Note that the E1, E5a, E5b and E6 channels also include dataless pilot signals which can be integrated over a longer time. A longer integration time turns into a larger E_s/N_0 and, thus, a lower CRB.

A3. Float solution of baseline and ambiguities

The baseline and double difference ambiguities are first estimated as real-valued parameters by disregarding the integer nature of ambiguities. The code measurements of receiver r, satellite k and frequency m are modeled as

$$\begin{aligned} \rho^k_{m,r}(t_n) &= \|\boldsymbol{r}_r(t_n) - \boldsymbol{r}^k(t'_n)\| + c\left(\delta\tau_r(t_n) - \delta\tau^k(t'_n)\right) + I^k_{m,r}(t_n) + T^k_r(t_n) \\ &\quad + b_{m,r} + b^k_m + \eta^k_{m,r}(t_n), \end{aligned} \tag{7.29}$$

where t_n is the time of reception and t'_n is the unknown time of transmission respectively. Similarly, the phase measurements are written as

$$\begin{aligned} \lambda_1\phi^k_{m,r}(t_n) &= \|\boldsymbol{r}_r(t_n) - \boldsymbol{r}^k(t'_n)\| + c\left(\delta\tau_r(t_n) - \delta\tau^k(t'_n)\right) + I^k_{m,r}(t_n) + T^k_r(t_n) \\ &\quad + \lambda_m N^k_{m,r} + \beta_{m,r} + \beta^k_m + \epsilon^k_{m,r}(t_n). \end{aligned} \tag{7.30}$$

Both (7.29) and (7.30) represent a nonlinear relationship between the receiver position and the measurement and, thus, require an iterative solution.

The satellite position $\boldsymbol{r}^k(t'_n)$ and the satellite clock offset $c\delta\tau^k(t'_n)$ are computed from the ephemeris data of the navigation message, the time of reception t_n, and the pseudorange measurements $\rho^k_r(t_n)$ to correct for the traveltime between the satellite and receiver. The time of transmission t'_n is estimated as

$$t'_n = t_n - \frac{\rho^k_r(t_n)}{c} - \delta\hat{\tau}^k\left(t_n - \frac{\rho^k_r(t_n)}{c}\right), \tag{7.31}$$

where the satellite clock correction is given by

$$\delta\hat{\tau}^k(t) = a_{f_0} + a_{f_1}\cdot(t - t_{\mathrm{oe}}) + a_{f_2}\cdot(t - t_{\mathrm{oe}})^2 - t_{\mathrm{gd}} + d_{\mathrm{rel}}, \tag{7.32}$$

with the satellite clock offset a_{f_0}, the satellite clock drift a_{f_1}, the satellite clock acceleration a_{f_2}, the time of ephemeris t_{oe}, the group delay correction t_{gd} and the relativistic correction d_{rel}. The satellite clock correction is then re-estimated with (7.32) using the corrected time of transmission t'_n of (7.31). The satellite position in an elliptical orbit (Fig. 7.1) is

given by

$$\boldsymbol{r}(t'_n) = \frac{a(1-e^2)}{1+e\cos(\nu(t'_n))} \begin{bmatrix} \cos(\nu(t'_n)) \\ \sin(\nu(t'_n)) \\ 0 \end{bmatrix}, \tag{7.33}$$

with the semi-major axis a, the eccentricity e and the true anomaly ν. Alternatively, $\boldsymbol{r}$ can be expressed as a function of the eccentric anomaly E, i.e.

$$\boldsymbol{r}(t'_n) = \begin{bmatrix} a\cos(E(t'_n)) - ae \\ a\sqrt{1-e^2}\sin(E(t'_n)) \\ 0 \end{bmatrix}. \tag{7.34}$$

The magnitude of this vector is the orbital radius

$$r(t'_n) = a(1 - e\cos(E(t'_n))). \tag{7.35}$$

Combining (7.33) and (7.33) yields the true anomaly ν:

$$\nu(t'_n) = \operatorname{atan}\left(\frac{\sqrt{1-e^2}\cdot\sin(E(t'_n))}{\cos(E(t'_n)) - e}\right). \tag{7.36}$$

The velocity vector is obtained from (7.34) as

$$\dot{\boldsymbol{r}}(t'_n) = \begin{bmatrix} -a\sin(E(t'_n))\dot{E}(t'_n) \\ a\sqrt{1-e^2}\cos(E(t'_n))\dot{E}(t'_n) \\ 0 \end{bmatrix}. \tag{7.37}$$

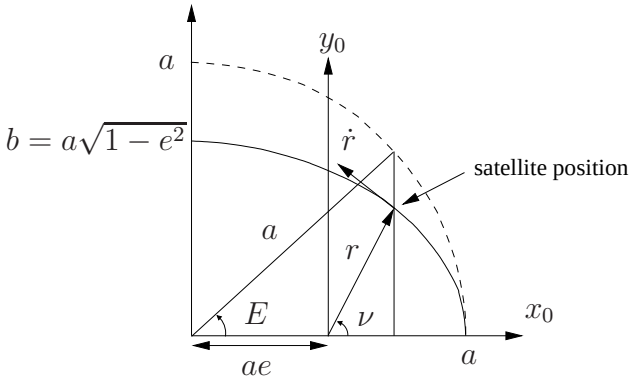

Figure 7.1: Position and velocity of a satellite in Keplerian orbit. An artifical circular orbit has been added for the derivation of the true anomaly.

The angular momentum is derived from (7.34) and (7.37) as

$$\boldsymbol{L} = m(\boldsymbol{r}\times\dot{\boldsymbol{r}}) = L\cdot\boldsymbol{e}_z = mab\cdot\dot{E}(t)'_n\,(1 - e\cos(E(t'_n)))\cdot\boldsymbol{e}_z \tag{7.38}$$

with the mass m of the satellite and the semi-minor axis b . Eq. (7.38) can be rearranged

as

$$\dot{E}(t'_n)\,(1 - e\cos(E(t'_n))) = \frac{L}{mab}, \tag{7.39}$$

which can be rewritten with Kepler's second law as

$$\frac{L}{mab} = \frac{2\pi}{T} = n, \tag{7.40}$$

with the orbital period T and the mean motion n. The latter one is easily obtained from Kepler's third law, i.e.

$$n = \sqrt{GM/a^3}. \tag{7.41}$$

Integrating (7.39) yields

$$E(t'_n) - e\sin(E(t'_n)) = n(t'_n - t_{\mathrm{oe}}) + M_0(t_{\mathrm{oe}}) = M(t'_n), \tag{7.42}$$

where M is called the mean anomaly that increases linear with time. Eq. (7.42) can be solved only iteratively, e.g. by the Gauss-Newton method:

$$\hat{E}_{i+1}(t'_n) = \hat{E}_i(t'_n) - \frac{f(\hat{E}_i(t'_n))}{f'(\hat{E}_i(t'_n))}, \tag{7.43}$$

which converges within a few iterations with the initialization $\hat{E}_1(t'_n) = M$.

The receiver computes the satellite positions from the Keplerian parameters and their linear and harmonic corrections as follows: First, the mean motion $n = \sqrt{GM/a^3} + \delta n$ is determined, followed by the mean anomaly M of (7.42), the eccentric anomaly of E (7.43), the orbital radius r of (7.35) and the true anomaly ν of (7.36). The argument of perigee ω and ν are then combined to the argument of latitude which is given by

$$\phi(t'_n) = \omega + \nu(t'_n). \tag{7.44}$$

In the next step, the second harmonic corrections are applied to the argument of latitude, the orbital radius and the inclination i, i.e.

$$\begin{aligned}
\tilde{\phi}_k(t'_n) &= \phi_k(t'_n) + C_{\mathrm{uc}}\cos(2\phi(t'_n)) + C_{\mathrm{us}}\sin(2\phi(t'_n)) \\
\tilde{r}(t'_n) &= r(t'_n) + C_{\mathrm{rc}}\cos(2\phi(t'_n)) + C_{\mathrm{rs}}\sin(2\phi(t'_n)) \\
i(t'_n) &= i_0(t_{\mathrm{oe}}) + \dot{i}(t'_n - t_{\mathrm{oe}}) + C_{\mathrm{ic}}\cos(2\phi(t'_n)) + C_{\mathrm{is}}\sin(2\phi(t'_n)),
\end{aligned} \tag{7.45}$$

and linear correction is used for the right ascension of the ascending node Ω:

$$\Omega(t'_n) = \Omega_0 + (\dot{\Omega} - \dot{\Omega}_{\mathrm{e}})(t'_n - t_{\mathrm{oe}}) - \dot{\Omega}_{\mathrm{e}} t_{\mathrm{oe}}, \tag{7.46}$$

where $\dot{\Omega}_{\mathrm{e}} = 7.2921151467 \cdot 10^{-5}$ rad/s denotes the angular velocity of the earth rotation. Finally, the satellite position is transformed from the orbital into the earth-centered, earth

fixed coordinate (ECEF) frame by rotations about the x and z axes:

$$\boldsymbol{r}^k(t'_n) = \begin{bmatrix} r_x(t'_n) \\ r_y(t'_n) \\ r_z(t'_n) \end{bmatrix} = \boldsymbol{R}_z(-\Omega(t'_n))\boldsymbol{R}_x(-i(t'_n)) \begin{bmatrix} r(t'_n)\cos(\phi(t'_n)) \\ r(t'_n)\sin(\phi(t'_n)) \\ 0 \end{bmatrix}. \tag{7.47}$$

Both $c\hat{\delta}^k(t'_n)$ and $\boldsymbol{r}^k(t'_n)$ are used for the estimation of the float baseline solution, which is determined iteratively with the Gauss-Newton method. The measurements are processed as double differences to eliminate biases, i.e.

$$\begin{aligned} \Delta\rho^{1k}_{\mathrm{o},12}(t_n) &= \left(\rho^k_1(t_n) - \rho^1_1(t_n)\right) - \left(\rho^k_2(t_n) - \rho^1_2(t_n)\right) \\ \lambda_1\Delta\phi^{1k}_{\mathrm{o},12}(t_n) &= \left(\lambda_1\phi^k_1(t_n) - \lambda_1\phi^1_1(t_n)\right) - \left(\lambda_1\phi^k_2(t_n) - \lambda_1\phi^1_2(t_n)\right), \end{aligned} \tag{7.48}$$

where an additional index has been introduced to distinguish between computed (c) and observed (o) ranges. The Gauss-Newton method is initialized by a guess of the receiver position $\hat{\boldsymbol{r}}_2(t_n)$ (which results in $\hat{\boldsymbol{b}}(t_n) = \boldsymbol{r}_1(t_n) - \hat{\boldsymbol{r}}_2(t_n)$) and float ambiguities $\hat{N}^{1k}_{12}$.

Each iteration starts with the computation of the traveltime correction that is given by

$$\delta t^k_r(t_n) = \frac{1}{c} \cdot \|\boldsymbol{r}^k(t'_n) - \hat{\boldsymbol{r}}_r(t_n)\|. \tag{7.49}$$

It is used to transform the satellite position in ECEF coordinates due to the earth rotation during the traveltime, i.e.

$$\boldsymbol{r}'^k(t'_n) = \boldsymbol{R}_z\left(\dot{\Omega}_\mathrm{e}\delta t^k_r(t_n)\right)\boldsymbol{r}^k(t'_n), \tag{7.50}$$

which enables the computation of the range from the satellite and receiver positions:

$$\rho^k_{\mathrm{c},r}(t_n) = \|\boldsymbol{r}'^k(t'_n) - \hat{\boldsymbol{r}}_r(t_n)\|. \tag{7.51}$$

Assuming a short baseline, the differential geometry matrix is given by

$$\boldsymbol{H} = \left[\begin{array}{ccc|ccc} \boldsymbol{H}(t_1) & & & \lambda_1\mathbf{1} & & \\ & \ddots & & & \ddots & \\ & & \boldsymbol{H}(t_N) & & & \lambda_1\mathbf{1} \\ \hline \boldsymbol{H}(t_1) & & & & & \\ & \ddots & & & \mathbf{0} & \\ & & \boldsymbol{H}(t_N) & & & \end{array}\right] \tag{7.52}$$

with

$$\boldsymbol{H}(t_n) = \begin{bmatrix} (\boldsymbol{e}^2(t_n))^T - (\boldsymbol{e}^1(t_n))^T \\ \vdots \\ (\boldsymbol{e}^K(t_n))^T - (\boldsymbol{e}^1(t_n))^T \end{bmatrix} \quad \text{and} \quad \boldsymbol{e}^k(t_n) = \frac{\hat{\boldsymbol{r}}_2(t_n) - \boldsymbol{r}'^k(t'_n)}{\|\hat{\boldsymbol{r}}_2(t_n) - \boldsymbol{r}'^k(t'_n)\|}. \tag{7.53}$$

The double difference *computed* ranges are obtained from (7.51) as

$$\Delta\rho^{1k}_{\mathrm{c},12}(t_n) = \left(\rho^{k}_{\mathrm{c},1}(t_n) - \rho^{1}_{\mathrm{c},1}(t_n)\right) - \left(\rho^{k}_{\mathrm{c},2}(t_n) - \rho^{1}_{\mathrm{c},2}(t_n)\right). \tag{7.54}$$

The float ambiguity corrections from the previous iteration are then applied to the double difference *observed* ranges, i.e.

$$\lambda_1\Delta\phi^{1k}_{\mathrm{o},12}(t_n) := \lambda_1\Delta\phi^{1k}_{\mathrm{o},12}(t_n) - \lambda_1\Delta\hat{N}^{1k}_{12}. \tag{7.55}$$

The residuals between the double difference computed and observed ranges are calculated from (7.54), (7.48) and (7.55):

$$\begin{aligned} \Delta\rho^{1k}_{\mathrm{omc},12}(t_n) &= \Delta\rho^{1k}_{\mathrm{o},12}(t_n) - \Delta\rho^{1k}_{\mathrm{c},12}(t_n) \\ \lambda_1\Delta\phi^{1k}_{\mathrm{omc},12}(t_n) &= \lambda_1\Delta\phi^{1k}_{\mathrm{o},12}(t_n) - \lambda_1\Delta\phi^{1k}_{\mathrm{c},12}(t_n). \end{aligned} \tag{7.56}$$

A least-squares estimation provides new baseline and ambiguity corrections, i.e.

$$\begin{bmatrix} \Delta\hat{\boldsymbol{b}}(t_1) \\ \vdots \\ \Delta\hat{\boldsymbol{b}}(t_N) \\ \Delta\hat{\boldsymbol{N}} \end{bmatrix} = \left(\boldsymbol{H}^T\boldsymbol{\Sigma}^{-1}\boldsymbol{H}\right)^{-1}\boldsymbol{H}^T\boldsymbol{\Sigma}^{-1}\begin{bmatrix} \lambda_1\boldsymbol{\Delta\phi}_{\mathrm{omc}} \\ \boldsymbol{\Delta\rho}_{\mathrm{omc}} \end{bmatrix}, \tag{7.57}$$

which are used to update the float ambiguities and position estimates:

$$\begin{aligned} \hat{\boldsymbol{N}} &:= \hat{\boldsymbol{N}} + \Delta\hat{\boldsymbol{N}} \\ \hat{\boldsymbol{r}}_2(t_n) &:= \hat{\boldsymbol{r}}_2(t_n) - \Delta\hat{\boldsymbol{b}}(t_n). \end{aligned} \tag{7.58}$$

Eq. (7.49)-(7.58) are repeated until the residuals have converged to an irreducible error. The float baseline estimate is obtained from the known reference station position $\boldsymbol{r}_1(t_n)$ and $\hat{\boldsymbol{r}}_2(t_n)$, i.e. $\hat{\boldsymbol{b}}(t_n) = \boldsymbol{r}_1(t_n) - \hat{\boldsymbol{r}}_2(t_n)$.

Bibliography

[1] C. Günther, Satellite Navigation, to appear, **2010**.

[2] R. Zandbergen, S. Dinwiddy, J. Hahn, E. Breeuwer and D. Blonski, Galileo Orbit Selection, *Proc. of ION GNSS*, Long Beach, USA, pp. 616-624, **2004**.

[3] J. Betz, Binary Offset Carrier Modulations for Radionavigation, *Navigation*, vol. 48, no. 4, pp. 227-246, **2002**.

[4] G. Hein, J. Avila-Rodriguez, S. Wallner, A. Pratt, J. Owen, J.-L. Issler, J. Betz, C. Hegarty, S. Lenahan, J. Rushanan, A. Kraay and T. Stansell, MBOC: The New Optimized Spreading Modulation Recommended for GALILEO L1 OS and GPS L1C, *Proc. of IEEE/ ION Pos., Loc. and Nav. Symp. (PLANS)*, pp. 883-892, **2006**.

[5] Galileo Open Service Signal-in-Space ICD, Draft 1, Feb. 2008, http://www.gsa.europa.eu, accessed on: February 10, 2010.

[6] G. Hein, J. Godet, J.-L. Issler, J. C. Martin, P. Erhard, R. Lucas-Rodriguez and T. Pratt, Status of Galileo Frequency and Signal Design, *Proc. of ION GPS*, **2002**.

[7] J. Avila-Rodriguez, G. Hein, S. Wallner, J.-L. Issler, L. Ries, L. Lestarquit, A. de Latour, J. Godet, F. Bastide, T. Pratt and J. Owen, The MBOC Modulation: A Final Touch for the Galileo Frequency and Signal Plan, *Inside GNSS*, **2007**.

[8] P. Misra and P. Enge, Global Positioning System - Signals, Measurements, and Performance, Ganga-Jamuna Press, Lincoln (MA), USA, 2nd edition, **2006**.

[9] S. Kay, Fundamentals of statistical signal processing, *Prentice-Hall*, Englewood Cliffs, NJ, **1993**.

[10] J. Sennott and D. Senffer, The use of satellite constellation geometry and a priori motion constraints for prevention of cycle slips in a GPS signal processor, *Navigation*, vol. 39, no. 2, pp. 217-236, **1992**.

[11] J. Spilker, Fundamentals of Signal Tracking Theory, *Global Positioning System: Theory and Application Volume I*, edited by B. Parkinson and J. Spilker, Progress in Aeronautics and Astronautics, vol. 163, **1996**.

[12] K. Giger, P. Henkel and C. Günther, Multifrequency multisatellite carrier tracking, *Proc. of 4-th Europ. Worksh. on GNSS Sig. and Sig. Proc.*, Oberpfaffenhofen, Germany, **2009**.

[13] K. Giger, P. Henkel and C. Günther, Joint satellite code and carrier tracking, *Proc. of ION Int. Techn. Meet. (ITM)*, San Diego, USA, **2010**.

[14] G. Jee, GNSS receiver tracking loop optimization for combined phase, frequency and delay locked loops, *Proc. of Europ. Nav. Conf. (ENC)*, Munich, Germany, **2005**.

[15] C. Driscoll and G. Lachapelle, Comparison of traditional and Kalman filter based tracking archictures, *Proc. of Europ. Nav. Conf. (ENC)*, Naples, Italy, **2009**.

[16] P. Henkel, G. Gao, T. Walter and C. Günther, Robust Multi-Carrier, Multi-Satellite Vector Phase Locked Loop with Wideband Ionospheric Correction and Integrated Weighted RAIM, *Proc. of Europ. Nav. Conf. (ENC)*, Naples, Italy, **2009**.

[17] S. Bassiri and G. Hajj, Higher Order Ionospheric Effects on the Global Positioning Systems Observables and Means of Modelling them, *M. Geod.*, vol. 18, pp. 280-289, **1993**.

[18] M. Hoque and N. Jakowski, Higher order ionospheric effects in precise GNSS positioning, *J. of Geodesy*, **2003**.

[19] P. Joosten and M. Irsigler, GNSS ambiguity resolution in the presence of multipath, *Proc. of ION GNSS*, **2003**.

[20] M. Irsigler, G. Hein and A. Schmitz-Peiffer, Use of C-Band frequencies for satellite navigation: benefits and drawbacks, *GPS Solut.*, vol. 8, pp. 119-139, **2004**.

[21] M. Zhodzishsky, S. Yudanov, V. Veitsel and J. Ashjaee, Co-Op Tracking for carrier phase, *Proc. of ION-GPS*, pp. 653-664, Nashville (TN), USA, Sep. 1998, also U.S. patent (6.313.789 B1), **1998**.

[22] P. Henkel, K. Giger and C. Günther, Multi-Carrier Vector Phase Locked Loop for Robust Carrier Tracking, *Proc. of Europ. Nav. Conf.*, Toulouse, France, **2008**.

[23] P. Henkel, K. Giger and C. Günther, Multifrequency, Multisatellite Vector Phase-Locked Loop for Robust Carrier Tracking, *IEEE J. of Sel. Topics in Signal Proc.*, Vol. 3, No. 4, **2009**.

[24] S. Pullen, Y.-S. Park and P. Enge, The Impact and Mitigation of Ionosphere Anomalies on Ground Based Augmentation of GNSS, *Proc. of 12-th Int. Ionosph. Effects Symp.*, **2008**.

[25] R. Stengel, Optimal Control and Estimation, Dover Publ., New York, USA, **1994**.

[26] A. Niell, Global Mapping Functions for the Atmosphere Delay at Radio Wavelengths, *J. Geophys. Res.*, vol. 101, pp. 3227-3246, **1996**.

[27] A. Dierendonck, GPS Receivers, Global Positioning System: Theory and Application Volume I, edited by B. Parkinson and J. Spilker, Progress in Aeronautics and Astronautics, vol. 163, **1996**.

[28] E. Kaplan and C. Hegarty, Understanding GPS - Principles and applications, 2nd edition, Artech House, **2006**.

[29] P. Teunissen, Adjustment theory - an introduction, *Series on Math. Geod. and Pos.*, TU Delft, The Netherlands, **2003**.

[30] C. Hegarty, M. El-Arini, T. Kim and S. Ericson, Scintillation modeling for GPS-Wide Area Augmentation System receivers, *Radio Science*, vol. 36, no. 5, pp. 1221-1231, **2001**.

[31] S. Pullen, G. Opshaug, A. Hansen, T. Walter, P. Enge and B. Parkinson, A Preliminary Study of the Effect of Ionospheric Scintillation on WAAS User Availability in Equatorial Regions, *Proc. of ION-GPS '98*, pp. 687-699, Nashville, USA, **1998**.

[32] S. Basu, 250 MHz/GHz Scintillation parameters in the Equatorial, Polar, and Auroral Envrionments, *IEEE J. of Sel. Areas in Comm.*, vol. SAC-5, no. 2, pp. 102-115, **1987**.

[33] J. Seo, T. Walter, E. Marks, T. Chiou and P. Enge, Ionospheric Scintillation Effects on GPS Receivers during Solar Minimum and Maximum, *Proc. of Int. Beacon Sat. Symp.*, Boston (MA), USA, **2007**.

[34] G. Gao, S. Datta-Barua, T. Walter and P. Enge, Ionospheric Effects for Wideband GNSS Signals, *ION Ann. Meet.*, Cambridge (MA), USA, **2007**.

[35] P. Hwang, G. Graw and J. Bader, Enhanced Differential GPS Carrier-Smoothed Code Processing Using Dual-Frequency Measurements, *J. of Navigation*, vol. 46, no. 2, pp. 127-137, Summer **1999**.

[36] T. Walter and P. Enge, Weighted RAIM for Precision Approach, *Proc. of ION-GPS*, pp. 1995-2004, Palm. Springs (CA), USA, **1995**.

[37] Y. Georgiadou and A. Kleusberg, On carrier signal multipath effects in relative GPS positioning, *M. Geod.*, Springer, vol. 13, pp. 172-179, **1988**.

[38] Bernese GPS Software, Astronomical Institute, University of Bern, pp. 1-640, **2007**.

[39] M. Cocard, S. Bourgon, O. Kamali and P. Collins, A systematic investigation of optimal carrier-phase combinations for modernized triple-frequency GPS, *J. of Geodesy*, vol. 82., pp. 555-564, **2008**.

[40] M. Cocard and A. Geiger, Systematic search for all possible widelanes, *Proc. of 6-th Int. Geod. Symp. on Sat. Pos.*, Ohio, USA, pp. 312-318, **1992**.

[41] P. Collins, An overview of GPS inter-frequency carrier phase combinations, *Techn. Memor.*, Geodetic Survey Division, University of New Brunswick, Canada, pp. 1-15, **1999**.

[42] P. Henkel and C. Günther, Three frequency linear combinations for Galileo, *Proc. of 4-th IEEE Worksh. on Pos., Nav. and Comm. (WPNC)*, Hannover, Germany, pp. 239-245, **2007**.

[43] T. Richert and N. El-Sheimy, Optimal linear combinations of triple frequency carrier phase data from future global navigation satellite systems, *GPS Solut.*, vol. 11, pp. 11-19, DOI 10.1007/s10291-006-0024-x, **2007**.

[44] G. Wübbena, New GNSS Signals and Ambiguity Resolution, *Proc. of EGU Gen. Ass.*, Vienna, Austria, **2007**.

[45] P. Henkel, V. Gomez and C. Günther, Modified LAMBDA for absolute carrier phase positioning in the presence of biases, *Proc. of Int. Techn. Meet. (ITM)*, Anaheim, USA, pp. 642-651, **2009**.

[46] P. Henkel and C. Günther, Joint L-/C-Band Code and Carrier Phase Linear Combinations for Galileo, *Int. J. of Nav. and Obs.*, vol. 2008, pp. 1-8, doi:10.1155/2008/651437, **2008**.

[47] P. Henkel, Bootstrapping with Multi-Frequency Mixed Code Carrier Linear Combinations and Partial Integer Decorrelation in the Presence of Biases, *Proc. of Int. Assoc. of Geod. Scient. Ass.*, Buenos Aires, Argentina, **2009**.

[48] R. Hatch, The Synergism of GPS Code and Carrier Measurements, *Proc. Third Int. Geod. Symp. on Sat. Doppl. Pos.*, vol. II, New Mexico, USA, pp. 1213-1232, **1982**.

[49] P. Hwang, G. Mc Graw, and J. Bader, Enhanced Differential GPS Carrier-Smoothed Code Processing Using Dual-Frequency Measurements, *J. of Navigation*, vol. 46, no. 2, pp. 127-137, Summer **1999**.

[50] G. Mc Graw and P. Young, Dual Frequency Smooting DGPS Performance Evaluation Studies, *Proc. of ION Nat. Techn. Meet. (NTM)*, San Diego (CA), USA, pp. 16-24, **2005**.

[51] C. Günther and P. Henkel, Reduced noise, ionosphere-free carrier smoothed code, *IEEE Trans. on Aerosp. and Elec. Systems*, **2008**.

[52] J. Angus, RAIM with multiple faults, *Navigation*, 53(4), pp. 249-257, **2006**.

[53] R. Hatch, A new three-frequency, geometry-free technique for ambiguity resolution, *Proc. of ION GNSS 19th Int. Techn. Meet. (ITM)*, Fort Worth, USA, pp. 309-319, **2006**.

[54] H. Henderson and S. Searle, On Deriving the Inverse of a Sum of Matrices, *J. of the Soc. for Ind. and Appl. Math. (SIAM)*, vol. 23, no. 1, pp. 53-60, **1981**.

[55] A. Genz, Numerical Computation of Multivariate Normal Probabilities, *J. of Comp. and Graph. Stat.*, pp. 141-149, **1992**.

[56] P. Teunissen, Integer estimation in the presence of biases, *J. of Geodesy*, vol. 75, pp. 399-407, Springer, **2001**.

[57] P. Teunissen, Success Probability of Integer GPS Ambiguity Rounding and Bootstrapping, *J. of Geodesy*, vol. 72, pp. 606-612, Springer, **1998**.

[58] G. Blewitt, Carrier-phase ambiguity resolution for the Global Positioning System applied to geodetic baselines up to 2000 km, *J. Geophys. Res.*, vol. 94, pp. 10187-10203, **1989**.

[59] P. Teunissen, A new method for fast carrier phase ambiguity estimation, *Proc. of IEEE Pos., Loc. and Nav. Symp.* (PLANS), Las Vegas, USA, pp. 562-573, **1994**.

[60] P. Teunissen, GNSS Ambiguity Bootstrapping: Theory and Application, *Proc. of Int. Symp. on Kin. Syst. in Geod., Geomat. and Nav.*, Banff, Canada, pp. 246-254, **2001**.

[61] P. Teunissen, Statistical GNSS carrier phase ambiguity resolution: A review, *Proc. of the 11-th IEEE Worksh. on Stat. Sign. Proc.* (SSP), pp. 4-12, **2001**.

[62] P. Teunissen, Least-Squares Estimation of the Integer GPS Ambiguities, Invited lecture, Section IV "Theory and Methodology", *Proc. of Gen. Meet. of the Int. Assoc. of Geodesy*, Beijing, China, pp. 1-16, **1993**.

[63] P. Teunissen, The least-squares ambiguity decorrelation adjustment: a method for fast GPS ambiguity estimation, *J. of Geodesy*, vol. 70, pp. 65-82, **1995**.

[64] P. de Jonge and C. Tiberius, The LAMBDA method for integer ambiguity estimation: implementation aspects, LGR-Series, *Publ. of the Delft Geod. Comp. Centre*, no. 12, pp. 1-59, **1996**.

[65] T. Apostol, Multi-variable calculus and linear algebra, with applications to differential equations and probability, *Calculus*, vol. 2, Second edition, Wiley, New York, **1969**.

[66] P. Teunissen, Integer Aperture GNSS Ambiguity Resolution, *Art. Satellites*, vol. 38, Nr. 3, pp. 79-88, **2003**.

[67] S. Verhagen, The GNSS integer ambiguities: estimation and validation, *PhD thesis*, Delft University of Technology, **2004**.

[68] P. Teunissen, The LAMBDA method for the GNSS Compass, *Art. Satellites*, vol. 41, nr. 3, **2006**.

[69] G. Giorgi, P. Teunissen, S. Verhagen and P. Buist, Improving the GNSS Attitude Ambiguity Success Rate with the Multivariate Constrained LAMBDA Method, *Proc. of IAG Int. Assoc. of Geod. Scient. Ass.*, Buenos Aires, Argentina, **2009**.

[70] P. Teunissen and A. Kleusberg (Eds.), GPS for Geodesy, Springer, 2nd edition, Heidelberg, Germany, **1998**.

[71] J. Zumberge, M. Heflin, D. Jefferson, M. Watkins and F. Webb, Precise point positioning for the efficient and robust analysis of GPS data from large networks, *J. of Geophys. Res.*, vol. 102, no. B3, pp. 5005-5017, **1997**.

[72] P. Teunissen, P. de Jonge and C. Tiberius, The least-squares ambiguity decorrelation adjustment: its performance on short GPS baselines and short observation spans, *J. of Geodesy*, vol. 71, pp. 589-602, **1997**.

[73] G. McGraw, T. Murphy, M. Brenner, S. Pullen and AJ Van Dierendonck, Development of the LAAS Accuracy Models, *Proc. of ION GPS*, Salt Lake City, USA, **2000**.

[74] P. Henkel and C. Günther, Partial integer decorrelation for optimum trade-off between variance reduction and bias amplification, *J. of Geodesy*, pp. 1-13, **2009**.

[75] R. Hatch, The promise of a third frequency, *GPS World*, vol. 7, no. 5, pp. 55-58, **1996**.

[76] B. Forssell, M. Martin-Neira and R. Harris, Carrier Phase Ambiguity Resolution in GNSS-2, *Proc. of ION-GPS*, Kansas City, USA, pp. 1727-1736, **1997**.

[77] J. Jung, High integrity carrier phase navigation using multiple civil GPS signals, *PhD thesis*, Stanford University, **2000**.

[78] J. Jung, P. Enge and B. Pervan, Optimization of Cascade Integer Ambiguity Resolution with Three Civil GPS Frequencies, *Proc. of ION GPS*, 2000.

[79] P. Henkel and C. Günther, Integrity Analysis of Cascaded Integer Resolution with Decorrelation Transformations, *Proc. of ION Nat. Techn. Meet. (ITM)*, San Diego, USA, pp. 903-910, **2007**.

[80] P. Teunissen, P. Joosten and C. Tiberius, Geometry-free Ambiguity Success Rates in case of Partial Fixing, *Proc. of ION Nat. Tech. Meet. (ITM)*, San Diego, USA, 7 pages, **1999**.

[81] W. Cao, K. O'Keefe and M. Cannon, Partial Ambiguity Fixing within Multiple Frequencies and Systems, *Proc. of ION GNSS*, Fort Worth, USA, pp. 312-323, **2007**.

[82] P. Henkel, Geometry-free linear combinations for Galileo, *Proc. of 58-th Int. Astron. Congr. (IAC)*, Hyderabad, India, pp. 1-14, **2007**.

[83] P. Henkel, Geometry-free linear combinations for Galileo, *Acta Astron.*, vol. 65, pp. 1487-1499, doi:10.1016/j.actaastro.2009.03.076, **2009**.

[84] G. Wübbena, Software developments for geodetic positioning with GPS using TI-4100 code and carrier measurements, *Proc. of 1-st Int. Symp. on Prec. Pos. with the Glob. Pos. Sys.*, Rockville, USA, pp. 403-412, **1985**.

[85] R. Schmid, M. Rothacher, D. Thaller and P. Steigenberger, Absolute phase center corrections of satellite and receiver antennas, *GPS Solut.*, vol. 9, pp. 283û293, DOI 10.1007/s10291-005-0134-x, **2005**.

[86] R. Schmid and M. Rothacher, Estimation of elevation-dependent satellite antenna phase center variations of GPS satellite, *J. of Geodesy*, vol. 77, pp. 440-446, DOI 10.1007/s00190-003-0339-0, **2003**.

[87] R. Dach, U. Hugentobler, P. Fridez and M. Meindl, *Bernese GPS Software, version 5.0*, Astronomical Institute, University of Bern, 640 pages, **2007**.

[88] M. Gabor and S. Nerem, Satellite-satellite single difference phase calibration as applied to ambiguity resolution, *Navigation*, vol. 49, nr. 4, pp. 223-242, **2002**.

[89] M. Ge, G. Gendt, M. Rothacher, C. Shi and J. Liu, Resolution of GPS carrier-phase ambiguities in Precise Point Positioning (PPP) with daily observations, *J. of Geodesy*, Springer, **2007**.

[90] D. Laurichesse and F. Mercier, Integer ambiguity resolution on undifferenced GPS phase measurements and its application to PPP, *Proc. of ION-GNSS*, Forth Worth, USA, **2007**.

[91] G. Wübbena, GPS carrier phases and clock modeling, Lecture Notes in Earth Sciences: *GPS Techn. Appl. to Geod. and Surv.*, vol. 19, pp. 381-392, DOI: 10.1007/BFb0011350, **1988**.

[92] P. Henkel, Z. Wen and C. Günther, Estimation of phase and code biases on multiple frequencies with a Kalman filter, *Proc. of 4-th Europ. Worksh. on GNSS Signals and Sign. Proc.*, Oberpfaffenhofen, Germany, **2009**.

[93] P. Henkel, Z. Wen and C. Günther, Estimation of satellite and receiver biases on multiple Galileo frequencies with a Kalman filter, *Proc. of ION Int. Techn. Meet. (ITM)*, San Diego, USA, **2010**.

[94] S. Schlötzer, High integrity carrier phase based relative positioning for precise landing using a robust nonlinear filter, *Mast. thesis*, Technische Universität München, 174 pp., **2009**.

[95] R. Brown and P. Hwang, Introduction to random signals and applied Kalman filtering, 3rd edition, John Wiley and Sons, New York, **1997**.

[96] B. Arbesser-Rastburg, Ionospheric corrections for satellite navigation using EGNOS, *Proc. of XXVII-th URSI Gen. Ass.*, Maastricht, **2002**.

[97] RTCA, Minimum Aviation System Performance Standards for the Local Area Augmentation System (LAAS), RTCA/DO-245A, **2004**.

[98] S. Khanafseh and B. Pervan, A New Approach for Calculating Position Domain Integrity Risk for Cycle Resolution in Carrier Phase Navigation Systems, *Proc. of ION/ IEEE Pos., Loc. and Nav. Symp.* (PLANS), Monterey, USA, pp. 583-591, **2008**.

[99] B. Hofmann-Wellenhof, H. Lichtenegger and E. Wasle, GNSS - Global Navigation Satellite Systems: GPS, GLONASS, Galileo, and more, Springer, Wien, **2008**.